STUDY OF THERMO-PHYSICAL PROPERTIES, HEAT TRANSFER, AND FRICTIONAL LOSS OF GNPS, NDG AND rGO NANOFLUIDS IN CLOSED CONDUIT FLOW

EMAD SADEGHINEZHAD

THESIS SUBMITTED IN PARTIAL FULFILMENT OF THE REQUIREMENTS FOR THE DEGREE OF DOCTOR OF PHILOSOPHY

FACULTY OF ENGINEERING
UNIVERSITY OF MALAYA
KUALA LUMPUR

2015

UNIVERSITI MALAYA

ORIGINAL LITERARY WORK DECLARATION

Name of Candidate: EMAD SADEGHINEZHAD

Registration/Matric No: KHA110037

Name of Degree: **DOCTOR OF PHILOSOPHY**

Title of Project Paper/Research Report/Dissertation/Thesis (“this Work”):

STUDY OF THERMO-PHYSICAL PROPERTIES, HEAT TRANSFER AND FRICTIONAL LOSS OF GNPS, NDG AND rGO NANOFLUIDS IN CLOSED CONDUIT FLOW

Field of Study: **HEAT TRANSFER**

I do solemnly and sincerely declare that:

1. I am the sole author/writer of this Work;
2. This Work is original;
3. Any use of any work in which copyright exists was done by way of fair dealing and for permitted purposes and any excerpt or extract from, or reference to or reproduction of any copyright work has been disclosed expressly and sufficiently and the title of the Work and its authorship have been acknowledged in this Work;
4. I do not have any actual knowledge nor do I ought reasonably to know that the making of this work constitutes an infringement of any copyright work;
5. I hereby assign all and every rights in the copyright to this Work to the University of Malaya (“UM”), who henceforth shall be owner of the copyright in this Work and that any reproduction or use in any form or by any means whatsoever is prohibited without the written consent of UM having been first had and obtained;
6. I am fully aware that if in the course of making this Work I have infringed any copyright whether intentionally or otherwise, I may be subject to legal action or any other action as may be determined by UM.

Candidate’s Signature Date

Subscribed and solemnly declared before,

Witness’s Signature Date

Name:

Designation:

ABSTRACT

Heat transfer fluids have inherently low thermal conductivity that greatly limits the heat exchange efficiency. While modification of surface materials, extension of surfaces, alternation of process parameters and redesigning heat exchange equipment to increase the heat transfer rate has reached a limit, many research activities have now focused on improvement of heat transfer liquid. Improvement of the thermal transport properties of the fluids by adding more thermally conductive solids into liquids has become a prominent research avenue. A nanofluid is recognized as the suspension of nanoparticles in a base fluid. Nanofluids are promising heat exchanger fluids for heat transfer enhancement due to their high thermal conductivity. Presently, discrepancy exists in nanofluid's thermal conductivity data in the literature, and also the enhancement mechanisms have not been fully understood yet. Experimental studies are involved with the effects of some parameters such as particle concentration, particle size, and temperature on thermal conductivity. The major efforts given here are: to determine methods to characterize a nanoparticle colloid's mass loading, chemical constituents, particle size, and pH; to determine temperature and loading dependent viscosity and thermal conductivity; to determine convective heat transfer coefficient and viscous pressure losses in a heated horizontal tube; and finally to determine the feasibility for potential use as enhanced performance heat exchanger fluid in energy transport systems. The thermal transport properties of nanofluids, including thermal conductivity, viscosity, heat capacity, contact angle, and electrical conductivity were characterized and modeled. In these nanofluid study the thermal conductivity of the nanofluids are observed higher than those of the base fluids.

Forced convection research on nanofluids is important for practical application of nanofluids. The heat transfer coefficient was investigated experimentally in a flow loop with a horizontal tube test section subjected to constant heat flux at a various flow rate ranges. Initial experiments were conducted with pure water for validation of experimental data and accuracy. The experimental results, represented in Nusselt number (Nu) are compared to the classical Gnielinski, Petukhov and Dittus-Boelter equations. It was observed that Petukhov equation had shown less deviations and it is applicable in turbulent flow range for single phase fluid. For the recent experimental observations the heat transfer enhancement to nanofluids have exceeded the associated thermal conductivity enhancement, which might be explained by thermal dispersion, which occurs due to random motion of nanoparticles. Addition of the nanoparticles to the base fluid significantly increases their heat transfer coefficient compared to pure water as observed in this study. However, increasing of small amount of concentrations in the lower concentration range of this work has shown much effect on heat transfer enhancement. The ultimate goal is to contribute the understanding of the mechanisms of nanoparticle colloid behavior, as well as, to broaden the experimental database of these new heat transfer media.

However, the present investigation results have upgraded the thermo-physical properties and heat transfer enhancement graphene family, where 200% increase of heat transfer coefficient and it is remarkable observation at low concentration of 0.1wt%. From this study it is observed that this types of nanofluids could be selected for the specific cases, where high heat transfer rate should be concern.

ABSTRAK

Cecair pemindahan haba mempunyai kebendaliran haba yang rendah yang sangat menghadkan kecekapan pertukaran haba. Ketika pengubahsuaian permukaan bahan, penambahan permukaan, penukaran bersilih ganti parameter proses dan merekabentuk semula peralatan pertukaran haba bagi meningkatkan kadar pemindahan haba telah mencapai had, banyak aktiviti penyelidikan kini telah memberi tumpuan kepada peningkatan pemindahan haba cecair. Peningkatan sifat pengangkutan haba cecair dengan menambah lebih banyak pepejal yang mengkonduksikan haba ke dalam cecair telah menjadi saluran penyelidikan yang terkemuka. BendalirNano diiktiraf sebagai penggantungan nanopartikel dalam cecair asas. BendalirNano adalah cecair tukaran haba yang berpotensi untuk meningkatkan pemindahan haba kerana kekonduksian haba yang tinggi. Pada masa ini, wujud percanggahan dalam data kekonduksian terma BendalirNano dalam penulisan terdahulu, dan mekanisme peningkatan juga masih belum difahami sepenuhnya. Kajian eksperimen adalah melibatkan kesan beberapa parameter seperti: konsentrasi partikel, saiz partikel, dan suhu pada kekonduksian terma. Usaha utama yang ditekankan di sini adalah: untuk menentukan kaedah bagi mencirikan amaun koloid , komponen kimia, saiz partikel, dan pH; untuk menentukan suhu dan kelikatan berdasarkan muatan partikel dan kekonduksian terma; untuk menentukan pekali perolakan pemindahan haba dan kehilangan tekanan likat dalam tiub mendatar yang dipanaskan ; dan akhir sekali untuk menentukan kebolehlaksanaan dan kemampuan untuk digunaan bagi meningkatkan prestasi penukar haba dalam sistem pengangkutan tenaga bendalir. Sifat-sifat pengangkutan haba BendalirNano, termasuk kekonduksian terma, kelikatan, kapasiti haba, sudut sentuhan, dan kekonduksian elektrik telah diciri dan dimodelkan. Dalam kajian BendalirNano ini didapati keberaliran haba bagi BendalirNano diperhatikan lebih tinggi daripada cecair asas.

Penyelidikan melibatkan perolakan secara paksaan terhadap BendalirNano adalah penting untuk kegunaan praktikal. Pekali pemindahan haba telah disiasat secara uji kaji dalam gegelung aliran dengan bahagian ujian tiub yang mendatar dikenakan fluk haba secara malar pada julat kadar aliran yang pelbagai. Eksperimen awal telah dijalankan dengan air tulen untuk pengesahan eksperimen data dan ketepatan. Keputusan eksperimen, diwakili dalam kiraan Nusselt (Nu) telah dibandingkan dengan persamaan klasik Gnielinski, Petukhov dan Dittus-Boelter. Pemerhatian menunujukkan persamaan Petukhov menunjukkan penyasaran yang kurang dan ianya terpakai pada julat aliran gelora untuk bendalir satu fasa. Untuk pemerhatian eksperimen yang telah dijalankan, peningkatan pemindahan haba keatas BendalirNano didapati melebihi peningkatan kekonduksian terma, yang mana ianya mungkin boleh dijelaskan melalui penyerakan haba, yang berlaku disebabkan gerakan rawak nanopartikel. penambahan nanopartikel pada cecair asas meningkatkan pekali pemindahan haba berbanding dengan air tulen seperti yang diperhatikan dalam kajian ini. Walau bagaimanapun, sedikit peningkatan kepekatan dalam julat kepekatan yang rendah telah menunjukkan kesan yang jelas ke atas peningkatan pemindahan haba. Matlamat utama adalah untuk menyumbang kepada pemahaman mekanisme sifat dan kelakuan nanopartikel koloid, dan juga, untuk memperluas pangkalan data yang diperolehi secara eksperimen bagi media pemindahan haba yang baru ini.

Walau bagaimanapun, keputusan siasatan terkini telah menaiktarafkan sifat termo-fizikal dan peningkatan pemindahan haba dalam keluarga graphene , di mana peningkatan 200% keatas pekali pemindahan haba dan ia adalah pemerhatian yang luar biasa pada kepekatan serendah 0.1wt%. Dari kajian ini pemerhatian menunjukkan jenis nanofluids Ini boleh dipilih untuk kes-kes tertentu, di mana kehilangan geseran mungkin diserap atau tidak menjadi kebimbangan yang menonjol.

DEDICATION

To my beloved mother and father

ACKNOWLEDGMENTS

In the name of ALLAH, the most Gracious, the most Compassionate

First and foremost, I wish to sincere gratitude to my supervisors, Dr. Kazi Md. Salim Newaz, Dr. Ahmad Badarudin Mohd Badry and Dr. Madhizal Dahary for their advice and guidance of this research project and thesis. Working with them have been a fruitful learning and research experience.

I would also like to thank Mr. Mohamad Mehrali and Mr. M.N.M. Zubir for their help on experimental design, and valuable suggestions.

I would like to thank to my colleague Mr. Hussein Togun for the useful discussions and helps, which we experienced in all steps of my study.

The writing of this thesis had been the most challenging undertaking of my life to date. I could not have completed this work without the support and help of many people.

I would also like to convey thanks to the University of Malaya and High Impact Research (MOHE-HIR), for providing the financial support and laboratory facilities.

Last but not the least; heartfelt thanks are extended to my lovely parents and my sister for their support and encouragement. This would be incomplete without sincere thanks to my Father who always encouraged me to achieve the best, and to my Mother for their support and faith in me during the hardship…

TABLE OF CONTENTS

LIST OF FIGURES

LIST OF TABLES

NOMENCLATURE

A	absorbency
AFM	Atomic force microscopy
ANNs	Artificial neural network
b	optical path (cm)
B	Optical path (cm)
c	molar concentration (mol/dm^3)
C_p	Specific heat capacity, J/kg K
$C_{1\varepsilon}$, $C_{2\varepsilon}$, $C_{3\varepsilon}$, σ_k, σ_ε	Model constants
CTAB	Hexadecyltrimethylammonium bromide
CHF	Critical heat flux
CNT	Carbon nanotube
CVD	Chemical vapor deposition method
D	Tube diameter, m
DSC	Differential scanning calorimetry
DW	Distilled water
ECG	Epicatechin gallate
EDL	Electrical double layer
EGCG	Epigallocatechin gallate
f	Friction factor
FT-IR	Fourier transform infrared spectroscopy
G_b	generation of turbulence kinetic energy
GA	Gum Arabic

GO	Graphene oxide
GNP	Graphene nanoplatelets
GT	Green tea
GTPs	Green tea polyphenols
h	Convective heat transfer coefficient
HC	Hamilton-Crosser
I	Electrical current, A
k	Thermal conductivity, W/m.K
L	Tube length, m
MW-CNT	Multiwall carbon nanotube
NDG	Nitrogen-doped graphene
Nu	Nusselt number
P	Heater power, W
Pe	Péclet number
Pr	Prandtl number
PVD	Physical vapor deposition method
q''	Heat flux, W/m^2
Re	Reynolds number
rGO	reduced graphene oxide
SDBS	Sodium dodecyl benzene sulfonate
SDS	Sodium dodecyl sulfonate
SEM	Scanning electron microscopy
SL	Sodium Laurate
SSA	Specific surface area
SW-CNT	Single-wall carbon nanotube
T	Temperature, K

TEM	Transmission electron microscopy
THW	Transient hot-wire
TPS	Transient plane source
U	Mean velocity, m/s
V	Volts, V
v	Mean velocity, m/s
w	Water
W	Watt
wt%	weight percentage
X, Y, Z	Cartesian coordinates
x	Axial distance
XRD	X-ray diffraction
XPS	X-ray photoelectron spectroscopy

Greek

ΔP	pressure drop, Pa
wt%	weight percentage
ϕ	nanoparticle volumetric fraction
μ	viscosity, Pa.s
ε	Turbulent dissipation
ρ	density, kg/m^3
η	thermal performance factor
σ	Electrical conductivity

Subscripts

avg	average

b	bulk
avg	average
b	bulk
bf	base fluid
i	inner
in	inlet
m	mean
nf	nanofluid
np	nanoparticle
o	outer
out	outlet
w	wall

CHAPTER 1

INTRODUCTION

1.1 Background

Heat transfer plays a major role in many types of industries; such as, transportation, air conditioning, power generation, process plants, electronic devices etc. Modifications of heat exchanger surfaces, use of high performance materials, change of process parameters were performed to enhance performance of heat exchangers. At present researchers have given emphasis on developing heat exchanging fluids. Moreover, high-performance heat exchanging fluid is widely needed for heat exchangers in industrial technologies. Due to this fact, various studies and researches are aimed to increase cooling and heating performance of working fluids. Various types of particles such as metallic, non-metallic and polymeric have been suspended into fluids to form suspensions containing millimeters or micrometer sized particles. However, they are not applicable for practical application due to problems such as sedimentation, erosion of pipelines, clogging of flow channels and increase in pressure drop due to their momentum transfer. Furthermore, they often suffer from rheological problems and instability. In particular, the particles tend to settle rapidly. However, these increase in thermal conductivity of the liquid enhances their practical importance. A research group at Argonne National Laboratory was the first who continuously studied the use of nano-sized particles around a decade ago. A nanofluid is a suspension of ultra-fine particles with extremely high thermal conductivity compare to conventional base fluid. Nanofluids have the potential increase of heat transfer characteristics in comparison to the original fluid. Recently, newly developed material nanometer sized particles have been used as suspension in conventional heat transfer fluids. Among the nano and micro matter sized suspensions as heat exchanging liquids, the nanofluids are more preferable. The Importance of nano-sized particles and their benefits compared to microparticles have been investigated and it could be stated that the nanoparticles possess have the following advantages.

1. Longer suspension time (More stable)
2. Much higher surface area
3. Larger surface area/volume ratio (1000 times larger)
4. Higher thermal conductivity
5. Lower erosion, corrosion and clogging
6. Lower demand for pumping power
7. Reduction in inventory of heat transfer fluid
8. Significant energy saving

Over the last several years, considerable research has been carried out leading to development of currently used heat transfer enhancement liquids. Generally, additives have been used to increase the heat transfer performance of the base fluid. Furthermore, these nanofluids are expected to ideally suit in practical application as their use incurs little or no penalty in pressure drop but changes the transport properties and heat transfer characteristics of the base fluid. Due to ultra-fine nature of these nanoparticles, nanofluids behave as a single phase fluid rather than multiphase, i.e., solid-liquid mixture.

A lot of research have been conducted to enhance the thermal properties of the heat transfer fluids by adding high thermally conductive nanoparticle with quantities ranging from 0.001wt% to 50wt% (Mehrali et al., 2014a). More common nanoparticles and basefluids exploited in synthesis are presented in Figure 1.1. It is worth noting that good dispersion of nanoparticles and high stability of the nanofluids are necessary for their extensive applications (Togun et al., 2014). Recently, a number of studies have been conducted on the use of carbon-based nanostructures to prepare nanofluids (Moghaddam et al., 2013). Hence, a variety of applications of graphene have come to the fore front (Mehrali et al., 2013a; Mehrali et al., 2013b). Graphene, a single-atom-thick sheet of hexagonally arrayed sp^2-bonded carbon atoms, which has received much attention since it has been discovered by Novoselov et al. (2004). Even though several other forms of sp^2 carbon nano-structured materials such as carbon nanotubes (Kroto et al., 1985) and fullerene (Iijima, 1991) have been prepared. In the last few years, a significant number of studies have been conducted with graphene due to its unique thermal, electrical, optical, mechanical and other favorable characteristics. Characterization of graphene provides an important part of graphene research and involves measurements based on various spectroscopic and microscopic techniques (*Graphene: Synthesis, Properties, and Phenomena*, 2013).

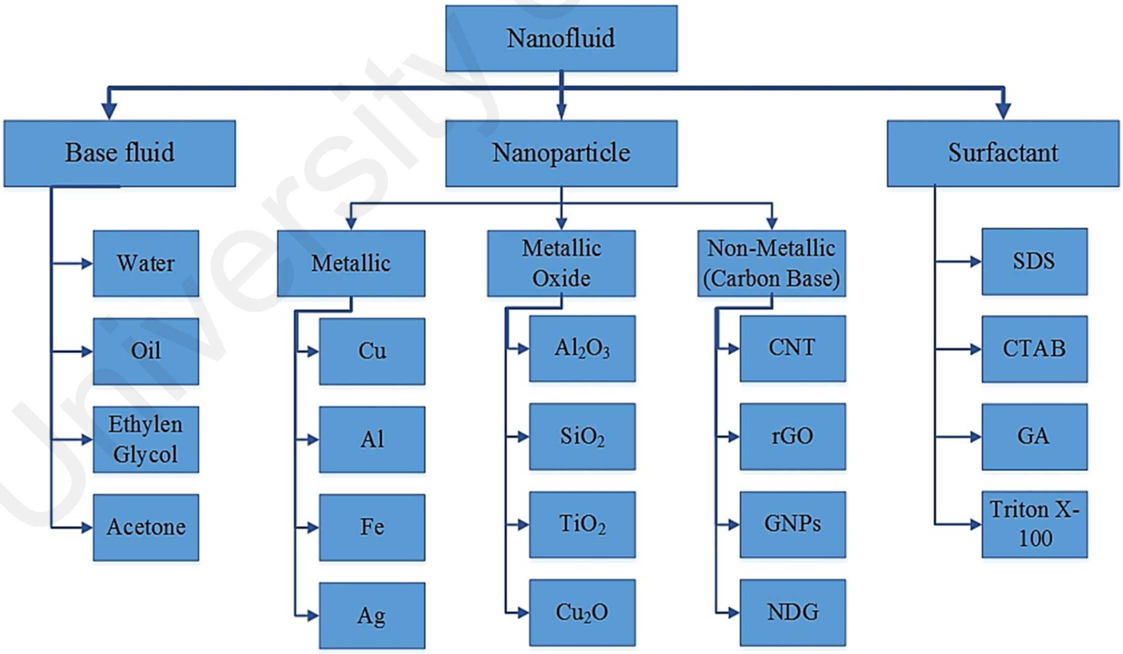

Figure 1.1 Common base fluids, nanoparticles, and surfactants for synthesizing nanofluid

1.2 Importance of Study

Heat transfer fluids such as water, ethylene glycol, Freon and mineral oil play an important role in many industrial processes such as power generation, heating and cooling processes, chemical productions, transportations and microelectronics. The primary problem to the high compactness and effectiveness of the heat exchangers is the poor heat transfer characteristics of these fluids compared to solids. An improvement in thermal conductivity of these conventional fluids is a key idea to improve the heat transfer characteristics. Thus, the essential initiative is to seek solid particles especially nano-sized particles having thermal conductivity several thousand orders higher than those of conventional fluids (Sadeghinezhad et al., 2014). A sizable amount of research have been performed on thermo-physical properties of metal and oxide nanofluids but a little has been done on non-metallic nanoparticles nanofluids. This study focuses on experimental investigation of thermo-physical properties and heat transfer characteristics of GNPs nanofluid, NDG nanofluid and highly stable G-rGO nanofluid.

However, no work has thus far be conducted to investigate the influence of these nanofluids on heat transfer and pressure drop characteristics in the turbulent flow regime of smooth tubes. Moreover, the carbon base nano-particles could safe the channels and pipelines from the damage and corrosion problems due to the size of nano-particles and less effect on pH. Therefore, the purpose of this study is to experimentally measure, for theses nanofluids suspended in water, the heat transfer and pressure drop characteristics of nanofluids in the turbulent flow regime in a horizontal smooth tube.

Figure 1.2 shows recent research output through publications on this field in the last decade, where it is clearly seen that nanofluids are an issue which is becoming very important in engineering world, where high expectations are presented about their applications in diversified fields.

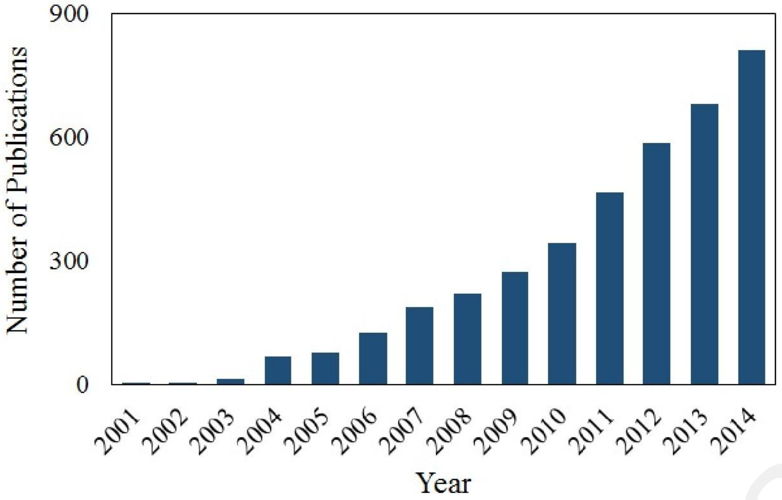

Figure 1.2 Number of publications on study of nanofluids during last decades.

1.3 Expected applications of nanofluids

Nanofluids could be used in many industrial sectors. The main proposed applications of nanofluids can be highlighted as follows.

1. The use of nanofluids is expected to help the efforts to optimize the design of compact heat exchanging equipment.
2. Nanofluids can be used in heat exchanger and pool boiling applications such as in electronics equipment cooled by enhanced Critical Heat Flux (CHF).
3. Nanofluids can be used in wide variety of industries ranging from transportation industry, energy supply, production, textiles and paper by expected reduced pumping needs or diminishing heat exchangers sizes.
4. The nanofluids should have less erosion and corrosion problems to the channels and pipelines.

1.4 Properties of nanofluids

1.4.1 Production of Nanofluids

In this study, nanofluids refer to solid nanoparticles dispersed into liquids at ordinary conditions (not amorphous solids or gases). Successful preparation of stable nanofluids is one of the important issues in this study. There are several factors of interest when considering a given synthetic approach: thermal stability, dispersibility in diverse media, chemical compatibility and ease of chemical manipulation. In this study, we use the bottom-up approach to make nanofluids; the bottom-up approach is to use small particles, sometimes constituent atoms to form bigger clusters during synthesis process. Nano sized particles were synthesized or purchased and then dispersed into various base fluids by sonicating and mechanical stirring to investigate the dispersability of them. In this approach, the precursor species (i.e. metal ions, organometallics, complexes, etc.) are reduced, decomposed, or hydrolyzed, as the case may be, some nanofluids remain stable for relatively long period; some may need stabilizers to remain dispersed. Depending on the type of reaction, the synthetic conditions vary and for the present case, these variables were controlled by maintaining temperature, pH and dispersing medium (base fluid). Hence, various nanoparticles and base fluids are considered in this study.

1.4.2 Thermal Properties and Rheological Properties of Nanofluids

The most interested property of nanofluids being investigated in the past decade was its thermal conductivity. In order to study convection heat transfer of the fluids, it has the importance to understand the thermal properties and rheological properties of the manufactured nanofluids. There are two major methodologies in thermal conductivity measurements: steady-state method and transient method. The thermal conductivity measurements of the liquid samples from the system by steady-state methods are not good choices, because it needs a relatively longer time period to reach steady state and the heat loss during this period can not be quantified, which shows larger errors in results. In addition the natural convection may set in during this period, which could produce the results even less accurate. Therefore, transient methods are better to the measure thermal conductivity of the liquid sample from the system. There are many transient methods of thermal conductivity measurements, for instance, transient hot-wire method, temperature oscillation method, etc. Measurement method for nanofluids need to be carefully considered, because the solid nano particles are always charged and they may be attracted to contact measuring surface of the device, and these problems cause inaccuracy.

1.4.3 Convection heat transfer and Pressure loss Measurements of Nanofluids

Convection and pressure measurements are carried out in a horizontal SS pipe test section. The closed system is specially designed for water based fluids to run in the turbulence region and the silicone oil based fluids in the laminar regime. Convection coefficient at various Reynolds numbers are measured and calculated for constant heat flux surface condition. Meanwhile, pressure drop along the test section is measured by using a pressure transducer. By comparing convection coefficients and pressure drop at different velocities of nanofluids with those of base fluids, the impact of nanoparticles in heat transfer fluids could be estimated.

1.5 Objectives of present research

The main objectives of this research can be summarized as follows:

1- To characterize the thermo-physical properties of nanofluids and find out the physical mechanisms behind the thermal conductivity enhancement of nanofluids through the investigation of the effects of nanoparticle properties.

2- To develop a new mass production method of nanofluids and synthesize new nanofluids. Simultaneously improve the thermal conductivity, heat capacity and convective heat transfer coefficient.

3- To investigate experimentally the performance of nanofluid in a circular tube heat exchanger and to compare that with conventional working fluids.

4- Simulation of the heat transfer to nanofluids in the pipe flow and compare the numerical data with the experimental results for validation.

1.6 Layout of thesis

The thesis starts with a look at the different mechanisms of energy transport in nanofluids, followed by a summary of previous literature review of thermo-physical properties, stability, convective heat transfer and pressure drop of nanofluids. This forms part of the literature survey presented in CHAPTER 2. In CHAPTER 3 characterization method, instrument, the experimental setup, test section, calibration of instruments are discussed. The preparation methods and thermo-physical properties of the GNPs (with three different specific surface areas of 300, 500, 750 m^2/g), NDG, G-rGO nanofluids are discussed in CHAPTER 4. The method of data reduction, uncertainty analysis of the experimental set-up and validation of the test section are well discussed in CHAPTER 4. Heat transfer and friction factor results are discussed in CHAPTER 6 and they are followed by the performance evaluation of the GNPs nanofluids. The CHAPTER 7 contains a summary of the work done and proposed recommendations for future work. APPENDIX A contains discussion about calibration of the test section, from which the current setup is based. APPENDIX B provides the full uncertainty analysis of the heat transfer coefficients and friction factors of water. APPENDIX C includes the whole the cleaning procedure of the test rig.

CHAPTER 2

LITERATURE REVIEW

2.1 Background

Throughout history, people worked on the subject of heat transfer phenomenon for a better heat transfer performance, which directly affects the standard of their life. With the development of heat engines, heat pumps and similar devices, the requirement for a better heat transfer became more important. Heat exchanger devices, heat transfer fluids or other components related to heat transfer were invented and improved with thriving technology. Usage of more compact, larger heat transfer area heat transfer devices are common in today's industry. However, heat transfer requirements of these devices are becoming larger while their sizes are becoming smaller. At this point, increasing the heat transfer area of a device may no longer be a solution because the practical limitations of manufacturing smaller channels or components can be a problem with usage of conventional methods.

Researchers targeted two different ways to overcome these problems in the heat transfer research world, which are improving micro or nano sized channels and different types of heat transfer fluids. The second alternative includes nanofluid improvement and usage in heat transfer applications such as heat exchangers and heat sinks. Energy transport is an integral part of a wide range of areas, such as chemical industry, oil and gas, nuclear energy, electrical energy, etc. In previous decades, ethylene glycol (EG), oil and water were used as heat transfer fluids. However, development of heat transfer fluids with improved thermal conductivity has become more and more critical to the performance of energy systems (LotfizadehDehkordi et al., 2013). S. U. S. Choi et al. (1995) have introduced the term nanofluids referring to fluids containing dispersed nano sized particles having higher thermal conductivity. Nanoparticles have great potential to more effectively improve the thermal transport properties of heat transfer systems than micrometer and millimeter sized particles. This is mainly due to the tininess of nanoparticles or other nanostructures, which not only improves the stability and the applicability of liquid suspensions, but also increases the thermal conductivity, specific surface area and the diffusion mobility of Brownian motion of the particles. Nanoparticles are generally considered to be a discovery of modern science; however their history is long and rich. Naturally occurring nanoparticles and nanostructures of all types are as common as the macro-sized objects that surround us. Indeed, the universe itself was built from the bottom up, and that by necessity, dictates that an astoundingly complex micro-world exists. Nanoparticles are common in nature as trace metals, organics, and inorganics formed through varied natural processes. These include the production of carbon structures such as fullerenes, through the combustion of any complex carbon molecule, and the creation of organic, inorganic, and metallic nanostructures through thermal, chemical, biological, and physical processes. Truly, the collection of naturally occurring nanoparticles is noteworthy and can be reviewed further in the literature. The use and discovery of nanoparticles by humans dates back hundreds of years. Nanoparticles were employed in the 9th century as additives to paintings and pottery to add luster. They were also used as pigments in the alveoli of mummies which date back more than 5000 years and as coloring agents for stain glass windows and tattoos. Although humanity did not fully realize the impact or importance of their discoveries, their ability to manipulate and utilize nanoparticles at such an early date is impressive. The first truly scientific study of nanoparticles was done by Michael Faraday in 1857 when he discussed the optical properties of nanoscale metals. Since that time, a great deal of scientific research has focused on the physical and transport properties of nanoparticles. Indeed, the entire field of nano-science and nanoparticles has blossomed along with their applications and potential.

The heat transfer enhancement by using nanofluids is important because of the reasons mentioned above. The heat transfer enhancement was defined as ratio between heat transfer coefficient of nanofluid and heat transfer coefficient of base fluid (described in the next section) at a constant parameter. The constant parameter may be different in various studies. Typically, it is selected as velocity, Reynolds number or Peclet number. Researchers thought that the enhancement was directly related to Nusselt number ($Nu = h.D/k$) and thermal conductivity enhancement of a fluid in a system according to notion of comparison of heat transfer coefficients in a system. Thermal conductivity enhancement was defined as ratio between nanofluid thermal conductivity and base fluid thermal conductivity. A comparison can be made between the base fluid and the nanofluid, thus; it can be observed that how much heat transfer coefficient enhancement is achieved. The challenging topic on this issue is accurate prediction of heat transfer enhancement.

In this chapter, a literature survey on the studies about the different preparation methods, thermo-physical properties of nanofluid, stability measurement of nanofluids and forced convection heat transfer with nanofluids are presented.

2.2 Nanofluid Composition

Nanofluids are made from generally one type of base fluid and one type of nanoparticles. As it is mentioned above, the aim is to increase the thermal conductivity of the fluid matrix for using in heat transfer applications. For this reason, the nanoparticles are generally selected as metallic or metal oxide materials which have higher thermal conductivity. Common metallic and metallic oxide nanoparticles used in these case are Alumina (Al_2O_3), Copper Oxide (CuO), Copper (Cu), Titanium di Oxide (TiO_2). Other types of materials such as graphite, carbon and diamond are also used in research. In addition to enhancement in thermal conductivity, an enhanced Nusselt number is also observed in the experiments.

Common heat transfer fluids can also be used as the base fluid of the nanofluid. The important point of the selection of the base fluid is still dependent on suitability for a specific heat transfer application. Moreover, the diameter of the microcapsules is several micrometers, and these large particles could cause damage and corrosion problems to the channels and pipelines due to the high momentum and energy carried by large particles. All heat transfer base fluids can be used for nanofluid production as long as they are suitable for production techniques. However, it is important to note that the addition of nanoparticles in a fluid provides more enhancement if the fluid has poor heat transfer capabilities. In other words, it is much more beneficial to use the nanoparticle addition technology when the working base fluid of a system has low thermal conductivity.

2.2.1 Preparation and Characterization of Nanofluids

Preparation of nanofluids is the important step in the use of nanoparticles to improve the thermal conductivity of nanofluids. There are two main production techniques which have been employed in producing nanofluids. One is a single-step method and the other is a two-step method.

2.2.1.1 The Single-Step Method

The production of a nanofluid is not a simple process. Indeed, the final behavior of any nanofluid is greatly influenced by the synthesis steps taken in production of nanofluid. Nanofluid production can be broken up into two broad categories, One-step and two-step methods. The first is that of creating the nanofluid and its inclusion particles in one step. This often involves some kind of chemical, electrical, or explosive dispersion/condensation/reduction process. Physical vapor deposition method (PVD) or chemical reduction technique can be used for preparation of the nanoparticles. The processes such as drying, storage, transportation, and dispersion of nanoparticles into the base fluid are avoided in this method, therefore the agglomeration of nanoparticles is minimized and the stability of fluids is increased. A single-step method is usually applied for metal nanofluid preparation. But the main disadvantages of this method are that the only low vapor pressure fluids are compatible with the process and low concentration of nanoparticles. This limits the application of this method. A sample of one step method shown in Figure 2.1.

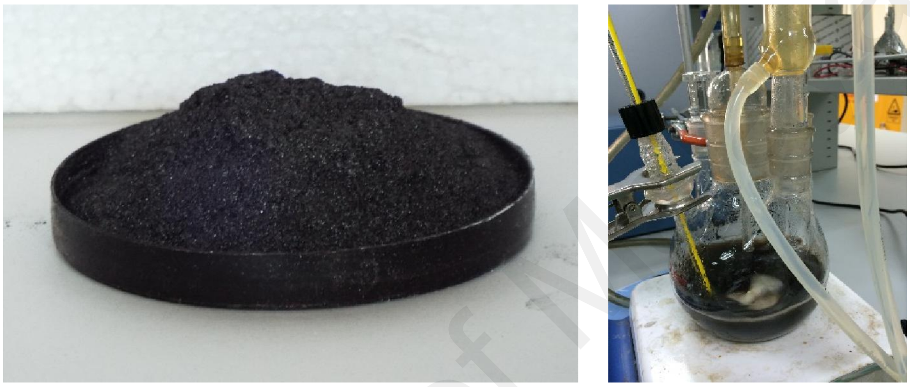

Raw material After one-step method

Figure 2.1 One-step method of preparation of nanofluids

2.2.1.2 The Two-Step Method

In the two-stage techniques, the nanoparticles are firstly prepared and then introduced into the base fluid. Metal oxide nanoparticles, nano-fibers or nanotubes used in this technique are first prepared as a dry powder by chemical vapor deposition (CVD), inert gas condensation, mechanical alloying or other suitable techniques, and the nano-sized powder is then dispersed into a fluid in a second processing step. This step-by step method isolates the preparation of the nanofluids from the preparation of nanoparticles. Consequently, agglomeration of nanoparticles due to attractive Van der Waals Forces may occur in both steps, especially in the process of drying, storage, and transportation of nanoparticles. The agglomeration will not only cause the settlement and clogging of micro-channels, but also decrease the thermal conductivity. Several techniques such as use of ultrasonic agitation equipment, pH control or addition of stabilizers to the fluids are often applied to minimize particle aggregation and improve dispersion behavior. Since nano-powder synthesis techniques have already been scaled up to industrial production levels by several companies, there are prospective economic advantages in using two-step synthesis techniques that depend on the use of such powders. But an important problem, which needs to be solved is the stabilization of the prepared suspension. Figure 2.2 depicts the procedure of two step method.

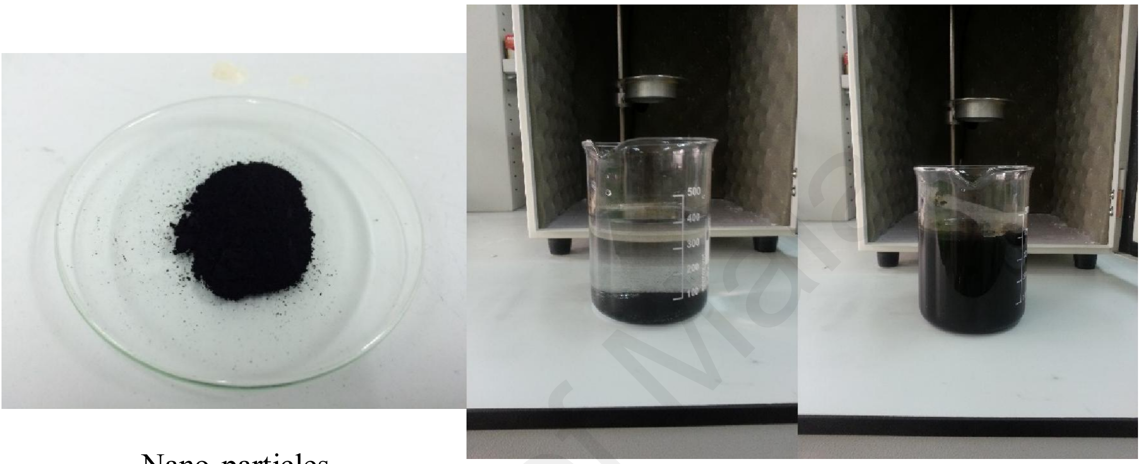

Nano-particles

Nano-particle and base fluid before sonication

Nano-particle and base fluid after sonication

Figure 2.2 Two-step method of preparation of nanofluids

Another part of the two-step process is the chemical-dispersion method. This method is aimed to disrupt the long-range attractive Van der Waals forces. This is done by electrostatic, steric dispersion or functional group coating technique.

The electrostatic method is to charge particles with similar charges and create the repulsive electrostatic forces that oppose the long-range Van der Waals forces. This is done by changing the pH of the suspension, since it controls the properties of the nanoparticle surface. At the optimal pH of the solution the surface charge of the nanoparticle increases because of the more frequent attraction of the surface hydroxyl groups (H^+ and OH^-) by potential-determining ions. This leads to an increase of the electrostatic repulsion force between the particles which results in a stable suspension with reduced agglomeration.

Steric stabilization is the process by which a surfactant is added to prevent agglomeration. Some examples of previously tested surfactants are sodium laurate (SL), sodium dodecyl benzene sulfonate (SDBS), sodium dodecyl sulfate (SDS), Triton X-100, and Gum Arabic (GA).

Functionalization generally involves treating the nanoparticle with acids at high temperature. This results from addition of polar groups like -COOH or -OH at defect sites on the nanoparticle surface, thus making nanoparticles more hydrophilic in nature.

2.2.2 Carbon based Nanoparticle

Since graphene is only a single layer of carbon atoms, it was predicted that it could not be existed at finite temperature. In 2004, this thinnest material was developed by peeling off graphite using adhesive tape by researchers in Britain (Novoselov, et al., 2004). This method is called micromechanical exfoliation. This method is much easier than other methods as it does not require any sophisticated equipment and more importantly it yields high quality graphene flakes. Another way of synthesis graphene is by epitaxial growth on SiC substrate which was invented by researchers of USA (Berger et al., 2006). Simplified method of making graphene starts from bulk graphite like HOPG, Kish, HPHT. Figure 2.3 shows the steps involved in micro-mechanical exfoliation method to prepare single layer graphene from bulk graphite. Clean environment during production process is important for good quality of graphene. Attach a HOPG flake to about six inches of adhesive tape with tweezers and press it down carefully and peel the tape apart slowly enough so that graphite cleaving smoothly in two. Repeat the step above for several minutes until the graphite flakes spread a larger area on the tape. Then, carefully lay the tape with graphite flakes onto a small silicon dice and press the tape gently for a few minutes. This silicon has silicon dioxide layer of 300 nm on the top, which helps to find graphene under white light optical microscope. The final step is to peel off from silicon dice. Then it is ready to find graphene under optical microscope.

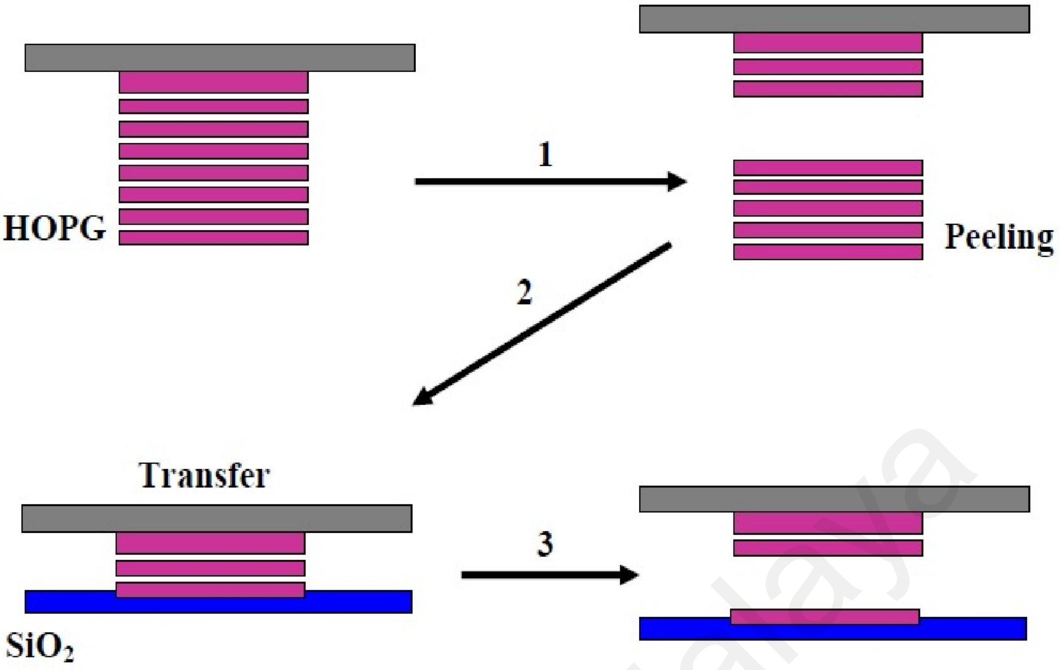

Figure 2.3 Micro-mechanical exfoliation method to prepare single layer graphene from bulk graphite.

A lot of research has been conducted to enhance the thermal properties of the heat transfer fluids by adding quantities ranging from 0.001wt% to 50wt% of high thermally conductive solids of various nano-materials including oxides (Minea et al., 2012), nitrides (Zhi et al., 2011), metals (Sundar et al., 2007), diamond (Yeganeh et al., 2010), carbon fiber (K. J. Lee et al., 2007), carbon black (Dongxiao et al., 2011), carbon nanotubes (CNT) (Nasiri et al., 2012), single-walled carbon nanotubes (SWNTs) (Nanda et al., 2008), double-walled carbon nanotubes (DWCNT) (MJl Assael et al., 2004), multi-walled carbon nanotubes (MWNTs) (L. Chen et al., 2012), graphite (Y. Yang et al., 2005), graphene oxide (GO) (S. W. Lee et al., 2013), graphene (Wei Yu et al., 2011), graphite flakes (Zheng et al., 2011), graphene nanoplatelets (GNPs) (G.-J. Lee et al., 2014; Mohammad Mehrali, et al., 2014a) and hybrids (Baby et al., 2011) of different shapes (particle, disk, tube, sheet, fiber, etc.) (E. K. Goharshadi et al., 2006). One of the most important partial issues is to achieve a good stability of the nanofluids (Özerinç et al., 2010). It is worth noting that good dispersion of nanoparticles and high stability of the nanofluids are necessary for their extensive applications (Togun, et al., 2014). Recently, a number of studies have been conducted on the use of carbon-based nanostructures to prepare nanofluids (Moghaddam, et al., 2013). Hence, a variety of applications for graphene has come to the fore front (Mehrali, et al., 2013a; Mehrali, et al., 2013b). Graphene, a single-atom-thick sheet of hexagonally arrayed sp^2-bonded carbon atoms, which has received much attention since it was discovered by Novoselov, et al. (2004). Even though several other forms of sp^2 carbon nano-structured materials such as carbon nanotubes (Kroto, et al., 1985) and fullerene (Iijima, 1991) have been prepared. In recent years, a significant number of studies have been conducted with graphene due to its unique thermal, electrical, optical, mechanical and other relevant characteristics. Characterization of graphene provides an important part of graphene research and involves measurements based on various spectroscopic and microscopic techniques (*Graphene: Synthesis, Properties, and Phenomena*, 2013).

2.3 Thermo-physical properties

Thermo-physical properties are an essential parameters to the understanding of the convective heat transfer behavior of nanofluids. Experimental determination of their thermo-physical properties is a major part of the overall scope of this project. Properties of interest are the density, specific heat capacity, thermal conductivity, and viscosity. The viscosity and thermal conductivity cannot be predicted a priori; the heat capacity and density are easily found from weighted averaging as shown in this chapter. This chapter will cover the experimental techniques for measuring the viscosity, thermal conductivity and other thermal properties for nanoparticle colloids.

2.3.1 Thermal Conductivity Enhancement in Nanofluids

Thermal conductivity is the ability of a material to transport energy in the form of heat (energetic vibrations). For the case of solids, it is the direct energy exchange through atomic level lattice vibrations and free electron diffusion, whereas for fluids/gases it takes the form of direct molecular contact and molecular diffusion. It is a fundamental and natural property of any physical material, and is defined as energetic power per unit temperature and per unit length over which the thermal conductivity is acting. Ultimately, a material’s thermal conductivity is based upon the physical structure of the material, and its current state. Thermal conductivity is one of the very important thermal transport characteristics of a material, which plays an important role in many design problems. Therefore, a great deal of effort has gone into characterizing, and measuring thermal conductivity over the last few centuries.

2.3.1.1 Effective parameters of thermal conductivity

Literature states different features influencing thermal conductivity of nanofluids. Based on literature, some parameters influence on thermal conductivity of nanofluids with no doubt such as size, temperature, concentration, particle motions and so on. In this section, some of these parameters have been reviewed.

Nanoparticle can be considered as the key element of nanofluid, which plays major role in this case. Situation of nanoparticles either during synthesis or after that can be highly effective on different thermo-physical properties of it (Mehrali et al., 2014b).

1. Morphology

   In material science, morphology would be defined as study of shape, size, texture and phase distribution of physical objects. The study of nanoparticles on the effect of size has been investigated by some researchers and they have declared strong effect of nanoparticle size on thermal conductivity of nanofluid. Other characteristic of nanoparticle is specific surface area (SSA), which is supposed to be taken into account by researchers during preparation since it is effective on thermal conductivity of nanofluid and can be defined as Equation (2.1):

$$SSA = \frac{Particle\ surface\ area}{Particle\ Volume} \tag{2.1}$$

2. Temperature

   In recent researches, it has been approved that temperature and thermal conductivity have direct relationship which means when temperature increases, thermal conductivity of nanofluid rises as well.

3. Concentration

   The other key issue that can highly affect thermal conductivity of nanofluid is concentration of nanoparticles inside the basefluid. In different reports, concentration has been stated in both types including volume as well as weight percentage.

4. Motion

   Three types of motion have been vastly discussed in literatures namely:

   - Thermophoretic motion (Motion caused by temperature gradient)
   - Brownian motion (force)
   - Osmophoretic motion (Motion in concentration gradient)

   The motion of particles caused by temperature gradient, which is called Thermophoretic motion. However, most effective type of motion which has been investigated by different researchers and has stated as very effective reason in increasing thermal conductivity of nanofluids is called Brownian motion. The osmophoretic motion which can be defined as motion in concentration gradient and vary by concentration of particles.

5. Thermal conductivity of nanoparticles

   Inside one specific basefluid, thermal conductivity of particles would greatly influence on thermal conductivity of one sample comparing the other one while both possess same basefluid. In this case, higher thermal conductivity of particles is expected to lead in higher thermal conductivity of nanofluid. This fact has been proved by different researches and experiments.

6. Thermal conductivity of base-fluid

   As it was mentioned earlier, motion of particles especially Brownian motion can affect thermal conductivity of nanofluids. One noticeable parameter, which is in direct relationship with motion of particles, is viscosity of basefluid. Effect of electric double layer around nanoparticles could be considered as one influential parameter on thermal conductivity of nanofluids, depending on basefluid. Table 2.1 denotes thermophysical properties, molecular diameter and freezing point temperature of common heat transfer base fluids, which are important in nanofluid heat transfer phenomena.

Table 2.1 Selected Base Fluid Properties Affecting Nanofluid Heat Transfer at 20°C with Desired Tendency for Better Enhancement

Fluid Type	Pr	c_p (J/kg·K)	ρ (kg/m^3)	k (W/m·K)	μ (N·s/m^2)	~d_f (nm)	T_{fr} (K)
Desired Tendency	↑	↓	↓	↑	↓	↓	↓
Water	7.00	4184	998	0.599	0.10×10^{-3}	0.38	273
EG(ethylene glycol)	209	2383	1117	0.250	0.22×10^{-1}	0.56	261
R-134a	3.51	1405	1125	0.083	0.21×10^{-3}	0.64	247
EO (engine oil)	10863	1881	888	0.145	0.84	1.17	-

7. Clustering

   Other feature effecting thermal conductivity of nanofluids, which always can be taken into account, is clustering. It is interesting to note that in different models presented by different researches, regarding thermal conductivity of nanofluids, the effect of clustering has been regarded by some researchers.

8. Acidity (pH)

   Literature survey reveals that there are not a lot of researches investigating impact of pH of basefluid on thermal conductivity of nanofluid.

9. Additives

   Additives are utilized to keep nanoparticles in suspension and prevent them from agglomeration. Thus, they are expected to cause thermal conductivity enhancement of nanofluids.

2.3.1.2 Thermal conduction of carbon based materials

There is a discrepancy in the degree of thermal conductivity enhancement along with the progress of research in thermal property of nanofluids. Some researchers found abnormal thermal conductivity enhancement in nanofluids; on the other hand, researchers participated in International Nanofluid Property Benchmark Exercise, they tested the same type of nanofluids from the same source and found no abnormal thermal conductivity enhancement.

Earlier measurements by several investigators indicated that the thermal conductivity of nanofluids could be influenced by so many parameters in the colloid system. A comparison between different carbon-based nanofluids in recent works is shown in Table 2.2.

Table 2.2 Thermal conductivity enhancement of different carbon based nanofluids over base fluids

Base fluid	particle	Average Particle size	Concentration	thermal conductivity enhancement/ ratio	Reference	Remarks
DW	MWCNT	10–50 µm	1-3 vol%	3-7%	(Y Hwang et al., 2007)	Concentration and particle size effect
DW+ sodium dodecyl benzene	MWCNT	20–60 µm (diameter)	0.04–0.84 vol%	1.04–1.24	(Wen et al., 2004a)	Two-step method
DW+GA	MWCNT	-	0.05–0.49 wt%	1.18–1.8	(Shanbedi et al., 2012)	Temperature effect
diesel oil (Shell Rotella 15W-40)	SWCNT	0.3–10 µm	0.25–1.00 wt%	1.10–1.46	(Marquis et al., 2005)	Two-step Method
Ethylene Glycol	MWCNT	OD 1-4 ID 0.8-1.1	2.5 vol%	20%	(Amrollahi et al., 2008)	Temperature effect
DW	carbon black	-	4-8 vol%	0.8-6%	(Dongxiao, et al., 2011)	Concentration effect
Ethylene Glycol	GO nanosheet+GO	-	0-21 wt%	4.1-123%	(B. Wang et al., 2013)	Concentration effect
DW	Graphite	1-2 µm	2-2.5 wt%	1-1.23	(Y. Yang, et al., 2005)	Heat Transfer effect
Ethylene Glycol	graphene nanosheet	0.7-1.3 µm	0.01-11.03 wt%	20-86%	(Wei Yu, et al., 2011)	Concentration effect
DW	graphene nanosheets	1-3 µm	0.05–0.2 vol%	2-27%	(Sen Gupta et al., 2011)	Concentration effect
Ethylene Glycol	xGnP	1.7–300 nm	0.5-4 vol%	1.030-1.332	(G.-J. Lee, et al., 2014)	Concentration effect
Ethylene Glycol DW	silver nanoparticles decorated graphene	-	0.01-0.07 vol% 0.005-0.05 vol%	2-14% 7-86%	(Baby, et al., 2011)	Concentration effect
DW	GNPs	2 µm (diameter)	0.025-0.1 wt%	14.8-27.6%	(Mohammad Mehrali, et al., 2014a)	Concentration and temperature effect
DW + Triton X-100	NDG	3–5 nm	0.01-0.06 wt%	22.15-36.78%	(Mohammad Mehrali, et al., 2014b)	Concentration and temperature effect

There is a discrepancy in the degree of thermal conductivity enhancement along with the progress of research in thermal property of nanofluids. Some researchers found abnormal thermal conductivity enhancement in nanofluids; on the other hand, researchers participated in International Nanofluid Property Benchmark Exercise, they tested the same type of nanofluids from the same source and found no abnormal thermal conductivity enhancement. In Table 2.3, the results of thermal conductivity measurement in the past 15 years from different research centers are summarized. Earlier measurements by several investigators indicated that the thermal conductivity of nanofluids could be influenced by so many parameters in the colloid system. Such parameters are: type of base fluids, particle size, shape of particles, pH value in aqueous fluids, and temperature. The effect of base fluid on thermal conductivity of nanofluid is reported by Keblinski et al. (2005). They dispersed treated Carbon Nano Tube in three different kinds of base fluids (Decene, Distilled water and Ethylene Glycol). Their results showed that Decene based nanofluids have the highest thermal conductivity enhancement, Ethylene Glycol based nanofluids are the second best, and Distilled water based nanofluids have the least improvement in thermal conductivity. Particle size effect on thermal conductivity enhancement is documented by Ganguly et al. (2009).

There are abundant investigations of thermal conductivity of nanofluids, but the discrepancy still exists. It is believed that nature of particles and heat transfer fluid, particle size and distribution affects the physical properties of nanofluid. It is of importance to have nanofluids synthesis process to be standardized and well understood. Also, the method of measurements has strong influence on the results of measured physical properties.

Table 2.3 Previous data for the thermal conductivity of nanofluids

Sample description	Measured k (W/mK)	Mesured k/kf	Predicted k/kf	
			Lower bound	Upper bound
Alumina nanorods (80×10 nm), 1 vol% in DI water	0.627±0.013	1.036±0.004	1.024	1.086
DI water	0.609±0.003	N/A	N/A	N/A
Alumina nanoparticles (10 nm), 1 vol% in DI+surfactant	0.162±0.004	1.039±0.003	1.027	1.03
Alumina nanoparticles (10 nm), 3 vol% in DI+surfactant	0.174±0.005	1.121±0.004	1.083	1.092
Alumina nanorods (80×10 nm), 1 vol% in DI+surfactant	0.164±0.005	1.051±0.003	1.07	1.116
Alumina nanorods (80×10 nm), 3 vol% in DI+surfactant	0.182±0.006	1.176±0.005	1.211	1.354
DI +surfactant	0.156±0.005	N/A	N/A	N/A
Gold nanoparticles (10nm), 0.001 vol% in DI+stabilizer	0.613±0.005	1.007±0.003	1	1
water+stabilizer	0.604±0.003	N/A	N/A	N/A
silica nanoparticles (22nm), 31vol% in water+stabilizer	0.729±0.007	1.204±0.010	1.008	1.312
DI water	0.604±0.002	N/A	N/A	N/A
Mn-Zn ferrite nanoparticles (7nm), 0.17 vol% in DI+stabilizer	0.459±0.005	1.003±0.008	1	1.004
DI+stabilizer	0.455±0.005	N/A	N/A	N/A

Aggressive scaling and complex device design cause increase of dissipation power density, switching speed and thermal resistance of the multi-layer structures; also formation of the local hot spots inside the chips. Thus, thermal management in electronic circuits is becoming an increasingly important issue. The thermal conduction of nanometer materials plays a fundamentally critical role that controls the performance and stability of nano/micro devices. Understanding of the thermal properties in novel materials and materials at nanometer scale are thus essential for thermal management of CMOS and beyond-CMOS heterogeneous and hybrid type devices. A wide variety of carbon materials like diamond, diamond-like carbon, polycrystalline diamond, tetrahedral amorphous carbon, graphite, carbon nanotubes, graphene etc. are possible candidates in this regard since they cover a large range of thermal conductivity. The thermal conductivity of carbon materials depends on the sp^3/sp^2 content, structural disorder, grain structure and size, thickness of the films and dimensionality of the material systems. The bulk of heat in carbon materials is carried by lattice vibrations, i.e. acoustic phonons.

The three dimensional form of carbon, diamond has remarkably high Young's modulus, record high thermal conductivity, chemical inertness, high mobility of charge carriers and high electron emission at low fields. Crystalline diamond is known to have the highest thermal conductivity among all bulk solids. At room temperature, it varies between 1000 - 2200 W/mK depending on the quality. These properties make diamond a preferable candidate for heat removal application. However, diamond's scarcity and hence cost makes this unappealing. Graphite is a layered material formed by stacks of two dimensional sheets of carbon atoms. It has one of the highest in plane thermal conductivity (2000 W/mK). But the thermal conductivity along c-axis is smaller compared to that along graphite basal plane. Again carbon nanotube (CNT) is a unique one dimensional form of carbon which has high thermal conductivity (ballistic conduction) along the tube. It is predicted that experimentally determined room temperature value of thermal conductivity for an individual multiwall carbon nanotube (MW-CNT) is 3000 W/mK and 3500 W/mK for an individual single-wall carbon nanotube (SW-CNT). Theoretical calculations of the thermal conductivity of CNTs mostly support the experimental results for individual CNTs, although some discrepancy exists. These values exceed those of the best bulk crystalline thermal conductor, diamond. Despite the high thermal conductivity, these materials are not well suited for integration with CMOS, instead newly discovered material graphene can be considered in this regard. The extracted near-room temperature thermal conductivity is on the high end of the values reported for CNTs or exceeds and was recently measured to be between $(4.84\pm0.44)\times10^3$ to $(5.30\pm0.48)\times10^3$ W/mK. This extremely high thermal conduction property of graphene allows it to be used for heat removal. The planer geometry of graphene provides more exposed contact to heat sink and much lower contact thermal resistance as compared to CNT. Such excellent properties allow graphene for better thermal management in the nanoelectronic devices and circuits.

Pradhan (2010) in his doctorate dissertation provides a thoughtful and detailed review of the history of nanowires and nanotubes, the most common synthesis techniques used in their production, the theoretical and experimental methodologies utilized in their study, and their resultant measured thermal properties. The author reports that based upon his own literature review, thermal conductivities of 3000 W/mK for MWCNT's and greater than 6600 W/mK for SWCNT's in their axial direction were reported. He also noted that according to current experimental results, carbon nanotubes of both types lose the vast majority of their conductivity when measured in large groups. Pradhan attributes this loss of effective thermal conductivity to the relatively large thermal contact resistances that exists between individual carbon nanofibers. Pradhan utilizes an AC Calorimeter to measure the specific heat and thermal conductivity of nanocomposites and provides the experimental and numerical background upon which their study was based. Pradhan provides his own study of the thermal properties of anisotropic MWCNT's, randomly oriented MWCNT's, and SWCNT's as they vary with temperature from 300-400 K. The research done by Pradhan is quite extensive and fascinating. Indeed for the current work, this review provides a great deal of background into the creation, use, and properties of carbon based nanotubes.

Han et al. (2011) in a doctorate dissertation and in a peer-reviewed paper focused on the effective thermal conductivity of CNT's and their potential applications as fillers for carbon based polymers. This review presented a rather in depth discussion of some of the current work on the thermal conductivity of SWCNT's and MWCNT's, specifically, the effects of a variety of factors such as carbon lattice structure, atomic structure, topological defects, dimensions, morphology, purity, etc. They concluded that based upon the current literature, the exact effective thermal conductivity of any type of carbon nanotube is based upon a dizzying variety of factors and requires a great deal of more knowledge to truly pinpoint. However, they noted that an effective thermal conductivity of greater than 3000 W/mK for MWCNT's and 2000 W/mK for SWCNT's is consistently reported in the literature. The authors note that because of the difficulties intrinsic in the experimental determination of the thermal conductivity of individual carbon nanotubes, a conductivity range of 2000-6000 W/mK is not unreasonable. This particular article helped to pinpoint the relative range of thermal conductivity that could be expected for a variety of carbon nanotubes.

P. Kim et al. (2001) detailed the design and use of a micro-fabricated suspension device to measure the thermal conductivity of individual MWCNT strands as they vary with temperature. The authors found conductivities greater than 3000 W/mK, and a peak value of the effective thermal conductivity of a MWCNT at 320 K. This particular work reported a significant value of thermal conductivity due to the fact that the MWCNT studied had a diameter of 14 nm and was measured with temperature variations well within the cryogenic ranges being studied in the current work.

Hone (2004) from Columbia University concluded a study on the thermal transport properties of carbon nanotubes. Specifically, the authors studied the phonon band structure of a variety of carbon nanotubes, and their interactions/coupling behavior. They also provided a brief review of the current literature on the effective thermal conductivity of MWCNT's and SWCNT's. In addition, the authors experimentally studied the specific heat and thermal conductivity of said carbon nanotubes. This research was extremely useful to the current research due to their study and subsequent graphical representation of the effective thermal conductivity of individual MWCNT's with respect to temperature at and near the cryogenic temperature range being utilized for this research.

Maruyama et al. (2011) studied the thermal conductivity of a single carbon nanotube in a liquid suspension with the use of a quantum dot hydrogel sensor. Murayama by using this unique experimental method, measured the thermal conductivity of a single carbon nanotube suspended within a liquid as approximately 412 W/mK. This research was of particular interest due to the fact that it studied the effective thermal conductivity of carbon nanotubes in fluid suspension, which is similar in the circumstances of the current work.

Behabtu et al. (2013) provided a fascinating work in terms of the design, creation, and testing of a truly exciting synthesis method for the creation of carbon nanotube based fibers. The authors report fiber specific strength, stiffness, and thermal/electrical conductivities consistent with current research and values that are similar to properties found in metals. They created a high throughput wet spinning process that is potentially scalable to industrial requirements. They also studied the electrical and thermal conductivities of a variety of their fibers as they varied with temperature. Fiber thermal conductivity values of greater than 700 W/mK were measured. This work has provided an understanding of the behavior of combined and interactive carbon nanotubes, for any real world application would exist.

2.3.1.3 Measurement techniques for thermal conductivity

Nanofluids have attracted a vast attention due to increment in thermal conductivity compared to basefluid. Measurement of these thermo-physical properties was a challenge for a long time since different methods and techniques presented different results. Thus, the method which is going to be used would be significant to lower the measurement error and uncertainty as much as possible. In this section, major thermal conductivity and the measurement methods from different literatures have been described briefly, and the following methods are going to be investigated:

1. Transient hot-wire techniques

2. Thermal constants analyzer techniques
3. Steady-state parallel-plate method
4. Cylindrical cell method
5. Temperature oscillation technique
6. 3ω method
7. Thermal comparator method
8. Laser Flash technique

Generally, Fourier's law for conduction heat transfer can be utilized to measure thermal conductivity of a material. Temperature difference can cause heat transfer through materials which is known as conduction heat transfer. Thermal conductivity is a particular property of the material which can differ from one material to another and can be calculated by Equation (2.2):

$$k = \frac{q/A}{\Delta T/L} \tag{2.2}$$

where, k is thermal conductivity, q is magnitude of heat transmission, ΔT is temperature difference, A is cross sectional area and L is the length (Bitaraf Haghighi et al., 2012). To simplify calculations, one-dimensional temperature filed and steady state flow could be considered.

In Case of liquids, convection should be avoided during measurements and since fluids does not have definite shape, size and cross sectional area, it would be more difficult to calculate thermal conductivity. Thus, measurement should take place in a very short time. Even the situation is worse in case of nanofluids, whereas suspended nanoparticles may cause a major problem. Figure 2.4 depicts utilization of different methods for measurement of thermal conductivity.

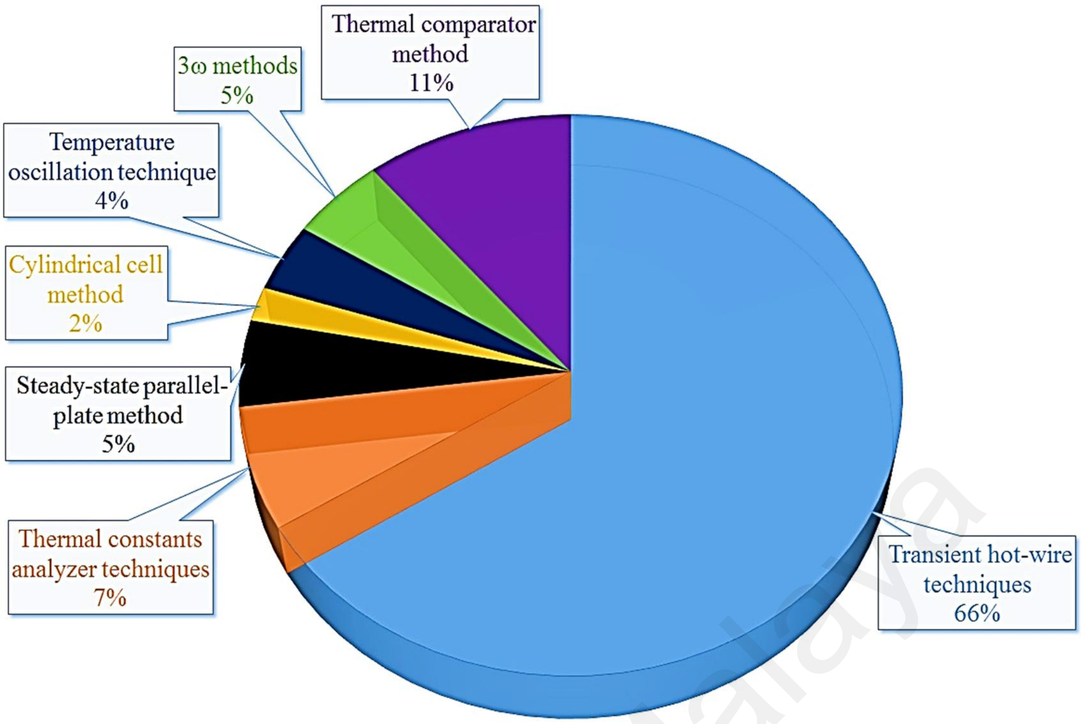

Figure 2.4 Share of different methods used for measurements of thermal conductivities presented in the literature (Behi et al., 2012)

2.3.1.3.1 Transient hot-wire (THW) method

This can be known as the most regular and the oldest method of measuring thermal conductivity. Comparing other methods, it can be known as a very fast measurement method and conceptual design of the apparatus is simple as well. It has been used to measure thermal conductivity of powders at the beginning. However, it has been improved by many researchers. The THW method is based upon using a long, thin platinum wire as a dual line heat source and temperature sensor. This is possible due to the relatively unique relationship between the temperature and thermal characteristics of platinum. The platinum filament is fully submerged within the fluid for which the thermal conductivity is to be determined, and a step increase in the electrical power supplied to the wire is introduced. This allows the platinum wire to heat up due to resistive heating. The excess heat from the hot filament is rejected to the surrounding fluid through conduction. Simultaneously, while this heating is occurring, the relative change in resistivity of the wire is being measured through a two or four wire resistive measurement system. The surface temperature of the hot wire and therefore the temperature of the immediate surrounding fluid can be calculated based upon this approach. The measured value of the total input power, and the power lost to the surrounding fluid are compared with the overall change in resistivity of the platinum wire due to electrical heating. These values, in conjunction with the measured experimental time and dimensional parameters of the hot wire setup, can be used to back calculate the thermal conductivity of the fluid of interest. As shown in Figure 2.5, the THW experimental setup is composed of Whetstone bridge circuit, DC power supply, stabilizer, switch, and data acquisition system (Behi, et al., 2012).

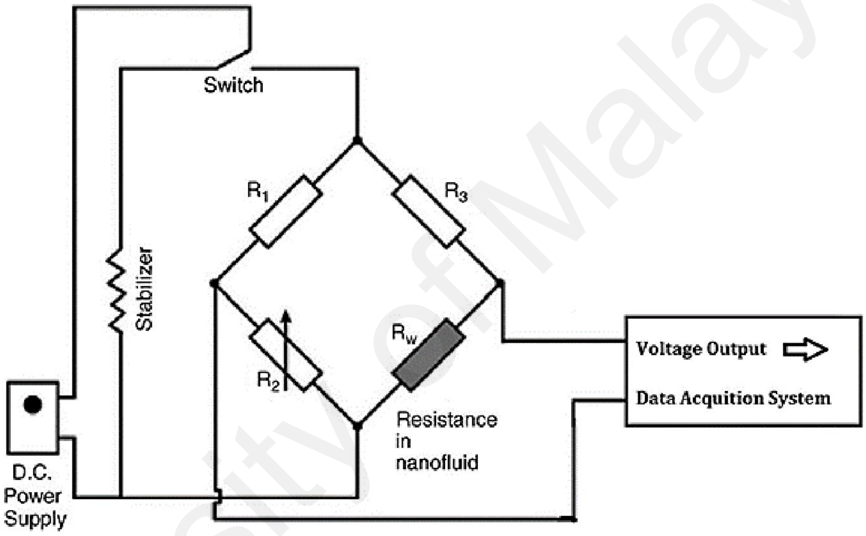

Figure 2.5 Schematic of transient hot-wire experimental setup (Shames et al., 1982)

2.3.1.3.2 Transient Plane Source (TPS) method

To compute thermal conductivity, transient plane source (TPS) theory is utilized by thermal constant analyzer. TPS sensor plays similar role as what probe or wire does in THW method; which means it acts as heating source together with temperature sensor. Followings are the advantages of this method as stated in the literature:

1. Fast measurement
2. Capability of measuring samples having wide range of thermal conductivity (From 0.02 to 200 W/m.K)
3. No sample preparation is required

4. Sample size can be flexible

Main components of experimental setup for transient plane source method are thermal bath with thermometer, TPS sensor, sample holder, thermal constants analyzer and computer. For calculating thermal conductivity of solids, probe of the analyzer is sandwiched between two sections of the material while for liquids it is immersed into the sample. The sample holder would be kept inside thermal bath with constant temperature and small amount of power will be supplied in short time to the sensor. Analyzer can calculate thermal conductivity later on.

It should be pointed out that convection can cause error in the result of thermal conductivity, thus parameters of analyzer should be controlled properly. This method has been used by some researchers.

2.3.1.3.3 Steady-state parallel-plate method

Nieto de Castro et al. (2012) described and used a guarded hot-plate design which is the basis of constructing an apparatus using steady-state parallel-plate method for measuring thermal conductivity. In this apparatus, small volume of fluid sample is located between two parallel round pure copper plates. Cross-sectional area and total area of the plate are determined. Sample holder is located in a larger cell made of aluminum. Two thermocouples are installed in top and bottom of the sample holder for measuring temperature differences of the samples. Heater is used to apply warm up of the sample as well. Moreover, heat conduction equation extracted from Fourier's law is applied to calculate thermal conductivity.

2.3.1.3.4 Cylindrical cell method

It might be known as one of the most common steady-state methods used for measuring thermal conductivity of fluids. Paul et al. (2010) utilized cylindrical cell method to measure thermal conductivity of water and ethylene glycol and compared the results with outcomes of artificial neural networks (ANNs) predictions. The instrument applying cylindrical cell method is composed of two coaxial cylinders which can be named as inner and outer cylinders. Inside the inner cylinder (made of copper), heater is placed while inside the outer cylinder where there is a gap between outer and inner cylinder, fluid sample would be kept. Two thermocouples are utilized to measure temperature difference after applying power and heat transform caused by heater of the fluid. Using Fourier's law in coaxial cylinders, thermal conductivity of sample in the gap could be computed.

2.3.1.3.5 Temperature Oscillation method

Temperature oscillation method uses oscillation method proposed by Roetzel et al. (1990). For the first time, it measures temperature response of the sample when a temperature response or heat flux is imposed.

Regarding experimental setup (Figure 2.6), the 7 main components for using temperature oscillation method are a test cell, cooling water, Thermal bath, DC power supply, amplifier and filter, data acquisition system and computer. A brief description of the device is as follows. Sample which hold inside test cell, which would be heated up by means of supplying power from DC power supply. Thermocouples measure temperature variations of the sample continuously and at the same time cooling water from bath is trying to control temperature at the preferred value or set point. Displaying temperature value on line would provide assessment of steady oscillation and recording data. Thermocouples data are amplified through amplifier with a filter. By this method, thermal diffusivity of the sample can be measured accurately. By means of that, thermal conductivity can be calculated having density and specific heat from handbook.

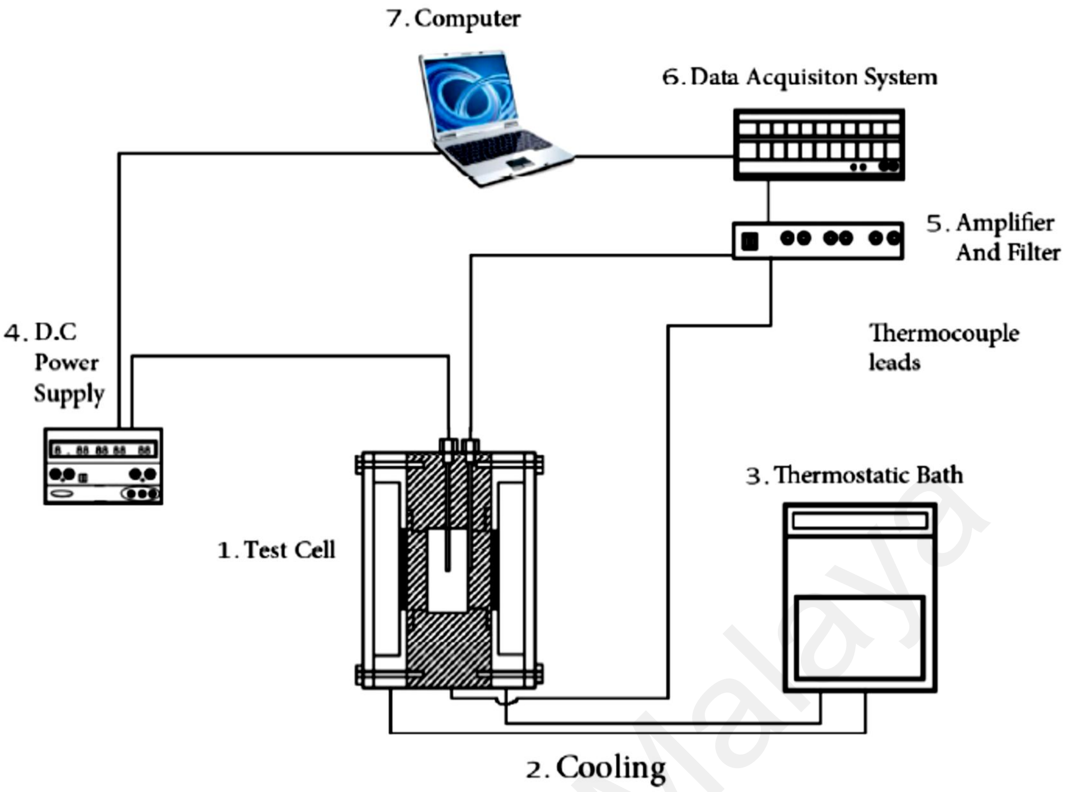

Figure 2.6 Schematic of transient temperature oscillation technique (Shames, et al., 1982)

2.3.1.3.6 3ω method

Similar to THW, 3ω is utilizing an element acting as heater and thermometer possessing radial flow of heat. However, the major difference between transient hot-wire and 3ω method is that in the former time dependent response is used while in the latter temperature oscillation is applied. Passing sinusoidal current at a frequency through metal wire, the heat wave at the frequency 2ω could be created. Afterwards, voltage components at the frequency 3ω could be reduced (Behi, et al., 2012).

2.3.1.3.7 Thermal comparator method

Powell (1957) posed an idea of thermal comparator in which two metal balls are located in block of a thermal insulation in parallel to measure thermal conductivity of materials such as aluminum, iron, alloy steel and so forth. Afterwards, the method has been used to measure thermal conductivity of different materials by other researchers. Through the years, idea was developed by some researches until Paul, et al. (2010) developed the idea inherently to measure thermal conductivity of nanofluids. Mainly, new device is composed of a copper probe, sample holder, DC voltmeter, voltage stabilizer and a heater. It is interested to note that unlike some other mentioned methods, in this technique, probe is required to have only a point contact with the sample. Thermocouple is placed between the sample and the probe which is supposed to have constant temperature by heater. Direct relationship should exist between thermal conductivity and observed differential emf after sensing temperature by thermocouple. It occurs when probe would be kept in point contact with the sample and thermo-emf is generated in circuit to cover the probe assembly and nanofluid. Considering different voltages in the circuit as well as boundary conditions and proper equations, thermal conductivity can be calculated.

2.3.1.3.8 Laser Flash technique

The Laser Flash technique is based on the measurement of the thermal transient of the rear surface of the sample when a pulsed laser illuminates the front and it avoids interferences between the thermal sensor and the heat source. The physical model of the Laser Flash measurement supposes to have a single pulsed heat source (delta like), for example a laser shot, on the sample front surface. The study of the thermal transient of the rear surface provides the desired thermal information. The temperature of the rear face is measured with an infrared detector and it can be expressed mathematically as a function of several variables that are grouped into dimensionless parameters. These variables include sample geometry, thermal diffusivity and heat loss from the sample (Behi, et al., 2012).

2.3.1.4 Thermal conductivity models for nanofluids

There are a number of different types of models developed to predict the newly observed thermal conduction behavior of nanofluids (J.-H. Lee et al., 2010). Five groups of mechanismbased k models for nanofluids include those based on (1) classical effective medium theory; (2) nanoscale layer; (3) Brownian motion; (4) agglomeration; and (5) other mechanisms. Each group of mechanismbased k models has been further broken into several subcategories.

There are several standard thermal conductivity models for composites including the Hamilton-Crosser (HC) model and Maxwell model and the weakness of these traditional models is predicting the thermal conductivities of nanofluids, which led to the proposition of various new mechanisms. As dispersions of solid particles in a continuous liquid matrix, nanofluids are expected to have a high thermal conductivity that obeys the effective medium theory developed by Maxwell. Maxwell's model for well dispersed particles culminates in a simple equation giving the ratio of the nanofluid thermal conductivity k_{nf} to the thermal conductivity of the based fluid k_{bf}.

It is noticeable that, once the nanoparticle material and the base fluid are assigned, the effective thermal conductivity of the nanofluid is dependent on temperature and concentration(φ). Moreover, $\Delta k/k\%$ depends marginally on the solid–liquid combination because most of the experimental data used to derive Equation (2.3) are related to the nanofluids with suspended NDG nanoparticle. Consequently, it is apparent that the thermal conductivity and thickness of interfacial layer have important effects on the enhanced thermal conductivity of nanofluids. The typical theoretical models have been developed for thermal conductivity of nanoparticles suspended in the base fluids are considering only thermal conductivities of the base fluid, nano-particles and volume fraction of particles while particle size, shape, distribution and the motion of dispersed particles are having significant impacts on thermal conductivity enhancement. Therefore, the experimental results could not be compared with the correlated values of theoretical models. Many researchers have accomplished different benchmark research on the thermal conductivity of nanofluids and the results indicated that the experimental data were in good agreement with the data obtained from Nan's model. According to Nan's model, the results in thermal conductivity of the nanofluid is expressed by Equation (2.3) (Mohammad Mehrali, et al., 2014a).

$$k_{nf} = k_{bf}\frac{3+\phi[2\beta_{11}(1-L_{11})+\beta_{33}(1-L_{33})]}{3-\phi(2\beta_{11}L_{11}+\beta_{33}L_{33})} \tag{2.3}$$

where, L_{ii} and ϕ are the geometrical factor and the volume fraction of particles, respectively. β_{ii} is defined as:

$$\beta_{ii} = \frac{k_p - k_{bf}}{k_{bf} + L_{ii}(k_p - k_{bf})} \tag{2.4}$$

Table 2.4 shows some classical effective medium theory based models.

Table 2.4 A list of the most frequently used models for evaluating effective thermal conductivity

Model	Expressions ($^{k_{eff}}/_{k_{bf}}$)	Remarks
Maxwell (1873)	$\frac{k_{np}+2k_{bf}+2(k_{np}-k_{bf})\phi}{k_{np}+2k_{bf}-(k_{np}-k_{bf})\phi}$	relates the thermal conductivity of spherical particle, base fluid and solid volume fraction
Hamilton and Crosser (1962)	$\frac{k_{np}+(n-1)k_{bf}-(n-1)(k_{bf}-k_{np})\phi}{k_{np}+(n-1)k_{bf}+(k_{bf}-k_{np})\phi}$	for non-spherical particles, k_{np}/k_{bf} >100, n is an empirical shape factor (n=3/ψ, ψ is the sphericity)
Jeffrey (1973)	$1+\frac{3\phi\left(\frac{k_{np}}{k_{bf}}-1\right)}{\frac{k_{np}}{k_{bf}}+2}$ $+3\phi^2(\frac{\frac{k_{np}}{k_{bf}}-1}{\frac{k_{np}}{k_{bf}}+2})^2.\left[1+\frac{1}{4}\left(\frac{\frac{k_{np}}{k_{bf}}-1}{\frac{k_{np}}{k_{bf}}+2}\right)\right.$ $\left.+\frac{3}{16}\left(\frac{\frac{k_{np}}{k_{bf}}-1}{\frac{k_{np}}{k_{bf}}+2}\right)\left(\frac{\frac{k_{np}}{k_{bf}}+2}{2\frac{k_{np}}{k_{bf}}+3}\right)+\cdots\right]$	High order terms represent pair interactions of randomly dispersed particles
Davis (1986)	$1+\frac{3\left(\frac{k_{np}}{k_{bf}}-1\right).[\phi+f\phi^2+O(\phi^3)]}{\left(\frac{k_{np}}{k_{bf}}+2\right)-(\frac{k_{np}}{k_{bf}}-1)\phi}$	High order terms represent pair interactions of randomly dispersed spheres, f=2.5&0.5 for k_{np}/k_{bf}=10 and ∞
Wasp (1977)	$\frac{k_{np}+2k_{bf}-2(k_{bf}-k_{np})\phi}{k_{np}-2k_{bf}+(k_{bf}-k_{np})\phi}$	special case of Hamilton and Crosser's model with ψ =1
Bruggeman (1935)	$\frac{1}{4}[(3\phi-1)\frac{k_{np}}{k_{bf}}+(2-3\phi)+\frac{1}{4}\sqrt{\Delta}$	$\Delta= [(3\phi-1)^2(k_{np}/k_{bf})^2+(2-3\phi)^2+2(2+9\phi-9\phi^2)(k_{np}/k_{bf})]$

2.3.2 Specific heat (C_p)

The specific heat is one of the important properties and plays an important role in influencing heat transfer rate of nanofluids. Specific heat capacity is defined as the ratio of the amount of energy that has to be transferred to or from one unit of mass or amount of substance to change the system temperature by one degree. It is measured usually with J/kgK. There are two expressions for determining the specific heat of nanofluids:

$$C_{p,nf} = \varphi C_{p,np} + (1 - \varphi) C_{p,bf} \tag{2.5}$$

and

$$(\rho C_p)_{nf} = \varphi (\rho C_p)_{np} + (1 - \varphi)(\rho C_p)_{bf} \tag{2.6}$$

It is thought that Equation (2.6) is theoretically more consistent since specific heat is a mass specific quantity whose effect depends on the density of the components of a mixture.

Differential scanning calorimetry (DSC) is a powerful tool to measure the heat capacity of nanofluids. The difference in the amount of heat flow required for heating up a sample pan and reference pan are measured as a function of temperature. During the whole process, the sample and reference pans are maintained at nearly the same temperature throughout the experiment. The heat capacity of the reference pan is already known. By measuring the difference in heat flow, the heat capacity of the sample is obtained. If there are phase transitions happened in the sample pan, more or less heat will need to flow to it than the reference to maintain both at the same temperature, so endothermal or exothermal peaks are shown on the DSC curves, corresponding to melting or freezing, respectively. The phase transition temperatures and latent heats are determined according to the DSC curves (Mohammad Mehrali, et al., 2014b).

2.3.3 The concept of viscosity

Viscosity is a measure of the resistance of a fluid to flow. This resistance arises from the attractive forces between the molecules of the fluid. A fluid will only flow if enough energy is supplied to overcome these forces. Isaac Newton (1642 - 1727) was the first to define viscosity scientifically. He derived a mathematical formula relating the viscosity to the resistive (drag) force experienced by a thin plate “cutting” its way (“shearing”) through the fluid. The definition was based on two quantities:

1. "Shear rate". This is the speed of the thin plate divided by its distance from some reference surface, such as the wall of the container.
2. "Shear stress". This is the drag force experienced by the thin plate divided by its surface area.

Viscosity describes a fluid's internal resistance to flow and may be thought of as a measure of fluid friction. For example, high-viscosity felsic magma will create a tall, steep stratovolcano, because it cannot flow far before it cools, while low-viscosity mafic lava will create a wide, shallow-sloped shield volcano. All real fluids (except superfluids) have some resistance to stress and therefore are viscous, but a fluid which has no resistance to shear stress is known as an ideal fluid or inviscid fluid (Symon, 1971).

In general, in any flow, layers move at different velocities and the fluid's viscosity arises from the shear stress between the layers that ultimately opposes any applied force. The relationship between the shear stress and the velocity gradient can be obtained by considering two plates closely spaced at a distance y, and separated by a homogeneous substance. Assuming that the plates are very large, with a large area A, such that edge effects may be ignored, and that the lower plate is fixed, let a force F be applied to the upper plate. If this force causes the substance between the plates to undergo shear flow with a velocity gradient u (as opposed to just shearing elastically until the shear stress in the substance balances the applied force), the substance is called a fluid (Figure 2.7).

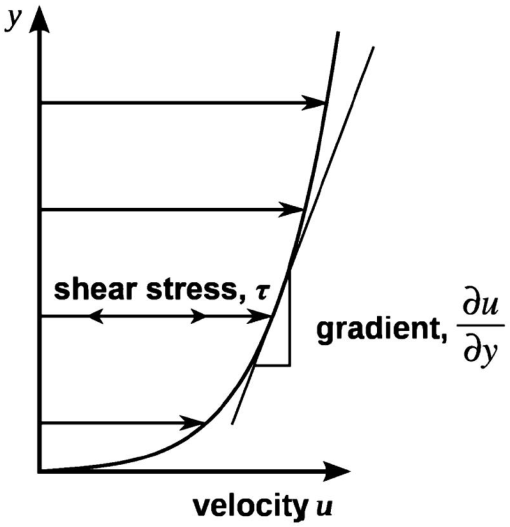

Figure 2.7 Laminar shear flow (Shames, et al., 1982)

The applied force is proportional to the area and velocity gradient in the fluid and inversely proportional to the distance between the plates. Combining these three relations results in the Equation (2.7).

$$F = \mu A \frac{u}{y} \tag{2.7}$$

where, μ is the proportionality factor called viscosity.

This equation can be expressed in terms of shear stress $\tau = \frac{F}{A}$. Thus as expressed in differential form by Isaac Newton for straight, parallel and uniform flow, the shear stress between layers is proportional to the velocity gradient in the direction perpendicular to the layers (Symon, 1971).

$$\tau = \mu \frac{\partial u}{\partial y} \tag{2.8}$$

Hence, through this method, the relation between the shear stress and the velocity gradient can be obtained.

Note that the rate of shear deformation is $\frac{u}{y}$ which can also be written as a shear velocity, $\frac{\partial u}{\partial y}$.

Rheological properties of colloids have been widely studied in the past century. Einstein (1906) had proposed theoretical equation to predict viscosity of very dilute colloid system (less than 1% by volume) a century ago. Many researchers have attempted to improve viscosity model for colloids. As the concentration increases, the hydrodynamic interaction between particles as important, because the disturbance of fluids around one particle will interact with that around other particles. In 1977, Batchelor (1977) took this factor into account and proposed an improved model to predict viscosity of colloids at relatively higher concentration for colloids. When the concentrations become even higher, multiple particles colloid and become important, however, there is no rigorous analysis addressing this aspect. In 1959, Krieger et al. (1959) proposed a semiempirical correlation for the shear viscosity to cover the whole range of concentrations. Also, many experiments have been conducted to understand colloid viscosity. Goodwin et al. (2008), Larson (2005) and Abdulagatov et al. (2006) had experimentally investigated rheological properties of their colloids. Chang et al. (1994) and Luckham et al. (1999) have investigated particle size and particle distribution effect on viscosity of colloids. These results showed that finer particle size would result in higher viscosity, and larger particle size distribution could help reduce viscosity of the mixture. However, the research on rheological property of nanofluids is still scarce.

2.3.3.1 Types of viscosity

Newton's law of viscosity is a constitutive equation (like Hooke's law, Fick's law, Ohm's law). It is not a fundamental law of nature but an approximation that holds in some materials and fails in others. Non-Newtonian fluids exhibit a more complicated relationship between shear stress and velocity gradient than simple linearity (Figure 2.8).

All materials that show flow behaviour are referred to as fluids. In all fluids, there are frictional forces between the molecules and, therefore, they display a certain flow resistance which can be measured as viscosity. Viscosity is a transport property which refers to the resistance of a material to flow. When dealing with nanofluids, one is often tempted to consider the dispersed medium under question as a homogeneous fluid characterized by properties such as density and viscosity which in turn will only require a single set of mass and momentum conservation equations. However, such a simple picture will not provide useful explanations for cases where the fluid is unsteady and non-uniform.

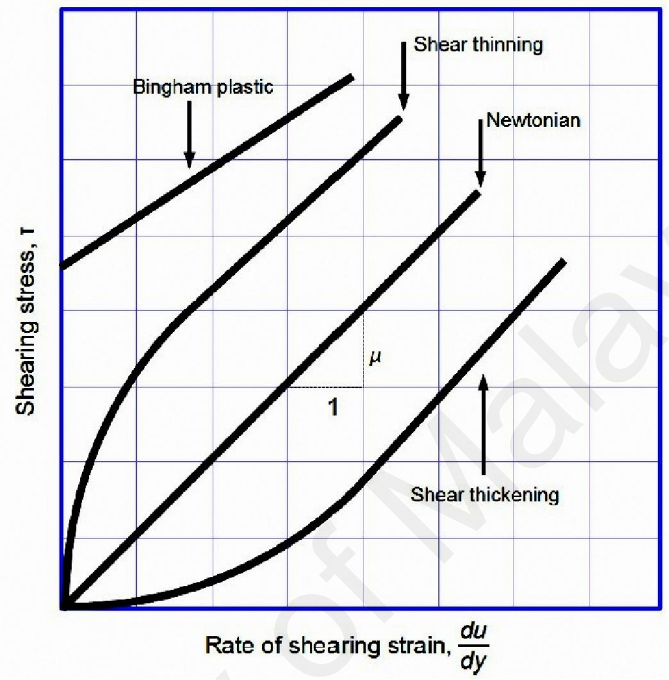

Figure 2.8 Viscosity, the slope of each line, varies among materials (Symon, 1971)

Thus there exist a number of forms of viscosity:

1. Newtonian: fluids, such as water and most gases which have a constant viscosity.
2. Shear thickening: viscosity increases with the rate of shear.
3. Shear thinning: viscosity decreases with the rate of shear. Shear thinning liquids are very commonly, but misleadingly, described as thixotropic.
4. Thixotropic: materials which become less viscous over time when shaken, agitated, or otherwise stressed.
5. Rheopectic: materials which become more viscous over time when shaken, agitated, or otherwise stressed.
6. A Bingham plastic is a material that behaves as a solid at low stresses but flows as a viscous fluid at high stresses.

7. A magnetorheological fluid is a type of "smart fluid" which, when subjected to a magnetic field, greatly increases its apparent viscosity, to the point of becoming a viscoelastic solid.

2.3.3.2 Viscosity coefficients

Viscosity coefficients can be defined in two ways:

1. Dynamic viscosity, also absolute viscosity, the more usual one (typical units Pa·s, Poise, P);
2. Kinematic viscosity is the dynamic viscosity divided by the density (typical units m^2/s, Stokes, St).

The viscosity of a fluid is a measure of its resistance to gradual deformation by shear stress or tensile stress. For liquids, it corresponds to the informal concept of "thickness" that can be disintegrated in different ways into two independent components. The most usual decomposition yields the following viscosity coefficients:

1. Shear viscosity, the most important one, often referred to as simply viscosity, describing the reaction to applied shear stress; simply put, it is the ratio between the pressure exerted on the surface of a fluid, in the lateral or horizontal direction, to the change in velocity of the fluid as you move down in the fluid (this is what is referred to as a velocity gradient).
2. Volume viscosity (also called bulk viscosity or second viscosity) becomes important only for such effects where fluid compressibility is essential. Examples would include shock waves and sound propagation. It appears in the Stokes' law (sound attenuation) that describes propagation of sound in Newtonian liquid.

Alternatively,

1. Extensional viscosity, a linear combination of shear and bulk viscosity, describes the reaction to elongation, widely used for characterizing polymers. For example,

at room temperature, water has a dynamic shear viscosity of about 1.0×10^{-3} Pa·s and motor oil of about 250×10^{-3} Pa·s (Symon, 1971).

2.3.3.3 Viscosity of nanofluids

Since the conventional base fluid such as water, EG, DEG, AFN, Oil, etc. have been used in different applications such as power plants, heating/cooling applications, chemical industry, automobile and so forth. However, they have not shown proper thermal properties, which impose higher cost to the system (Mohammad Mehrali, et al., 2014a).

In the past decades the investigation of nanofluids viscosities was not considered as same as thermal properties. Yet, viscosity of nanofluid is one of the most critical parameter in nanofluids, which should be considered by researches and need to be investigated thoroughly. The key point in a nanofluid is to compromise the Thermal conductivity and Viscosity because the viscosity increment offsets thermal conductivity increase.

In order to design a proper cooling system, it is expected that nanofluids as cooling media have almost considerable increment in thermal conductivity. On the other hand, almost less increment or constant viscosity is expected which means higher ratio of thermal conductivity and viscosity. There are different crucial parameters influencing the viscosity that are investigated by researches. These factors consist of temperature, volume concentration, particle size, morphology, time sonication, shear rate, etc.

Based on the literature, understanding viscosity of nanofluids is the one of fascinating challenge and the most critical parameters in heat transfer properties of nanofluids. It follows two important characteristics: (a) increase in viscosity with increases of nano-particle concentration and the internal viscous shear stress increases, (b) decrease in viscosity with temperature (Sadri et al., 2014). With increasing of the temperature, the nano-particles are motivated more, hence inter-particle and inter-molecular adhesion forces become weaken. Meanwhile, with the rise of temperature, thermal movement of molecules and Brownian motion intensifies and viscosity of the nanofluids decreases (Mohammad Mehrali, et al., 2014a).

First of all is better to define viscosity as a general concept. This is a measure of the resistance of a fluid which is being deformed by either shear or tensile stress; furthermore, viscosity describes a fluid's internal resistance to flow and may be thought of as a measure of fluid friction; moreover, in common terms, viscosity is the thinness or thickness of the fluid. It is equal to the tangential stress on a liquid undergoing streamline flow divided by its velocity gradient. Once absolute viscosity has been defined, it is turn to talk about the difference between dynamic and kinematic viscosities. The first one is the quantitative expression of a fluid's resistance to flow (shear), while kinematic is a ratio of the viscous force to the inertial force. In this study only dynamic viscosity will be used, because by its measurement, it is possible to guess the Newtonian or non-Newtonian behavior of the sample. For microelectronics application, it is better for nanofluids to show low viscosity values, since it is important that the fluid flows properly through the microchannels (Mohammad Mehrali, et al., 2014b).

The researchers have highlighted the different factors which can influence the viscosity.

1. Temperature
2. Volume fraction
3. Morphology
4. Shear rate
5. Dispersion method, stabilizers and Clustering

2.3.3.4 Viscosity Measurement Methods

There are generally a limited number of literatures which worked on the viscosity instrumentation measurement. Viscosity is one of critical issues in fluids and tightly contributes to costs in industry. Methods which are frequently used in nanofluids viscosity measurements are divided into two groups as flow type and drag type (Behi, et al., 2012).

2.3.3.4.1 Flow Type Viscometers:

Flow type method is composed of two main methods, namely capillary and orifice method.

2.3.3.4.1.1 Capillary viscometers

This method is introduced as the best method for fluid viscosity measurement. Capillary viscometers are basically used for Newtonian, incompressible and wall adherence liquids. The principle of capillary viscometers is the time at which a standard volume of fluid passes through a length of capillary tube. The pre-condition assumed for this measurement is having a laminar, incompressible and stationary fluid. Moreover, since flow influence at the entry and exit of capillary is negligible, the viscosity of fluids is considered to be pressure independent.

Capillary viscometers are working on the basis of Hagen-Poiseuille Law.

$$\frac{V}{t} = \frac{\pi r^4 \Delta P}{8L\mu} \tag{2.9}$$

where, V, t, R, ΔP, L, and μ are volume, time, and radius of capillary, pressure drop, and length of capillary and dynamic viscosity of fluids respectively. The modified formula for the capillary systems suggested as Poiseuille equation or Hagen-Poiseuille equation as follows:

$$\mu = \frac{\pi r^4 \rho g h t}{8V(L + nr)} - \frac{m\rho V}{8\pi(L + nr)t} \tag{2.10}$$

Where, r is the radius and L is the length of the capillary, h is the effective height of standard liquid column, which is the liquid density, V is the discharged volume at time t, and m and n are constants which can be determined experimentally. $\rho g h$ is the pressure which can be replaced by ΔP (the pressure drop along the capillary), and nr is defined as the end correction (for liquid exit and entry) which basically corrects the surface tension effects.

Figure 2.9 shows the capillary viscometer parts.

1. Cap nuts
2. Washers
3. Holding plate
4. Silicone rings
5. Fixing plate
6. Silicone O-ring
7. Quick-release closure
8. Tube ends
9. Tempering Jacket

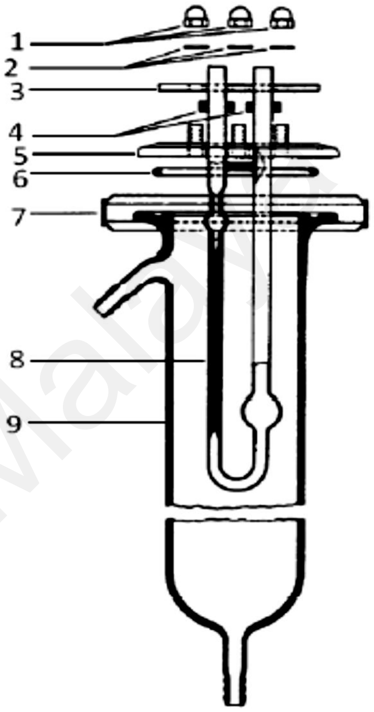

Figure 2.9 Falling ball viscometers schematic (Shames, et al., 1982)

2.3.3.4.1.2 Orifice type (Cup) viscometers

Orifice viscometers (efflux type) like draining vessel are very common in oil and industry viscosity measurements. These kinds of viscometers usually consists of reservoir (flow cup), an orifice and a receiver. The design concept of these viscometers is based on the Hagen-Poiseuille Law (constant volume efflux of liquid in a capillary is proportional to the viscosity of the fluid). Concerning Draining vessel method, time will be counted for a constant volume of liquid which flows through a small orifice at the bottom of the cup. Then, viscosity is derived from look-up tables.

2.3.3.4.2 Drag Type Viscometers

Drag type viscometers are also categorized as falling object, rotational and bubble tube methods.

2.3.3.4.2.1 Falling object (ball) viscometers

This type of viscometer has the principle, which specify the time of falling ball with known diameter and density through a liquid filled inside a vertical glass tube of known diameter and length.

The liquid has a dynamic viscosity, which results a resistance against the downward movement to the ball. This frictional force is derived from the Stokes's law. The falling ball method is based on Stokes' law which is expressed by Equation (2.11).

$$\mu = [\frac{2}{9}\frac{gr^2(\rho_k - \rho_{liq})}{\nu} \qquad (2.11)$$

Where, g is the gravitational constant, r is the radius of the ball, ρ_k and ρ_{liq} are the density of the sphere and the liquid, respectively and is the ascent velocity of the sphere.

Figure 2.10 shows the falling ball viscometer parts.

1. Stand
2. Viscometer
3. Spirit level
4. Adjusting screw
5. Adjustment screw
6. Falling tube
7. Upper plate
8. Lower plate
9. Water bath jacket
10. Olive shaped tubes
11. Fastening screw for thermometer
12. Screw neck
13. Sealing washer
14. Bearing
15. Nuts
16. Upper locking plug
17. Lower locking plug
18. Cap
19. Sealing
20. Lid
21. Falling tube screw fitting

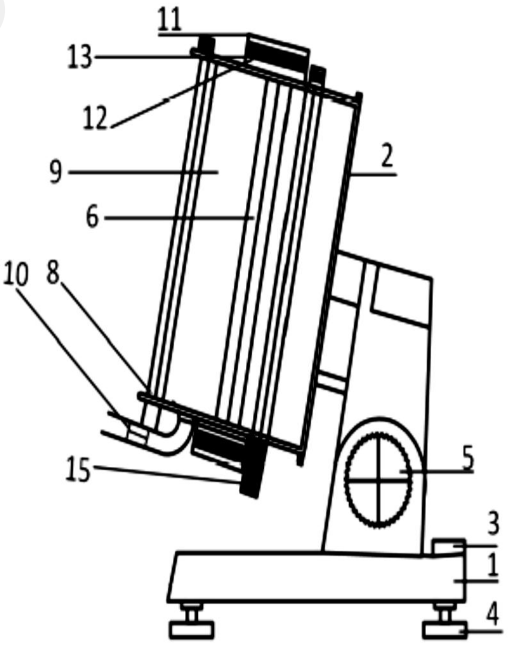

Figure 2.10 Falling ball viscometers schematic (Shames, et al., 1982)

2.3.3.4.2.2 Rotational viscometers

This is a kind of viscometer in which the principal of operation is to drive a spindle (which is immersed in the test fluid) through a calibrated spring. Torque applied on a cylinder rotating in the sample is applied to calculate the viscosity. The viscous resistant of the sample against the cylinder is measured by a spring deflection and spring deflection is measured with a rotary transducer. This genre of viscometers consists of two concentric cylinders namely a bob (spindle) and a crucible (cylinder) (Figure 2.11).

The measurement range of rotary cylinder viscometers (in centipoises / milliPascal seconds) is determined by the spindle rotational speed, size and shape of the rotary spindle, container in which spindle is rotating full-scale torque of the calibrated spring and so forth. At a constant rotational speed the viscosity of a fluid can be obtained using the Equation (2.12).

$$\mu = (\frac{1}{r_1^2} - \frac{1}{r_0^2})\frac{M}{8\pi^4 nh} \qquad (2.12)$$

Where M is the torque, n is the number of revolutions per second, r_1 is the radius of spindle, r_0 is the radius of spindle crucible, and h is the height of spindle.

1. Viscometer
2. Sample holder
3. Thermocouple
4. Constant temperature bath
5. Guard leg
6. Sample fluid
7. Rotating spindel

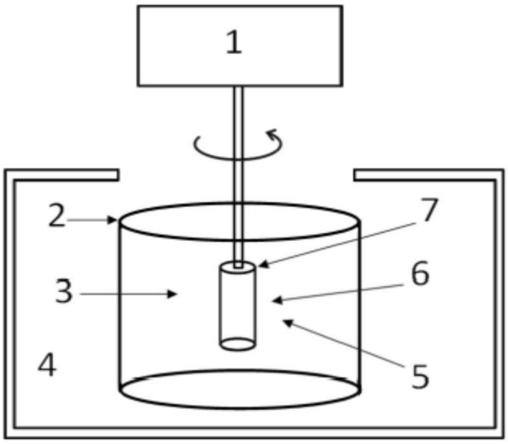

Figure 2.11 Coaxial cylinder viscometers schematic (Shames, et al., 1982)

2.3.3.4.2.3 Bubble (Tube) viscometers

It is a kind of viscometer in which bubble movement in liquid at a certain period of time, is the measurement principle. This kind of viscometers is used to determine kinematic viscosity quickly. Time at which the bubble rises inside the sample is proportional to the viscosity of liquid. The slower the bubble rises, the more viscose fluid, it would be, and vice versa. In this kind of viscometer, it is needed to know almost a close estimation of fluid viscosity to choose the proper tube for measurement (Figure 2.12).

Figure 2.12 The bubble viscometers (Shames, et al., 1982)

2.3.3.4.3 Vibrational/Oscillating Viscometers

The most common methods of oscillating (vibrational) measurements are oscillating vessel, palate and drop viscometers.

2.3.3.4.3.1 Oscillating vessel viscometer

It is a kind of viscometer in which the principle is oscillation damping by liquid at a specific time period. Sample of liquid is put in a vessel and exposed to a motion in vertical axis. The viscosity of sample is determined by considering the decrement of motion at a certain period of time.

2.3.3.4.3.2 Oscillating plate viscometer

This method is based on vibration of a flat plate and amplitude of plate oscillating inside the test sample. The oscillation of the flat plate with a constant driving force is measured in both liquid and air.

$$\rho\mu = \frac{R_M^2}{\pi A^2 f}\left(\frac{f_a E_a}{fE} - 1\right)^2 = K\theta_0 \tag{2.13}$$

where, ρ is density, R_M is the real digit of the mechanical impedance, f and f_a are frequencies of plate oscillation in liquid and air, E and E_a are also the amplitude of oscillation of plate inside the air and sample and A is the palate effective area.

Concerning the formulation in which the measurement is based on the assumptions stated below:

1. Sample test should be Newtonian one,
2. The constant force exerts and the amplitude of it should be in a way no turbulent flow happen.
3. There should be no slipping between the plate and the fluid.
4. Oscillating palate size should be large enough- larger than one oscillation wavelength.
5. The end damping influence of plate is negligible.
6. Vessel size should also be large enough so that the effects of reflected wave from the wall are negligible.

2.3.3.4.3.3 Oscillating (levitated) drop viscometer

It is a kind of method by which both surface tension and viscosity of liquids are measurable. In this method, there is no need of external forces and it can be done by falling a droplet. The measurement is based on the principle that relates the frequencies of liquid surface oscillation with surface tension using Rayleigh's formula. Cummings and Blackburn formula is a corrected version of Rayleigh's formula by which the earthbound levitation. Moreover, the viscosity of fluids are measured based on similar principle. The damping constant by which the viscosity is measured by Equation (2.14).

$$\Gamma = \frac{20\pi}{3}\left(\frac{r\mu}{m}\right) \tag{2.14}$$

where m and r are mass and radius of droplet, respectively and μ is viscosity. Meanwhile, to achieve a correct measurement the conditions below should be met:

1. Droplet of liquid should be spherical.
2. The oscillation have to stand in a time for about $t = \frac{1}{\Gamma}$
3. There should be no extra damping mechanisms.

2.4 Stability of Nanofluid

To provide better cooling using nanofluids in industry, they are expected to possess long-term stability which should be noted during preparation and synthesis of nanofluids. Indeed, to utilization of nanofluids in practice, stability might be one key issue. Therefore, reasons for fast sedimentation of nanoparticles or nanotubes should be recognized and dispelled (Mohammad Mehrali, et al., 2014b).

2.4.1 Effective parameters on stability

In general, there are three different techniques utilized by researchers to improve dispersion behavior of nanofluids and to minimize particles aggregation which acts against long-term stability. However, clustering and aggregation have been reported as features increasing thermal conductivity of nanofluids. Therefore, in preparation both issues should be taken into account to make a balance between stability and thermal conductivity, having a stable thermal conductive nanofluid. Those three common techniques for making stable nanofluid are stated below (Mohammad Mehrali, et al., 2014b):

2.4.1.1 Addition of surfactant

Surfactants can be defined as chemical compounds added to nanoparticles in order to lower surface tension of liquids and increase immersion of particles. Several literatures talk about adding surfactant to nanoparticles to avoid fast sedimentation; however, enough surfactant should be added to particle at any particular case.

In investigation, several types of surfactant had been utilized for different kinds of nanofluids. The most significant ones could be listed as below:

1- Sodium dodecylsulfate (SDS),
2- Sodium dodecylbenzenesulfonate (SDBS),
3- Salt and oleic acid,
4- Cetyltrimethylammoniumbromide (CTAB),
5- Dodecyl trimethylammonium bromide (DTAB),
6- Sodium octanoate (SOCT),
7- Hexadecyltrimethylammoniumbromide (HCTAB),
8- Polyvinylpyrrolidone (PVP),
9- Gum Arabic,
10- Triton X-100

It should be pointed out that this technique cannot be applicable for nanofluids working in high temperature on account of probable damage to bonding between surfactant and nanoparticle.

2.4.1.2 pH Control

Stability of nanofluid is directly related to its electro-kinetic properties; therefore, pH control of them can increase stability due to strong repulsive forces. General speaking, two types of behavior including attraction and rejection occurs among particles due to van der Waals and electrostatic forces and it is possible to control these forces by means of pH control.

2.4.1.3 Ultrasonic agitation (vibration)

After preparation of nanofluids, agglomeration might occur over the time which results in fast sedimentation of nanoparticles due to enhancement of downward body force from cumulative weight. Based on the literature (E. K. Goharshadi et al., 2009; Mehrali et al., 2014b; Sun et al., 2013), the sonication time is an important parameter for dispersing the aggregated nanoparticles. As it was mentioned before, all three methods might be used for one specific sample during synthesis and preparation; yet, it is difficult to make stable nanofluid and rare to maintain nanofluids synthesized by the traditional methods in a homogeneous stable state for more than 24 h (Sadeghinezhad, et al., 2014).

2.4.2 Stability Evaluation Method

Among limited number of studies on stability of nanofluids, evaluation of them has been considered by some researchers and six different methods were utilized which can be listed as below:

1. UV-Vis spectrophotometer
2. Zeta potential test
3. Sedimentation photograph capturing
4. TEM (Transmission Electron Microscopy) and SEM (Scanning Electron Microscopy),
5. Sedimentation balance method
6. 3ω method

2.4.2.1 UV-Vis spectrophotometer

Ultra Violet-Visible spectrophotometer is one of the most common methods used to investigate stability of nanofluids due to ease of using this instrument and getting fast analysis of results. It has been utilized to magnitude stability of suspensions in nanofluids; however, viscosity of base fluid would be known as one constraints of this method. This method is based on different wavelengths of light in which it can be scattered or absorbed by other materials. It is known when light is passing through fluids, intensity of it changes by absorption and scattering (Mohammad Mehrali, et al., 2014b).

The stability of the nanofluid was determined by measuring the different concentration of the suspensions with the sediment time by the UV–Vis spectrophotometer and it was widely used in evaluating the relative concentration of the nanofluids. UV–Vis spectrophotometer method is based on Beer–Lambert's law, which states that the absorbance was directly proportional to the concentration of the nano-particles in the nanofluids (Mohammad Mehrali, et al., 2014b).

The UV–vis spectrophotometer analysis is a convenient approach to characterize the stability of colloids quantitatively. The light absorbency ratio index can be calculated by the Beer Lambert Law as shown in Equation (2.15).

$$A = -\log\left(\frac{I}{I_i}\right) = \varepsilon bc \tag{2.15}$$

Equation (2.15) shows that at fixed molar optical path and absorptivity, the absorbency is relative to the weight percentage of the particles inside the suspension (Mohammad Mehrali, et al., 2014a).

2.4.2.2 Zeta-potential test

The colloidal stability of nanofluids is measured by zeta-potential values of the nanoparticles dispersed in DW and closely related to its electrophoretic properties. A well-dispersed suspension can be obtained with high surface charge density to generate strong repulsive forces. Nanofluids with zeta-potential value of more negative than -30mV or more positive than +30mV are considered stable and this is one of the common methods to determine the stability of nanofluids (Mohammad Mehrali, et al., 2014a).

The most important factor that affects the zeta-potential is pH and without statement pH is this only a virtually meaningless number. Generally, the zeta-potential versus pH curve will change from positive to negative with the variation of pH. The point where the plot passes through the zero value of the zeta-potential is called the isoelectric point and it is very important from a practical perspective. At the isoelectric point, the agglomeration and precipitation of nanofluids were observed (S. W. Lee et al., 2011; Navrátilová et al., 2012).

Vandsburger tabulated different values of zeta potential in mV and stated stability situation of the suspension in any specific zeta potential value which can be observed in Table 2.5 (Mohammad Mehrali, et al., 2014b).

Table 2.5 Zeta potential value and stability

Zeta potential (Absolute value (mV))	Stability
0	Little or no stability
15	Some stability but settling lightly
30	Moderate stability
45	Good stability, possible settling
60	Very good stability, little settling likely

2.4.2.3 Sedimentation photograph capturing

It can be introduced as a basic method to evaluate stability of nano suspensions inside the fluid. After preparation of nanofluid, it would be kept in a stationary standing condition inside glass tubes and settlement of particles would be recorded continuously by capturing photos. Waiting time for capturing photos links up with quality of nanofluid during preparation and well use of applied methods to make a stable nanofluid (Mohammad Mehrali, et al., 2014a).

2.4.2.4 TEM (Transmission Electron Microscopy) and SEM (Scanning Electron Microscopy)

These two are known as suitable tools for study and determination of microstructures. Shape, size and distribution of nanoparticles can be distinguished using them. Moreover, their aggregation which is related to stability of nanofluid could be monitored. They are capable to capture photos in small sizes to reveal suspension situation of nanoparticles inside the fluid after preparation (Mohammad Mehrali, et al., 2014a).

2.4.2.5 Sedimentation balance method

In this method, accurate balance with tray, which is able to collect nanoparticles while sedimentation, would be immersed inside nanofluid immediately after preparation phase. Monitoring weight of nanoparticles, suspension fraction of them is calculated by Equation (2.16).

$$F_s = \frac{(W_T - W)}{W_T} \tag{2.16}$$

Where, F_s is suspension of ethylene glycol fraction at an accepted time; W_T is total weight of nanoparticles inside the base fluid and W is weight of settled nanoparticles at an accepted time (Figure 2.13).

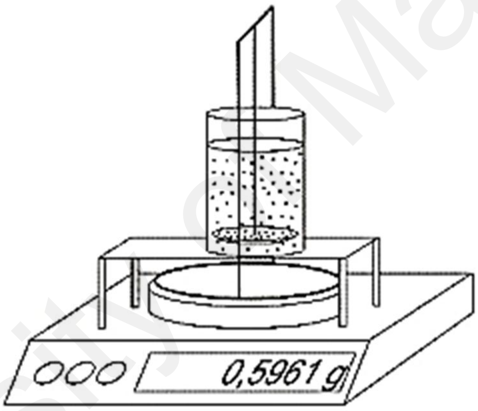

Figure 2.13 Absolute Sedimentation Gauge

2.4.2.6 3ω method

In this method, stability of suspensions can be evaluated considering thermal conductivity growth caused by the nanoparticles sedimentation in a wide nanoparticles volume fraction range. A few literatures were found using 3ω method for investigation of stability of nanofluids.

2.5 Wettability effects

Wettability studies usually involve the measurement of contact angles (θ) as the primary data, which indicates the angle between the liquid and a solid surface. Wetting liquid have angles between 0° and 90° and non-wetting liquids have angles between 90°

and 180°. The surface forces, such as cohesive and adhesive forces have great influence on the contact angle between liquid and solid surfaces. Many researchers have studied the wettability effect of working fluid on a solid surface in the heat transfer systems (Y.-j. Chen et al., 2013). The most popular measurement techniques of contact angle is tangent angle measurement at the three-phase contact point on a sessile drop profile by telescope-goniometer. As the tendency of a drop to spread out over a solid surface is dependent on change in the contact angle where the deformation of the drop due to gravity were considered to be negligible owing to its small surface area. Thus, good wetting surface shows a lower contact angle and a bad wetting surface shows a higher contact angle (Mohammad Mehrali, et al., 2014b).

The wettability is an effective parameter for the heat transfer coefficient and the friction factor, especially for heat transfer to two-phase flow, and higher contact angle surfaces tend to decrease the heat transfer coefficient compared with the lower contact angle surfaces (C. Choi et al., 2011). The initial equilibrium contact angle of the nanofluids was significantly affected by the nano-particle sizes and concentrations. Nanofluid molecules tumble along the tube wall, similar to two solid surfaces sliding over one another, when the forces between the nanofluid and the tube wall molecules are not strong enough to overcome the shear forces at the wall. This decoupling of the nanofluid from the wall results in a lower frictional pressure drop. Therefore, the lower contact angle provided more frictional pressure drop because of the adhesive force between the nanofluids and the tube wall (C. Choi, et al., 2011).

For convenience of the analysis, the obtained picture can be transferred to a binary image via digital image processing, as illustrated in Figure 2.14. The shape of the droplet is approximately of a spherical cap. If the variables r and h denote the radius of the base of the cap and the height of the cap, respectively, the contact angle can be expressed by the Equation (2.17).

$$\theta = 2\arctan(\frac{h}{r}) \qquad (2.17)$$

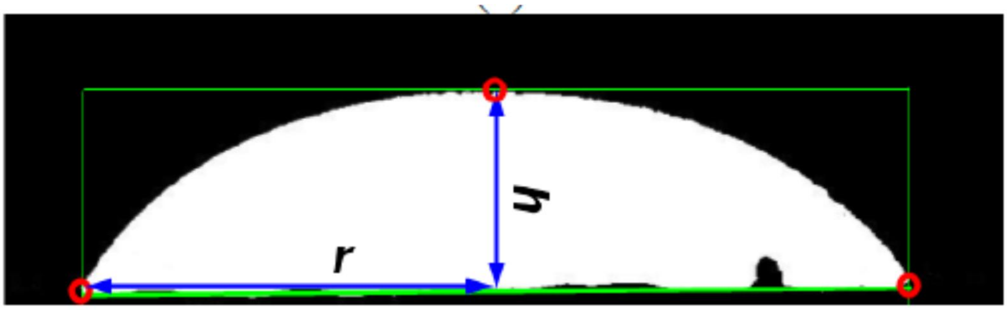

Figure 2.14 binary image of droplet

2.6 Electrical conductivity

The viscosity and thermal conductivity of nanofluids is the crucial influencing factor in the heat transfer properties of nanofluids. Pumping power requirements and convective heat transfer coefficients of fluids depend strongly on the fluid velocity and Prandtl numbers and they are highly influenced by viscosity of the fluid (Azizi-Toupkanloo et al., 2013). In addition, it can be noted that the importance of electrical conductivity characteristics of nanoparticle suspensions have largely been ignored in most of the studies (E. K. Goharshadi et al., 2013) and a few research works have been done on the electrical properties of nanofluids. Hence, among the thermo-physical properties, electrical conductivity might bring information on the state of dispersion, and performance of the nano-particles suspension (Ganguly, et al., 2009).

Electrical conductivity is the ability of a solution to conduct an electric current, which is carried by anions and cations. The electrical conductivity (σ) properties of nano-particle suspensions still remain poorly understood compared to the other thermo-physical properties of nanofluids (Chakraborty et al., 2008). The electrical conductivity of a suspension can either increase or decrease depending on the size, concentration and background of electrolyte of nano-particles. Electrical conductivity is normally measured in aqueous solutions of electrolytes, which can be either strong or weak and dependent on the temperature. Based on the surface and colloid theory, there is an electrical double layer (EDL) around each particles which is the major importance of colloidal stability of suspensions. As shown in Figure 2.15, EDL can exist around each particle and it include two parts; (a) an inner region (Stern layer) where the ions are strongly bound and (b) an outer (diffuse) region where they are less firmly associated.

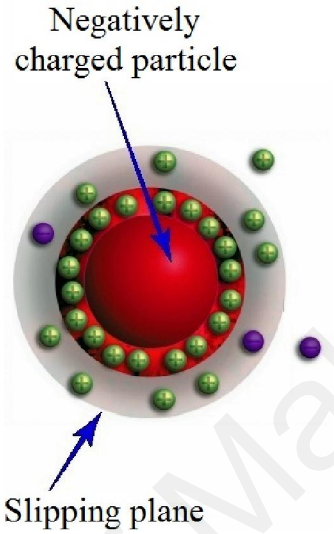

Figure 2.15 An example of Electric Double Layer (EDL)

In other hand, the effect of EDL can be understood by the zeta-potential, which is studied in the pH selection of the flotation process. The EDL theory is useful in the explanation of the electrostatic behaviors and the thickness of the EDL. Hence, the electrical conductivity can affect the nanofluid heat transfer properties (Kalteh et al., 2011).

2.7 Heat transfer properties

When put into application, the heat transfer coefficient of a nanofluid is more important than the thermal conductivity as this determines how effectively the heat can be transferred within a system. If nanofluids can improve the heat transfer coefficient of thermal energy systems, they can facilitate the reduction in size of such systems and lead to increase energy and fuel efficiencies, lower pollution, and improve reliability. To this end, it is essential to directly measure the heat transfer performance of nanofluids under flow conditions typical of specific applications. While not as common as reports on the enhancement of thermal conductivity in nanofluids, there are still several significant studies on the enhancement of the heat transfer coefficient under flow conditions. Most heat transfer studies were presented by using Nusselt number (Nu), which is the ratio of convective to conductive heat transfer across the boundary.

2.7.1 Flow in horizontal smooth tubes

Forced convective heat transfer is preferred and used in heat transfer applications because of its controllability and applicability. Since it has been widely used in order to obtain desired heat transfer, investigations on prediction of it has also been studied extensively. There are many theoretical and empirical approaches which cover laminar and turbulent flow and heat transfer phenomena.

An experimental investigation of the convective heat transfer coefficient for nanofluids flowing through different types of tubes has been conducted in several studies, and these have considered different types of nanoparticles, including oxides, nitrides, metals, diamond, and carbon-based nanoparticles (Memari et al., 2011; Shanbedi, et al., 2012). Early experiments with TiO_2, Al_2O_3, and SiO_2 nanofluids were undertaken by different researchers to determine the effect of the nanofluid concentration on the thermo-physical properties and the heat transfer coefficient (Azmi et al., 2014). They observed an increase in the convective heat transfer coefficients at various concentrations of the nanofluid under laminar and turbulent flow conditions from 20 to 350%. They concluded that the influence of the nanofluid concentration on the heat transfer coefficient is significant in the turbulent region in comparison to versus the laminar region (Azizian et al., 2014; Wu et al., 2012). However, only limited research has been performed on convective heat transfer with carbon-based nanofluids as the heat transfer liquid and compared with many results from the different thermo-physical properties of nanofluids (Wu, et al., 2012).

2.7.2 Different modes of energy transports in nanofluids

There are two different types of studies concerning nanofluids. The first one concerns itself with the study of the effective thermal conductivity and the other with the study of convective heat transfer enhancement. In the study of the effective thermal conductivity, correlations are developed for the thermal conductivity, which are then used in the study of heat transfer enhancement. The thermal conductivity of the nanofluid is a function of both the thermal conductivity of the nanoparticle and base fluid as well as the volume fraction, surface area, shape of the nanoparticle, the distribution of the dispersed particles and the thermal conductivity of the nanolayer. The heat transfer coefficient of the nanofluid depends upon a number of factors such as thermal conductivity and heat capacity of the base fluid and nanoparticles, the flow pattern, the viscosity of the nanofluid, the volume fraction of the suspended particles, the dimensions and the shape of these particles as well as on the flow structure. The methods, which are mentioned above, consider the nanofluid as a single phase fluid. The size of the dispersed particles presents some difficulty in analyzing the interaction between the fluid and the solid particles during heat transfer.

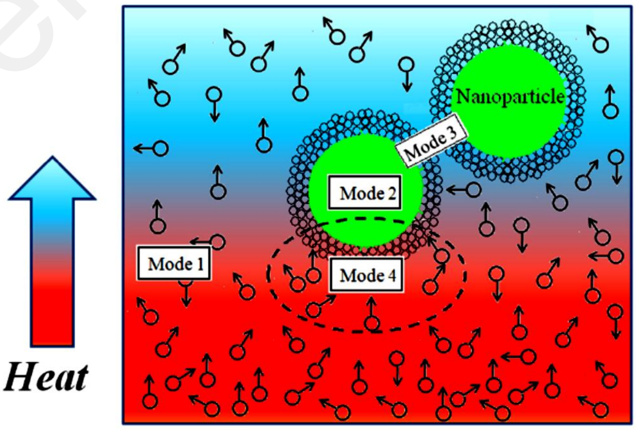

Figure 2.16 Modes of energy transport in nanofluids

Jang et al. (2004) derived four modes of heat transport in nanofluids as shown in Figure 2.16. The first mode of heat transport is the collision between base fluid molecules, which physically represents the thermal conductivity of the base fluid. The second mode is the thermal diffusion in nanoparticles. The thermal diffusion is carried by phonon's which are created at random, propagate in random directions through the particles and are scattered by each other or by defects in the particles, thus justifying the macroscopic description of heat transport. The third mode is Brownian motion, which is the collision between nanoparticles. This enables direct solid to solid transport of heat from one to another, but it is a very slow process and can be neglected. Brownian motion could, however, have an important indirect role in producing particle clustering which significantly enhances the thermal conductivity, since the particles are much closer together and thus enhance consistent phonon heat transfer among the particles. The last mode is the thermal interactions of the nanoparticles with the base fluid molecules, which translates into conduction at the macroscopic level. Hence the nanolayer forms a thermal bridge between the liquid base fluid, where the solid nanoparticles enhance the effective thermal conductivity (Grote, 2013).

2.7.3 Heat transfer and pressure drop for flow through tubes

A number of research have been carried out in the study of heat transfer and pressure drop in tubes for generating data, which have later ben used as the basis for designing heat exchanger and cooling systems in industry. But the research requirements for that arena is not over yet. The advancement of science and the rapid growth of emerging problems in industry have generated more avenues to continue research in this field (Kazi, 2001).

2.7.3.1 Flow through tubes

Theoretical studies to estimate the abnormal enhancement in convective nanofluid heat transfer exist in the literature. The researchers proposed several mechanisms to provide an explanation to this abnormal enhancement and some of them proposed new correlations or numerical methods to estimate nanofluid heat transfer phenomena. Empirical correlation are usually of greatest practical value for design an engineering purpose due to their simplicity. For fully-developed turbulent flow in hydraulically smooth pipe, the correlation generally used to estimate fanning factor are shown in Equations (2.18) and (2.19).

$$f = 0.079Re^{-0.25}\ , Re \leq 2 \times 10^4 \tag{2.18}$$

and

$$f = 0.046Re^{-0.20}\ , Re \geq 2 \times 10^4 \tag{2.19}$$

In practice the tube used in industry are generally not hydraulically smooth. The turbulent flow friction factor of real pipe is strongly influenced by the smoothness of the inside surface. J. Nikuradse (1933) experimentally investigated sand-grain roughened tubes to evaluate the effect of roughness (ε) on friction and velocity distribution but not much emphasis was placed on heat transfer measurements (Kazi, 2001).

J. Nikuradse (1933) identified the three regimes depending on the variation of f with Re_ε and ε/r. The classified regimes are presented in Equations (2.20), (2.21) and (2.22).

Hydraulically smooth regime $\quad f = F(Re)\ , 0 \leq Re_\varepsilon \leq 5 \quad$ (2.20)

Transition regime $\quad f = F(\varepsilon/r\ , Re)\ , 5 \leq Re_\varepsilon \leq 70 \quad$ (2.21)

Completely rough regime $\quad f = F(\varepsilon/r)\ , Re_\varepsilon \geq 70 \quad$ (2.22)

In the hydraulically smooth regime, ε is so small that the sand gains are contained within the laminar sublayer. Hence f is not affected by ε and f = F(Re). In the transition regime, the sand grains extend partly outside the laminar sublayer, exerting an additional resistance to flow in the nature of a profile drag. In this case the friction coefficient is dependent on ε/r as well as Re. Thus for the transition regime, laminar sublayer disrupting it completely disrupted. For this situation, friction coefficient must depend on the size and shape of sand grains alone, i.e., $f = F(\varepsilon/r)$.

Prandtl (1960), Von Karman (2012) and V. Nikuradse (1932) developed a correlation Equation (2.23) for f = F(Re) which has a theoretical basis and is valid for an arbitrarily large Re. its predictions agree with the extensive experimental measurements within ±2%. The equation recommended for Re range of 4×10^3 to 10^7.

$$\frac{1}{\sqrt{f}} = 1.7372\ln\left(Re\sqrt{f}\right) - 0.3946 \tag{2.23}$$

Later Colebrook (1939) suggested an Equation (2-24) for a smooth circular duct.

$$\frac{1}{\sqrt{f}} = 1.5635\ln\left(\frac{Re}{7}\right) \tag{2-24}$$

This is also valid in the Re range of 4×10^3 to 10^7.

Colebrook (1939) developed an implicit formula, Equation (2-25) which is applicable for $0 \leq Re_\varepsilon \leq 5$ spanning the entire transition, hydraulically smooth and completely rough flow regimes.

$$\frac{1}{\sqrt{f}} = 3.48 - 1.7372\ln\left(\frac{\varepsilon}{r} + \frac{9.35}{Re\sqrt{f}}\right) \tag{2.25}$$

The validity of Equation (2.25) is stated within the Re range of 4×10^3 to 10^7.

For turbulent heat transfer in smooth pipes, Colburn (1933) equation could be applied as general approach to calculate dimensionless Nusselt number (Nu). The Nu is correlated with the Re and Prandtl number (Pr) in an exponential function for fully developed turbulent pipe flow. The Colburn empirical Equation (2.26) has been widely applied in practice.

$$\mathrm{Nu} = C\,\mathrm{Re}^m\,\mathrm{Pr}^n \tag{2.26}$$

where C, m and n are constant to be determined from experimental data for a certain type of tube. Typically for smooth tube, $C \approx 0.023$, $m \approx 0.8$ and $n \approx 0.3$. if these values are used it is called the Dittus-Boelter (Dittus et al., 1930) Equation (2.27) and in the case where the fluid is heated.

$$\mathrm{Nu} = 0.023\,\mathrm{Re}^{0.8}\,\mathrm{Pr}^{0.3},\ 0.7<\mathrm{Pr}<160 \text{ and } Re \geq 10^4 \tag{2.27}$$

Equation (2-10) is recommended for general use but the associated standard deviation of error is approximately 13%.

Petukhov et al. (1958) developed correlations (Equations (2.28) and (2.29)) for fully developed turbulent flow Nu in a smooth circular duct for gases and liquids with validity for $0.5 \leq Pr \leq 10^6$ and $4000 \leq Re \leq 5 \times 10^6$.

$$Nu = \frac{(f/2)RePr}{C + 12.7\left(\frac{f}{2}\right)^{\frac{1}{2}}(Pr^{\frac{2}{3}} - 1)} \tag{2.28}$$

where $C = 1.07 + \frac{900}{Re} - [\frac{0.63}{1+10\mathrm{Pr}}]$

$$Nu = \frac{(f/2)RePr}{1.07 + 12.7\left(\frac{f}{2}\right)^{\frac{1}{2}}(Pr^{\frac{2}{3}} - 1)} \tag{2.29}$$

The first Petukhov correlation agrees with the most reliable experimental data on heat and mass transfer to an accuracy of ±5%. It is valid for $0.5 \leq Pr \leq 10^6$ and $400 \leq Re \leq 5 \times 10^6$. The second is a simplified version of the first and is modified by Gnielinski (1976) to arrive at his correlation (Equation (2.30)).

$$Nu = \frac{(f/2)(Re - 1000)Pr}{1 + 12.7\left(\frac{f}{2}\right)^{1/2}(Pr^{2/3} - 1)} \tag{2.30}$$

The Gnielinski correlation extending the Petukhov correlation to the range of $2300 \leq Re \leq 5 \times 10^6$. For $0.5 \leq Pr \leq 2000$ and $2300 \leq Re \leq 5 \times 10^6$, it is overall best accord with the experimental data; it agrees with the Petukhov correlation with -2% and 7.8%.

The effect on turbulent flow friction factor by the tube roughness leads on Nu number for a rough tube. The correlation for smooth tubes do not satisfy the experimental data obtained from a rough tube. Thus quite a few authors produced Nu number correlations for fully developed turbulent flow in the fully rough flow regime of a circular duct (Kazi, 2001). The correlation developed by Martinelli (1947) for fully rough flow regime is presented in Equation (2.31).

$$Nu = \frac{RePr\sqrt{f/2}}{5[Pr + \ln(1 + 5\mathrm{Pr}) + 0.5\ln\left(Re\sqrt{f/2}\ /60\right)} \tag{2.31}$$

2.7.4 Modeling of the Nanofluid Convective Heat Transfer

Numerical modeling of convective heat transfer of nanofluids can be conducted using single-phase or multi-phase approaches. Most of the studies in this area have been made using single-phase model (Alawi et al.; Haghshenas Fard et al., 2010). The numerical and experimental works on the effective thermal conductivity and convective heat transfer are needed to demonstrate the full potential of nanofuids (Kakaç et al., 2009) and to understand the fundamentals of heat transfer for developing new nanofluid. Although there are recent developments in the theoretical and experimental results to understanding the particle movements mechanisms, heat transfer and fluid flow behavior of nanofluids (Kakaç, et al., 2009). Many research works are available on the numerical study of convective heat transfer of nanofluids, there is no complete research on various effective parameters in this area, including base fluid, nanoparticle shape, and type of nanoparticles. However, improvement in heat transfer performance due to the nanofluids is accompanied by a number of undesired effects, including higher pressure drop and pumping power. Hence, it requires to obtain the proper nanofluid for optimum operation of heat transfer appliances (Ebrahimnia-Bajestan et al., 2011).

According to literature, and as mentioned in the previous section, there are two ways of modeling convective heat transfer of nanofluids; these are single phase modeling and two phase modeling. Single phase modeling assumes base fluid and nanoparticles mix homogeneously, there is no additional mechanism to contribute to heat transfer other than existing mechanisms for pure fluids. Two phase modeling states that there are other mechanisms caused by the relative motion between the base fluid and the nanoparticles; such as thermophoresis and thermal dispersion.

In the current study, single phase modeling of the convective heat transfer of nanofluid is performed. However, there are still several differences from conventional theories or correlations used to estimate convective heat transfer, which may affect heat transfer performance of nanofluids. In addition, the single phase modeling is relatively simpler approach and there is not much difference between the two approaches especially for higher nanoparticle volumetric fractions as used in V Bianco et al. (2009). When the literature survey on thermophysical properties and convective heat transfer sections are investigated, the most important issues observed are the followings.

1. Relative viscosity ($\mu_r = \mu_{nf}/\mu_{bf}$) , density, and specific heat of nanofluid nearly does not change with temperature,
2. Relative thermal conductivity of nanofluids significantly changes with temperature,
3. Brownian motion of nanoparticles affect nanofluid heat transfer phenomenon.

In the light of this information, modeling of forced convection heat transfer of nanofluids in a cylindrical pipe is performed with fundamental governing equations using numerical methods as an original study.

Since a complete understanding of the enhanced heat transfer of nanofluids is aimed, geometry of the problem should be as simple as possible so that fundamental procedures can be applied and any parameter that provides heat transfer enhancement can easily be recognized. Therefore, a straight pipe is the most proper instrument for this study.

Figure 2.17 describes the geometry of the problem used in the numerical work. This is a pipe which has diameter D and length L. The flow goes through the pipe from left to right. Heating of the pipe starts just after the flow becomes hydrodynamically fully developed. Boundary condition of the wall is applied in two ways: first is constant wall temperature (T_w) and second is constant wall heat flux ($q_w^{''}$). “x” is axial and “r” is radial direction while “ν” represents the local velocity of fluid.

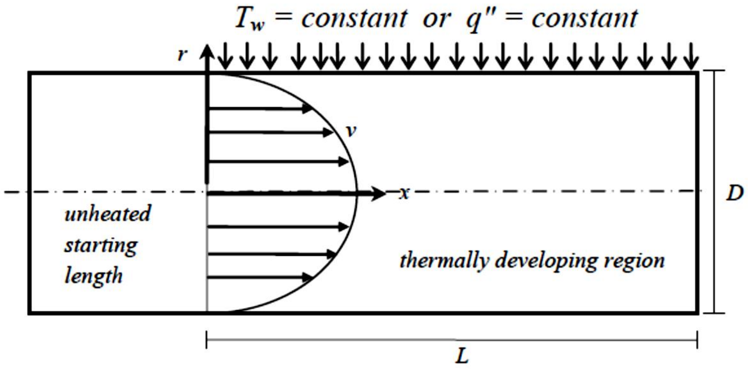

Figure 2.17 Geometry of the convective heat transfer problem

Thermally developing region of the nanofluid flow is investigated, thus; modeling and solution of flow and heat transfer in this domain is to be performed.

2.7.4.1 Governing Equations of the Problem

Governing equations for continuity, momentum and energy are available from the literature. They are extracted from mass conservation, Newton's Second Law of Motion and First Law of Thermodynamics, respectively. These fundamental equations are available in classical textbooks. The primitive continuity equation with variable density and time varying conditions is given in vector notation as Equation (2.32).

$$\frac{D\rho}{Dt} + \rho\nabla.\mathbf{V} = 0 \tag{2.32}$$

Here **V** is velocity vector, t is time, and ρ is density. The total differential, D/Dt, defined as Equation (2.33)

$$\frac{D\rho}{Dt} = \frac{\partial v_t}{\partial t} + \rho\frac{\partial v_r}{\partial r} + \frac{\rho}{r}\frac{\partial v_\varphi}{\partial \varphi} + \rho\frac{\partial v_x}{\partial x} \tag{2.33}$$

Here, $\varphi, r,$ and x are angular, radial and axial directions, and their subscripts show the direction of velocity, respectively.

The continuity equation can be reduced to the following form by assuming steady and incompressible flow:

$$\frac{\partial v_r}{\partial r} + \frac{v_r}{r} + \frac{1}{r}\frac{\partial v_\varphi}{\partial \varphi} + \frac{\partial v_x}{\partial x} = 0 \tag{2.34}$$

When the problem is considered as seen in Figure 2.17, it is realized that the flow does not experience any change in x direction because this is a hydrodynamically developed flow. Besides that this is an axisymmetric flow which means there is no variation in the φ direction. Therefore, the final form of the continuity equation is:

$$\frac{\partial v_r}{\partial r} + \frac{v_r}{r} = 0 \tag{2.35}$$

It is known that $v_r = 0$ at r = r$_0$. Thus, solution of the separable differential equation, Equation (2.35), with this boundary condition gives the following result:

$$v_r = 0 \tag{2.36}$$

At this point it is important to mention the viscosity of nanofluids. As it was mentioned, the viscosity variation does not significantly change with temperature. Therefore, it is reasonable to assume constant viscosity.

The momentum equations of the problem with constant viscosity assumption can be written for cylindrical coordinates in vectorial notation as Equation (2.37).

$$\rho_{nf}\frac{D\mathbf{V}}{Dt} = -\nabla P + \mu_{nf}\nabla^2\mathbf{V} + \mathbf{F} \tag{2.37}$$

where *P* is pressure, μ_{nf} is viscosity, and **F** is the body force vector.

Since the flow is axisymmetric, derivative terms including φ can be eliminated. Furthermore, $v_r = 0$ condition was obtained from the continuity equation. The momentum equations reduce to the following equations (Equations 2.38 to 2.40) with additional steady state ($\partial/\partial t = 0$), hydrodynamically developed flow ($\partial/\partial x = 0$ for velocity terms) and no body force (**F**=0) assumptions,

$$\rho\frac{v_\varphi^2}{r} = -\frac{\partial P}{\partial r} \tag{2.38}$$

$$0 = \frac{\partial}{\partial r}\frac{1}{r}\frac{\partial}{\partial r}rv_\varphi \tag{2.39}$$

$$0 = -\frac{1}{r}\frac{\partial P}{\partial x} + \mu_{nf}\frac{1}{r}\frac{\partial}{\partial r}r\frac{\partial v_x}{\partial r} \tag{2.40}$$

Boundary conditions of hydrodynamic flow, which are applied to simplified momentum equations are as follows:

$$\nu_{\varphi} = 0 \; at \; r = r_0 \tag{2.41}$$

$$\upsilon_{\varphi} = 0 \; at \; r = r_0 \tag{2.42}$$

$$\frac{\partial \nu_x}{\partial r} = 0 \; at \; r = r_0 \tag{2.43}$$

Solution of the simplified momentum equations with the boundary conditions of the flow gives the following equations (Equation 2.44 to 2.47) after mathematical calculations. Therefore, the profile of velocity is shown in Equation (2.45).

$$\nu_{\varphi} = 0 \tag{2.44}$$

$$\nu_x = 2\nu_m(1 - \frac{r^2}{r_0^2}) \tag{2.45}$$

Here, ν_m is the mean velocity of the fluid in the channel. Energy equation of the system can be written in the vector form as Equation (2.46).

$$\rho C_{np}\frac{DT}{Dt} = -\nabla P + \nabla k_{nf}\nabla T + q''' + \phi \tag{2.46}$$

Here q''' is the volumetric heat generation and ϕ is viscous dissipation. The energy equation can be simplified by considering steady and hydrodynamically developed flow as in the equation shown below by implementing the velocity profile in Equation (2.45).

$$\rho C_{nf} \cdot \nu_x \frac{\partial T}{\partial x} = \frac{1}{r}\frac{\partial}{\partial r} k_{nf} r \frac{\partial T}{\partial r} + \frac{\partial}{\partial x} k_{nf}\frac{\partial T}{\partial x} + \mu_{nf}(\frac{\partial \nu_x}{\partial r})^2 \tag{2.47}$$

As seen above, the thermal conductivity of the nanofluid depends on nanofluid local temperature. This approach is preferred because the thermal conductivity of nanofluids is strongly dependent on temperature, as mentioned earlier.

Once the final form of the energy equation is obtained, it can be converted to a dimensionless form, which provides an easier solution. The equations shown below are non-dimensionalization both for constant wall heat flux and constant wall temperature boundary conditions. However, Brinkman number defined as the parameter which determines viscous dissipation effect, and temperature non-dimensionalization terms are different for other. Equation (2.48) represents ratio of x and r_0 at any instance of flow.

Equation (2.50) shows dimensionless thermal conductivity, which was previously used by Özerinç, et al. (2010). Dependency of thermal conductivity on temperature is described with ratio of local thermal conductivity to bulk thermal conductivity. Local thermal conductivity is calculated with local temperature value while bulk thermal conductivity is calculated with average temperature of inlet and outlet mean temperature values, shown in Equation (2.53).

$$x^* = \frac{x}{r_0} \tag{2.48}$$

$$r^* = \frac{r}{r_0} \tag{2.49}$$

$$k^* = \frac{k_{nf,T}}{k_{nf,b}} \tag{2.50}$$

$$v_x^* = \frac{v_m d}{v_m} \tag{2.51}$$

$$Pe_{nf,b} = \frac{v_m d}{\alpha_{nf,b}} \tag{2.52}$$

$$T_{m,b} = \frac{T_{m,i} + T_{m,o}}{2} \tag{2.53}$$

In the Equations (2.49)-(2.53), the subscript "*nf,b*" refers to nanofluid property calculated with bulk mean fluid temperature, $T_{m,b}$, where $T_{m,i}$ and $T_{m,o}$ are inlet and exit mean fluid temperatures of the fluid. The subscript "*nf,T*" describes nanofluid property calculated at local temperature. Pe_{nf} is the bulk Peclet number of the flow where $\alpha_{nf,b}$ $k_{nf,b}/\rho C_{nf,b}$ is the thermal diffusivity with bulk mean temperature.

2.7.4.2 Boundary Conditions

2.7.4.2.1 Constant Wall Temperature

Dimensionless temperature and Brinkman number definitions are given in the following equations (Equations (2.54) and (2.55)) for constant wall temperature condition.

$$\theta = \frac{T - T_W}{T_i - T_W} \tag{2.54}$$

$$Br_{nf} = \frac{\mu_{nf,b} v_m^2}{k_{nf,b}(T_i - T_W)} \tag{2.55}$$

Here, Brinkman number $\mathrm{Br}_{\mathrm{nf}}$ shows the importance of viscous dissipation in flow. The non-dimensional energy Equation (2.56) is:

$$\frac{Pe_{nf}}{2} v_x^* \frac{\partial \theta}{\partial x^*} = \frac{1}{r^*} \frac{\partial}{\partial r^*} k^* r^* \frac{\partial \theta}{\partial r^*} + \frac{\partial}{\partial x^*} k^* \frac{\partial \theta}{\partial x^*} + Br_{nf} \left(\frac{\partial v_x^*}{\partial r^*} \right)^2 \tag{2.56}$$

Boundary conditions of the energy equation with constant wall temperature are,

$$\theta = 0 \; at \; r^* = 1 \tag{2.57}$$

$$\frac{\partial \theta}{\partial r^*} = 0 \; at \; r^* = 0 \tag{2.58}$$

$$\theta = 1 \; at \; x^* = 0 \tag{2.59}$$

2.7.4.2.2 Constant Heat Flux

Non-dimensionalization of temperature and Brinkman number for this boundary condition is given below in the Equations (2.60) and (2.61). The dimensionless energy equation is the same as in Equation (2.56). In addition, values of dimensionless boundary conditions are shown in Equations (2.62) and (2.63).

$$\theta = \frac{k_{nf,b}(T - T_i)}{q_w'' r_0} \tag{2.60}$$

$$Br_{nf} = \frac{\mu_{nf,b} v_m^2}{q_w'' r_0} \tag{2.61}$$

$$\frac{\partial \theta}{\partial r^*} = 0 \; at \; r^* = 0 \tag{2.62}$$

$$\theta = 0 \; at \; x^* = 0 \tag{2.63}$$

2.7.5 Previous study on nanofluids

Results on heat transfer performance of nanofluids are different from one researching center to another. There are two major schools of thoughts in heat transfer performance in nanofluids. One school of thought claims that there are significant increase in heat transfer coefficient, and no much pumping power sacrifice, this school of thought is led by U.S.U.Choi from University of Illinois in Chicago and another researchers from University of Leeds. Another school of thought claims that the heat transfer coefficient enhancement is limited and the enhancement in heat transfer coefficient is offset by the increase of pumping power for nanofluids. However, in nanofluids concentration and size of nanoparticles could be selected on the basis of specific requirement.

Results on heat transfer performance of nanofluids are different from one researching center to another. Table 2.6 summarizes the convective heat transfer results for different nanofluids. The available experimental data from different research groups vary widely, and further investigations are necessary to clarify the results.

Table 2.6 Summary of the experimental studies of the convective heat transfer of nanofluids.

Nanofluid	Geometry	Reference	Observation
Cu/water	parallel channels tube (D = 10, L = 800 mm),	(Xuan et al., 2003)	Turbulent region, large enhancement of the heat transfer coefficient
Al_2O_3/water (27–56 nm)	tube (D = 4.5, L = 970 mm)	(Wen et al., 2004b)	Heat transfer coefficient increases with the Reynolds number and the particle concentration
Au/water (17 nm)	disk-shaped heat pipe (D = 9, H =2 mm)	(Chien et al., 2003)	Significant reduction of the thermal resistance
Au/water (2–35, 15–75 nm)	heat pipe (D = 6, L = 170 mm)	(Tsai et al., 2004)	High potential to take place for conventional fluids in heat pipe applications
CNT/water	tube (D = 4.5, L = 970 mm)	(Ding et al., 2006)	Significant enhancement of the convective heat transfer, which depends on the flow condition, CNT concentration, and the pH level
Graphite nanofluid	tube (D = 4.57, L = 457 mm)	(Y. Yang, et al., 2005)	The enhancement of h is lower than the increase of the effective thermal conductivity
Al_2O_3(20 nm), CuO (50–60 nm)/water	annular tube (Din =1 mm, D_{out} = 32 mm, L =1 m)	(Zeinali Heris et al., 2006)	Enhancement of h with ϕ and Pe. Al_2O_3 showed more enhancement than CuO
GNPs/ DW (2 µm)	Tube (D=10, L=1400 mm)	Current study	Turbulent region, large enhancement of Nu and h with increases in the concentration and velocity

2.8 Summary

More than ever before, cooling and heating are the most pressing challenges of many technologies nowadays. Nanofluids are promising for heat transfer enhancement due to their high thermal conductivity. Presently, discrepancy exists in nanofluid thermal conductivity data in the literature, and enhancement mechanisms have not been fully understood yet. The major efforts are: to determine methods to characterize a nanoparticle colloid's mass loading, chemical constituents, particle size, and pH; to determine temperature and loading dependent viscosity and thermal conductivity; to determine convective heat transfer coefficient and viscous pressure losses in a heated horizontal tube. Nanofluids containing metal nanoparticles were found to be Newtonian, whereas nanofluids containing metal oxides as well as carbon nanotubes showed non-Newtonian, shear thinning behaviour. Since the interaction forces between particles usually decrease during flow conditions, the flow resistance is also decreased. With no significant interaction forces between the particles, separation of the particles in the form of sedimentation may occur and therefore, rheological studies could possibly provide more information about the stability of the nanofluids and also the interactions between the particles and fluid molecules.

In addition, literature shows that there is an enhancement in heat transfer when working with nanofluids. The enhancement mainly depends on the thermal conductivity and heat capacity of the base fluid and nanoparticles, the flow pattern, the viscosity and density of the nanofluid, the volume fraction of the suspended particles, the dimensions and the shape of these particles as well as on the flow structure. The thermal conductivity of the nanofluid is a function of both the thermal conductivity of the nanoparticle and base fluid as well as the volume fraction, surface area, shape of the nanoparticle, the distribution of the dispersed particles and the thermal conductivity of the nanolayer. Many studies were done on the convective heat transfer enhancement of nanofluids containing metallic oxide particles and only a few containing carbon based. The correlations were mainly developed for nanofluids containing metallic oxide particles and then only for the laminar or turbulent flow regime.

Studies on the friction factor in nanofluids indicate that there is a pressure increase which is also directly related to the particle concentration. The penalty in pumping power is the greatest in the laminar flow regime but decreases as one enters the turbulent flow regime due to the viscosity behavior of the nanofluids. The pumping power can be reduced by proper preparation of the nanofluid.

Even though, there has been a lot of literature reported on the pressure losses and heat transfer enhancement in the different flow regime for nanofluids. Thus a study on carbon based nanofluids in the turbulent flow regime and developing a correlation for prediction purposes is of a great interest.

CHAPTER 3

CHARACTERIZATION METHOD, INSTRUMENT AND EXPERIMENTAL SET-UP

3.1 Analysis methods

As stated earlier, it is important to be able to fully characterize the nanofluids specimen for heat transfer enhancement study and methods for finding these experimental results. Details of the methods are stated the following sections.

3.1.1 FE-SEM

Field emission scanning electron microscopy (FE-SEM) is utilized for inspecting topographies of specimens at very high magnifications using a piece of equipment called the scanning electron microscope. During FE-SEM inspection, a beam of electrons is focused on a spot volume of the specimen, resulting in the transfer of energy to the spot. These bombarding electrons, referred to as primary electrons, dislodge electrons from the specimen itself. The dislodged electrons, also known as secondary electrons, are attracted and collected by a positively biased grid or detector, and then translated into a signal.

To produce the FE-SEM image, the electron beam is swept across the area being inspected, producing many such signals. These signals are then amplified, analyzed, and translated into images of the topography being inspected. Finally, the image is shown on a CRT. The energy of the primary electrons determines the quantity of secondary electrons collected during inspection. The emission of secondary electrons from the specimen increases as the energy of the primary electron beam increases, until a certain limit is reached. Beyond this limit, the collected secondary electrons diminish as the energy of the primary beam is increased, because the primary beam is activating electrons deep below the surface of the specimen. Electrons coming from such depths usually recombine before reaching the surface for emission.

Aside from secondary electrons, the primary electron beam results in the emission of backscattered (or reflected) electrons from the specimen. Backscattered electrons possess more energy than secondary electrons, and have a definite direction. As such, they cannot be collected by a secondary electron detector, unless the detector is directly in their path of travel. All emissions above 50 eV are considered to be backscattered electrons. Backscattered electron imaging is useful in distinguishing one material from another, since the yield of the collected backscattered electrons increases monotonically with the specimen's atomic number. Backscatter imaging can distinguish elements with atomic number differences of at least 3, i.e., materials with atomic number differences of at least 3 would appear with good contrast on the image. Field emission scanning electron microscopy (FESEM- CARL ZEISS- AURIGA 60) was used to observe the microstructures of the nano-particles.

3.1.2 BET

The specific surface area of a powder is determined by physical adsorption of a gas on the surface of the solid and by calculating the amount of adsorbate gas corresponding to a monomolecular layer on the surface. Physical adsorption results from relatively weak forces (van der Waals forces) between the adsorbate gas molecules and the adsorbent surface area of the test powder. The determination is usually carried out at the temperature of liquid nitrogen. The amount of gas adsorbed can be measured by a volumetric or continuous flow procedure. The Brunauer–Emmett–Teller (BET-Autosorb-iQ2) specific surface area of the nano-particle sample was measured from the nitrogen adsorption–desorption isotherms.

3.1.3 TEM

Transmission electron microscopy (TEM) is the primary technique to verify single particle dimensions and to identify agglomerations of particles. The electron beam can be used to see features on the nanometer level. A major drawback to the use of TEM is that samples must be dried out of solution in order to be attached to the carbon matrix and placed in the vacuum chamber of the TEM; therefore the particles are not exactly in the colloid state and agglomeration might occur during drying. However, TEM can be used in combination with dynamic light scattering to acquire exact sizing in nanofluid form. Another drawback of TEM is the cost and time investment needed to prepare and view the sample. It was decided that only some initial imaging will be done as a feasibility study. Transmission electron microscopy (TEM) measurements were conducted on a CARL ZEISS-LIBRA120 microscope.

3.1.4 FT-IR

Fourier transform infrared spectroscopy (FT-IR) samples were prepared by grinding a very low concentration of dry material with potassium bromide (KBr) to form a very fine powder. This powder is then compressed into a thin pellet which can be analyzed. Functional groups on the basis of the surface of the graphene were analyzed by Fourier Transformation Infrared Spectrometer (Perkin Elmer-spectrum100 model FT-IR) at the wave ranges of 4000-400 cm^{-1}.

3.1.5 XPS

X-ray photoelectron spectroscopy (XPS) is a surface-sensitive quantitative spectroscopic technique that measures the elemental composition at the parts per thousand range, empirical formula, chemical state and electronic state of the elements that exist within a material. XPS spectra are obtained by irradiating a material with a beam of X-rays while simultaneously measuring the kinetic energy and number of electrons that escape from the top 0 to 10 nm of the material being analyzed. An X-Ray photoemission spectrometer (PHI 5400 ESCA) with an Al-Kα (hν=1486.69 eV) X-ray source was used to identify the bonded elements in the nano-particle.

3.1.6 XRD

X-ray diffraction (XRD) is an analytical techniques revealing information about the crystallographic structure. The reason for microstructure characterization is that the thermal conductivity is sensitive to the microstructure of materials. For nanoparticles having same elemental compositions but different microstructures, there is much difference in thermal conductivities. For example, single crystals have higher thermal conductivity than polycrystalline and amorphous materials. X-ray diffraction (XRD) patterns were measured on a Empyrean PANALYTICAL diffractometer.

3.1.7 Raman

Raman spectroscopy is a spectroscopic technique used to observe vibrational, rotational, and other low-frequency modes in a system. It relies on inelastic scattering, or Raman scattering, of monochromatic light, usually from a laser in the visible, near infrared, or near ultraviolet range. The laser light interacts with molecular vibrations, phonons or other excitations in the system, resulting in the energy of the laser photons being shifted up or down. The shift in energy gives information about the vibrational modes in the system. Infrared spectroscopy yields similar, but complementary, information. Typically, a sample is illuminated with a laser beam. Electromagnetic radiation from the illuminated spot is collected with a lens and sent through a monochromator. Elastic scattered radiation at the wavelength corresponding to the laser line due, called elastic Rayleigh scattering, which is filtered out while the rest of the collected light is dispersed onto a detector by either a notch filter or a band pass filter. Raman spectra were collected using a Renishaw Invia Raman Microscope with laser excitation at 514nm.

3.1.8 AFM

The Atomic force microscopy (AFM) consists of a cantilever with a sharp tip (probe) at its end that is used to scan the specimen surface. The cantilever is typically silicon or silicon nitride with a tip radius of curvature on the order of nanometers. When the tip is brought into proximity of a sample surface, forces between the tip and the sample lead to a deflection of the cantilever according to Hooke's law (Cappella et al., 1999). Depending on the situation, forces that are measured in AFM include mechanical contact force, van der Waals forces, capillary forces, chemical bonding, electrostatic forces, magnetic forces (see magnetic force microscope, MFM), Casimir forces, solvation forces, etc. Along with force, additional quantities may simultaneously be measured through the use of specialized types of probes (see scanning thermal microscopy, scanning joule expansion microscopy, photothermal microspectroscopy, etc.). Typically, the deflection is measured using a laser spot reflected from the top surface of the cantilever into an array of photodiodes. Other methods that are used include optical interferometry, capacitive sensing or piezoresistive AFM cantilevers. These cantilevers are fabricated with piezoresistive elements that act as a strain gauge. Using a Wheatstone bridge, strain in the AFM cantilever due to deflection can be measured, but this method is not as sensitive as laser deflection or interferometry. Atomic force microscopy (MultiMode 8, Bruker, Germany) in tapping mode was used to show the size of GO and rGO.

3.1.9 DSC

Differential scanning calorimetry (DSC) is a powerful tool to measure the heat capacity of nanofluids. The difference in the amount of heat flow required for heating up a sample pan and reference pan are measured as a function of temperature. During the whole process, the sample and reference pans are maintained at nearly the same temperature throughout the experiment. The heat capacity of the reference pan is already known. By measuring the difference in heat flow, the heat capacity of the sample is obtained. If there are phase transitions happened in the sample pan, more or less heat will need to flow to it than the reference to maintain both at the same temperature, so endothermal or exothermal peaks are shown on the DSC curves, corresponding to melting or freezing, respectively. The phase transition temperatures and latent heats are determined according to the DSC curves. The heat capacity of nanofluids was obtained on a differential scanning calorimeter (METTLER TOLEDO 820C-Error ±0.25–1℃) at a heating rate of 5℃/min in purified nitrogen atmosphere.

3.1.10 Rheometer

Viscosity of nanofluids is one of the most critical parameters, which determines the quality of the heat transfer fluid. As with simple fluids, the viscosity of a nanofluid depends largely on the temperature (Mohammad Mehrali, et al., 2014b). Moreover, the viscosity of nanofluids is measured at different rotor RPMs to investigate if the nanofluids are Newtonian or non-Newtonian fluids. The rheological behavior of nanofluids with amounts of nano sized particle was measured on Anton Paar rheometer (Physica MCR 301). In order to verify the accuracy of viscometer as well as to assess the reliability of the experimental procedures, the obtained values from water tests are validated by the following equation which could be the correlation for the dynamic viscosity of distilled water (Hagen, 1999):

$$\mu = e^{(1.12646-0.039638*T)/(1-0.007\ 297\ \epsilon*T)}/10000 \tag{3.1}$$

where T is the temperature in Kelvin and μ is the viscosity in mPa.s.

Figure 3.1 shows that the relative error between the measured viscosity values and the corresponding tabulated ones did not exceed more than 1%.

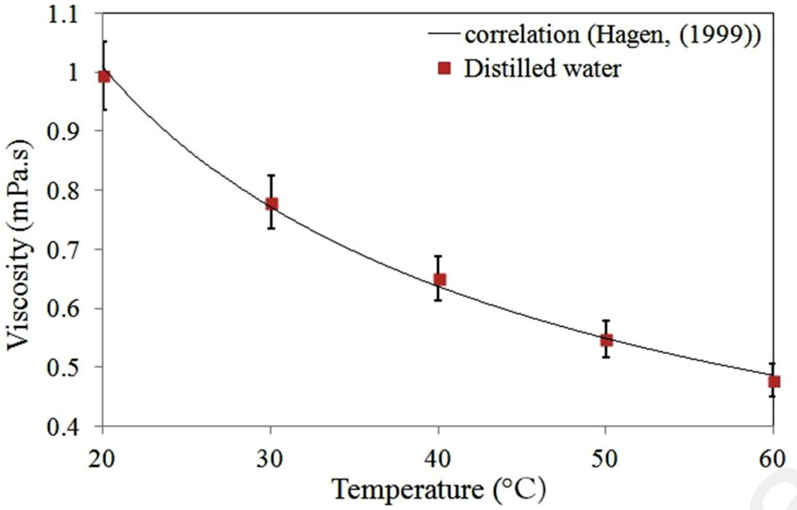

Figure 3.1 Results from validation tests using distilled water

3.1.11 Contact angle

The most widely used technique of contact angle measurement is a direct measurement of the tangent angle at the three-phase contact point on a sessile drop profile. Bigelow et al. (1946) set up a simple and convenient instrument, which they referred to as a "telescope-goniometer" to measure contact angles of various liquids on polished surfaces. Later, the first commercial contact angle goniometer, designed by W.A. Zisman, was manufactured by ramé-hart instrument company in the early 1960s. . Contact angle was measured on a dataphysics (OCA 15EC, Germany).

3.1.12 Stability

Although the stability of nanofluid is very important in order for practical application, the data of is limited on estimating the stability of nanofluids (Mohammad Mehrali, et al., 2014b). The zeta potentials of the nanofluids were measured on a zetasizer nano (Malvern instruments ltd., United Kingdom). The light transmission of all samples were measured with a Shimadzu UV spectrometer (UV-1800) operating between 190 and 1100 nm. The nanofluid solution was diluted with distilled water to allow sufficient transmission while each measurement was repeated three times to achieve a better accuracy.

3.1.13 Electrical conductivity

Electrical conductivity of the nanofluids both as functions of loading and fluid temperature were measured using a AB200 pH/Conductivity Meter (Fisher Scientific). The conductivity meter has a measuring range between 0 to 500mS/cm and a resolution of 0.1%. Prior to the measurements, the meter is calibrated using the buffer solutions of known electrical conductivities. Measurements are performed using ~40 ml of the nanofluid sample in a beaker which is located in an isothermal bath, with the conductivity probe immersed in it. At each temperature, the measurements are repeated for 5 times, and the average value is taken.

3.1.14 Thermal conductivity

An important property to be characterized in this study is the thermal conductivity of the nanofluid. In order to select the desired fluids to be fully characterized, enhanced thermal conductivity is possibly the most important element in this study, because it points to the nanofluid with high heat transfer potential. There is an inexpensive commercially available system for the measurement of the thermal conductivity (Mohammad Mehrali, et al., 2014a). The Decagon Devices KD2 thermal properties analyzer (KD2 Pro, Decagon Devices, Inc., USA), after some initial testing, is used on all nanofluids at room temperature as a first check. In later sections, the transient hot wire method, on which the KD2 operates, will be described in full along with the true thermal conductivity measurement apparatus. The accuracy of the KD2 is given as 5% by the manufacturer over a span of temperatures of 0 to 60°C. However it is found, through trial and error, that the KD2 operates very accurately if the probe is setup perfectly vertical and an isothermal bath is used to maintain the sample at 25°C. These measures prevent convection problems and the external boundary effect problems. A schematic of the KD2 setup with the isothermal bath is shown in Figure 3.2.

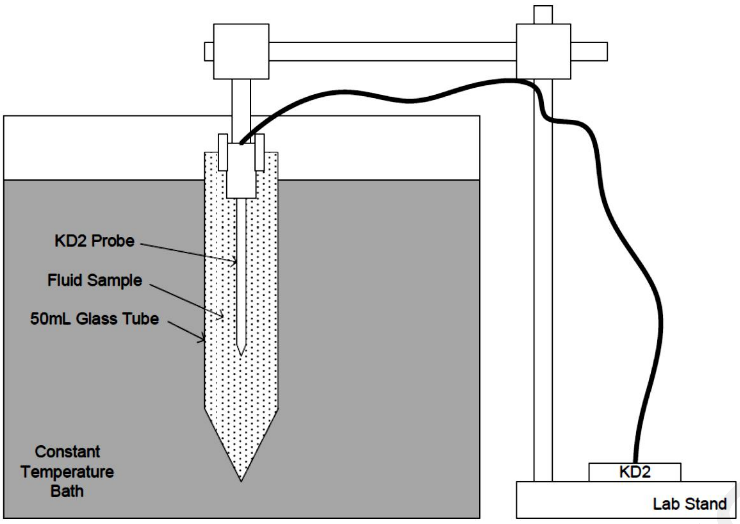

Figure 3.2 Schematic setup of KD2 thermal properties analyzer

Thermal conductivity measurements in this work were done based on THW method and the used analyzer device has 5% accuracy between 5°C and 40°C (Mohammad Mehrali, et al., 2014b). The thermal conductivity measurement for distilled water are within 2-4% of previous report date (Buongiorno et al., 2009; Ramires et al., 1995), as shown in Figure 3.3. The thermal conductivity measurements are repeated ten times and the average values were reported.

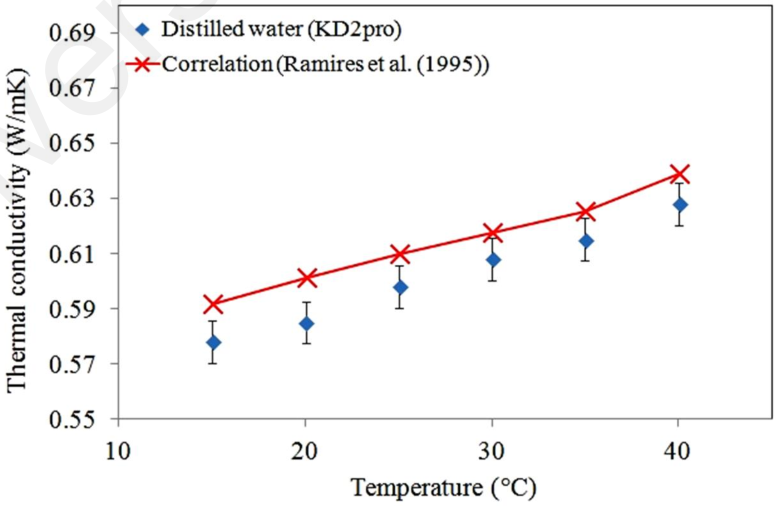

Figure 3.3 Comparison between distilled water and previous data

3.2 Description of the experiment

3.2.1 Experimental system

The schematic diagram of the experimental setup for this work is shown in Figure 3.4. It consists of a flow loop (with a bypass), a heating unit, a cooling part, measuring instruments, and a control unit. The flow loop includes a pump, a magnetic flow meter, a reservoir tank, a differential pressure transmitter, and a test section. The nanofluids were pumped from a 14-L capacity stainless steel jacketed tank by a Cole-Parmer magnetic drive pump at a flow rate of 0-10 L/m, and the pump flow was controlled by regulating motor rpm with a Hoffman Muller inverter. The flow rate and the pressure loss were measured using a magnetic flow meter and a differential pressure transmitter, respectively. A straight stainless steel tube with a length of 1400 mm, a 12 ± 0.2-mm outer diameter, and a 10-mm inner diameter was used as the test section. The test section was heated using an ultra-high-temperature heating tape (Omega, USA) at a maximum power supply capacity of 900 W, which was regulated by a Variac transformer and linked to a watt/amp meter. Five K- type thermocouples (Omega, Singapore) were fixed using a high-temperature epoxy glue at equal axial distances on the outer surface of the test tube (Figure 3.5).

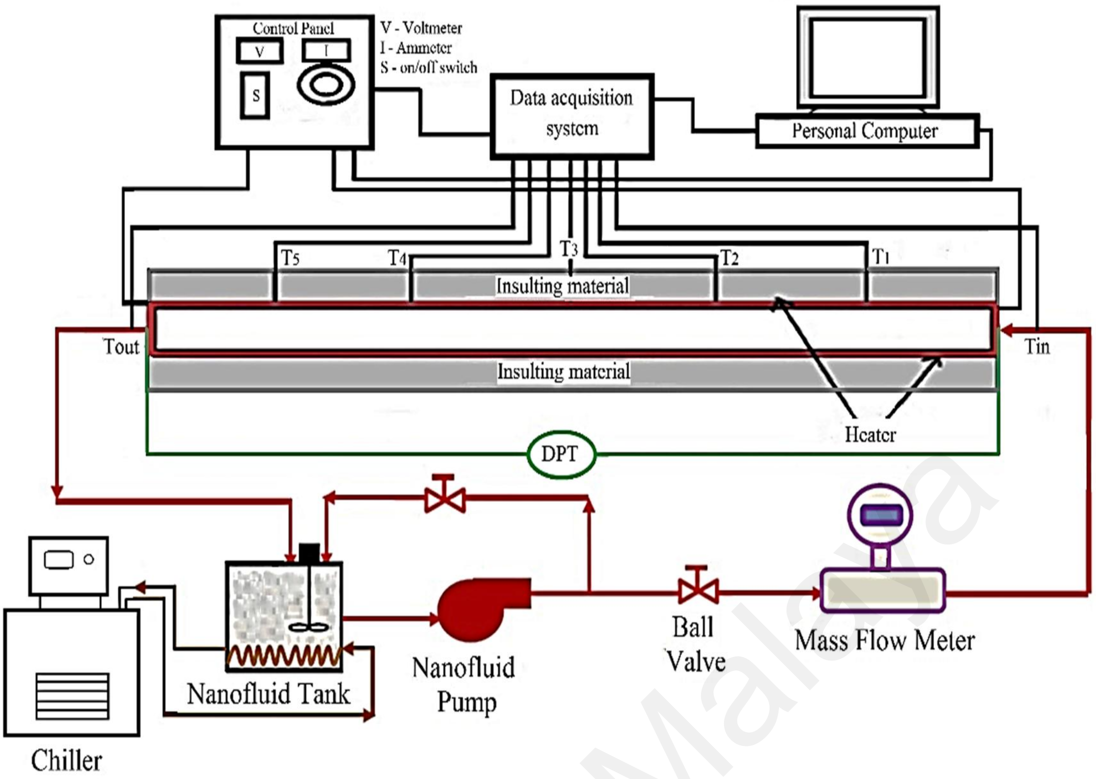

Figure 3.4 The schematic diagram of the experimental setup for the measurement of the convective heat transfer coefficient.

To measure the cold and hot nanofluid temperatures, two RTD (PT-100) sensors (Omega, Singapore) were inserted to measure the bulk temperature at the inlet and outlet of the test section. All thermocouples and RTDs were calibrated against an Ametek temperature calibrator (AMETEK Test & Calibration Instruments, Denmark). The thermocouples were connected to the Graphtec (midi logger gl220), and the RTDs were connected to the Scada system for the continuous monitoring and recording of the temperature data by a personal computer. To minimize the heat loss to the surroundings, a thick glass wool wrapping was used. The three type K thermocouples were installed on the outer surface of the insulation to measure the average outer surface temperature of the insulation.

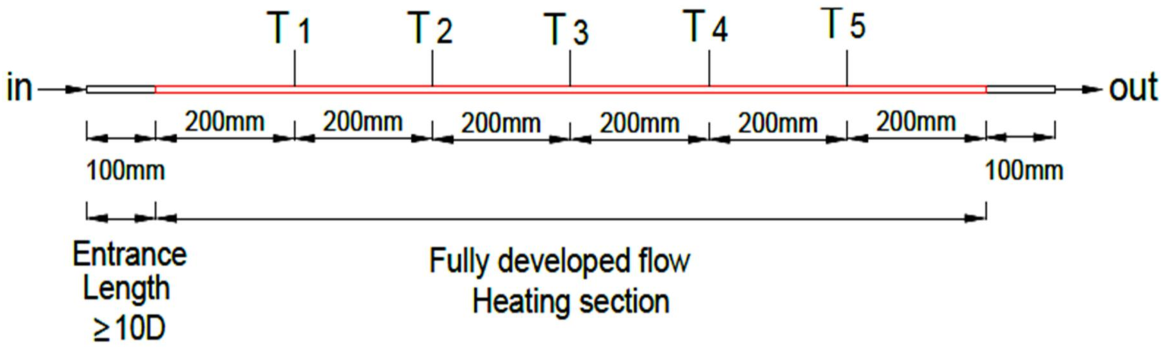

Figure 3.5 Sectional view of the experimental test section

The specifications and the accuracy of the measuring instruments and sensores used in the present experimental setup are presented in Table 3.1.

Table 3.1 Specifications and errors of the measuring instruments and sensors used in the present experiment.

Measured parameter	Instrument and sensor type	Operating	Error
Surface temperature	Type K thermocouple	0-300℃	±0.1℃
Bulk Temperature	RTD (PT-100) sensor	0-200℃	±0.1℃
Fluid flow rate	Schmierer, Electromagnetic Flow Meter	0.03 m/s ~ 12 m/s	±0.5%
Fluid pressure drop	ALIADP, Differential Pressure Transmitter (DPT)	0-25 kPa	±0.075%
Cooling unit	WiseCircu, DAIHAN Scientific, Refrigerated circulating bath	2.2 kW	±0.1℃

3.2.2 Design and Construction

Some basic requirements are developed as design considerations for the convection loop. These requirements are generated in order to meet certain goals: some to mimic heat exchanger conditions, some to meet existing equipment and lab requirements, and finally some arbitrary conditions.

3.2.2.1 Reservoir Tank

The reservoir tank is a Jacketed Stainless steel made and in cylindrical shape with a capacity of 14 liters. The reservoir is kept 30 cm above the gear pump so that the gear pump will have adequate pressure avoiding it to run dry. At the bottom of the reservoir a piping connects to the gear pump while at the top a bypass line, return line and top stirrer to mixing fluid inside the tank are connected (Figure 3.6).

Figure 3.6 Photograph of the Reservoir Tank

3.2.2.2 Gear Pump

The gear pump used for the experiment is a Liquid flow sealed gear pump (Cole-Parmer magnetic drive pump), see Figure 3.7. It is rated for a maximum flow of 64 LPM and Max Head is 6.3M. This pump is capable of operating at variable speed with maximum rated speed as 3200 RPM. The suction side of the pump is connected to the reservoir.

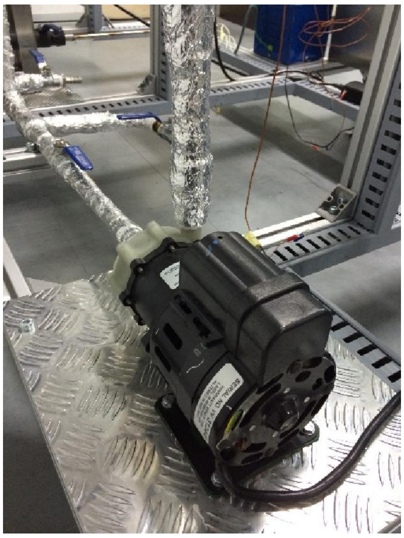

Figure 3.7 Photograph of the Magnetic gear pump

The pump is capable of operation with water up to 80℃, due to the shaft seal limitations. After rough estimation of the total loop pressure losses, assuming 10mm inner diameter tubing, and from knowledge of the pump characteristic curve, it is found that the pump should be capable of producing around 10LPM.This will deliver a significantly turbulent flow rate for water at room temperature, up to Reynolds of 20,000. Therefore, the pump is deemed usable for the experiment.

3.2.2.3 Inverter

A Hoffman Muller inverter was used to control the speed of the pump, see Figure 3.8.

Figure 3.8 Photograph of the Hoffman Muller inverter

The specifications of the inverter were presented in Table 3.2.

Table 3.2 Technical specifications for V8 series inverters

Items	Contents
Model	HM-V8A11P5B
Input	AC, 1PH, 230V, 50/60HZ
Output	3PH, 1.5KW, 7A, 0-650HZ

3.2.2.4 Electromagnetic Flow Meter

The Electromagnetic flow meter (Schmierer SEA) was used to measure fluid flow rate (Figure 3.9). A magnetic flow meter (mag flowmeter) is a volumetric flow meter which does not have any moving parts and is ideal for wastewater applications or any dirty liquid which is conductive or water based. Magnetic flowmeters will generally not work with hydrocarbons, distilled water and many non-aqueous solutions). Magnetic flowmeters are also ideal for applications where low pressure drop and low maintenance are required.

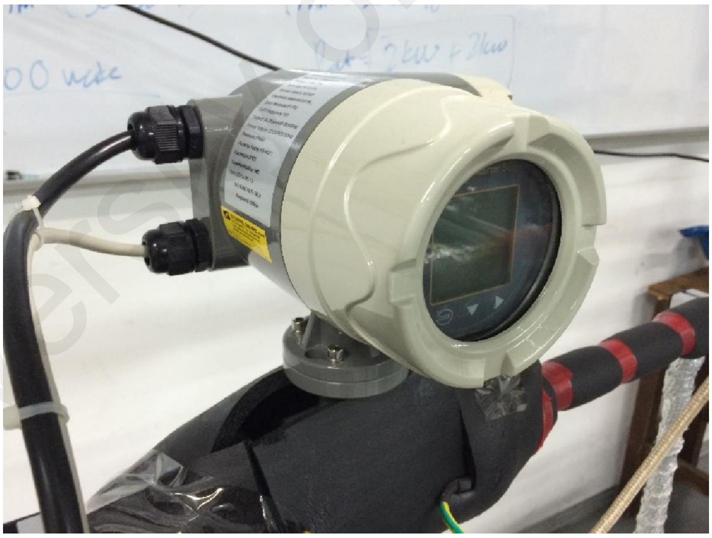

Figure 3.9 Photograph of the Electromagnetic flow meter

The operation of a magnetic flow meter or mag meter is based upon Faraday's Law, which states that the voltage induced across any conductor as it moves right angles through a magnetic field is proportional to velocity of that conductor. The technical specifications were presented in Table 3.3.

Table 3.3 Technical specifications of Schmierer SEA flow meter

Items	Contents
Model	Schmierer SEA, SSEAMF-10
Sensor range	DN10-DN3000
Operational pressure	PN 10 (1.0 MPa) for DN 15 to 300, Tri Clover
Measurement flow range	0.03-12m/s
Measurement accuracy	±0.5%
Repeatability	0.1%
Environment temperature	-20-50℃
Minimum conductivity of measured liquid	$5\mu s/cm$
Lining	Teflon (PTFE)
Measuring electrodes	Hastelloy C4 standard

As stated above, the flow meters come calibrated from the manufacturer, as shown in Table 3.4. Fluid viscosity can become an issue if the viscosity is higher than that of water. The deviation of the flow meter reading becomes an issue when the meter is running in the lower 25% of its operating range for fluids of viscosity less than 30 times that of water. Nanofluids that will be run in this loop are typically only 5 times more viscous than water, therefore the calibration should not be an issue.

Table 3.4 Flow meter calibration data

Flow (m^3/hr)	Volume (L)	Actual (L)	Error (%)	Repeatability (%)
0.3	5.201	5.214	0.24	0.062
0.8	12.374	12.368	-0.05	0.105
1.60	20.871	20.787	-0.40	0.019

3.2.2.5 Differential Pressure Transducers

The smart pressure transmitters (Model ADP9000 Series) with accuracy of ±0.075% of span connected to the inlet and outlet of the test section was used in this test (see Figure 3.10).

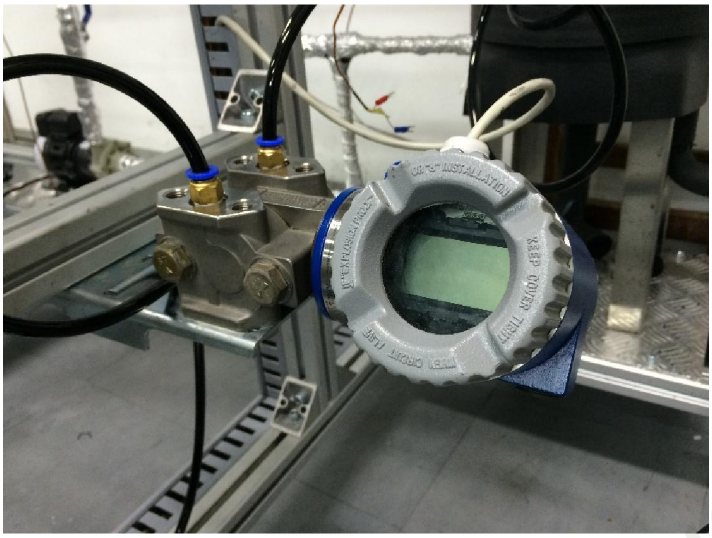

Figure 3.10 Photograph of the Differential Pressure Transducers

The standard specifications of the Differential Pressure Transducers were presented in Table 3.5. The calibration condition, static pressure test and differential pressure test were presented in Table 3.6, Table 3.7 and Table 3.8, respectively.

Table 3.5 Standard specifications of the Differential Pressure Transducers

Items	Contents
Model	ALIADP, Model ADP9000 Series
Process Fluid	Liquid, Gas of Vapor
Application	Differential Pressure, Gauge Pressure, Absolute Pressure
Measuring Range	0 - 0.125 Kpa ~ 0 - 1.5 Kpa (Minimum) 0 - 4.0 Mpa ~ 0 - 25.0 Mpa (Maximum)
Accuracy	± 0.075% of span
Stability	± 0.15% of URL for 2 years
Working Temperature	-25 to 95℃
Max. Pressure	40 Mpa
Body material	SS 304
Diaphragm	SS 316L

Table 3.6 Calibration conditions

Ambient temperature	20℃	Relative humidity	60%
Grounding resistance	$> 200M\Omega$	Calibration range	0~50 KPa

Static pressure = 4.00 MPa

Table 3.7 Static pressure test

Differential pressure value	1 ATM	Error (%)	4 MPa	Error (%)
0.0 KPa	4.000 mA	0.000	4.012 mA	0.075
50.0 KPa	20.003 mA	0.019	20.000 mA	0.000

Table 3.8 Differential pressure test

D/P Value	output	Zero to F.S.	Error (%)	F.S. to Zero	Error (%)
0.0	4.000 mA	3.998 mA	-0.012	4.009 mA	0.056
12.5	8.000 mA	7.991 mA	-0.056	7.997 mA	-0.019
25.0	12.000 mA	11.992 mA	-0.050	11.992 mA	-0.050
37.5	16.000 mA	15.990 mA	-0.062	15.999 mA	-0.006
50.0	20.000 mA	19.997 mA	-0.019	19.992 mA	-0.050

3.2.2.6 Cooling unit

A Refrigerated Bath Circulators (DAIHAN-brand, WCR- P30) was used to to balance the heat input and which is inside the jacketed tank (Figure 3.11). This refrigerated bath has:

1. RS232C Interface for Remote Monitoring and Controlling with PC
2. Stainless steel Bath (#304) for Superior Durability & High Thermal Efficiency.
3. Powerful Circulation Pump ensures Temp. Uniformity: Internal and External Circulation.
4. Locking Mode Supported for Experimental Safety (Input to Jog-Shuttle can be Disabled)

Figure 3.11 Photograph of the Refrigerated Bath Circulators

The specification of the Refrigerated Bath are listed in Table 3.9.

Table 3.9 Specifications of the Refrigerated Bath

Items		Contents
Capacity & Models		30 L, WCR- P30
Temp. Range & Accuracy		−25℃~ +150℃, ±0.1℃
Temp. Resolution		0.1℃-Display, 0.1℃-Control
Temp. Uniformity & Probe		±0.2℃ at −10℃, PT100
Heating Power		2.2 kW
Refrigerator		7/8 HP
Cooling Capacity	at +20℃	631 W
	at 0℃	429 W
	at -20℃	284 W
Refrigerant		CFC -Free(R-404A) Refrigeration System

3.2.2.7 Digital multimeter and clamp meter

The Digital multimeter and clamp meter are the single most important piece of the data acquisition system. All of the voltage, current for heater and power supply are measured by these instruments (Figure 3.12). Voltmeter and clamp meter were purchased from Agilent and were calibrated by the manufacturer.

Clamp meter Multimeter

Figure 3.12 Photograph of the Digital Voltmeter and clamp meter

The full specifications for the voltmeter and clamp meter are available in the Table 3.10 and Table 3.11, respectively.

Table 3.10 Specifications of the Multimeter

Items	Contents
Model	Agilent, U1253B
Display	OLED
True RMS	AC + DC
Voltage	Up to 1000V AC, DC
Basic dcV accuracy	Up to 0.025%
Current	Up to 10 A
True RMS AC Voltage	50 V With 0.001V Resolution
	500 V With 0.01V Resolution
True RMS AC Current	5 A With 0.0001A Resolution
	10 A With 0.001A Resolution
Resistance	Up to 500MΩ With 0.01nS Resolution

Table 3.11 Specifications of the Clamp Meter

Items	Contents
Model	Agilent, U1273A
Display	OLED
True RMS	AC + DC
Voltage	Up to 1000V AC, DC
Basic dcV accuracy	0.05% + 2 counts
Current	Up to 10 A (20 A for 30 s)
True RMS AC Voltage	30 V With 0.001V Resolution
	300 V With 0.01V Resolution
True RMS AC Current	3 A With 0.0001A Resolution
	10 A With 0.001A Resolution
Resistance	Up to 300 MΩ

3.2.2.8 Power Supply

A Variac Auto Transformer (success electronics & transformer manufacturer SDN. BHD, Model: VT2-1) with maximum power output of 10A and output voltage of 0~260V was used to regulate the voltage (Figure 3.13). An autotransformer has a single winding with two end terminals, and one or more terminals at intermediate tap points, or a transformer in which the primary and secondary coils have part or all of their turns in common. The primary voltage is applied across two of the terminals, and the secondary voltage taken from two terminals, almost always having one terminal in common with the primary voltage. The primary and secondary circuits therefore have a number of windings turns in common. Since the volts-per-turn is the same in both windings, each develops a voltage in proportion to its number of turns. In an autotransformer part of the current flows directly from the input to the output, and only part is transferred inductively, allowing a smaller, lighter, cheaper core to be used as well as requiring only a single winding.

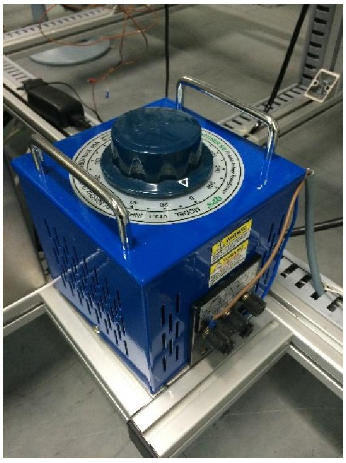

Figure 3.13 Photograph of the Variac Auto Transformer

3.2.2.9 Heater

The test section is heated by a Ultra-High Temperature Heating Tapes (Omega, Modell: STH052-120) rapped around the outside of test section. The heater has specification of 940W, 13W/in^2, 240V, 1/2×12" size and maximum exposure temperature of 760℃. A photograph of the heater used in the experimental set-up is presented in Figure 3.14. this heater is then attached to the Variac Auto Transformer for regulating the amount of heat input to the test section.

Figure 3.14 Photograph of the heater around the test section

This heating tapes are made from fine gage stranded resistance wires that are double insulated with braided Samox and knitted into flat tapes for maximum flexibility. A heavy insulated tape is made by taking a standard tape and braiding it between layers of Samox yarn. Flexible Heating Tapes and Cords are constructed of high quality resistance wire and braided insulation and are designed to provide the user with long life and high performance.

3.2.2.10 Thermocouple

There are two different type of thermocouples used for the experiment. The thermocouples used for the bulk fluid inlet and outlet (bulk) temperatures in respect to the test section are thermocouples from Omega (Model: PR-12-2-100-1/8-6-E-RP) with Temperature Range -50 to 250°C. It is a RTD sensor (PT-100) thermocouple with 3mm sheath diameter and 100mm length. The tip of the thermocouple is inserted into the middle of the flow path of the fluid. The thermocouple is then attached to the data acquisition unit where the bulk temperature are recorded and analyzed.

Another type of thermocouples used for surface temperature are type-K from Omega (Model: KMTXL-125G-6) with Liquid Crystal Polymer Molded Transition Junction Rated to 260°C. This type-K thermocouple has 3mm sheath diameter and 5mm length. The thermocouples come specified from the manufacturer to have ±1℃ accuracy.

All thermocouples are not calibrated in the technical sense and they are tested with standard temperatures to ensure no manufacturing or connection flaws are creating erroneous readings. The heat transfer results are directly affected by the temperature measurements. Thus, all the thermocouples (Type-K and RTD sensor) used in this experiment must be calibrated to determine their accuracy. The thermocouples are calibrated by two ways:

1. 650SE - Reference Temperature Calibrator

   The system gives significant improvement in the calibration accuracy up to ±0.04°C with use of the external reference sensor. Axial homogeneity in the calibration well is important, as the typical thermo-sensitive element of a sensor can vary from 5mm to 60mm. The actual temperature in the well will inherently deviate from the ideal temperature as a function of the proximity to the bottom of the well (Figure 3.15).

Figure 3.15 Photograph of the Thermocouple calibrator

2. The thermocouples are immersed in well mixed boiling-water bath which is at 100.16°C for the laboratory pressure and a well-mixed ice-water bath maintained is at 0°C.

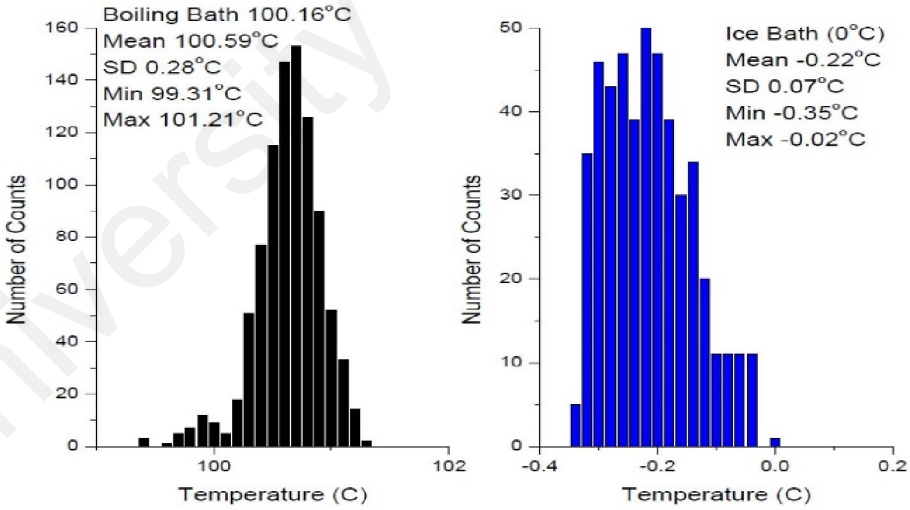

Figure 3.16 Thermocouple testing

3.2.2.11 Data logging system

The several types data acquisition systems are used for this experiment including Graphtec (midi logger gl220), Scada system (TK4H) and Multi Power monitor (Figure 3.17). All this systems are connected to a PC for continuous data logging and monitoring.

Figure 3.17 Photograph of the Data acquisition instruments

All the type-K thermocouples are attached to the channels of Graphtec data logger. This multi-channel data logger provides 10 analog measurement channels, in addition to four channels each of discrete logic and pulse inputs. The GL220 supports one external trigger input and four alarm outputs. The GL220 connected to a PC to allow data upload in real time as well as remote configuration and real time data acquisition.

The RTD sensors, flow meter, pressure transducer are attached to the channels of standard PID temperature controller (Scada Autonics, Model: TK4H) (Figure 3.18). This systems are linked with PC loader program (DAQ Master) that is a comprehensive device management program for Auntonics TK series providing GUI control for easy and convenient management of parameters and multiple device monitoring. The system linked to the PC with the USB cable and RS485 communication (Modbus RTU) to log the data in real time.

Figure 3.18 Photograph of the controlling unit that attached with sacada system

The amount of the heating power is measured by input volt and current to the heater. A multi power monitor (Model: 53U) was used to monitor and log the heating power, amount of volts and currents. RS-485/Modbus communication is a standard feature of the 53U. All measured and computed values from multiple power supply lines can be sent to a host PC to be monitored and analyzed (Figure 3.19).

Figure 3.19 Photograph of the heating control units

3.2.2.12 Test Section

The heat transfer test section is the main part and design of that take much effort and it was constructed by the Advanced Fluid dynamics lab, University of Malaya. The sectional view of the experimental test section is presented in Figure 3.5 and major dimension of the test section are tabulated in Table 3.12.

Table 3.12 Dimensions of the test section

Parameters	Values
Overall length	1400 mm
Inside diameter	10 mm
Heating length	1200 mm
Thermal entry length	100 mm

The heat transfer test section is a straight stainless steel 316 tube with a length of 1400 mm, a 12 ± 0.2-mm outer diameter, and a 10-mm inner diameter. Five grooves were cut along the tube length that was used to house the thermocouple. The groove were cut as deep as possible while ensuring that the inside surface of the pipe was not disturbed. The distance between groove surface and inner surface of the tube was maintained at 1mm (Figure 3.20).

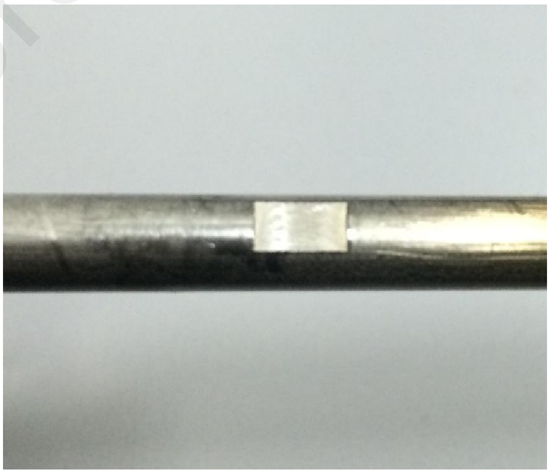

Figure 3.20 Photograph of the grove on a pipe

To keep thermocouple in location a stainless steel tube with 4mm outer diameter were installed and fixed with high temperature epoxy glue (Figure 3.21). The thermocouple were installed inside the tube and filled by thermo oil to confirm the uniform heating to thermocouple sensor.

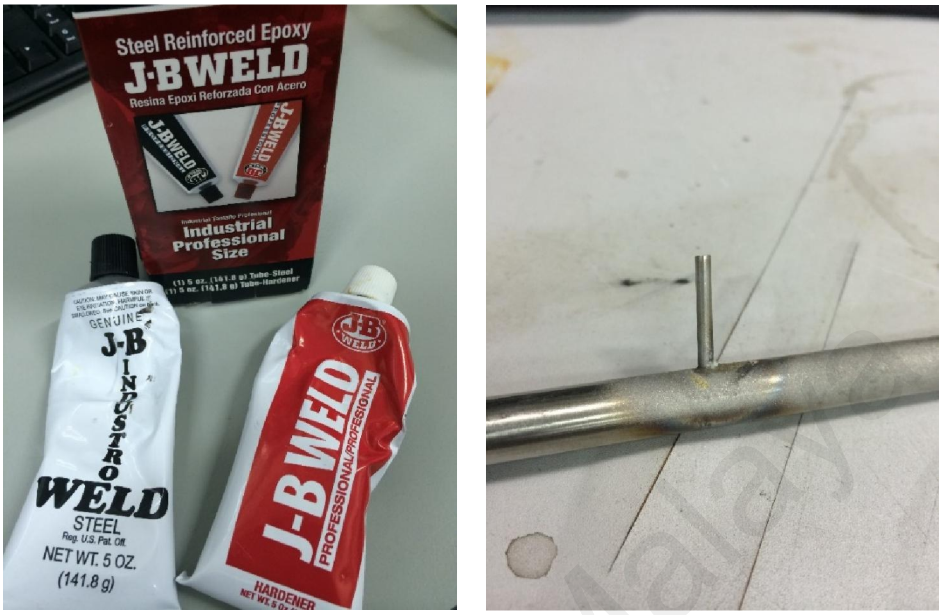

High temp. Epoxy up to 200℃ Thermo-wells installation

Figure 3.21 Thermocouple installation

The thermocouples were calibrated to measure the surface temperature according to Equation (3.1).

$$T_W = T_{Tc} - \frac{\dot{q}}{\lambda/x} \tag{3.1}$$

Details of the calibration are given in section A.1.1 (APPENDIX A) and also the λ/x values of all the individual thermocouples are presented in Table A.1 APPENDIX A). A Teflon flange was used to connect the test section to the test rig and reduce the heat loss, as shown in Figure 3.22.

Figure 3.22 Photograph of connection

This experimental system is designed and constructed to conduct experiments to investigate constant surface heat flux convection heat transfer and pressure drop in pipe flow. The flow regions investigated include thermally developing region in turbulent flow region and the main test setup is depicted in Figure 3.23.

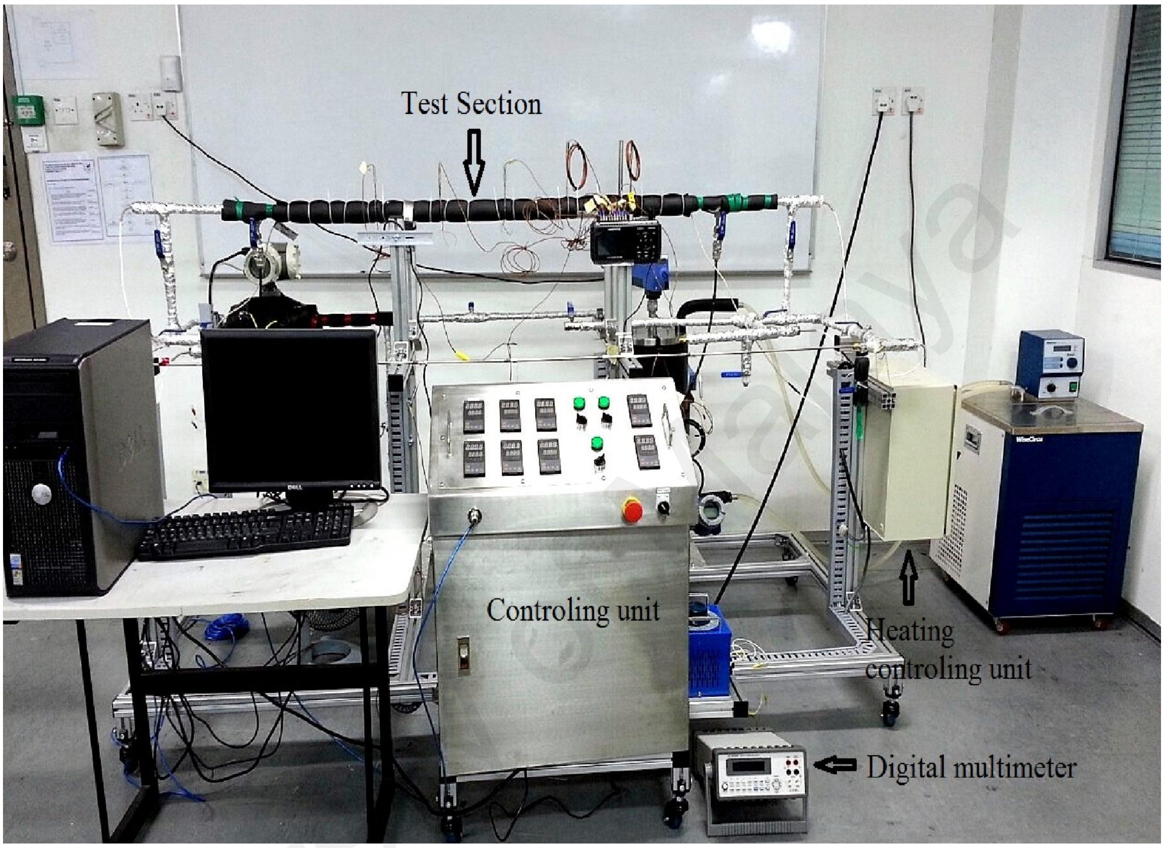

Figure 3.23 Photograph of the heat transfer test rig

CHAPTER 4

NANOFLUID PREPARATION AND CHARACTERIZATION

4.1 Introduction

There are several methods used to prepare nanofluids. Many types of base fluids were examined to identify the stable combination of nanofluids. The goal is to find out how well commercially viable nanoparticles could be dispersed in heat transfer fluids. So, the base fluids used in the present work was choosen DW water. In this chapter the preparation and properties of the different nanofluids used in this study are discussed. The chapter starts off with the preparation methods and after that a discussion on the thermo-physical properties, stability, and rheological properties of nanofluids are presented.

4.2 Nanofluid preparation

4.2.1 Graphene nanoplatelets nanofluids

Graphene nanoplatelets are two-dimensional (2D) with an average thickness of 5–10 nanometers and a specific surface area of 50-750 m^2/g and it can be produced of different sizes, 1 to 50 microns. These interesting nanoparticles, including short stacks of platelet-shaped graphene sheets which are identical to those found in the walls of carbon nanotubes, but in a planar form (Mehrali et al., 2013c). The Graphene nanoplatelets (GNPs) have drawn a lot of interest due to their excellent electrical conductivity, high mechanical properties and the in-plane thermal conductivity of GNPs is reported to be as high as 3000-5000 W/m.K (Mehrali, et al., 2013b). Further, as this is a 2D material, the heat transfer properties are expected to be much different from the zero dimensional nanoparticles and one dimensional carbon nano-tubes. Moreover, GNPs itself being an excellent thermal conductor, the graphene based nanofluids are normally expected to display significant thermal conductivity enhancement (Fang et al., 2013). The graphene nanoplates are also offered in granular form which could be dispersed in water, organic solvents and polymers with the right choice of dispersion aids, equipment and techniques.

Graphene nanoplatelets (GNPs) have special properties dependent on the number of layers, such as the saturable absorption, linear monochromatic optical contrasts and electric field assisted band gaps, which are not found in previously produced materials. These materials (Grade C, XG Sciences, Inc., USA) were used for the preparation of nanofluids. Each grade contains particles with a similar average thickness and specific surface area. Grade C particles have an average thickness of a few nanometers and a particle diameter of less than 2 μm. The average specific surface areas are 300, 500 and 750 m^2/g and all Specifications are shown in Table 4.1 (Mohammad Mehrali, et al., 2014a).

Table 4.1 Nanoparticle specification

Particle	Graphene nanoplatelets (GNPs)
Color	Black granules/powder
Carbon content	>99.5
Bulk density	0.2-0.4 g/cm^3
Relative gravity	2.0-2.25 g/cm^3
Specific surface area	300, 500 and 750 m^2/g
Particle diameter	2 μm
Peak in UV-vis spectrophotometer	265-270 nm
Thickness	2 nm
Thermal conductivity (parallel to surface)	3000 W/m.K
Thermal conductivity (perpendicular to surface)	6 W/mK
Electrical conductivity (parallel to surface)	10^7 siemens/m
Electrical conductivity (perpendicular to surface)	10^2 siemens/m

Figure 4.1 presents SEM images of the GNPs of different specific surface areas. From the figures, it can be seen that the GNPs are flat and smooth flake with sharp corners of various in-plane sizes.

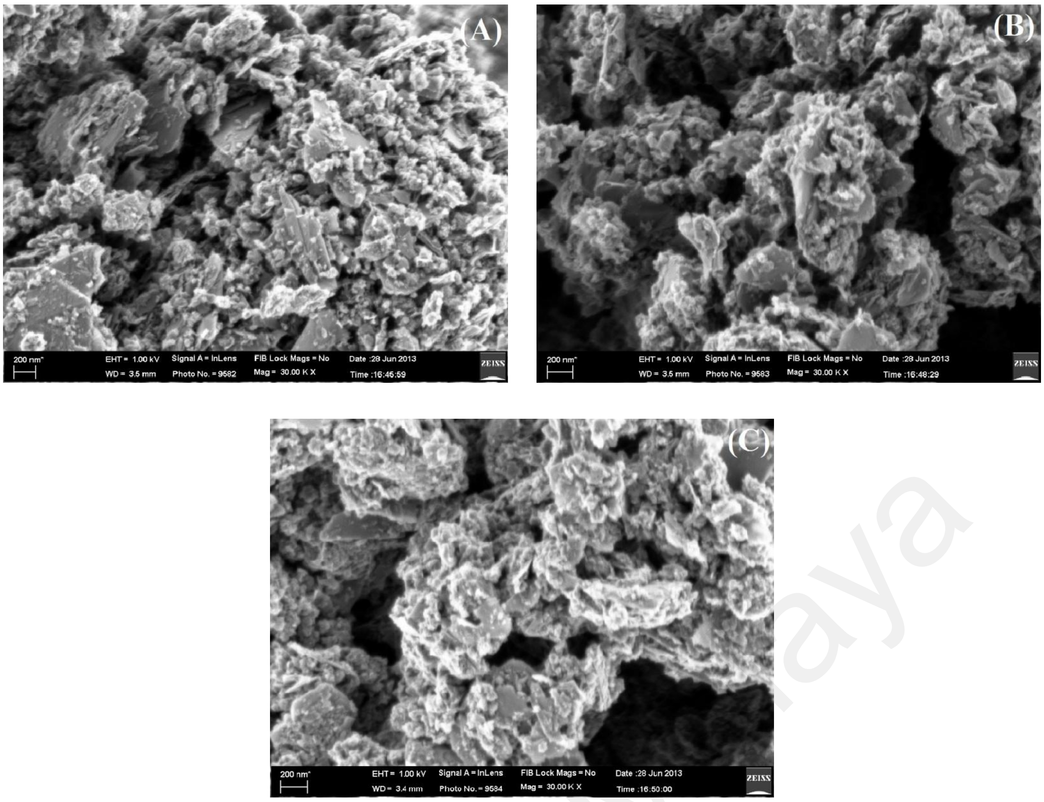

Figure 4.1 SEM photographs of the GNPs (x30k) of different specific surface areas; (A) GNPs 300, (B) GNPs 500, (C) GNPs 750.

The FTIR spectra of the GNPs are shown in Figure 4.2. It can be observed that for GNPs, the peaks are at around 3450 and 1736 cm^{-1} due to the O-H (hydroxyl groups) and C=C (carbonyl groups) functional groups. These functional groups help the GNPs to disperse in water (Ramanathan et al., 2008; Tong et al., 2011).

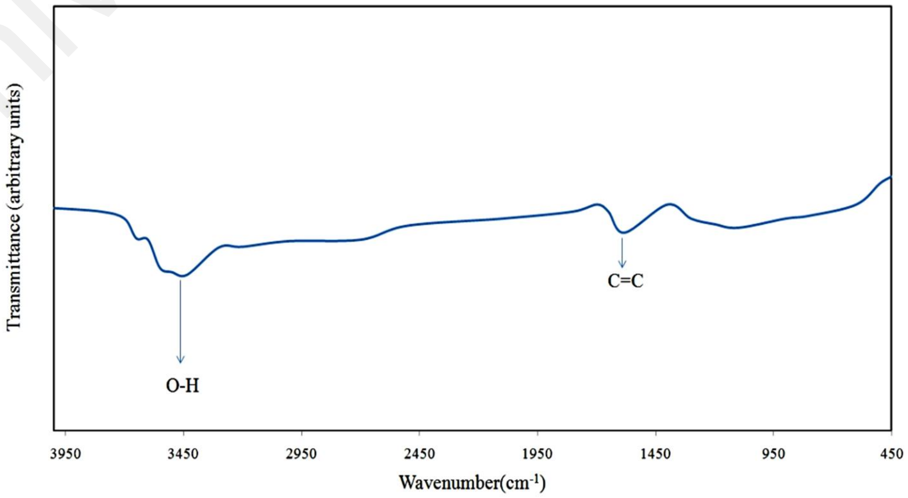

Figure 4.2 FTIR spectra of GNPs

Figure 4.3 shows the X-ray diffraction (XRD) patterns of GNPs. The intense crystalline peak of GNPs occurs at $2\theta \sim 26.22°$ related to a spacing of 0.335 nm which is the interlayer spacing of graphite (Shao et al., 2010). It is observed that the GNPs normally maintain a highly ordered structure and also confirms that the graphene is not oxidated. No other peaks were observed. The increased intensity recorded at higher GNPs of specific surface areas could be attributed to the higher number of GNPs layers organized in stacks (Sengupta et al., 2011; Yasmin et al., 2006)

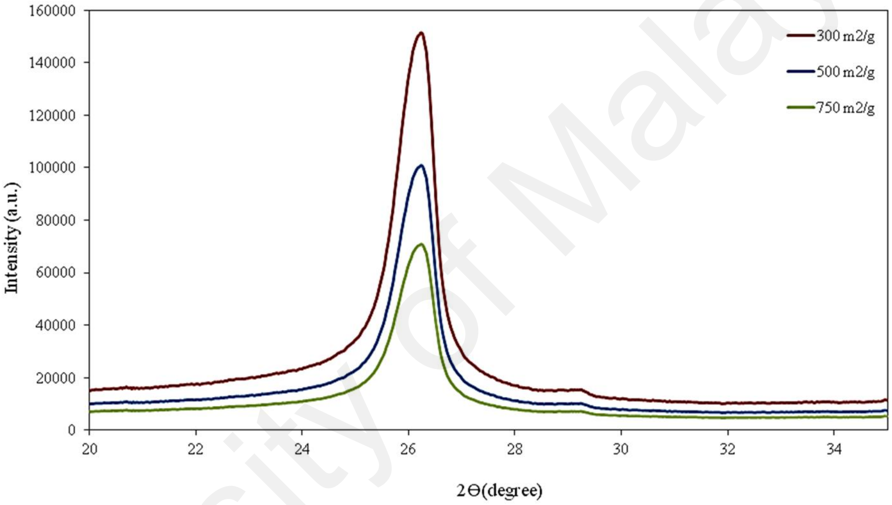

Figure 4.3 XRD patterns

Dispersion of nanoparticles into the base fluid is an important process requiring special attention. The prepared nanofluid should be an agglomerate-free stable suspension without sedimentation for long durations. Graphene nanoplatelets are offered in a granular form that is soluble in water with the right choice of dispersion aids, equipment and techniques. The graphene nanoplatelets were dispersed in distilled water by high power ultrasonication probe (Sonics Vibra Cell, Ningbo Kesheng Ultrasonic Equipment Co., Ltd. China) having 1200W output power; 20kHz frequency power supply. The concentrations of nanofluids were maintained at 0.025, 0.05, 0.075 and 0.1wt% for specimens of three average specific surface areas of 300, 500 and 750 m^2/g. The stable homogeneous GNPs nanofluids were prepared for the first time without using any surfactant. Photos of three typical samples of GNPs nanofluids at concentration after 600h are shown in Figure 4.4.

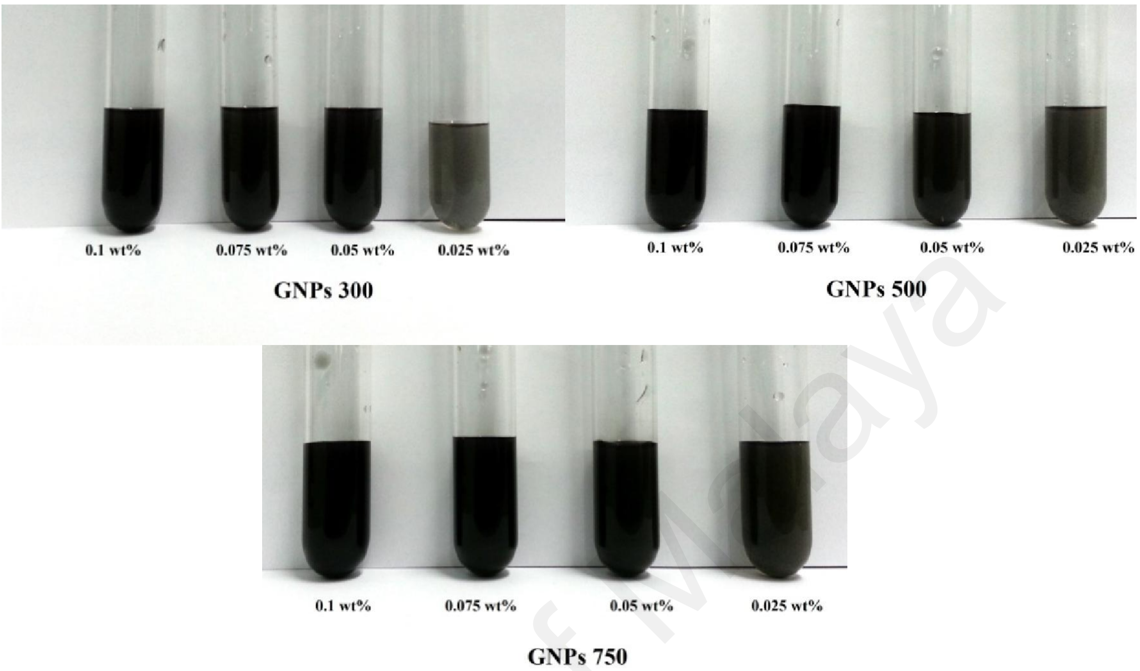

Figure 4.4 Photo of GNPs nanofluids after 600h storage time

4.2.2 Nitrogen-Doped Graphene

Doping in graphene-related systems has attracted a lot of research activity in recent years (Wehling et al., 2008). Doping of graphene may be briefly classified as electrical doping achieved by changing gate voltage, and chemical doping obtained by using chemical species. Doping in graphene with other elements can modulate its electronic properties and open the bandgap in graphene for device applications. By incorporating nitrogen atoms into graphene, its physico-chemical properties could be significantly altered depending on the doping configuration within the sub-lattices. Currently, several methods have been developed to synthesize NDG, such as arc-discharge (N. Li et al., 2010), chemical vapor deposition (Wei et al., 2009), solvo-thermal reaction of tetrachloromethane and lithium nitride (Deng et al., 2011), thermal annealing of graphite oxide (GO) in ammonia solution (X. Li et al., 2009) and thermal annealing of GO with urea (Wakeland et al., 2010).

In addition, N-doping could also enhance the biocompatibility of carbon nanomaterials and therefore is favorable for bio-sensing applications. Although some attention has been paid to the synthesis and potential applications of NDG, the atomic configurations of the N-dopants within the graphene sub-lattices have not been studied. Besides the doping concentration, the nature of the dopants, e.g. the bonding type, the dopant location and the induced perturbation within the graphene sublattices, are important to both basic research and practical applications (Lv et al., 2012).

Graphene oxide (GO) was synthesized from natural graphite powder (99.99%, <45 μm, Sigma-Aldrich) employing a simplified Hummers' method. In brief, 1g of graphite and 0.5 g of sodium nitrate were mixed together followed by the addition of 23ml of concentrated sulphuric acid under constant stirring. After 1hr, 3g of $KMnO_4$ was added gradually to the above solution while keeping the temperature less than 20°C to prevent overheating and explosion. The mixture was stirred at 35°C for 12h and the resulting solution was diluted by adding 500 ml of water under vigorous stirring. To ensure the completion of reaction with KMnO4, the suspension was further treated with 30% H_2O_2 solution (5 ml). The resulting mixture was washed with 1mole HCl and H_2O solution, followed by filtration, graphene oxide was obtained (Marcano et al., 2010).

The NDG was prepared by a hydrothermal process with GO as raw material. The pH of a dispersion of 50 mg GO in 100mL H_2O after 1 hour ultrasonication was adjusted to 11 using ammonia. The dispersion was treated hydrothermally in a Teflon-lined autoclave at a temperature of 160℃ for 12 hour. A black woolly precipitate was collected with centrifugation, followed by washing with deionized water. Finally, the obtained NDG samples were dried at 50℃ under vacuum (Mohammad Mehrali, et al., 2014b).

Figure 4.5 (a) and (b) show the FESEM images of the NDG, displaying a uniform structure like crumpled silk veil waves with a porous architecture while NDG nanosheets are randomly stacked together. It can be seen that the two dimensional graphene structures with high specific surface area and volume ratio are well retained after hydrothermal treatment with amonia. As shown in Figure 4.5(c) the XPS spectrum of NDG displays three peaks centered at 284.2, 399.3 and 532eV, related to C1s, N1s and O1s, respectively, showing the incorporation of nitrogen within the graphene (Guo et al., 2013). The atomic percentage of doping nitrogen inside the as-prepared NDG sample was found to be about 2.6%. The N1s peak could be resolved into two components based at 399.1 and 400eV, assigned to pyridinic and pyrrolic nitrogen species, respectively. They refer to the nitrogen atoms which might be positioned in a π conjugated system and contribute to the π system with one or two p-electrons, respectively (Lu et al., 2013). The specific surface area of the NDG sample was measured and the graph is shown in Figure 4.5(d). The unique mesoporous structure of NDG contributes to the high specific surface area (793 m^2/g) with a uniform pore size distribution around 3–5nm. During the preparation of N-graphene, not only can nitrogen atoms substitute some carbon atoms (most likely located on the reactive edge) but ammonia can also react with graphene to form hydrogen cyanide and hydrogen ($C + NH_3 = HCN + H_2$) (Panchakarla et al., 2009). This process consumed some carbon and has made the material more porous, which in turn resulted in the higher specific surface area, pore volume, and pore size.

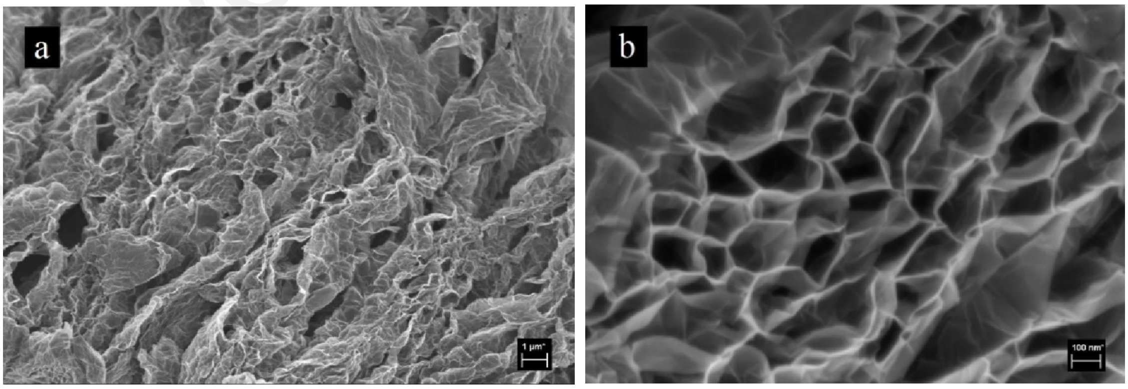

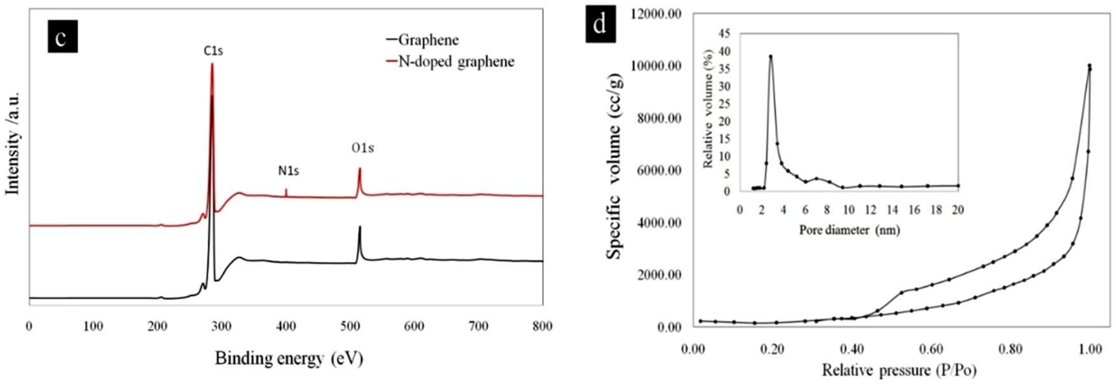

Figure 4.5 (a and b) FESEM images of NDG (×5K, ×60K); (c) XPS spectra of NDG and graphene; (d) Nitrogen adsorption/desorption isotherms of NDG. Inset in (d) is the BJH pore size distribution.

Water is a common heat transfer fluid while NDG cannot be directly dispersed in water, as there is no chemical affinity between them. Mixing of these materials directly leads to non-uniform suspensions and sedimentation of NDG starts almost immediately. The prepared nanofluid should be a homogeneous and agglomerate-free suspension without any sedimentation for long durations. Dispersion of nanoparticles into the base fluid is an important process requiring special attention. The prepared nanofluid should be an agglomerate-free stable suspension without sedimentation for long durations. The most effective surfactant was selected by examining the stability of nanofluids dispersed with different dispersants and sonication time.

Dispersion of NDG is a challenging task in the preparation of nanofluids. The first step towards preparation of a stable suspension was to find a suitable surfactant. Gum Arabic (GA), Sodium dodecyl sulfate (SDS), Hexadecyltrimethylammonium bromide (CTAB) and Triton X-100 were used to produce aqueous suspensions with same concentration of NDG. Table 4.2 summarizes the detailed experimental conditions of various nanofluid preparation methods to choose the most active surfactant and base fluid for 15min ultrasonication (probe) time.

Table 4.2 Combination of nanofluids from base fluids

Sample	Base fluid	Surfactant
A	DW	SDS
B	DW	CTAB
C	DW	Triton X-100
D	DW	GA
E	DW	-

Figure 4.6 shows a visual inspection of the nanofluids and shows that the sample C was stable over a 3 month period with little visible sedimentation or settling. According to the literature (Yousefi et al., 2012), Triton X-100 as a non ionic surfactant is the best dispersing agent for making NDG suspension due to the benzene ring in Triton X-100. Molecules having a benzene ring are adsorbed more strongly to the NDG surface due to $\pi - \pi$ stacking. Nonionic surfactants, such as Triton X-100, dispersed NDG mainly by forming a large solvation shell around it. Figure 4.7 illustrates the manner of adsorbing amphiphilic molecules onto NDG surfaces, in which, hydrophobic alkyl chains and aromatic rings lay flat on NDG surfaces.

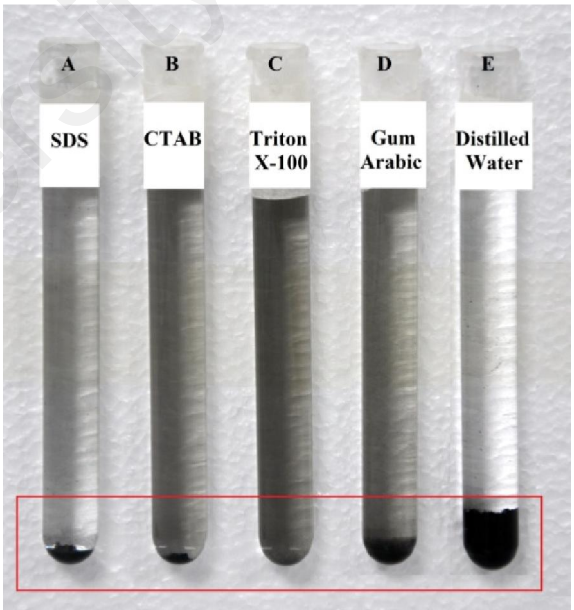

Figure 4.6 Visual investigation of sedimentation of nanofluids prepared by different surfactants 3 month ago

In addition, the optimum amount of surfactant required to prepare a stable suspension is different for different surfactants. Triton X-100 has smallest optimum amount which could be an advantage. After several tests, the ratio of Triton X-100 and distilled water was chosen 1:400 for preparation of NDG nanofluids.

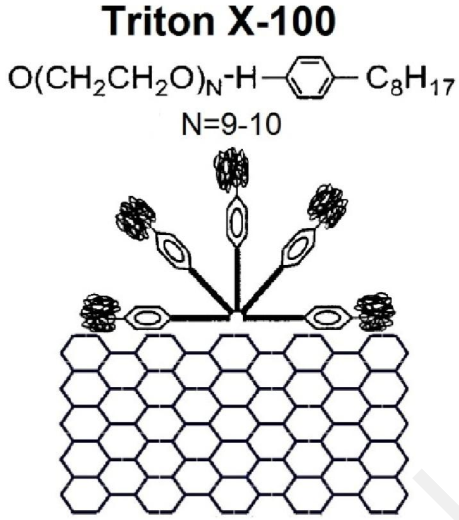

Figure 4.7 Schematic representation of adsorption of NDG surface by π-π stacking.

The second step towards dispersion was to find a suitable sonication time. Based on the literature (Mehdi Mehrali, et al., 2014b; Sun, et al., 2013), the sonication time is an important parameter for dispersing the aggregated nanoparticles. Table 4.3 summarizes the various sonication time at the same concentration of NDG and triton X-100 were investigated.

Table 4.3 Methods of producing nanofluids at different sonication time

Sample	Ultrasonication Method	Time (min)
A	Ultrasonication bath	120
B	Ultrasonication Probe	15
C		30
D		60

Therefore, the suspension stability of the prepared nanofluids is verified by measuring periodically reflective index (absorption) from UV–vis spectrophotometer of the stationary nanofluid maintained at 30°C. Figure 4.8 shows a visual inspection of nanofluids (same amount of NDG and Triton X-100) after 6 months, the smallest quantity of sedimentation was observed in sample B.

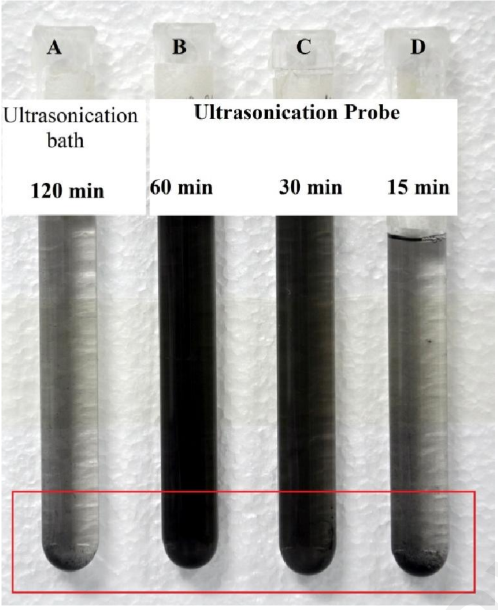

Figure 4.8 Visual investigation of sedimentation of nanofluids prepared with different sonication time after 6 months

The dispersion was greatly improved due to the combined effect of surfactant and sonication time. Sonication separates all the NDG clumps and equally dispersed them throughout the liquid. The high frequency acoustic waves from the sonicator also helps in formation of the coating the NDG with the surfactant. Results indicate that best ultrasonication time was reached at 60min.

After these stage, the concentrations of nanofluids were maintained at 0.01, 0.02, 0.04 and 0.06wt% with Triton X-100 as a surfactant used in preparation of the present nanofluids. A dispersant was added in to the beaker and the mixture was homogenized by ultrasonication probe (Sonics Vibra Cell, Ningbo Kesheng Ultrasonic Equipment Co., Ltd. China) having 1200W output power; 20kHz frequency of power supply within 60 min.

4.2.3 Green reduced graphene Oxide

Todays, synthesis of graphene (a thin layer of sp^2-bonded carbon atoms in a hexagonal lattice) has been one of the hottest subject in the scientific investigation due to the unique electronic, mechanical, heat transfer properties (Thakur et al., 2012; Y. Wang et al., 2011). Synthesis of graphene have been established by different methods including chemical vapor deposition (CVD), ultrasonic or mechanical exfoliation, epitaxial growth and chemical route via reduction of graphene oxide (GO) (Akhavan et al., 2012). The solution-based chemical reduction method has been offered the most effective case for functionalization and good possibility of producing graphene on large and industrial scale. The solution processable graphene was suitable for several applications including transparent conductive thin films, polymer composites and nanofluids (Y. Wang, et al., 2011). In addition, the hazardous waste, which were produced by the reduction process of GO may significantly enhance the cost on commercial scale. Another obstacle in chemical applications for reduced graphene oxide (rGO) is the poor processability due to irreversible aggregation of rGO, which effects from strong van der Waals attractive forces between the graphene planes (Y. Wang, et al., 2011).

In the past decades there has been a considerable improvement in the investigation for green synthesis processes because of the environmental issues, industrial safety and sustainable development, which makes it an attractive replacement for the typical synthesis processes (Kumar et al., 2012). Hence, study on replacing of the present reduction methods by low-temperature, eco-friendly, biocompatible and efficient reduction processes have been attracted much interest. Several research works have been attempted to propose eco-friendly options for reduction of GO, including hydrothermal dehydration, flash photo reduction, solvothermal reduction, photocatalytic and catalytic. The replacement of hydrazine by some natural reducing agents including protein bovine serum albumin, vitamin C, melatonin, sugar, and bacteria for reduction of GO was investigated by some researcher (Akhavan, et al., 2012). Although these proposed reduction methods can be useful in certain special applications but it has experienced some restrictions including high temperature requirement, producetion of hazardous gases and residues, need stabilizer for preventing the aggregation of the reduced sheets (Akhavan, et al., 2012).

Among the natural antioxidants, green tea is one of the common drinks, which is content of the highest concentration of polyphenols (approximately upto 30% of the oven dry weight). The green tea polyphenols (GTPs) mostly originated from epigallocatechin, epigallocatechin gallate (EGCG), epicatechin and epicatechin gallate (ECG). Among them, EGCG contains the highest concentration of the catechins in green tea (9–13% of the dry weight). Furthermore, EGCG is recognized as the strongest antioxidant active element of green tea (GT) (Akhavan, et al., 2012).

Recently, researchers tried many types of nano-particles to produce stable homogeneous nanofluids with various methods and the green tea application for dispersing of nano-particles has been attracted much attention. Nanofluids have been found to have better thermo-physical properties such as thermal diffusivity, thermal conductivity, convective heat transfer coefficients and viscosity than base fluids (Hassan et al., 2013; Mohammad Mehrali, et al., 2014a). Some investigation on the EGCG found that the carbon nanotube (CNT), single-walled carbon nanotubes (SWCNTs) and boron nitride nanotube (BNNT) can dispersed in water due to the π-π interactions between tube-walls and aromatic rings of GTPs (Y. Chen et al., 2010). Further study on green synthesis of gold nanoparticles, silver and palladium by using GTPs was reported by several researcher (Nadagouda et al., 2008; Nune et al., 2009).

This work has presented a facile and green strategy to produce soluble rGO by reducing GO in green tea solution. The reasons behind this decision are: (a) it is biocompatible and no chemicaly reduced agent was used in the reduction process of GO (b) it is economic, safe and does not require a complicated process (c) no harmful waste materials was generated in the reduction method (d) the bio-compatible GTPs used to make the soluble GTPs reduced graphene in water and it is a promising candidate in bio-related materials and heat transfer systems. The G-rGO was characterized by different spectroscopic and analytical techniques.

GO was synthesized from graphite as the raw materials by a modified version of Hummers' method (Mehrali, et al., 2013b; Mehrali et al., 2014a). For the tea solution preparation, 2g of oven dry green tea powder was added in 100mL of DW and boiled at 100℃ for 20min and then it was filtered through a 0.45μm cellulose membrane several times. 50mg of GO was added in the tea solution and sonicated in a bath sonicator for 30min. Then, the solution was refluxed at 90℃ in a nitrogen atmosphere for 5h. After that, the green reduced graphene oxide was collected and washed several times with distilled water to remove the excess of GTPs (Y. Wang, et al., 2011). The resultant was added in to the beaker, the mixture was homogenized by sonication and the concentrations of nanofluids were maintained at 1, 2, 3 and 4% volume fraction. The structure of GTPs and the procedure for making soluble graphene is illustrated in Figure 4.9.

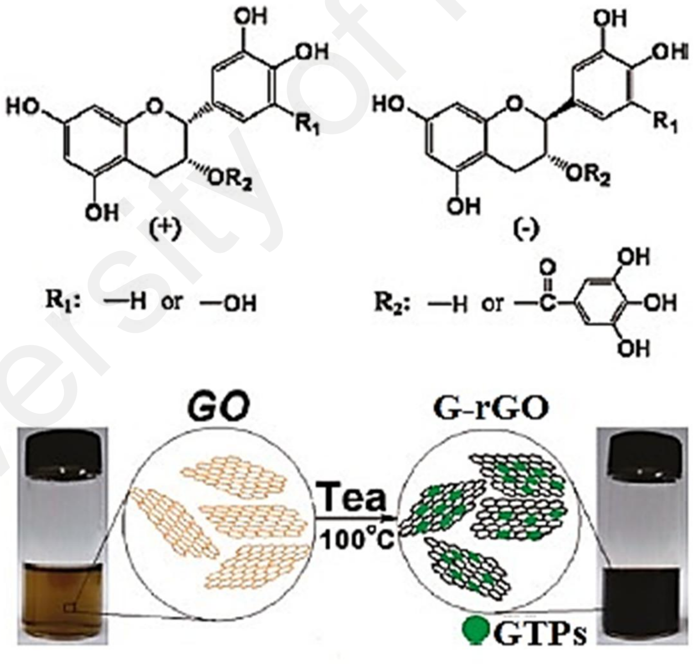

Figure 4.9 Chemical structure of GTPs and Schematic illustration of the preparation of G-rGO.

Besides, the colour change from brownish yellow of the GO solution to deep black for G-rGO, the reduction process was monitored by UV–vis absorption of GO and G-rGO as a function of wavelength. As shown in Figure 4.10, GO solution shows two bands: a maximum peak was at 228nm, which was related to the π- π* transitions of the aromatic

C–C bonds and a weak shoulder at 300nm due to n– π* transitions of C=O bonds. The G-rGO showed a absorption peak position at 270nm that show the efficient reduction of GO by GTPs (Y. Wang, et al., 2011). The strong absorption peak at around 200 nm belong to GTPs and occurred in all G-rGO samples even after several runs washing that indicating the strong adsorption between aromatic GTPs and graphene.

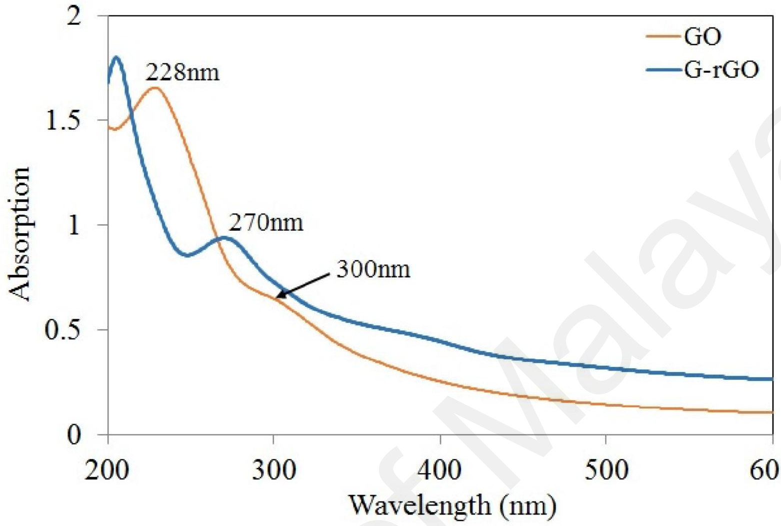

Figure 4.10 UV–vis spectrophotometer of GO, and G-rGO

The crystalline and morphology structure of G-rGO were studied by SEM and TEM. Figure 4.11 (a and b) shown G-rGO sheet after reduction and it was cleared that the size of a few micrometers and it tends to scroll on sheet edges, which a natural form of graphene nanosheets (Zhang et al., 2012).

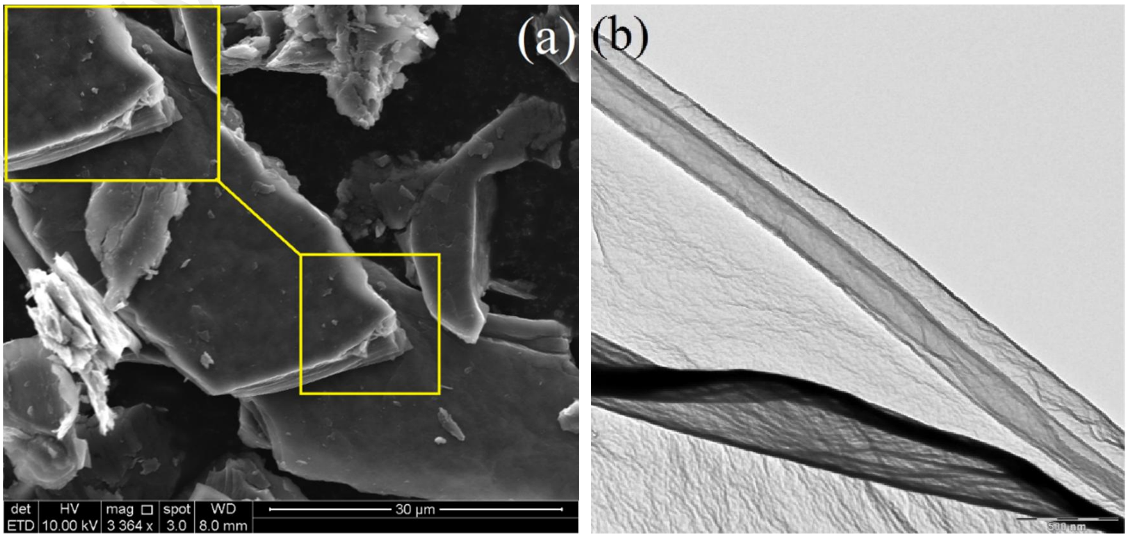

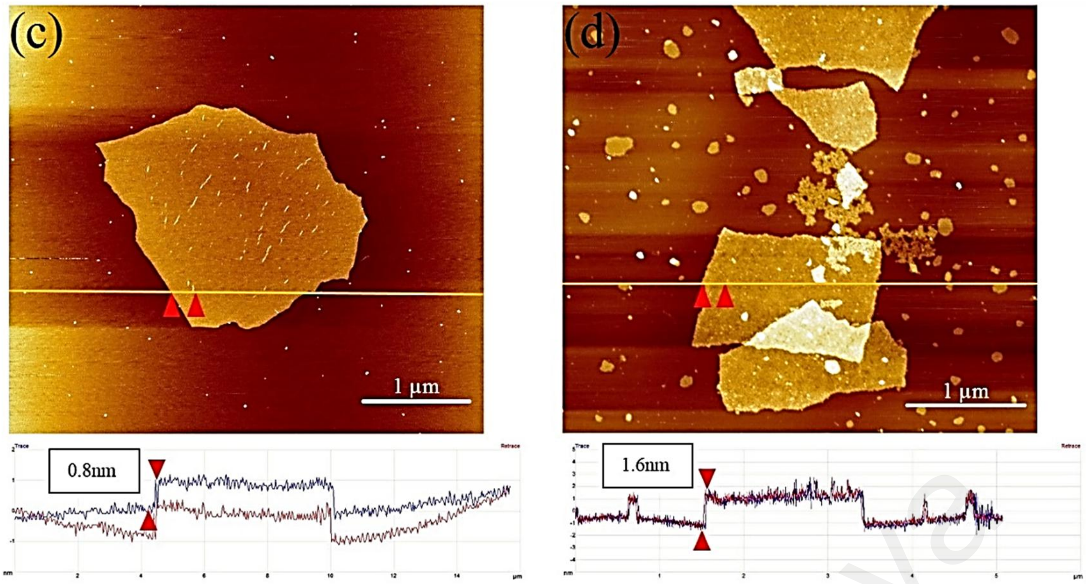

Figure 4.11 (a) SEM, (b) TEM images of G-rGO and (c, d) AFM image of GO and G-rGO.

The GO and G-rGO were characterized by AFM, which was usually employed to determine the lateral size and thickness of graphene. Figure 4.11(c, d) shows the AFM images and height profiles of GO and G-rGO. The average thickness of GO was found to be about 0.8nm and it shows that the GO is single-layered. The G-rGO has an average thickness of about 1.6 nm. Considering the single-layered graphene has a thickness of 0.8nm and the G-rGO molecules were adsorbed on both sides of the graphene, it is rational that the resultant G-rGO has thickness up to 1.6nm.

Figure 4.12 shows the XRD features of GO and G-rGO. The GO, the G-rGO shows two dominate peaks, one peak appears at $2\theta = 9.7°$, corresponding to d-spacing of 0.906nm, and it was due to the intercalation of water molecules and the formation of oxygen containing functional groups between the layers of the graphite. Therefore, the interlayer spacing between the two adjacent G-rGO sheets is about 1.05 nm. Another broaden peak is centered at $2\theta = 23.8°$, corresponding to a d-spacing of 0.36 nm, which may be resulted from some restacked graphene layers. Note that this spacing is very close to the pristine graphite, indicating the functional groups of GO, which have been efficiently removed.

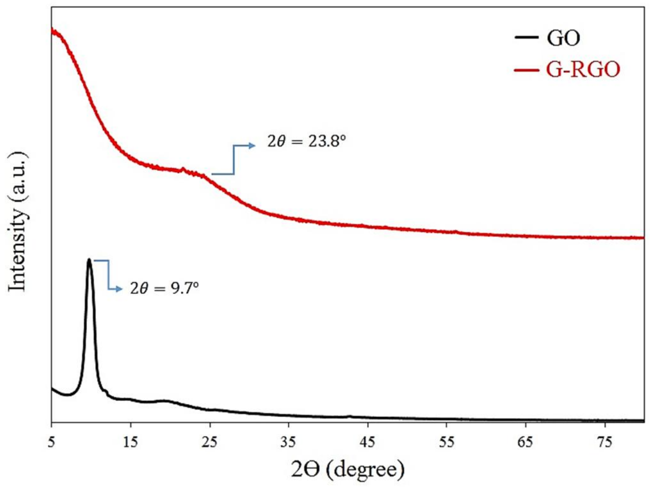

Figure 4.12 XRD patterns of GO and G-rGO

This reveals that the interlayer distance between two adjacent G-rGO layers is about 0.8nm, which is in good agreement with the value obtained by XRD study. Both GO and G-rGO has polydispersed the lateral sizes ranging from hundred nanometers to several micrometers. TEM images (Figure 4.11b) indicate that there is no significant difference in morphology between GO and G-rGO, both display silklike appearances.

4.3 Morphology of the dispersions

4.3.1 GNPs

A drop of diluted suspention was placed onto a carbon-coated copper grid, air-dried, and observed under TEM. Figure 4.13 shows the image of dried GNPs suspensions of different specific surface areas of GNPs. For the GNPs, the sheet-like structure with a lateral size at the micrometer length scale has been well captured as shown in Figure 4.13. Notably, the GNPs show good flexibility as proved by the folded and/or rolled parts. This indicates that each of the GNPs sheets only contains a very limited number of graphene layers, which is consistent with the parameter provided by the manufacturer. When GNPs were dispersed by ultrasonic treatment, the lateral size of GNPs was decreased. The edges of GNPs layers are clearly seen as the straight lines. At higher specific surface area, the GNPs size become smaller. The sonication process tends to break the flake: longer sonication time improves the exfoliation degree, further sonication is advantageous from the aspect of dispersion and colloidal stability.

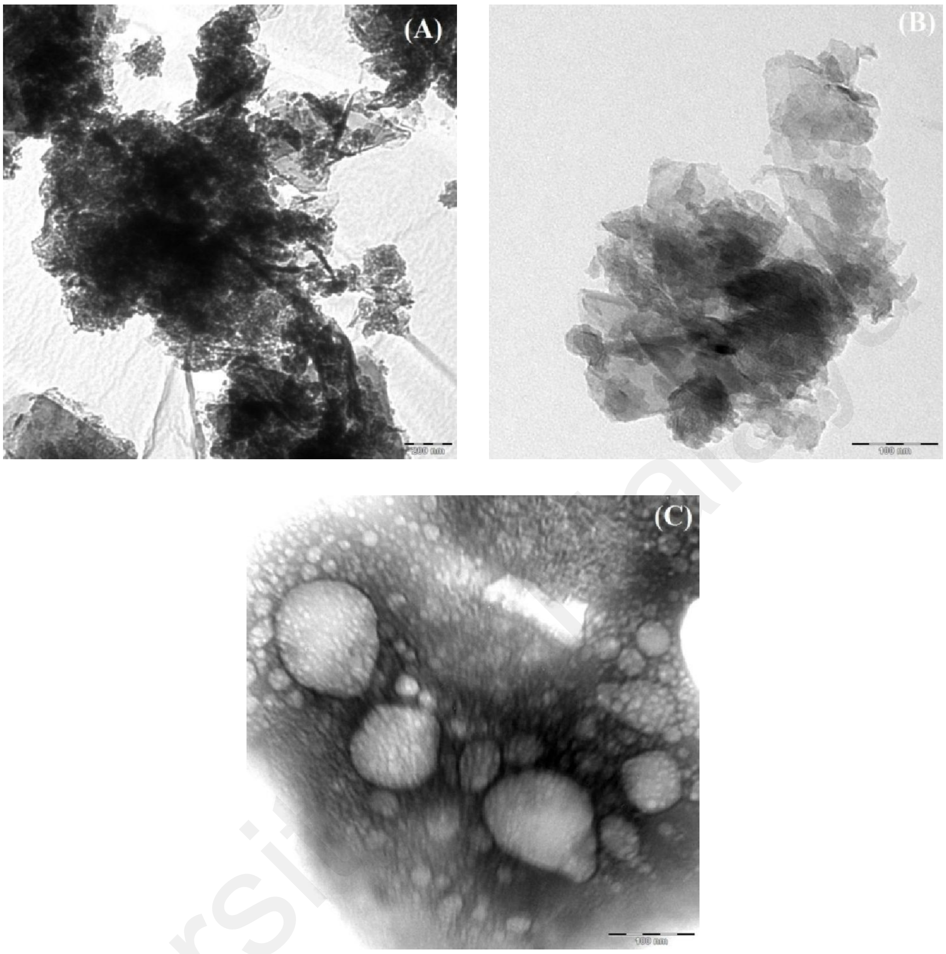

Figure 4.13 TEM images of GNPs nanoparticles; (A) GNPs 300, (B) GNPs 500 and (C) GNPs 750

4.3.2 NDG

SEM is a useful tool to distinguish the size, shape and distribution of nanoparticles. The dispersion and stabilization effect of NDG nanofluid was visualized via SEM images (Figure 4.14). To obtain the SEM images and distributions, surfactant-stabilized nanofluids were deposited onto a silicon wafer. Figure 4.14 shows that the nanoparticles have no aggregation and they appeared in an aggregate phenomenon and well dispersed. For higher concentrations, the samples were more uniform and subjected to become homogeneous suspensions.

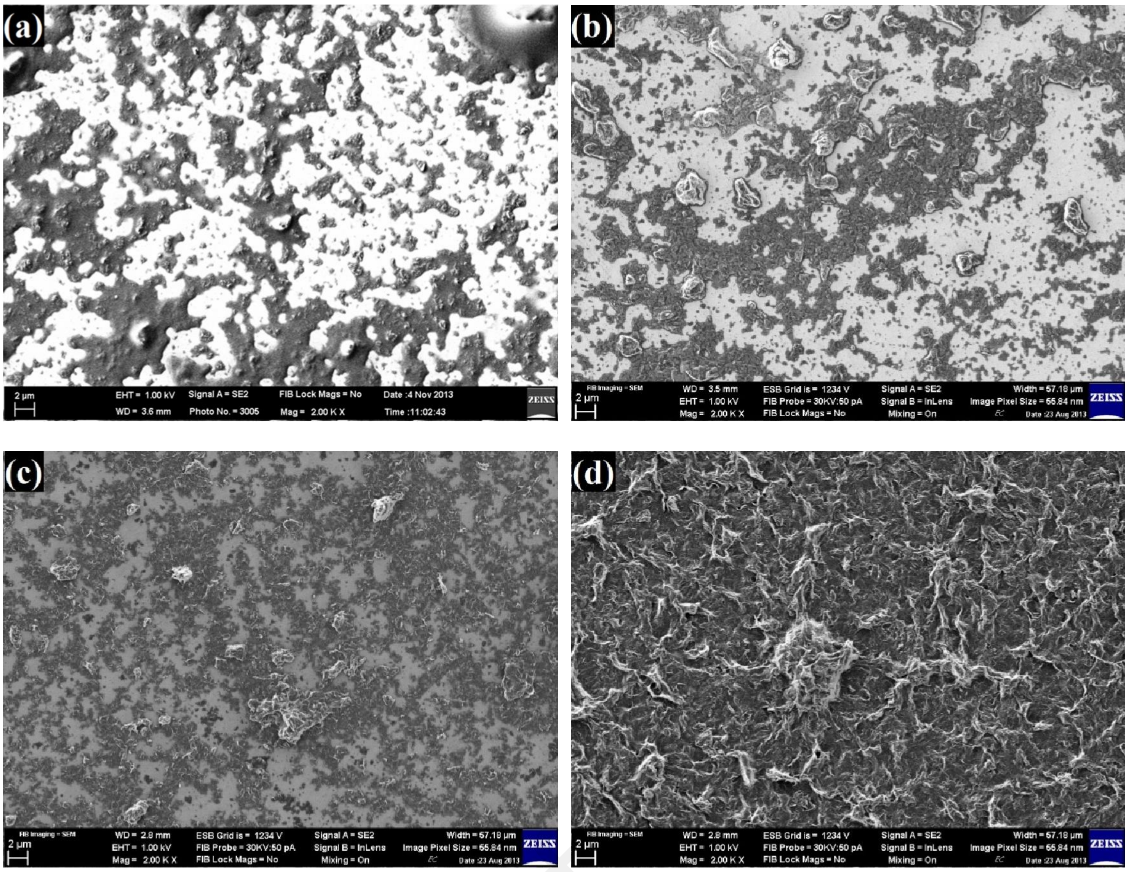

Figure 4.14 SEM images of nanoparticles after dispersion: (a) 0.01wt%, (b) 0.02wt%, (c) 0.04wt%, (d) 0.06wt%

4.4 Stability investigation with UV–Vis spectroscopy

4.4.1 GNPs

Figure 4.15A, B and C show the UV–vis spectrophotograph of the GNPs dispersions at different concentrations with different specific surface areas. The UV–vis spectrum of GNPs dispersion in distilled water is featureless with a monotonic decrease in absorbance with increasing wavelength, except below 320 nm where a strong absorption band is observed which scales with GNPs concentration but is less independent on GNPs specific surface area. Moreover, the absorbance of GNPs decreases from 0.1wt% to 0.025wt%, by knowing that the increasing amount of dispersed GNPs will increase the absorbance that refers to the better nanofluid dispersion. From results it can be indicated that by increasing specific surface area of GNPs the absorption value of λ_{max} was increased for the same concentration means that higher specific area provides better GNPs dispersion. As can be seen in Figure 4.15 the absorption value of λ_{max} at 280 nm shows no visible changes, the GNPs nanofluids are considered to be stable. The suddenly decreased absorption value indicates that the GNPs nanoparticles in the nanofluids start to aggregate and deposit. As shown in Figure 4.15D, E and F, there is a good linear relationship between the absorbance and the concentration of GNPs, which satisfies the Beer’s law and indicates that GNPs sheets were dispersed well in base fluid.

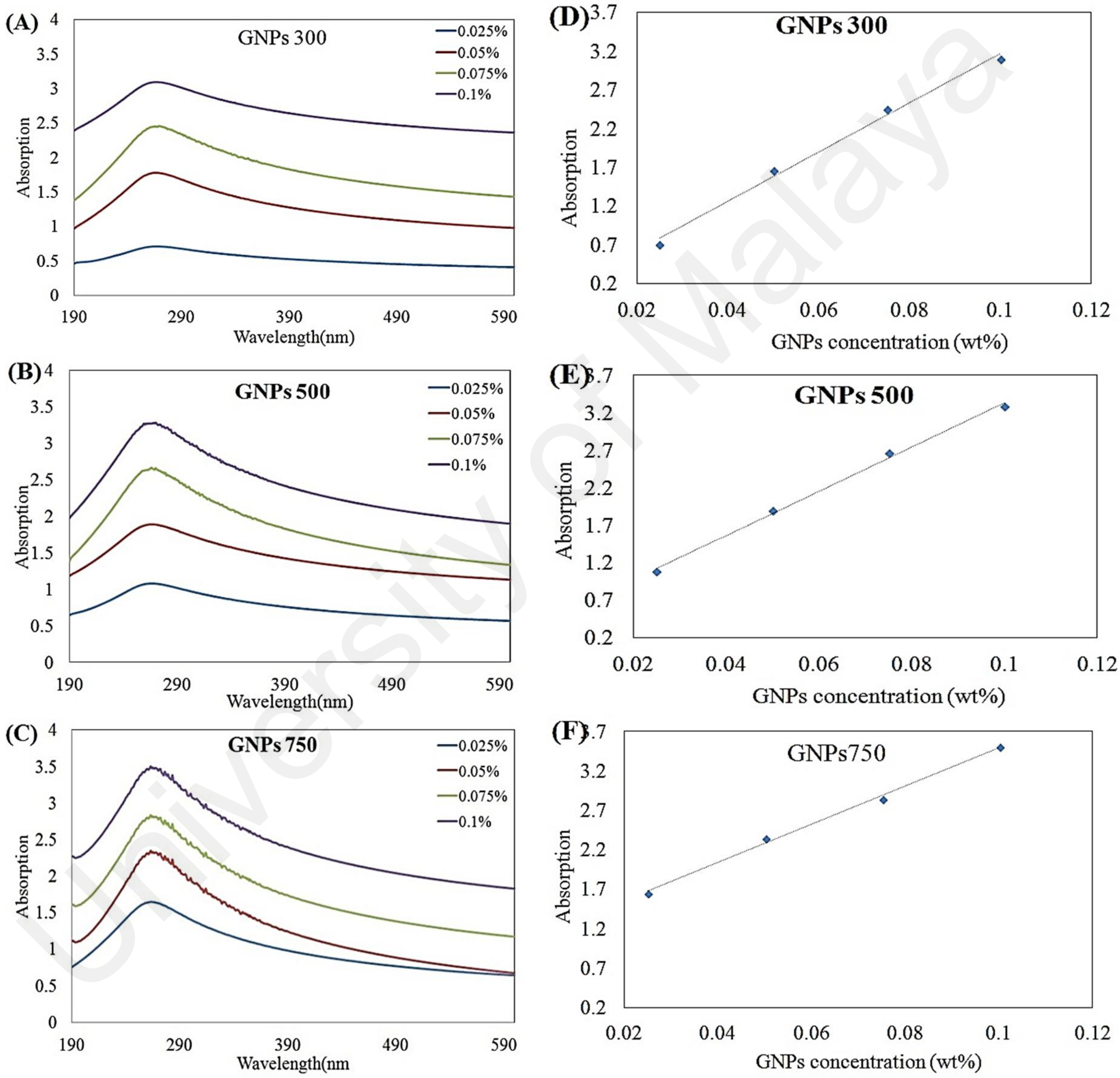

Figure 4.15 (A, B and C) UV–vis spectrophotometer of GNPs nanofluids at different concentrations and wavelength, and (D, E and F) UV–vis spectrophotometer of GNPs dispersed in distilled water at different concentrations.

Figure 4.16 shows colloidal stability of aqueous GNPs of nanofluids as a function of sedimentation time. From the results it can be seen that the relative concentrations for the same specific surface area and at different concentrations were decreased due to slight agglomeration and precipitation, which is more at increased concentrations. The most suitable relative concentration of nanofluid compared with the fresh one is GNPs 750 with concentration of 0.025w%, due to its higher specific surface area and lower concentration of GNPs. As a result, specific surface area of GNPs shows a very effective influence on the stability of nanofluid.

The rate of sedimentation after 600h is different among these 12 samples as different concentration and specific surface areas are imposed. This rate is changing as lowest precipitation rate appears from 1% by the GNPs 750 (0.025wt %) to the highest of 24% by the GNPs 300 (0.1wt%). These results show that different concentrations and specific surface area affect the rate of sedimentation as well as properties which agrees well with the results of the previous studies (Yujin Hwang et al., 2008).

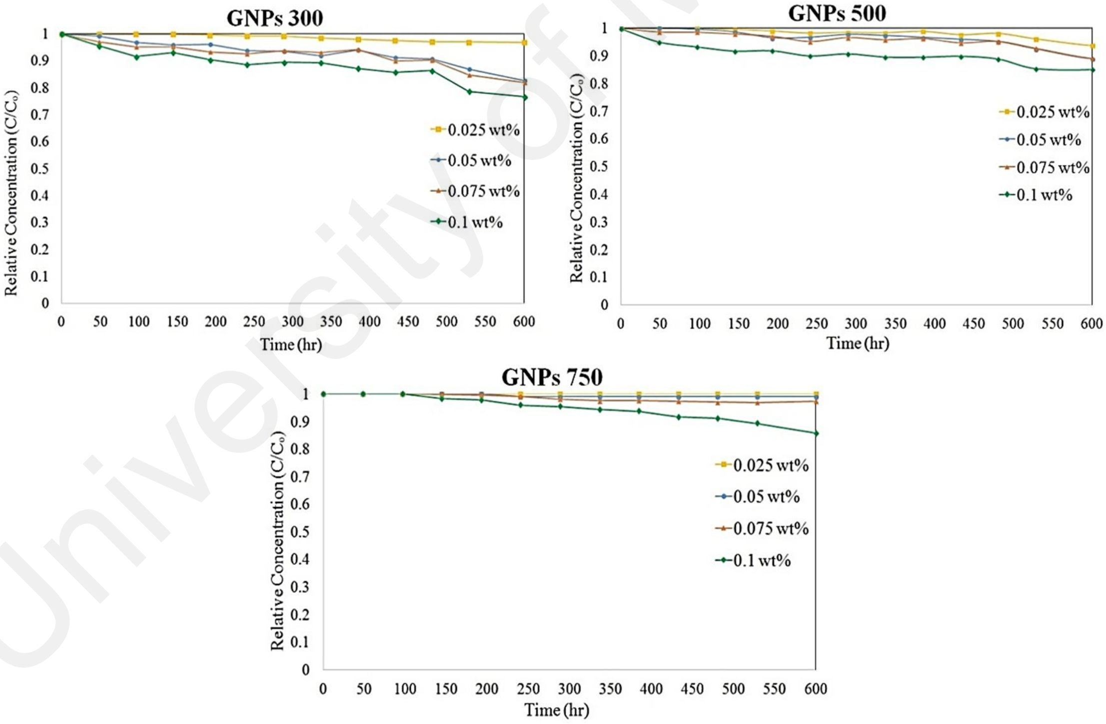

Figure 4.16. Relative particle concentration of nanofluids with sediment time

4.4.2 NDG

Figure 4.17 shows the UV–vis spectrophotograph of the NDG dispersions at different sonication methods with the same concentration of NDG. It can be seen that a longer sonication time leads to a higher absorbance value of λ_{max}, means a higher stability of nanofluid. It is concluded that sonication for 60min gives the best dispersion of nanoparticles. Figure 4.17 shows that the absorbance of NDG nanofluids at different sonication time.

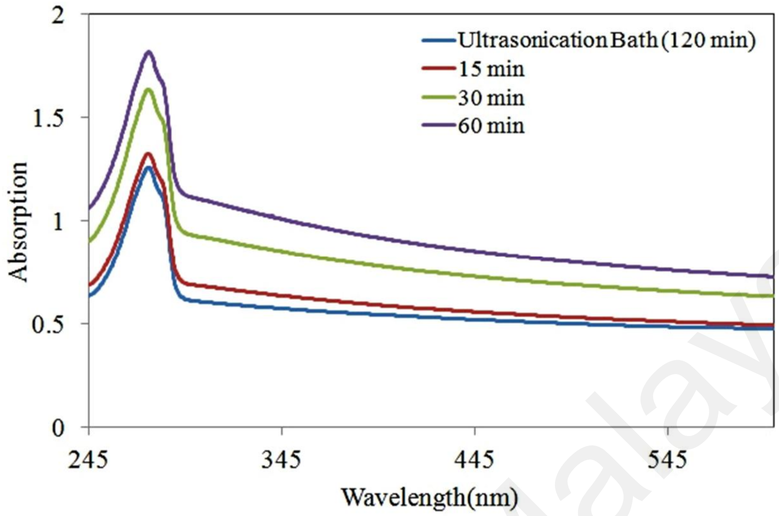

Figure 4.17 UV–vis spectrophotometer of NDG nanofluids at different sonication time

Figure 4.18 a shows the UV–vis spectrophotograph of the NDG dispersions with different concentrations at 60min sonication time. As shown in Figure 4.18b, a linear calibration curve was constructed at a wavelength of 275 nm, which satisfies the Beer's law and indicates that NDG was dispersed well in the base fluid. It shows that the suspension can be considered as a stable nanofluid.

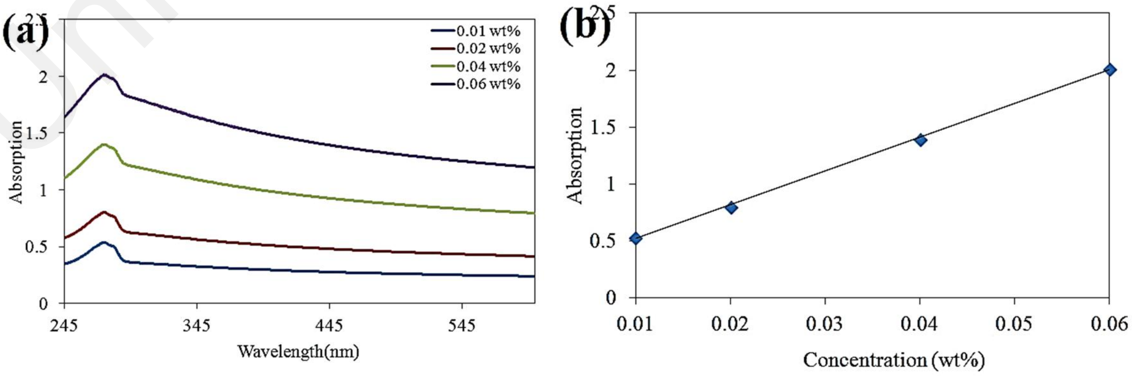

Figure 4.18 (a) UV–vis spectrophotometer of nanofluids at different concentrations and wavelength, (b) UV–vis spectrophotometer of NDG dispersed in base fluid at different concentrations.

Nanoparticles in the base fluids are mostly under the influence of gravity, as well as particle–fluids and particle–particle interactions. Therefore, the concentration of the nanofluids changes from the initial state of preparation and it is crucial to study the effect of concentration and sonication time. Figure 4.19 shows the colloidal stability of the NDG nanofluids with time. It is evident that the concentration of NDG nanofluids decreases with time which is mostly attributed to particle aggregation and sedimentation.

Figure 4.19a shows that the NDG nanofluid with 120min bath sonication exhibited a sharp drop of 47% for the first 85 days from the measurement and maintained steady state afterwards, exhibiting a 64% total reduction. The concentration at 30 and 60min sonication time was reduced by 28% and 10%, respectively after 180 days. However, the concentration of 120min ultrasonication bath exhibited almost no change after 40 days with a 38% reduction.

Figure 4.19b represents the colloidal stability of the NDG nanofluid at different concentrations. The relative concentrations of nanofluid at 0.01wt% exhibit almost no change and remain steady for 6 months. After 180 days, the concentrations for 0.02, 0.04 and 0.06wt% remains relatively constant and only reduced by 10%, 16% and 20%, respectively. Although the amount of reduction was different for each nanofluid, the reductions were comparatively low in all nanofluids observed in the study.

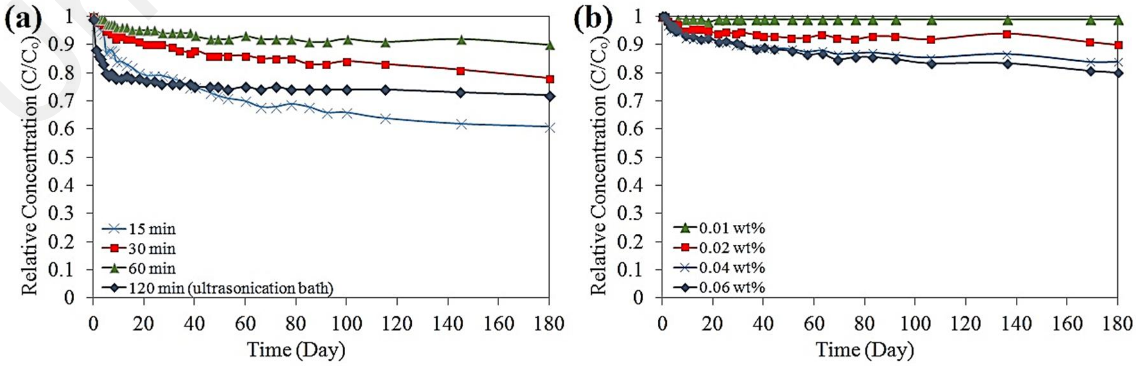

Figure 4.19 Relative supernatant particle concentration of nanofluids with sediment time; (a) different sonication time (same concentration of NDG), (b) different concentration (60min sonication time)

4.4.3 G-rGO

The stability of the nanofluid was determined by measuring the different concentration of the suspensions with the sediment time by the UV–Vis spectrophotometer and it was widely used in evaluating the relative concentration of the nanofluids. UV–Vis spectrophotometer method is based on Beer–Lambert's law, which states that the absorbance was directly proportional to the concentration of the nano-particles in the nanofluids. Figure 4.20a shows UV–vis spectrophotograph of the G-rGO aqueous at different volume fraction. It shows that the G-rGO nanofluid absorption was in the UV-vis range and reveal that the characteristic bands corresponding to additional absorption due to the 1D van Hove singularities (Aravind et al., 2011a). To measure the relative concentration of the suspensions with the sediment time, the same sample of DW and G-rGO solution were used as a reference to eliminate the absorbance of nanofluid. As shown in Figure 4.20b, a linear calibration curve was constructed at a wavelength of 270 nm, which satisfies the Beer–Lambert's law and indicates that G-rGO was dispersed well in the base fluid.

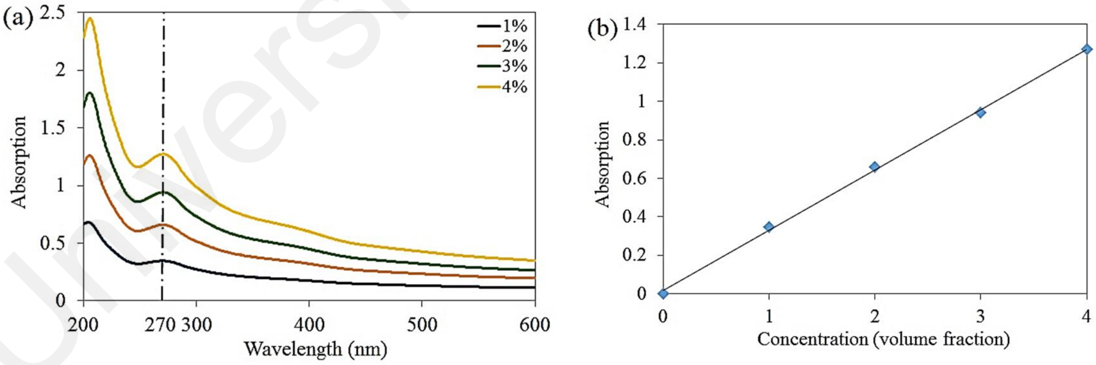

Figure 4.20 UV–vis spectrophotometer of nanofluids at different concentrations and wavelength, (b) UV–vis spectrophotometer of G-rGO dispersed in base fluid at different concentrations.

Nanoparticles concentration in the base fluids are mostly under the influence of gravity, as well as particle–fluids and particle–particle interactions. Figure 4.21 shows the volume fraction change of the G-rGO nanofluids with the sedimentation time. The absorptions of nanofluids are directly relative to the nanoparticles concentration, and decrease in absorption wavelength with time that would mean that nanoparticles concentration reduced. The relative concentrations of nanofluid at ϕ=1% exhibit about 3.9% change and remain steady for 1000hr. After 1000hr, the concentrations for ϕ=2%, 3% and 4% remains relatively constant and reduced by 12.8%, 15.1% and 18%, respectively. Although the amount of reduction was different for each nanofluid, the reductions were comparatively low in all nanofluids observed in this study.

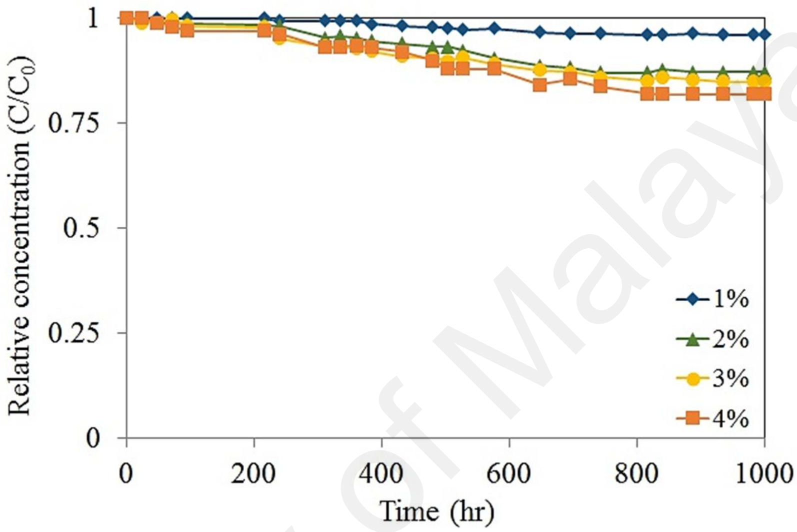

Figure 4.21 Relative supernatant particle concentration of nanofluids with sediment time

4.5 Stability investigation with zeta potential

4.5.1 GNPs

The measurement of the zeta potential has carried out the electrophoretic behavior and additional details to comprehend the dispersion behavior of GNPs in water. Zeta potential values of GNPs nanofluid was obtained for various specific areas. Figure 4.22 demonstrates the changes of zeta potential for GNPs 750 suspensions as a function of pH values. In the GNPs suspension while using water as a base fluid, the GNPs tend to be positive charged before pH=3 and negative charged within the entire pH ranges after pH=3. At pH of about 10, the absolute value of zeta potential will be the maximum, while the maximum excess 50mV. The nanofluids which has a measured zeta-potential above +30 mV or below -30 mV are having good stability (Vandsburger, 2010). It implies that the force of electrostatic repulsion between GNPs is sufficient to get over the attraction force between particles. Higher electrostatic force may also cause form much more free particles by improving particle–particle distance, in order that the distance exceeds the hydrogen bonding range between particles and further decreases the chance of particle coagulation and settling. The pH value of prepared nanofluids was measured about pH=8 while zeta potential value appears to be 31.8, 40.9 and 45.7 mV for GNPs 300, 500 and 750 m^2/g, respectively. The inclination is that the zeta potential values demonstrate enhancement for the higher specific surface areas GNPs. This phenomenon suggests that the GNPs nanofluid with higher specific surface areas might have better stability.

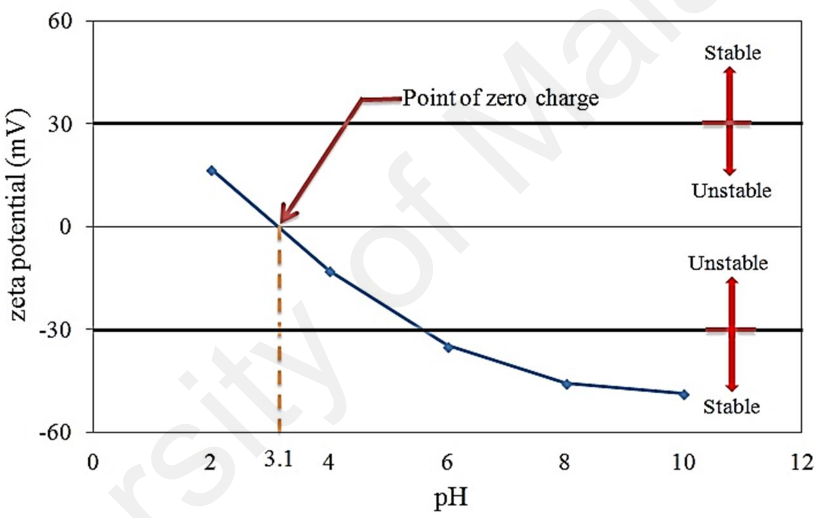

Figure 4.22 Zeta potential values of GNPs (750 m^2/g) nanofluids as a function of pH value

4.5.2 NDG

The stability of nanofluid is closely related to its electrokinetic properties. A well-dispersed suspension can be acquired with a high zeta-potential to get strong repulsive forces. The dividing line between stable and unstable nanoparticle suspensions is generally taken at either +30 or -30mV. Nanofluids with zeta-potentials more positive than +30mV or more negative than -30mV are normally considered stable and this is one of the most common methods to determine the stability.

Determining the processing time for ultrasonication (probe) requires care because longer than optimum durations may cause agglomeration. The result of various timing of ultrasonic process in terms of zeta-potential and particle size can be seen in Table 4.4 and is evident that the NDG are negatively charged. The zeta-potential of all NDG nanofluids was negative and ζ values greater than -30mV, which is in line with the excellent stability found by UV-vis studies. The ultrasonication bath has a much less energy than the ultrasonication probe and it is clean from both zeta-potential value and particle size that the ultrasonication bath is not powerful enough for dispersion of the nanoparticles.

Table 4.4 Particle size distribution and zeta potential at different ultrasonic processor timing immediately after preparation

Method	Time (min)	Zeta potential	Size (nm)
Ultrasonicaion probe	15	-41.5	981.2
	30	-44.8	615.4
	60	-46.3	412.4
Ultrasonication Bath	120	-38.1	1450.9

Figure 4.23 illustrates the zeta-potentials of the NDG dispersions prepared with 60min ultrasonication probe as a function of pH. It is seen that a stable dispersion can be expected at a pH above 7. In the water based NDG suspension, the NDG tends to be positively charged below pH=2.5 and negatively charged within the entire pH ranges after pH=2.5. At pH of about 10, the absolute value of zeta potential will be the highest, while the maximum magnitude is 60mV. Therefore, the zeta-potential values of NDG nanofluid at natural (pH 8.0) can be selected arbitrarily as an operating pH for the suspensions with Triton X-100 dispersants.

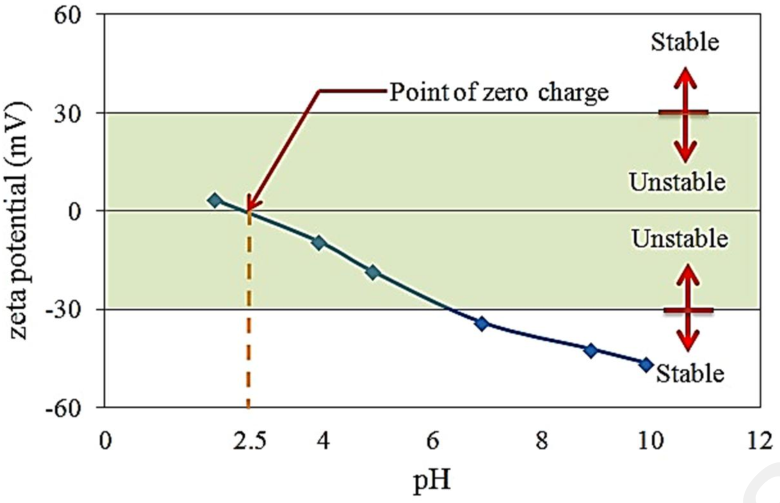

Figure 4.23 Zeta-potential of NDG as a function of pH

4.5.3 G-rGO

The colloidal stability of G-rGO nanofluids is measured by zeta-potential values of the nanoparticles dispersed in DW and closely related to its electrophoretic properties. A well-dispersed suspension can be obtained with high surface charge density to generate strong repulsive forces. Nanofluids with zeta-potential value of more negative than -30mV or more positive than +30mV are considered stable and this is one of the common methods to determine the stability of nanofluids (Mohammad Mehrali, et al., 2014a).

The most important factor that affects the zeta-potential is pH and without a stated pH is only a virtually meaningless number. Generally, the zeta-potential versus pH curve will change from positive to negative with varying the pH. The point where the plot passes through the zero value of the zeta-potential is called the isoelectric point and it is very important from a practical perspective. At the isoelectric point, the agglomeration and precipitation of nanofluids were observed (S. W. Lee, et al., 2011; Navrátilová, et al., 2012). Figure 4.24 illustrates the zeta-potentials of the G-rGO nanofluid as a function of pH. It was shown that the G-rGO nanofluid becomes stable at pH values above 5 and it does not reach isoelectric point. The zeta potential of the G-rGO particles in distilled water (pH 5) reaches approximately -31 mV, the zeta potential is negative. With increasing addition of alkali to the suspension, the particles tends to acquire a more negative charge and it shows the nanofluids becomes more stable.

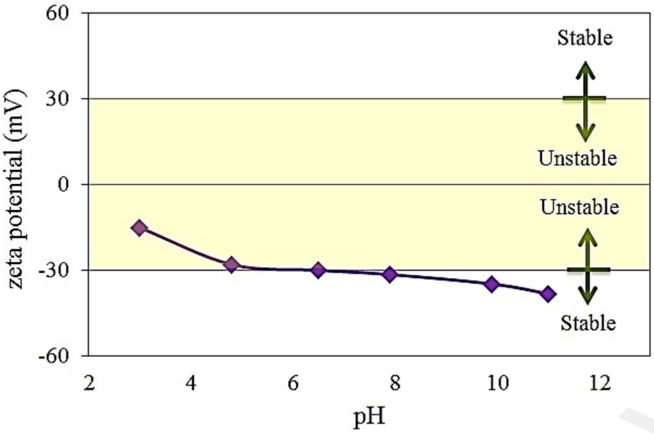

Figure 4.24 Zeta-potential of G-rGO nanofluid as a function of pH

4.6 Rheological behavior of nanofluids

4.6.1 GNPs

Viscosity of nanofluids is one of the most critical parameters, which determines the quality of the heat transfer fluid. Similar to simple fluids, temperature is the main effective parameter on viscosity of nanofluids. As expected, distilled water exhibits a Newtonian behavior within the shear rate range investigated. The viscosity value of distilled water was 1.034, which closely matches with its theoretical values at 20°C. The relative deviation is less than 2.5%. This is of the same order of magnitude as the experimental uncertainty. Figure 4.25 reports the viscosity at a high shear rate of 500 s^{-1} for different concentrations and specific surface areas as a function of all tested temperatures. While nanofluids and base fluids are strongly dependent on temperature, it is also observed in Figure 4.25 that the viscosity was decreased at higher temperatures. This is expected due to the weakening of the inter-particle and inter-molecular adhesion forces and similar trends have also been observed in almost all other varieties of nanofluids. It can be seen clearly that viscosity was increased for higher concentration of GNPs that the viscosity of nanofluid was improved by 44% compared to the viscosity of the base fluid for 0.1wt% of GNPs. This can be realized in such a way that, once the concentration increases, the nanoparticles make agglomeration within the suspension. This consequently, results in the increase of internal shear stress in nanofluid because of the greater force needed for dissipating the solid element of the dispersion and hence an increase in viscosity.

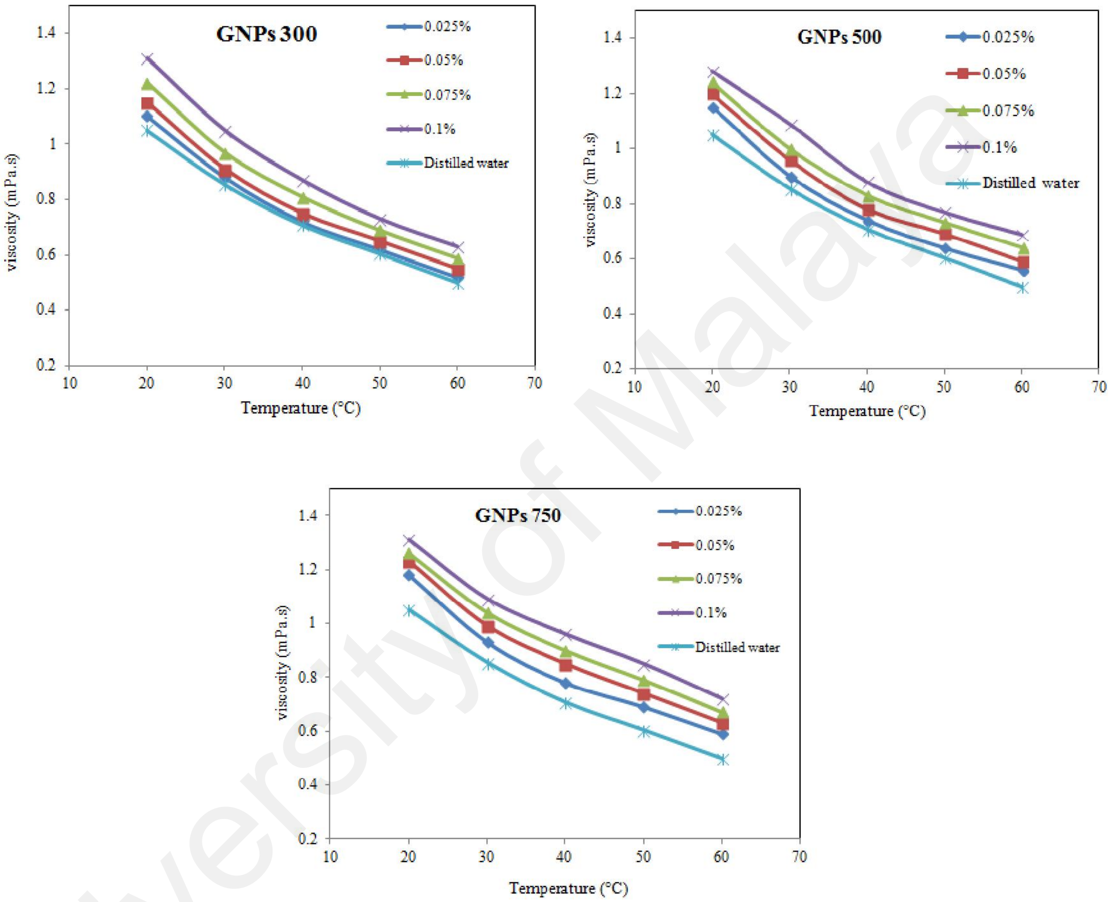

Figure 4.25 Viscosity vs. concentration at various temperatures and constant shear rates

In order to determine the rheological behaviors of GNPs nanofluids, the viscosity of the aqueous GNPs versus shear rate was measured at the temperature range of 20 to 60°C and the results are shown in Figure 4.26. The viscosity of distilled water decreases exponentially as a function of shear rate which indicates its shear thinning (Pseudoplastic) behavior. Following the trend of water, the samples of GNPs nanofluid also exhibit the shear thinning property. The cause of this non-Newtonian shear thinning can be explained generally as follows. At low shear rates, as the spindle rotates in the fluid, the structure of the fluid molecule changes temporarily and gradually align themselves in the direction of increasing shear and produce less resistance and hence a reduction in viscosity. When the shear rate is high enough the maximum amount of shear ordering possible is attained, the aggregates are broken down to smaller size decreasing the friction and hence the viscosity (Nabeel Rashin et al., 2013) . If the shear rate is further increased it will not make any alteration to the viscosity. Due to small size and large surface area of nanoparticle there is possibility for structuring at low shear rates and a deformation and restructuring at high shear rates. Hence, nanofluid also follows the same trend. It is observed at all the temperatures that the shear thinning property is more pronounced at higher concentrations. This points out that at low concentrations the nature of base fluid plays a major role in shear thinning, but at higher concentrations there is significant contribution from the interaction between nanoparticle and fluid.

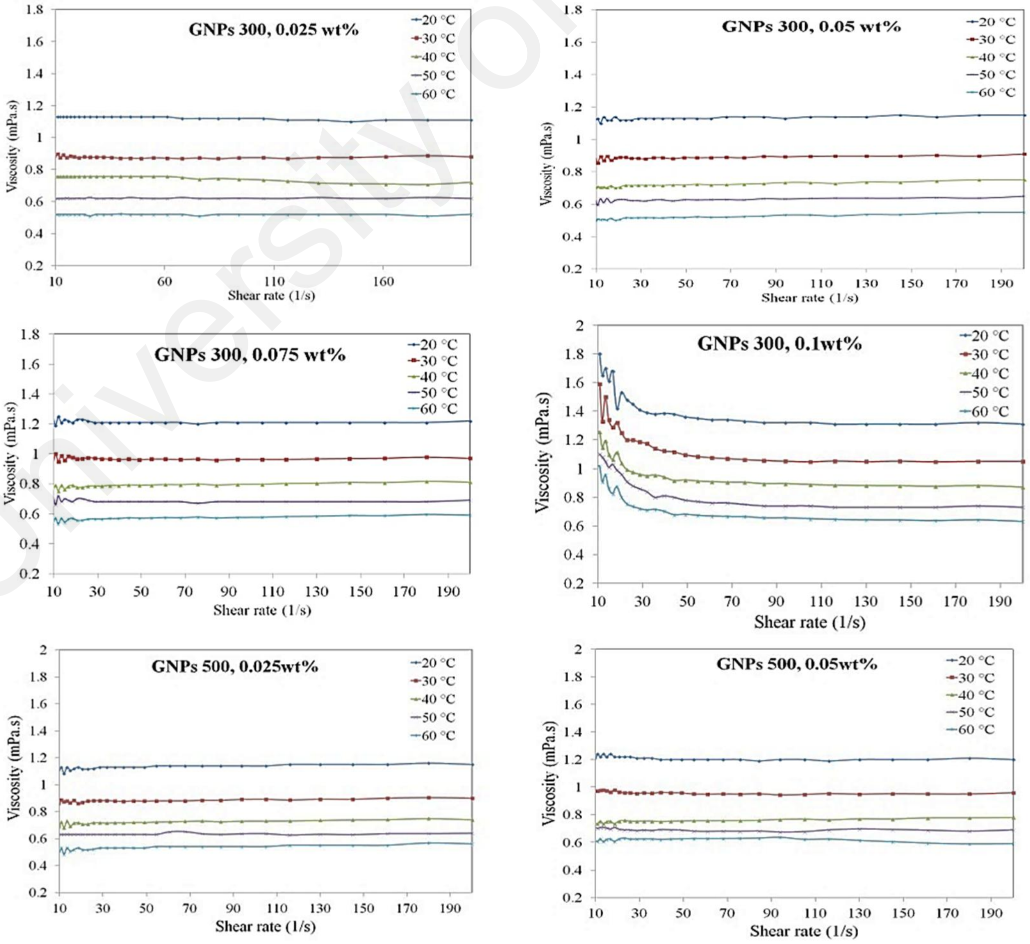

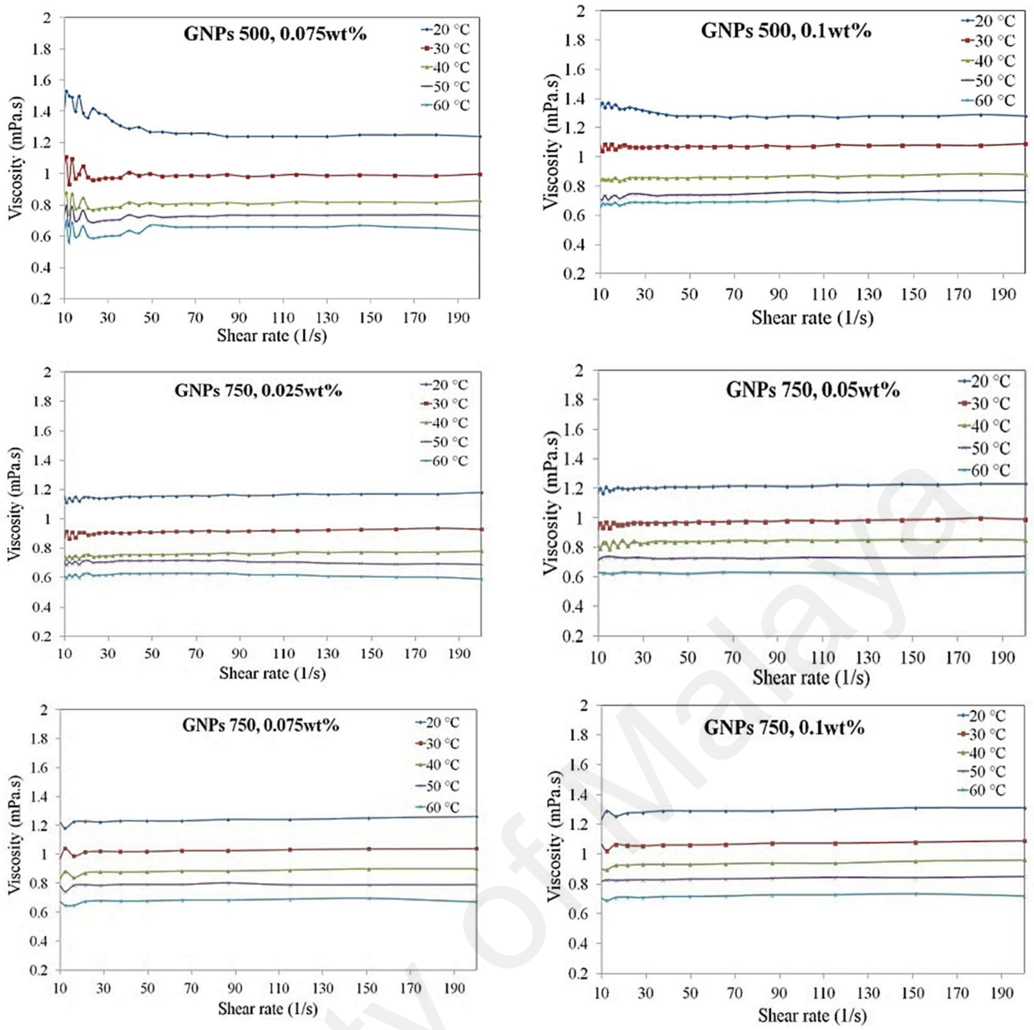

Figure 4.26. Plots of viscosity versus shear rate at various concentrations and temperatures

The results indicate that prepared nanofluids are suitable to use at elevated temperatures. Since, by increasing the temperature, thermal movement of molecules and Brownian motion intensifies, and intra-molecular interactions become weakened. In addition, rheological test on nanofluids revealed that the higher concentration will increase the viscosity; however, other investigated parameters such as temperature and specific surface areas have an important influence on viscosity behavior of nanofluids.

4.6.2 NDG

Figure 4.27 reports the viscosity at a high shear rate of 300 s^{-1} for different concentrations as a function of all the tested temperatures. Similar to conventional fluids, the viscosity of nanofluid depends on the temperature. It can be observed that viscosity reduces with the raising of temperature. It can be clearly seen that viscosity decrease between 51.19-51.50%. Results indicate that nanofluids with higher concentrations have higher viscosities. It is also interesting that nanofluids of low concentrations showing almost same viscosity values of the higher concentration. It shows that loading of the NDG nanoparticles increase the friction and flowing resistance of fluids which ultimately causes increase of viscosity. While by rising the temperature, the nanoparticles are motivated more and create a higher space for them. This is expected due to the weakening of the inter-particle and inter-molecular adhesion forces and similar trends are also been observed for almost all other varieties of nanofluids.

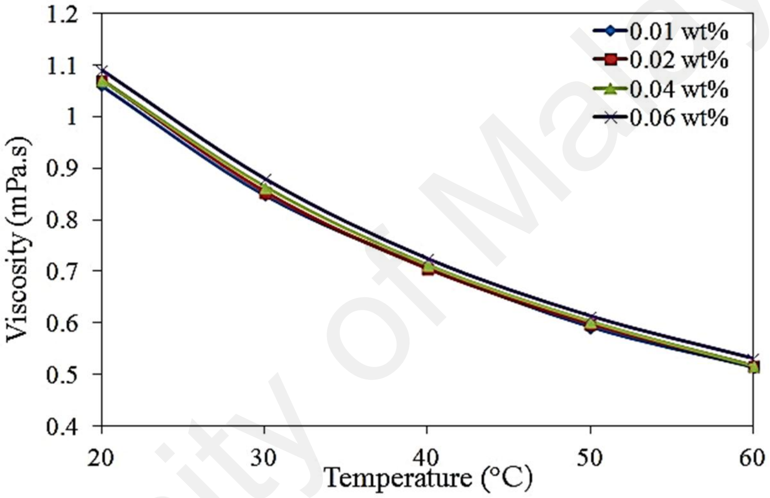

Figure 4.27 Viscosity versus concentration at various temperatures and shear rates of 300 s^{-1}

In order to determine the rheological behaviors of NDG nanofluids, the viscosity versus shear rate was measured in the range of 20°C to 60°C and the results are presented in Figure 4.28. It shows that the viscosity remains unchanged with increasing shear rate and the NDG nanofluid acts as a Newtonian fluid manner. At low shear rates, as the spindle rotates in the nanofluid, the structure of the nanofluid molecule changes temporarily and slowly align themselves in the direction of increasing shear and create less resistance and therefore a decreases in viscosity. When the ideal level of shear ordering is achieved, the aggregates are broken down to smaller size and then the friction and viscosity will decreases. If shear rate increases further it will not make any alteration to the viscosity. Due to large surface area of nanoparticle, there is possibility for structuring at low shear rates and a restructuring and deformation at high shear rates.

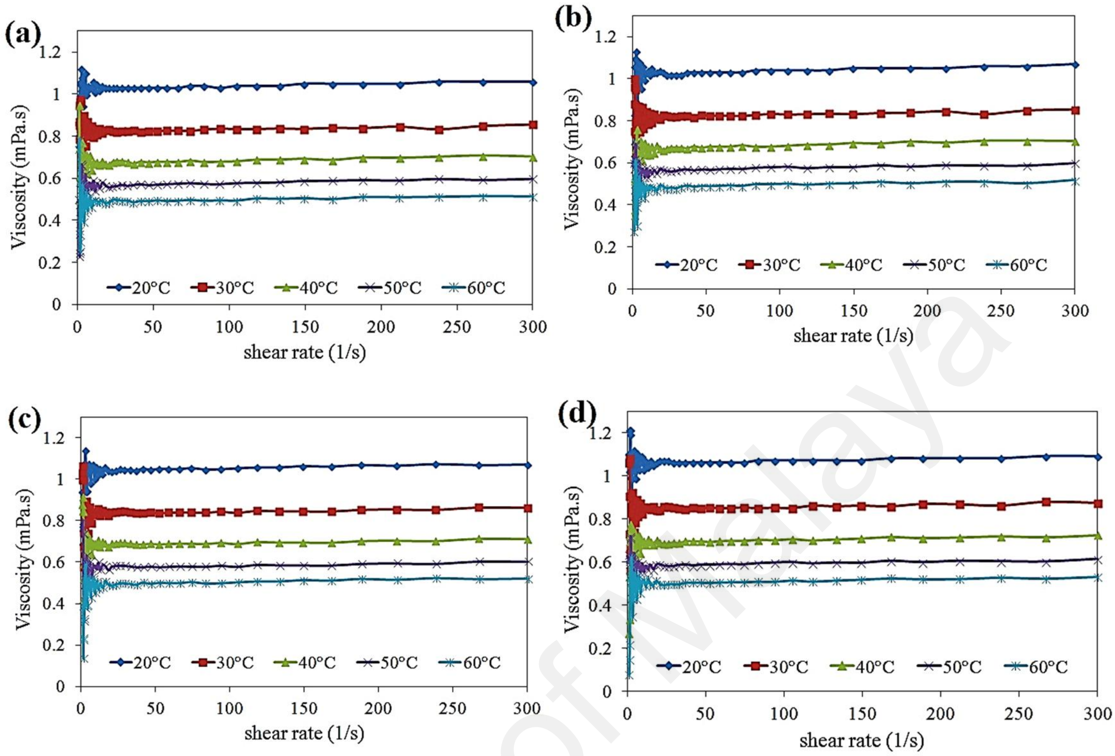

Figure 4.28 Viscosity as a function of shear rate for NDG nanofluid: (a) 0.01wt%, (b) 0.02wt%, (c) 0.04wt%, (d) 0.06wt%

It is observed experimentally that the prepared nanofluids are suitable to use at elevated temperatures. Since, with the rise of temperature, thermal movement of molecules and Brownian motion intensifies and intra-molecular interactions become weakened. In addition, rheological test on nanofluids revealed that the changing of concentration will increase the viscosity; however, other investigated parameters such as temperature and concentration have an important influence on viscosity behavior.

4.6.3 G-rGO

Based on the literature, understanding viscosity of nanofluids is the one of fascinating challenge and the most critical parameters in heat transfer properties of nanofluis. It follows two important characteristics: (a) increase in viscosity with increases of nano-particle concentration and the internal viscous shear stress increases, (b) decrease in viscosity with temperature (Sadri, et al., 2014). With increasing of the temperature, the nano-particles are motivated more, hence inter-particle and inter-molecular adhesion forces become weaken. Meanwhile, with the rise of temperature, thermal movement of molecules and Brownian motion intensifies and viscosity of the nanofluids decreases (Mohammad Mehrali, et al., 2014a). Figure 4.29 reports the viscosity at shear rate of 500 s^{-1} for different concentrations as a function of temperatures ranging from 20 to 70°C. It can be seen that viscosity decreased between 86.2-87.9% and it is interesting that G-rGO nanofluids with low concentrations (1 volume fraction) shows almost similar to the viscosity at higher concentration (4 volume fraction).

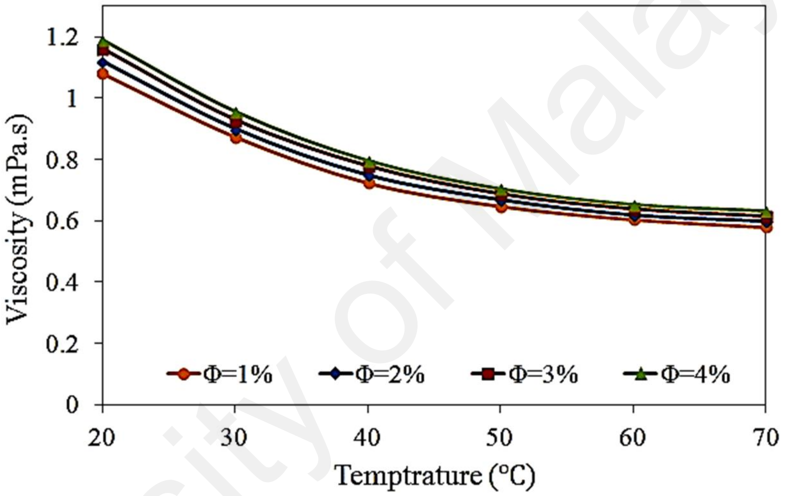

Figure 4.29 Viscosity versus concentration at various temperatures and shear rates of 500 s^{-1}

The viscosities of G-rGO nanofluids were measured at different concentrations, at different temperature range and the results are shown in Figure 4.30. In order to determine the rheological behaviors of G-rGO nanofluids, the viscosity versus shear rate was measured in the range of 20°C to 70°C and the results are present in Figure 4.30. It was shown that the nanofluids with volume fraction of 1% to 4% behave as a Newtonian fluid manner and temperature was the major factors affecting the viscosity of the nanofluids. In additional, a rheometer consists of outer (chamber) cylinder, and inner (spindle) cylinder and the nanofluid is located between them. As the spindle rotates in the nanofluid, the structure of the nano-particles molecule changes temporarily and slowly align themselves in the direction of increasing shear. A Newtonian fluid has the same viscosity when stronger or weaker forces (shear rate) are applied.

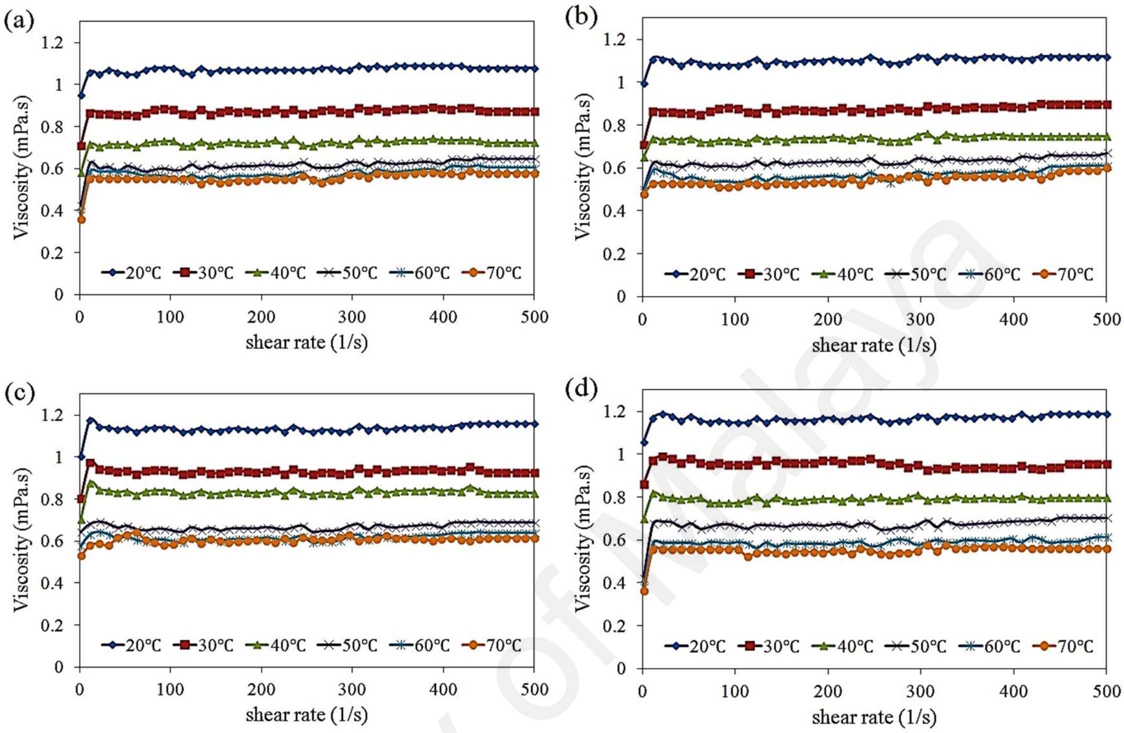

Figure 4.30 Viscosity as a function of shear rate for G-rGO nanofluid: (a) ϕ=1%, (b) ϕ=2%, (c) ϕ=3%, (d) ϕ=4%,

It is observed experimentally that the prepared nanofluids are suitable to use at elevated temperatures; however, other investigated parameters such as temperature and concentration have important influence on viscosity behavior (Mohammad Mehrali, et al., 2014a).

4.7 Wettability effects of nanofluid

Wettability studies usually involve the measurement of contact angles (θ) as the primary data, which indicates the angle between the liquid and a solid surface. Wetting liquids have angles between 0° and 90° and non-wetting liquids have angles between 90° and 180°. The surface forces, such as cohesive and adhesive forces have great influence on the contact angle between liquid and solid surfaces. Many researchers have studied on the wettability effect of working fluid on a solid surface in the heat transfer systems (Y.-

j. Chen, et al., 2013). The most popular measurement techniques of contact angle is tangent angle measurement at the three-phase contact point on a sessile drop profile by telescope-goniometer. As the tendency of a drop to spread out over a solid surface, which is cause of change in the contact angle and the deformation of the drop due to gravity were considered to be negligible owing to its small surface area. Thus, good wetting surface shows a lower contact angle and a bad wetting surface shows a higher contact angle (Sadeghinezhad, et al., 2014).

The wettability is an effective parameter for the heat transfer coefficient and the friction factor, especially for heat transfer to two-phase flow, and higher contact angle surfaces tend to decrease the heat transfer coefficient compared with the lower contact angle surfaces (C. Choi, et al., 2011). The initial equilibrium contact angle of the nanofluids was significantly affected by the nanoparticle sizes and concentrations. Nanofluid molecules tumble along the tube wall, similar to two solid surfaces sliding over one another, when the forces between the nanofluid and the tube wall molecules are not strong enough to overcome the shear forces at the wall. This decoupling of the nanofluid from the wall results in a lower frictional pressure drop. Therefore, the lower contact angle provided more friction drop because of the adhesive force between the nanofluids and the tube wall (C. Choi, et al., 2011).

Figure 4.31 shows the images of the contact angles for the $2\mu L$ of GNP nanofluid when it was spread on a solid surface at 25℃. The contact angle of the distilled water (DW) on the solid surface was 99.8°, which was decreased to 95.3°, 95.1°, 94.5° and 93.5° for the GNP nanofluids at concentrations of 0.025, 0.05, 0.075, and 0.1 wt%, respectively. The contact angle of the GNP nanofluid decreased compared with the base fluid, which improves the wettability of the GNP nanofluids and leads to a reduction of the contact angle.

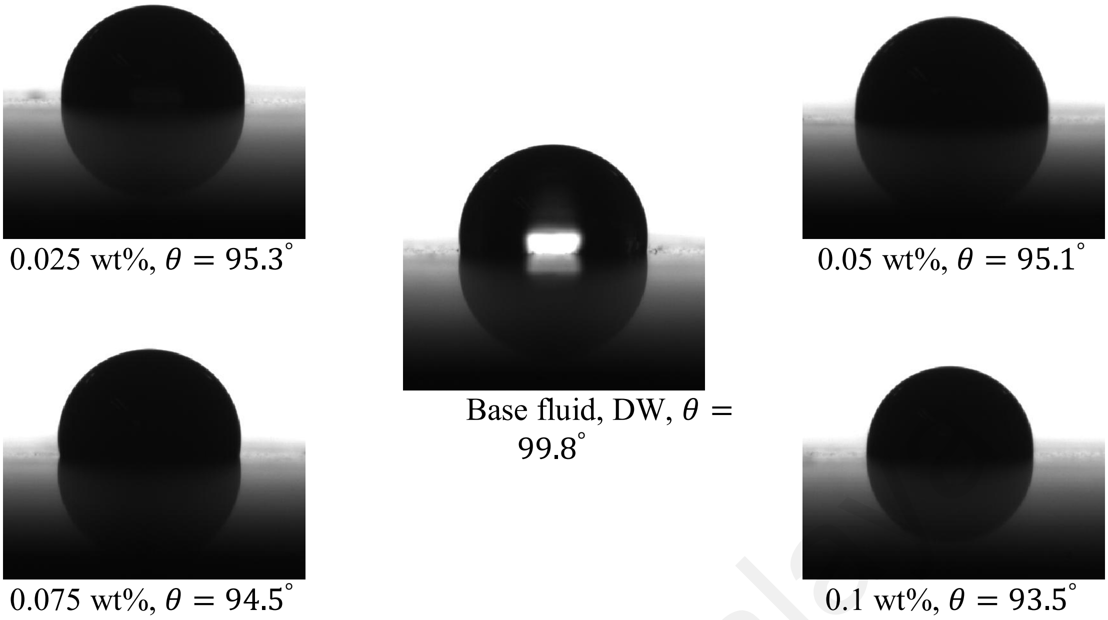

0.025 wt%, $\theta = 95.3^{\circ}$

0.05 wt%, $\theta = 95.1^{\circ}$

Base fluid, DW, $\theta = 99.8^{\circ}$

0.075 wt%, $\theta = 94.5^{\circ}$

0.1 wt%, $\theta = 93.5^{\circ}$

Figure 4.31 Contact angle image of the base fluid and the GNP nanofluids at different concentrations

Figure 4.32 shows the contact angle pictures of $1\mu L$ of NDG nanofluid on a solid surface at 25℃. As is shown, the contact angle of distilled water (DW) on the surface is 75.4° and base fluid (DW+Triton X-100) is decreased to 41°. The contact angle of NDG nanofluid decrease compared with base fluid and improves the wettability of nanofluids which leads to reduction of the contact angle.

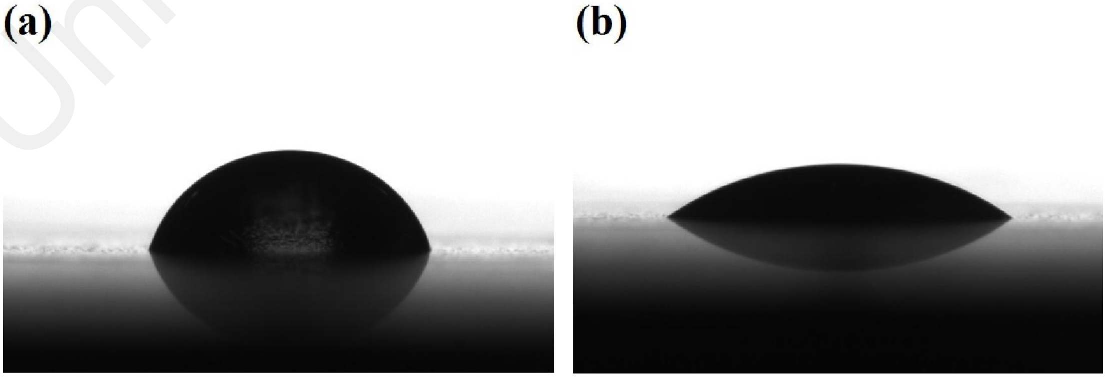

θ = 75.4°
Distilled water (DW)

θ = 41°
DW+Triton X-100 (1:400)

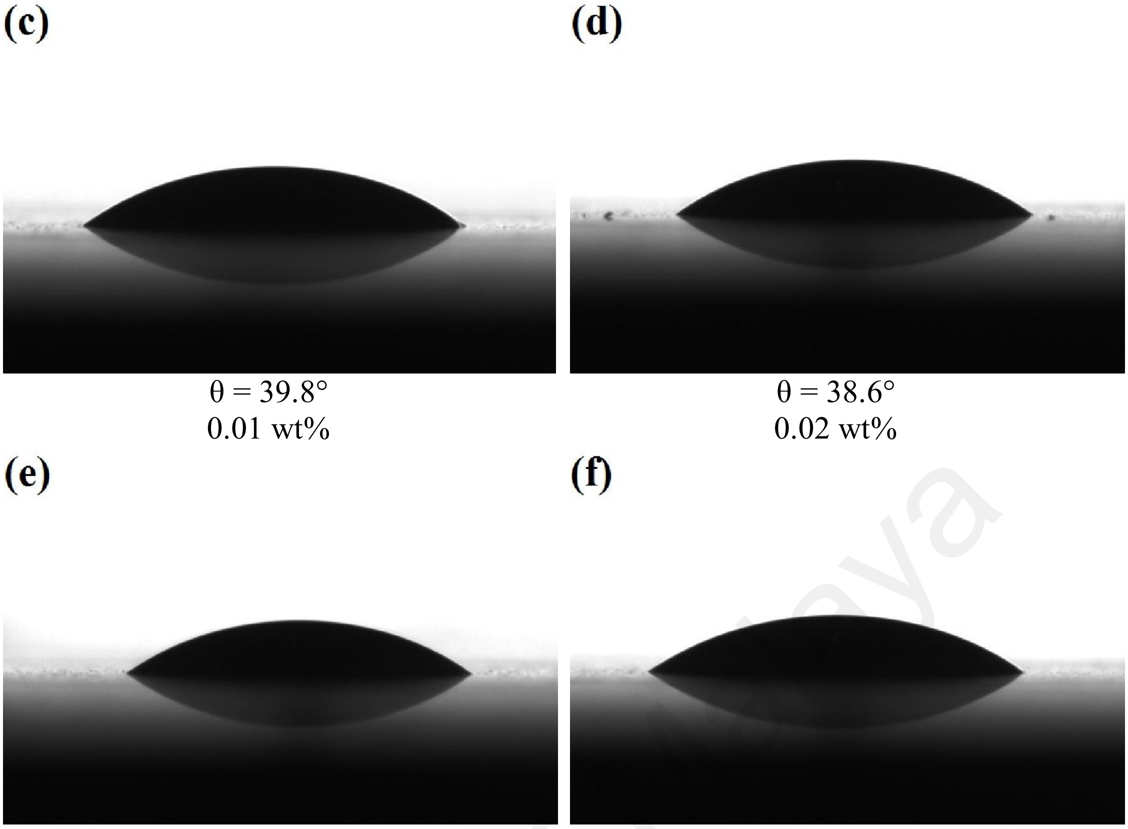

θ = 39.8°
0.01 wt%

θ = 38.6°
0.02 wt%

θ = 37.4°
0.04 wt%

θ = 36.7°
0.06 wt%

Figure 4.32 Contact angle photograph of the base fluid and NDG nanofluid with different concentration

Figure 4.33 shows the contact angle pictures of $1.5\mu L$ of G-rGO nanofluid on a solid surface at 25°C. As is shown, the contact angle of distilled water (DW) on the surface is 82.1° and it was decreased to 80.1°, 74.5°, 72.4° and 71.3° for the G-rGO nanofluid at ϕ=1%, 2%, 3%, and 4% volume fractions, respectively. The contact angles of G-rGO nanofluid decrease compared with base fluid and improves the wettability of nanofluids, which leads to reduction of the contact angle.

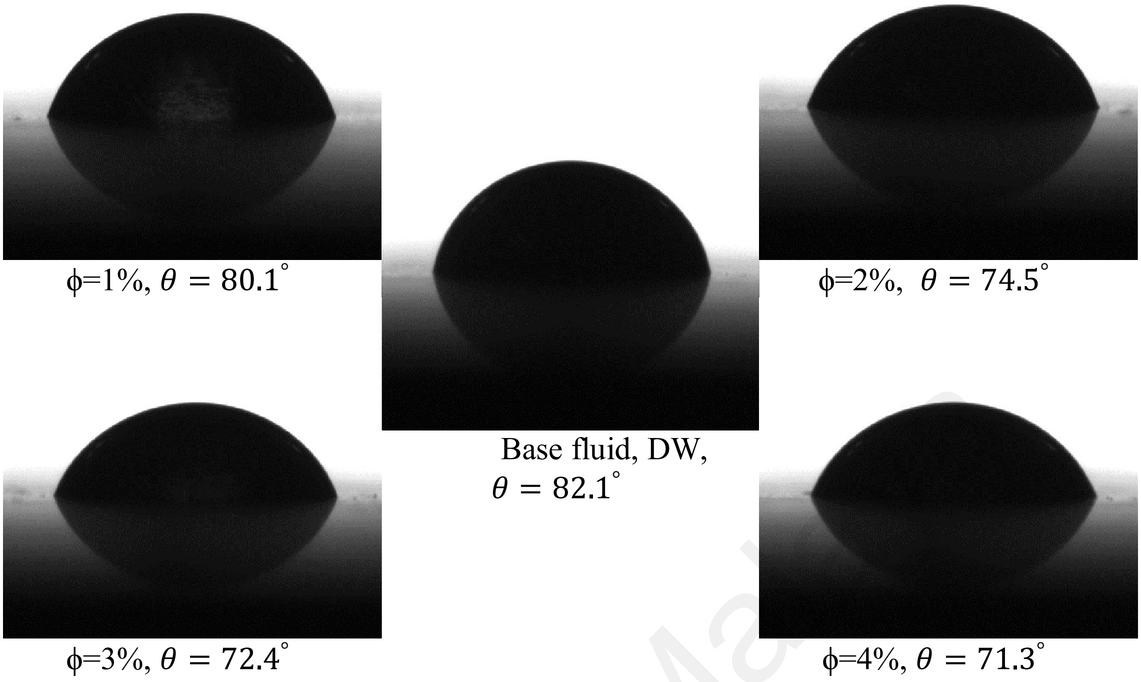

ϕ=1%, $\theta = 80.1^{\circ}$

Base fluid, DW, $\theta = 82.1^{\circ}$

ϕ=2%, $\theta = 74.5^{\circ}$

ϕ=3%, $\theta = 72.4^{\circ}$

ϕ=4%, $\theta = 71.3^{\circ}$

Figure 4.33 Contact angle photographs of the base fluid and G-rGO nanofluid with different volume fractions

4.8 Thermal conductivity

4.8.1 GNPs

The thermal conductivity of the nanofluids with various concentrations of GNPs was measured and results are shown in Figure 4.34 for the temperature ranging from 15 to 40°C .

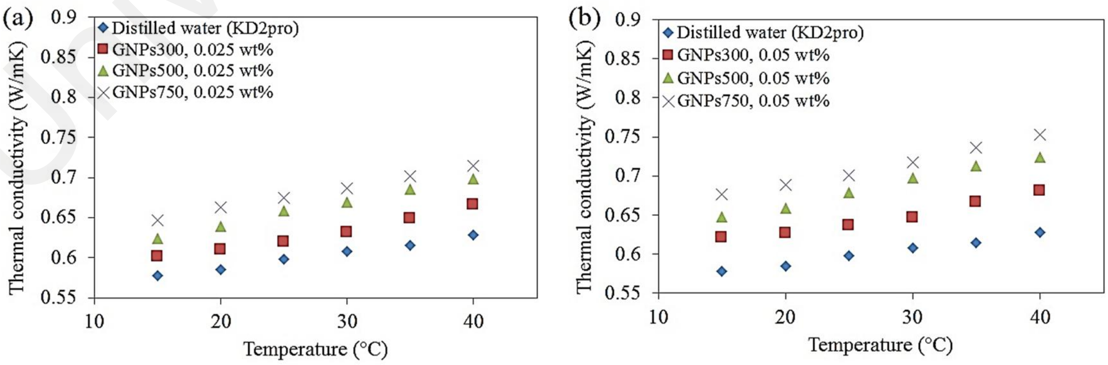

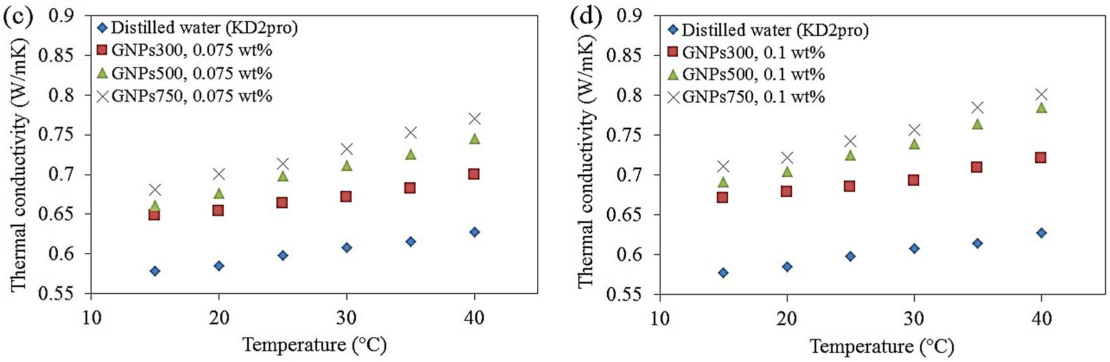

Figure 4.34 Thermal conductivity of GNPs nanofluids by changing of temperature with different GNPs concentration; (A) 0.025wt% (B) 0.05 wt% (C) 0.075 wt% (D) 0.1 wt%

From the results it can be seen that the higher thermal conductivity was belong to the GNPs with higher specific surface area as well as for higher particle concentrations. The standard thermal conductivity models for composites, such as the Maxwell model and the Hamilton-Crosser (HC) model and the weakness of these models in predicting the thermal conductivities of nanofluids, led to the proposition of various new mechanisms. Brownian motion of nano particles were indicated by several authors (Kole et al., 2013; W Yu et al., 2003) as a prime factor for the observed enhancement. However, it is now widely accepted that the existence of nano layer at the solid-liquid interface and nano particle aggregation may constitute major contributing mechanisms for thermal conductivity enhancement in nanofluids. The liquid molecules close to particle surfaces are known to form layered structures and behave much like a solid. Figure 4.35 shows the thermal conductivity ratio for different GNPs at different specific surface areas for temperatures between 15 and 40°C. The linear dependence of thermal conductivity enhancement on temperature was obtained (Figure 4.34). From the Figure 4.35, a similar trend of thermal conductivity enhancement is observed by increasing concentration and temperature. The enhancement in thermal conductivity for GNPs 300 was between 3.98% and 14.81%, for GNPs500 was between 7.96% and 25% and for GNPs750 was between 11.94% and 27.67%. It was also observed that for the same weight percentage and temperature, GNPs 750 based nanofluid presents higher thermal conductivity values than those of the other base fluids with GNPs had lower specific surface area.

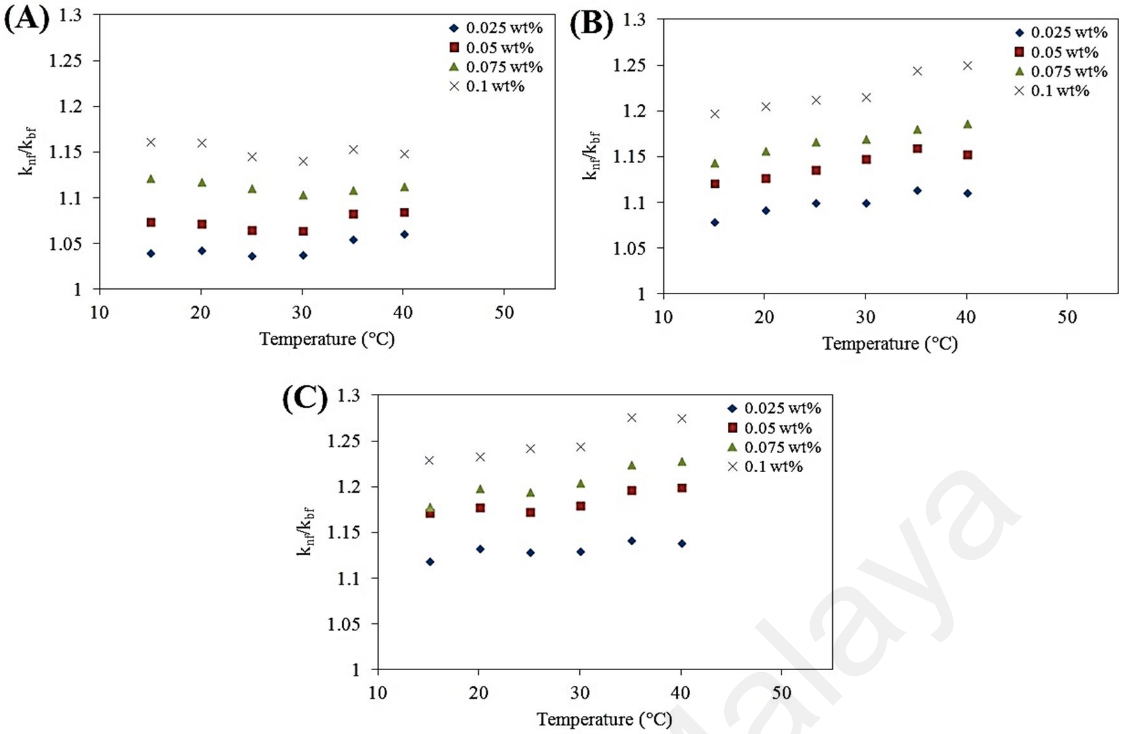

Figure 4.35 Thermal conductivity ratios of GNPs with different concentrations and specific surface areas. (A) GNPs 300, (B) GNPs500, (C) GNPs750

It is clear that, after the nanoparticle materials as well as the base fluid are assigned, the effective thermal conductivity of the nanofluid was relied on concentration (φ) and temperature. Consequently, it is apparent that the thermal conductivity and dimension (thickness) of interfacial layer have important effects on the enhanced thermal conductivity of nanofluids. The typical theoretical models that have been developed for thermal conductivity of nanoparticles suspended fluids are considered only thermal conductivities of base fluid and particles and volume fraction of particles while particle size, shape, the distribution and the motion of dispersed particles are having significant impacts on thermal conductivity enhancement. Therefore, the experimental results could not be compared with the correlated values of theoretical models. Scientists from different organizations throughout the world accomplished a benchmark research on the thermal conductivity of nanofluids and the results indicated that the experimental data were in good agreement by using Nan's model. According to Nan's model, the thermal conductivity of the nanofluid can be calculated as below:

$$k_{nf} == k_{bf}\frac{3+\phi[2\beta_{11}(1-L_{11})+\beta_{33}(1-L_{33})]}{3-\phi(2\beta_{11}L_{11}+\beta_{33}L_{33})} \quad (4.1)$$

Where L_{ii} and ϕ are the geometrical factor and the volume fraction of particles, respectively. β_{ii} is defined as:

$$\beta_{ii} = \frac{k_p - k_{bf}}{k_{bf} + L_{ii}(k_p - k_{bf})} \quad (4.2)$$

Where k_p is the thermal conductivity of the particles. For GNPs, the aspect ratio is very high, so $L_{11} = 0$ and $L_{33} = 1$. It should be mentioned that the thermal conductivity determined here by Nan's model has taken the matrix additive interface contact resistance into consideration. In Equation (4.2) the predicted thermal conductivity of composite is sensitive to the small change of nanoparticles thermal conductivity. Additionally, theoretical calculation established that the thermal conductivity of graphene can be influenced by the dimensions, the edge roughness and the defect density. Figure 4.36 shows the thermal conductivity enhancement of the GNPs nanofluids as a function of loading at constant tempreture of 30°C. From the results it can be clearly seen that the experimental results can be validated by Nan's model.

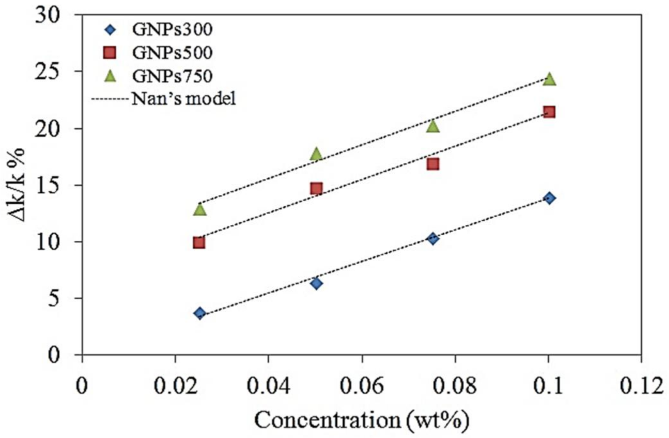

Figure 4.36.Thermal conductivity enhancement based on the Nan's model and experimental results at 30°C

Furthermore, the comparison between carbon based nanofluids in most recent works were presented in Table 4.5.

Table 4.5.Thermal conductivity enhancement of recently used nanofluids from literature

Base Fluid	Concentration (wt%)	Dispersant + Base fluid	Maximum enhancement (%)	Reference
MWNTs	0.60	DW	34	(MJ Assael et al., 2005)
Graphite	0.5	DW + PVP	23	(Zhu et al., 2010)
GO	12	EG	61	(Wei Yu et al., 2010)
GNP300	0.1	DW	14.8	Present study
GNPs500	0.1	DW	25	Present study
GNPs750	0.1	DW	27.6	Present study

Based on the results within Table 4.5; it can outstandingly be evident that the GNPs nanofluid provides significant thermal conductivity enhancement compared to other works while they had higher concentrations of nano particles. From these results it can be seen that use of low concentrations of GNPs can achieve acceptable thermal conductivity enhancement at the medium temperature applications including solar collectors and heat exchanger systems.

4.8.2 NDG

A significant increase in thermal conductivity is found all dispersion treatment as shown in Figure 4.37. The thermal conductivity of the nanofluid always increased with the sonication time. The ultrasonication (probe) is a very powerful tool in engineering particle shape and size. By applying ultrasonication, the particle size can be controlled and the average size of NDG can be reduced upto 412.4nm, with more regular and uniform shapes. The results show a large increase in the thermal conductivity at 60min sonication (probe) time and thermal conductivity of NDG nanofluids is dependent on particle size, whereas further mechanistic understanding is required.

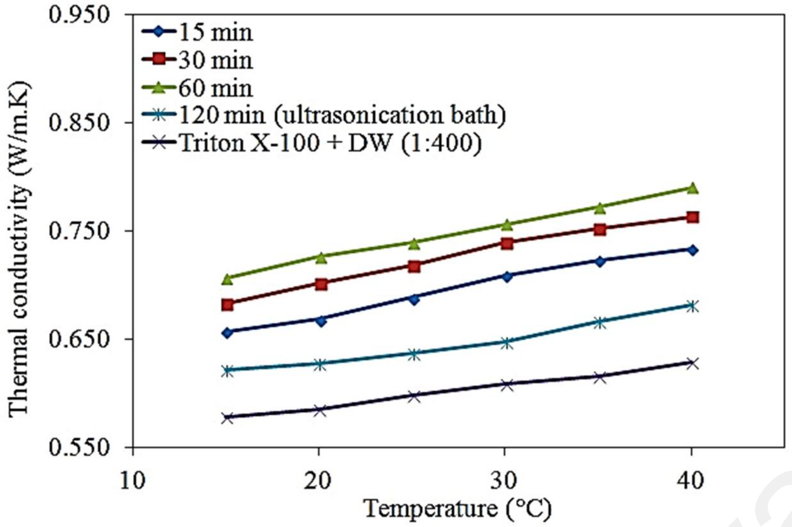

Figure 4.37 Thermal conductivity of nanofluid at varying temperatures for different sonication time (same amount of NDG+Triton X-100)

The thermal conductivity of the nanofluids with various concentrations of NDG at 1 hour sonication time was measured and results are shown in Figure 4.38 for the temperature ranging from 15 to 40°C. The results show the effect of concentration on the thermal conductivity enhancements of NDG nanofluids.

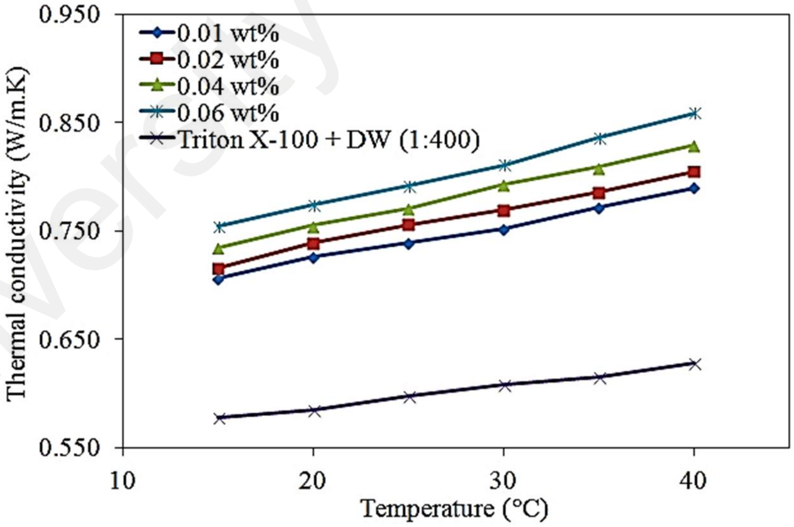

Figure 4.38 Thermal conductivity of nanofluid prepared with 60min ultrasonication time at varying temperatures for different concentrations

Figure 4.39 shows the thermal conductivity ratio for different concentrations of NDG for the temperature range of 15°C to 40°C. The results indicate that the nanoparticle, temperature and concentration have significant impact on the thermal conductivity of nanofluids. The enhancement in thermal conductivity for NDG was between 22.15% and

36.78%. There is considerable enhancement of such a small weight percentage due to the effects of nitrogen atom concentration. The principal mechanism of thermal conductivity enhancement can be considered as the stochastic motion of the nanoparticles. The Brownian motion is dependent on nanoparticle concentration and fluid temperature. At low temperature this motion was less significant giving the characteristics of normal slurries which rapidly changed at elevated temperature bringing more effect in the conducting behavior of the fluid.

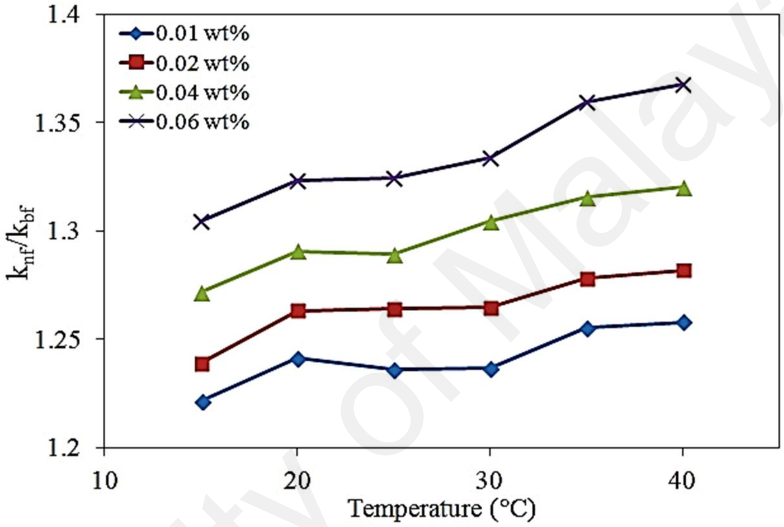

Figure 4.39 Thermal conductivity ratio at different concentrations

There are several standard thermal conductivity models for composites, the Hamilton-Crosser (HC) model and Maxwell model and the weakness of these models in predicting the thermal conductivities of nanofluids, led to the proposition of various new mechanisms. As dispersions of solid particles in a continuous liquid matrix, nanofluids are expected to have a high thermal conductivity that obeys the effective medium theory developed by Maxwell. Maxwell's model for well dispersed particles culminates in a simple equation giving the ratio of the nanofluid thermal conductivity k_{nf} to the thermal conductivity of the based fluid k_{bf} as illustrated in Equation (4.3) (Mohammad Mehrali, et al., 2014a):

$$\frac{k_{nf}}{k_{bf}} = \frac{k_p + 2k_{bf} + 2\phi(k_p - k_{bf})}{k_p + 2k_{bf} - \phi(k_p - k_{bf})} \tag{4.3}$$

Figure 4.40 shows the thermal conductivity enhancement of NDG nanofluid and thermal conductivity enhancement predicted by Maxwell's model, (k_p=150 W/m.K) (P. Yang et al., 2013).

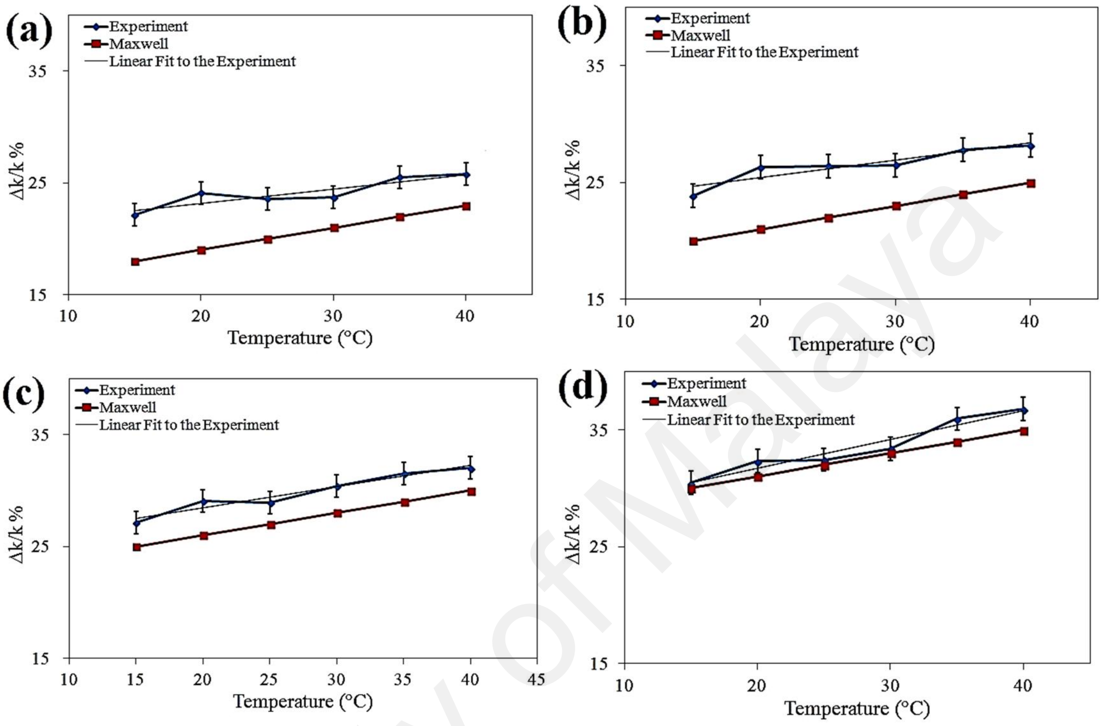

Figure 4.40 Comparison of experimental results and theoretical model on thermal conductivity enhancement: (a) 0.01wt%, (b) 0.02wt%, (c) 0.04wt%, (d) 0.06wt%

It is noticeable that, once the nanoparticle material and the base fluid are assigned, the effective thermal conductivity of the nanofluid was dependent on temperature and concentration(φ). Moreover, $\Delta k/k\%$ depends marginally on the solid–liquid combination which, may be due to the fact that most experimental data used to derive Equation (3) and it is related to the nanofluids with suspended NDG nanoparticles. Consequently, it is apparent that the thermal conductivity and thickness of interfacial layer have important effects on the enhanced thermal conductivity of nanofluids. According to Nan's model, it is difficult to determine the thermal conductivity of nanoparticles from nanoparticle-based nanofluid thermal conductivity. Figure 4.41 shows the thermal conductivity enhancement of the NDG nanofluids as a function of loading at 30°C.

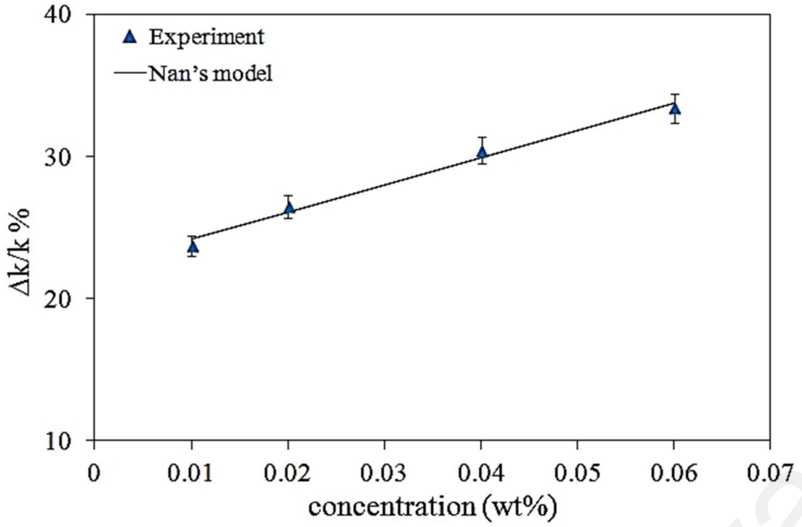

Figure 4.41 Thermal conductivity enhancement based on the Nan's model and experimental results at 30℃

4.8.3 G-rGO

Thermal conductivity of G-rGO nanofluids as a function of volume fractions and temperature was measured with a transient hot wire (THW) method, which is one of the common methods for measuring thermal conductivity of fluids. A notable enhancement in thermal conductivity was found in all concentrations, as shown in Figure 4.42.

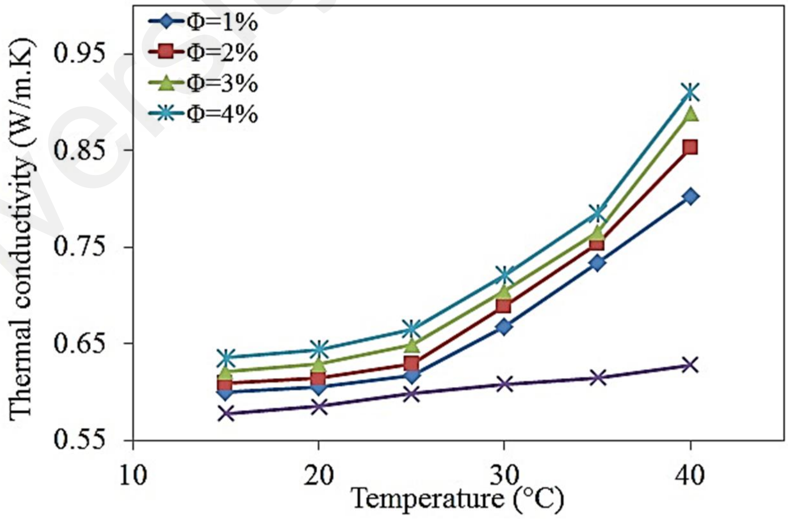

Figure 4.42 Thermal conductivity of G-rGO nanofluid at varying temperatures for different volume fractions

Figure 4.43 shows the thermal conductivity ratio for different volume fractions of G-rGO for the temperature range of 15℃ to 40℃. The results indicate that the nanoparticle, temperature and concentration have significant impact on the thermal conductivity of nanofluids. The enhancement in thermal conductivity for G-rGO was between 3.80% to 45.06%. An enhancement in thermal conductivity of G-rGO nanofluid has been observed nearly 3.80% at 15°C for low volume fraction of 1% and at 40°C, it was 27.70%. It was observed that the thermal conductivity increases with increasing G-rGO concentration and temperature. For the 4% volume fraction, the enhancement in thermal conductivity is 9.86% and 45.06% at 15°C and 40°C, respectively and the behaviour is the same as that reported by Aravind et al. (2011b). The principal mechanism of thermal conductivity enhancement can be considered as the stochastic motion of the nanoparticles. At low temperature, this motion has less effect on the characteristics of normal slurries, which rapidly changed at elevated temperature bringing more effect in the conducting behavior of the fluid. In addition, this preparation method of the G-rGO nanofluid generated many defects over the surface of the graphene oxide, and it is a green and simple process, which does not involve the help of the surfactants. Due to this reasons, significant enhancement in thermal conductivity was observed in all concentrations.

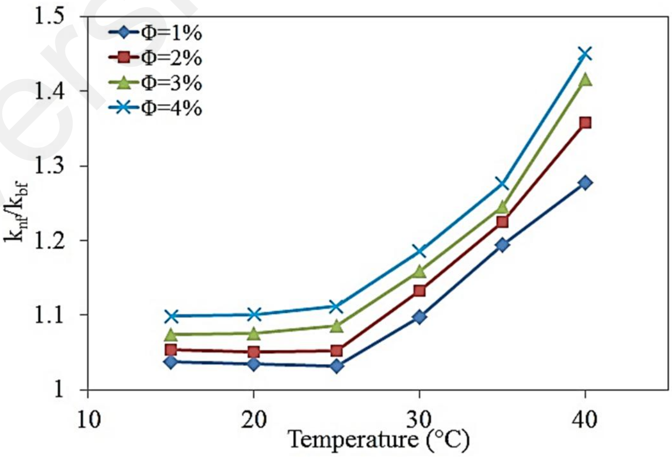

Figure 4.43 Thermal conductivity ratio at different volume fraction

Recently, Chu et al. (2013) has introduced new theoretical model for thermal conductivity of graphene-based nanofluids, and it expressed as:

$$\frac{k_{nf}}{k_{bf}} = \frac{2 + 2\eta^2\phi/[k_0\left(\frac{2R_k}{L} + 13.4\sqrt{t}\right)]}{3 - \eta\phi} \quad (4.4)$$

This is a general formulation for the graphene based and contains all the effect of length (L), thickness (t) and interfacial thermal resistance (R_k) and flatness of material (η) like graphene sheets. The parameters, which is used to predict the thermal conductivity of G-rGO are L=3 µm, t=1.6 nm, η=0.80, and $R_k = 2.4 \times 10^{-8}$ m^{2}K/W. At it is shown in Figure 4.44, the numerical results are agreed well with the experimental results. This model predicts a relatively linear increase of the thermal conductivity with the concentration and it can be used for the estimation of the G-rGO nanofluid thermal conductivity. The significant enhancement in thermal conductivity of the G-rGO nanofluids can be ascribed by large aspect ratio and reduction under a surfactant-free condition.

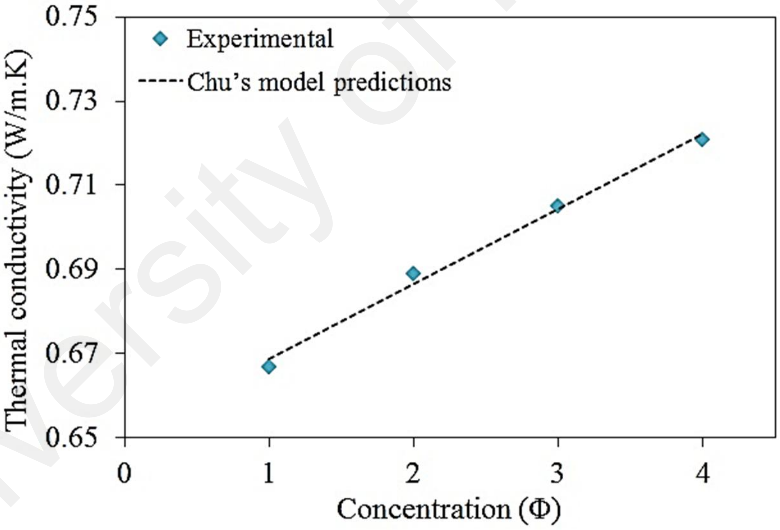

Figure 4.44 Numerical thermal conductivity as a function of volume fraction compared with the experimental data at 30°C.

4.9 Specific heat capacity measurements

The specific heat of nanofluids has not been received much attention. While research studies on prediction and measurement of the thermal conductivity and other heat transfer properties of nanofluids have been performed extensively, the accurate determination of specific heat is essential in analyzing the thermal performance of nanofluids. For example, it is necessary for the measurements of the thermal diffusivity and the thermal conductivity in force and natural convective heat transfer-based applications. Determination of specific heat capacity is one of the important parameters for describing the benefit of using nanofluids in the practical application in thermal management systems. Table 4.6 shows the specific heat capacity of GNPs at different concentration and at 35°C.

Table 4.6 Specific heat capacity of GNPs Nanofluid

Concentration (wt%)	c_p (J/g.K)
0.025	4.525
0.05	4.940
0.075	5.131
0.1	5.284

In the literature, little reliable data on specific heat capacities of distilled water and Trition X-100 are available. DSC results on distilled water were in agreement with handbook data and the results are obtained within 2% accuracy. Figure 4.45 shows the average specific heat capacities of NDG nanofluid between 35°C and 75°C.

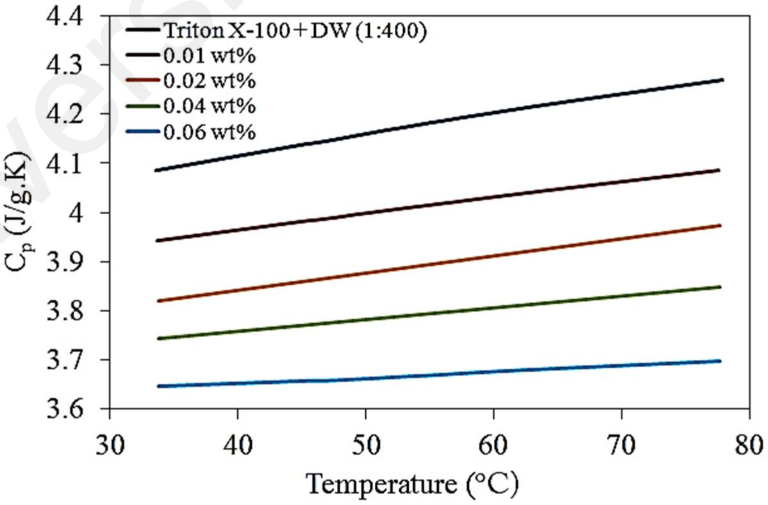

Figure 4.45 Specific heat capacities of NDG as function of the temperatures

The relation between temperature and specific heat capacity is linear for each concentration. Regression coefficient and error are presented in Table 4.7.

$$c_p = a + b\,.T \tag{4.5}$$

Moreover, assuming that the base fluid and the nanoparticles are in thermal equilibrium and the experimental specific heat capacities of NDG nanofluid are correctly justified on the basis of the First Law of Thermodynamics. In a process in which heat is added to the nanofluid, the energy conservation implies that

$$c_{p,nf} = \frac{\phi.\rho_{np}.c_{p,np} + (1-\phi).\rho_{bf}.c_{p,bf}}{\phi.\rho_{np} + (1-\phi).\rho_{bf}} \tag{4.6}$$

Where $c_{p,nf}$, $c_{p,np}$ and $c_{p,bf}$ are the specific heat capacities of nanofluid, nanoparticle and base fluid, respectively, ϕ is the volume fraction of nanoparticles and ρ_{nf} , ρ_{np} and ρ_{bf} are the densities of nanofluid, nanoparticles, and base fluid, respectively.

Table 4.7 Coefficients of Equation (4.5), root-mean-square deviations and standard errors

Concentration (wt%)	$a \pm \sigma_a$/ ($J.g^{-1}.°C^{-1}$)	10^6 ($b \pm \sigma_b$)/ ($J.g^{-1}. °C^{-2}$)	σ/ ($J.g^{-1}. °C^{-1}$)
Water + Triton X-100 (1:400)	3.9489 ± 0.0012	4200 ± 43	0.002
0.01	3.8323 ± 0.0011	3315 ± 34	0.002
0.02	3.7026 ± 0.006	3500 ± 20	0.001
0.04	3.6621 ± 0.0013	2400 ± 37	0.002
0.06	3.6040 ± 0.0014	1221 ± 35	0.002

In this research, the decrease in specific heat of nanofluids may be attributed to the specific heat of the nano additives and the higher thermal conductivity of the nanoparticle. Figure 4.45 shows that the specific heat capacities of nanofluids are significantly less than that of the base fluid and it is decreased with the increase of nanofluids concentrations. The specific heat of the NDG nanofluids containing 0.01wt% varies from 3.9422 to 4.0872 J/g.K as the temperature is increased from 35 to 75℃. Similarly it varies from 3.6477 to 3.6990 J/g.K when the NDG loading is 0.06wt%. Furthermore, the specific heat of 0.01wt% of NDG decreases by approximately 7.4% to 9.4% compared to the loading of 0.06wt%. The measured nanofluid specific heat capacities, show the specific heat of nanofluids at concentrations of 0.01, 0.02, 0.04 and 0.06wt% are about 3.7%, 6.9%, 8.6% and 12%, respectively lower than those of the base fluid (DW+Triton X-100) at 75°C.

Figure 4.46 shows the average specific heat capacities of G-rGO nanofluid between 35°C and 70°C.

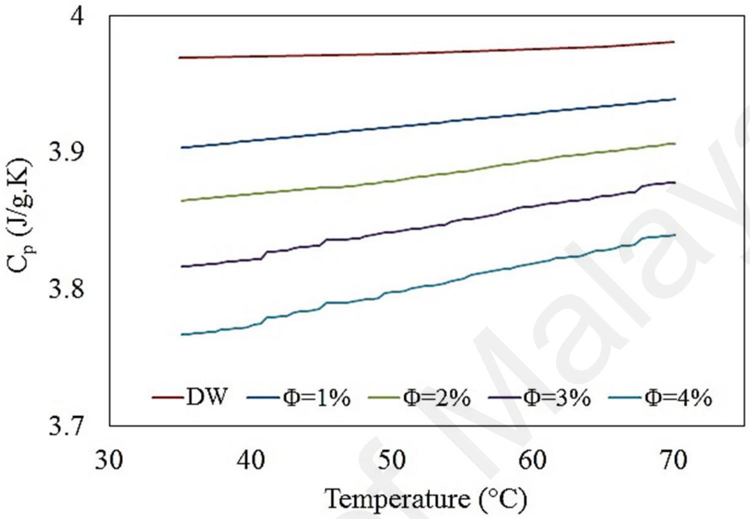

Figure 4.46 Specific heat capacity of G-rGO as a function of the temperatures

As shown in Figure 4.46, the decrease in specific heat capacity of nanofluids depend on the specific heat of the nano-particles and decreased with the increase of nano-particles concentrations. The specific heat of the ϕ=1%, G-rGO nanofluids decreases from 3.9035 to 3.8399 J/g.K as the temperature was increased from 35 to 70°C. Similarly, it decreases from 3.7669 to 3.9389 J/g.K, when the G-rGO loading was 4%. Furthermore, the specific heat of ϕ=1% of G-rGO decreased by 2.5% to 3.4% compared to the loading of ϕ=4%. The measured nanofluid specific heat capacities, show the specific heat of nanofluid with ϕ=1%, 2%, 3%, and 4% was about 10.4%, 18.5%, 25.6% and 35.2%, respectively, lower than the base fluid (DW) at 75°C.

Figure 4.46 shows that the relation between specific heat capacity and temperature are linear for each concentration. It proves that the base fluid and the nanoparticles are in thermal equilibrium and the experimental specific heat capacities of G-rGO nanofluid are correctly justified on the basis of the First Law of Thermodynamics. In the absence of experimental data, two traditional models have been used in the numerical and experimental nanofluid investigations (Zhou et al., 2008).

1. First model: The specific heat of a nanofluid in the mixing theory is expressed as:

$$C_{p,nf} = \phi C_{p,np} + (1-\phi) C_{p,bf} \tag{4.7}$$

where C_p is specific heat and the subscripts nf, np, and bf refer to the nanofluid, base fluid, and nanoparticle, respectively.

2. Second model: This model is based on the statistical and classical mechanism and base fluid and nanoparticles should be in thermal equilibrium.

$$C_{p,nf} = \frac{\phi(\rho C_p)_{np} + (1-\phi)(\rho C_p)_{bf}}{\phi \rho_{np} + (1-\phi)\rho_{bf}} \tag{4.8}$$

where ρ is the density. In this model, the density variations of the base fluid, nanoparticle and nanofluid are involved and has been used as a base formula in many nanofluids investigations.

Table 4.8 presents the coefficients of linear regressions with their standard errors and the root-mean-square deviations of the fits from the Equation (4.5).

Table 4.8 Coefficients of Equation (4.5), root-mean-square deviations and standard errors

Concentration (volume fraction)	$a \pm \sigma_a$ (J/g . °C)	10^{-6} $(b \pm \sigma_b)$ (J/g . °C^2)	σ (J/g . °C)

DW	3.957 ± 0.0024	300 ± 38	0.004
1	3.8681 ± 0.0070	1000 ± 18	0
2	3.8192 ± 0.0086	1200 ± 33	0.009
3	3.7519 ± 0.0034	1800 ± 13	0.003
4	3.6040 ± 0.0026	1221 ± 10	0.003

4.10 Electrical conductivity analysis

Electrical conductivity characteristics of nanofluids are a technological importance and have not been widely studied in comparison to their thermo-physical properties. The electrical conductivity of colloidal suspensions containing nano size particles is nontrivially depends on the electrolyte background, the particle size, the particle loading and the charge of the particle. According to the theory of colloid and surface chemistry, there is an electrical double layer (EDL) around each particle surface. The surface charge of the particles, together with ion cloud that constitutes the EDL, would contribute to the enhancement in conduction through the electrophoretic transactions. Generally, the particles are charges positively when their dielectric constant is larger than that of the base fluid. And in turn, the particles will be negatively charged. The nanoparticle has a Zeta potential relative to the base liquid. When an electrical field is applied, the charged particles will move towards the electrode and thus form the electrophoretic conductivity. That is to say that the nanoparticles are electric current carriers in the fluid. In nanofluid, both the dynamic viscosity and Zeta potential affected by changing the concentration of the nanofluids. For example, the dynamic viscosity will increase with the increase of the volumetric fraction, while the Zeta potential will decrease with the volume fraction because the electric double-layer suppressed at higher volumetric fraction. The electrical conductivity (σ) of water is related to the temperature and increases by 2-3% for each 1°C increase (Typical electrical conductivity of distilled water at 25°C is about $5.5*10^{-6}\mathrm{S/m}$). The electrical conductivity of the nanofluids was obtained at 25°C and the results are presented in Figure 4.47. For nanofluids with GNPs

300, electrical conductivity increases to about 21µS/cm for a mass percentage of 0.1%, while electrical conductivity of water was about 2µS/cm. The enhancement in electrical conductivity was determined by the formulation $[(\sigma - \sigma_0) \times 100]/\sigma_0]$ where "σ_0" refers to electrical conductivity of base fluid and "σ" that of nanofluid. The maximum enhancement of around 950% was observed at 25 °C which was for GNPs 300. From the results it could be seen that the electrical conductivity was enhanced by increasing mass percentage along with decreasing specific surface area.

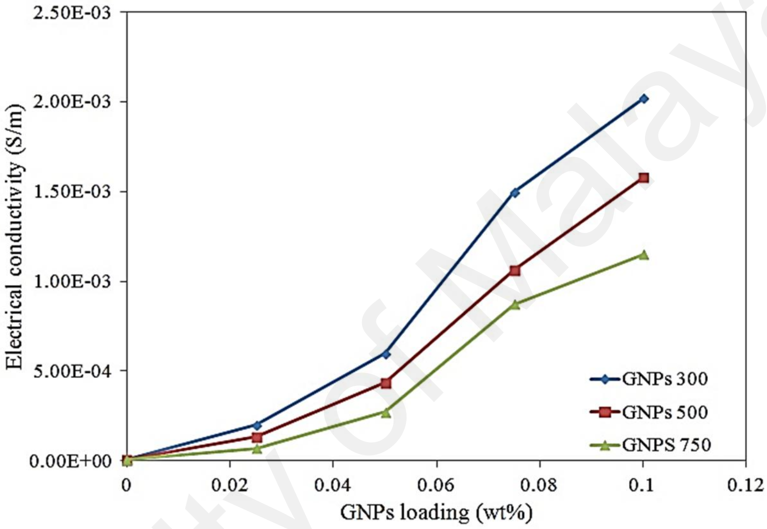

Figure 4.47. Electrical conductivity (σ) of GNPs

The electrical conductivity of the NDG nanofluids determined at different temperatures and different concentration and results are presented in Figure 4.48. The maximum enhancement of electrical conductivities are 308.16%, 667.34%, 1311.56% and 1814.96% at the loading of 0.01wt%, 0.02wt%, 0.04wt% and 0.06wt%, respectively. It was observed that there is no significant effect of fluid temperature on the electrical conductivity in the temperature range of 25–60 °C. This clearly indicates that the enhancement mechanism for electrical conductivity is completely different from that of thermal conductivity in the nanofluids.

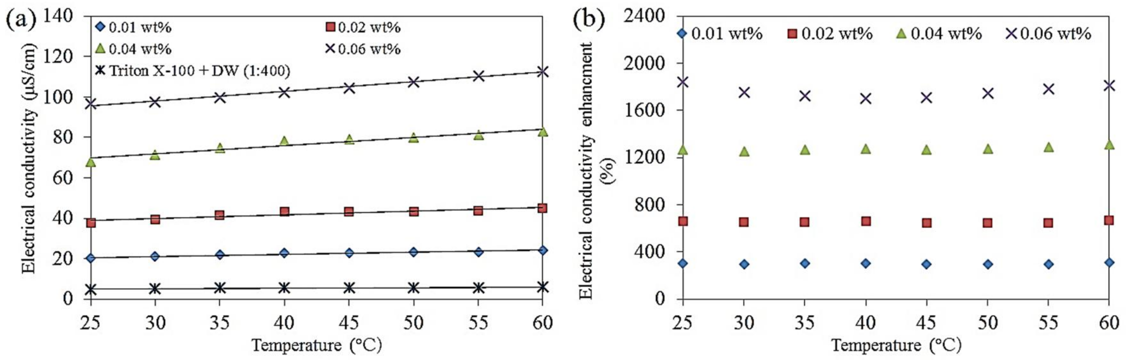

Figure 4.48 (a) Electrical conductivity (σ) of NDG as a function of temperature, (b) Electrical conductivity enhancement of NDG nanofluid at different concentration with 60min ultrasonication time

When NDG nanoparticles suspended in base fluid, electric charges develop on the particles surface (E. Goharshadi et al., 2014). Ions of opposite charge to that of the particle surface are attracted, causing the development of a charged diffuse layer surrounding the particles, which is known as EDL (electrical double layer) (Mohammad Mehrali, et al., 2014b), as shown in Figure 2.15. The ion cloud around the NDG nanoparticles, together with the surface charge of NDG could enhance the electrical conductivity of the NDG nanoflulds. The surface charges are shaped from the nanoparticles polarization, when dispersed inside the polar base fluid (Mohammad Mehrali, et al., 2014b).

The thickness of the EDL (t) often scales as a reciprocal Debye-Huckel parameter which is described by Equation (4.9) (D. Lee, 2007).

$$t = C(\sqrt{\epsilon_0 \epsilon_r R_0 T/2000F^2 I})^{-1} \qquad (4.9)$$

where, ϵ_0 is vacuum permittivity, R_0 is gas constant and F is Faraday constant. The remaining properties such as dielectric constant ϵ_r, temperature T and ionic strength I are all related to the solution.

It shows that the thickness of the interfacial layer has dependence on the base fluid and increase electrophoretic mobility, which consequently increases the electrical conductivity of the nanofluids. The availability of conducting pathways increases, with increase in concentration of nanofluids, thus increasing the overall electrical conductivity. According to the DLVO theory (Mohammad Mehrali, et al., 2014a), raising of the temperature make the EDL thicker, which enhanced the effective thermal conductivity of nanofluids (D. Lee, 2007). In the other hand, the viscosity of the nanofluids is strongly dependent on temperature, and this will increase the electrophoretic mobility, which leads to increase the electrical conductivity of nanofluids.

A simple linear relationship could be developed for the electrical conductivity of NDG at different concentrations as a function of temperature with the purpose of interpolating the experimental results, which were fitted by the Equation (4.10).

$$\sigma = \alpha + \beta \cdot (wt\%) \tag{4.10}$$

The fitted parameters (α and β) with the correlation coefficient, R^2, are presented in Table 4.9. The fitted parameters are functions of temperature and are represented by Equations (4.11) and (4.12).

$$\alpha = \alpha_0 T^n \tag{4.11}$$

$$\beta = \beta_0 T^m \tag{4.12}$$

Table 4.9. The parameters of Equation (4.10)

Temperature (°C)	α ($\mu S/cm$)	β ($\mu S/cm$)	R^2
25	5.7471	1517.8	0.9990
30	6.5345	1558.5	0.9967
35	6.7645	1595.3	0.9945
40	7.1147	1636.7	0.9918
45	7.2295	1674.9	0.9934
50	7.2438	1721.3	0.9955
55	7.6464	1773.7	0.9967
60	7.8515	1802.9	0.9963

The values of the Equations (4.11) and (4.12) are given in Table 4.10, and the correlation coefficients, R^2, for present Equations are 0.9835 and 0.9976, respectively.

Table 4.10. The fitting parameters of Equations (4.11) and (4.12)

α_0	n	β_0	m
2.176	0.3144	788.62	0.2002

The ability of the Equations (4.11-4.13) to predict the electrical conductivity value of NDG nanofluids at different temperatures and concentrations were evaluated by the absolute average deviation (AAD).

$$AAD = \frac{1}{N}\sum_{i=1}^{N} 100 \left|\frac{\sigma_{exp} - \sigma_{cal}}{\sigma_{exp}}\right| \tag{4.13}$$

where, σ_{cal} and σ_{exp} represent the predicted and experimental electrical conductivity values, respectively. The AAD of 12.03% shows that the predicted and experimental values were in a good agreement with each other.

In other hand, the effect of the EDL can be understood by the zeta-potential, which studied in the pH selection of the flotation process. The EDL theory is useful in the explanation of the electrostatic behaviors and the thickness of the EDL. Hence, the electrical conductivity can affect the nanofluid heat transfer properties (Kalteh, et al., 2011). The electrical conductivity of the G-rGO nanofluids were measured at varied temperatures and found to increase linearly with the increase of temperature and concentrations due to the increases in conducting pathways in the solution, as shown in Figure 4.49. The maximum enhancement of electrical conductivities were 84.1%, 90.9%, 95.1% and 96.7% at the ϕ=1%, 2%, 3%, and 4%, respectively. In addition, with enhancement of temperature, EDL thickness decreases that is leading to increase electrical conductivity of the nanofluids.

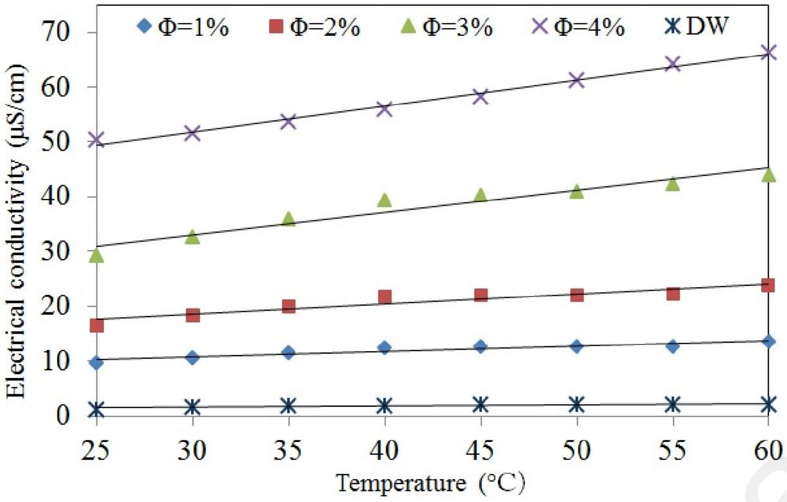

Figure 4.49 Electrical conductivity (σ) of G-rGO as a function of temperature

To understand the electrical conductivity of nanofluids, the experimental values of electrical conductivity of nanofluids as a function of volume fraction could be fitted by the Equation (4.14) (Azizi-Toupkanloo, et al., 2013):

$$\sigma = \gamma + \alpha[1 - \exp(\beta\phi)] \quad (4.14)$$

where, $\alpha, \beta, and\ \gamma$ are the fitting parameter and dependent on the temperature.

$$\alpha = \alpha_0 + b\exp(cT) \quad (4.15)$$

$$\gamma = \gamma_0 + g\exp(hT) \quad (4.16)$$

$$\beta = \beta_0 - eT \quad (4.17)$$

The constant and fitting values of the Equations (4.15, 4.16, and 4.17) for the G-rGO nanofluid are given in Table 4.11.

Table 4.11 The parameters of Equations (4.15, 4.16, and 4.17)

α_0	b	c	γ_0	g	h	β_0	e
39.602	7.1	0.07	-7.5	5.0752	0.02	4.55	0.19

The ability of the Equations (4.14-4.17) to predict the electrical conductivity values of G-rGO nanofluids at different temperatures and volume fractions were evaluated by the absolute average deviation (AAD).

The AAD of 0.80% shows that the predicted and experimental values were in a good agreement with each other.

4.11 Conclusions

In conclusion, there are many variables that must be accounted for when dealing with nanofluid (colloid) experiments. The conceptual and theoretical developments of colloid and surface science lead to a far better understanding of nanofluid properties and behavior. Some properties such as size and stability are easily altered by concentration, pH, and temperature modifications. It is determined that nanofluids can be purchased or made in a variety of ways. Surfactant addition and/or pH control are the standard techniques for the production of stable nanofluids. Ultrasonication is the selected method for breaking up larger agglomerations and homogenizing the fluids. It is also found that care should be taken when using purchased nanofluids, due to the possibility for contaminants and variation from the specified properties. Nevertheless, there are some reliable nanofluids which can be purchased and used after full in-house characterization.

Results show that there exists significant discrepancy in the experimental data. Effect of particle size on the thermal conductivity of nanofluids has not been completely understood yet. It is expected that Brownian motion of nanoparticles results in higher thermal conductivity enhancement with smaller particle size. Particle size distribution of nanoparticles is another important factor and it is suggested that average particle size is not sufficient to characterize a nanofluid due to the nonlinear relations involved between particle size and thermal transport. It is also known that particle shape is effective on the thermal conductivity. An important reason of discrepancy in experimental data is the clustering of nanoparticles. Although there are no universally accepted quantitative values, it is known as the level of clustering effects of the thermal conductivity of nanofluids.

When the application of nanofluids is considered, two important issues are erosion and settling. Before commercialization of nanofluids, possible problems associated with these issues should be investigated and solved. It should also be noted that, increase in viscosity by the use of nanofluids is an important drawback due to the associated increase in pumping power. Therefore, further experimental research is required in that area in order to determine the feasibility of nanofluids.

In order to predict the thermal conductivity of nanofluids, many theoretical models have been developed recently. However, there is still controversy about the underlying mechanisms of the thermal conductivity enhancement of nanofluids. As a result of this, none of the theoretical models are able to completely explain the thermal conductivity enhancement in nanofluids. On the other hand, some researchers report experimental data of thermal conductivity that is consistent with the predictions of the classical models. Consequently, further work is required in theoretical modeling of heat transport in nanofluids as well.

Stability and thermophysical properties of GNP nanofluids have been studied systematically, and the following conclusions could be drawn from the results. The nanofluids of GNPs prepared by ultrasonication were stable for a long period of time. Detailed measurements were carried out to determine the effects of particle mass concentration, specific surface area, and temperature on the thermophysical properties of GNP nanofluid. The rate of increase in thermal conductivity of nanofluids is found to be very significant at higher specific surface areas of GNPs due to factors like stability, homogeneity, and rate of agglomeration. The maximum percentage of enhancement in thermal conductivity was obtained at 27.64% for the loading of 0.1 wt% of GNP 750 at 35°C. The shear rate of nanofluids increased when higher specific surface areas and concentration of GNPs were used. It can be inferred that GNP nanofluids could be a useful and cost-effective material for heat transfer applications along with the development of a facile approach to a large-scale production of aqueous GNP dispersions without any surfactant stabilizers.

Systematic and concurrent approaches were used to prepare a highly stable NDG nanofluid. The effects of different parameters such as concentration, surfactant type and ultrasonication time on thermal conductivity and stability of NDG nanofluids were investigated experimentally. The nanofluids with 60min ultrasonication (probe) and triton X-100 as a surfactant were stable for 6 months. The thermal conductivity of NDG nanofluids were enhanced by using NDG as nano additive while proposed models, which consider volume fraction, interfacial layer and particle size presented good agreement with the experimental results and offered better predictions for the thermal conductivity of NDG nanofluids compared to the existing models such as Maxwell and Nan’s model. Moreover, the maximum enhancement for thermal and electrical conductivities were 26.78% and 1814.96%, respectively. The specific heat capacities of the prepared nanofluids were correctly justified based on the First Law of Thermodynamics. We believe that this novel type of fluids demonstrates outstanding potential for use as innovative heat transfer fluids in medium-temperature systems such as solar collectors.

The present green method for synthesis of graphene via chemical reduction of GO in green tea solution is a merit method with low-cost, non-use of toxic agent, no hazardous waste, high-efficient removal of functional groups in GO and easily scalable. It shows that the GTPs acts as both reducing agent and stabilizer, thus enable the resultant graphene good solubility in both aqueous and a variety of organic solvents. This simple approach should find practical applications in large-scale production of widely soluble graphene. As the GTPs molecules adsorbed on the graphene are nontoxic and biocompatible, therefore bioapplications using the present soluble graphene might be of interesting.

CHAPTER 5

DATA REDUCTION, CALIBRATION EXPERIMENT AND VALIDATION

5.1 Introduction

In this chapter the methodology of determining the heat transfer coefficient and friction factor are described. The experimental procedure and data reduction are discussed with the experimental results being validated for distilled water against the standard equations, such as the Gnielinski, Petukhov, and Dittus–Boelter equations for turbulent flow. Lastly the pressure drop results are compared to well-known turbulent flow equations. The purpose of this validation is to ensure that the experimental setup can take accurate measurements with water before any tests are done on nanofluids.

5.2 Data reduction

5.2.1 Heat transfer coefficient

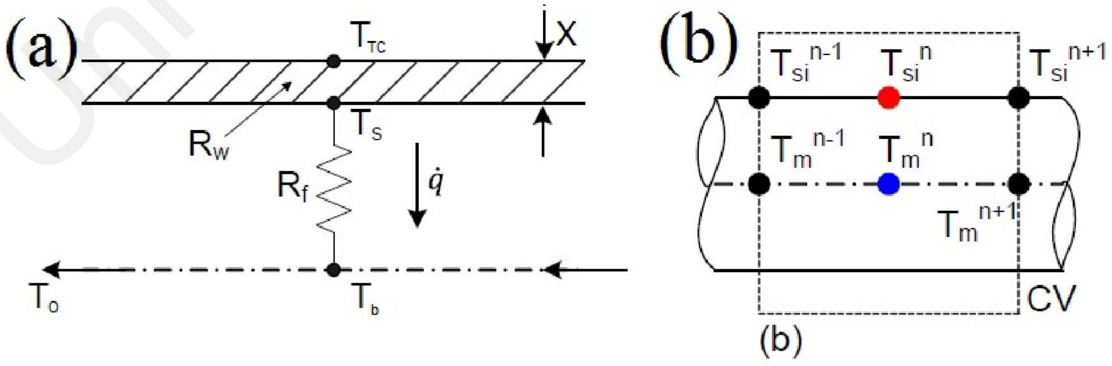

Figure 5.1 Schematic of the (a) resistances inside the test section and (b) control volume around the mean fluid temperature

Shown in Figure 5.1(a) is the schematic of the test section showing the thermal resistances from which the local heat transfer coefficient is calculated by Equation (5.1). All measurement were taken at constant heat flux (8,231 W/m^2, 10,351 W/m^2, and 12,320 W/m^2) and data were taken by steady state conditions at the chosen velocity, surface temperature and bulk temperature. The inlet temperature was fixed at 30℃ with the help of refrigerated bath circulators. The velocity was systematically increased, the heat flux was fixed, ΔT and the local surface temperatures were recorded using the data acquisition for heat transfer study. The local heat transfer coefficient, $h_c(x)$ was calculated from Equation (5.1).

$$h_c = \frac{\dot{q}}{T_w - T_b} \tag{5.1}$$

The terms in this equation were determined as explained below. The energy input to the heater, (the heat flux, $\dot{q}$) was the amount of total heat supplied through the phase angle power controller to the heaters divided by the heated surface area A. the wall temperature T_w was calculated from the temperature measured in the test section by the thermocouples, T_{TC} with a correction to account for the distance of the thermocouple below the heating surface to the inner wall of the pipe in fluid contact. Equation (3.1) represents the T_w and the wall resistance for each of the thermocouples (λ/x) was determined by calibration of the test rig with water as presented in APPENDIX A.

The wall temperature, T_b was a position-weighted of the inlet and outlet temperatures (T_i and T_b respectively). Equation (5.2) represents bulk temperature as a function of inlet and outlet temperatures. This was based on the assumption that the fluid temperature was increased linearly over the heated section and remained constant in the unheated section of the rig. Length

$$T_b = T_i + \frac{Thermocouples\ possition}{heating\ \mathrm{Length}}(T_o - T_i) \tag{5.2}$$

The heat flux, $\dot{q}$, was determined from the electrical energy input, $Q = V.I$, and the inner surface area, $A_s = \pi.D.L$. The electrical energy input remained constant at 400, 500 and 600W throughout the measurements thus resulting in a constant heat flux (8,231 W/m^2, 10,351 W/m^2, and 12,320 W/m^2, respectively). The equation of the heat flux is given below:

$$\dot{q} = \frac{P}{A} = \frac{V \times I}{\pi D L} \tag{5.3}$$

The temperature profile between the thermocouple and the fluid inside the circular pipe and the bulk temperature are calculated using the Wilson plot method (Fernández-Seara et al., 2007; Kazi et al., 2014). The exact and real wall, the fluid temperatures, and the heat flux are measured to calculate the convective heat transfer coefficient (Sadeghinezhad, et al., 2014).

An estimation of the heat flux, heat transfer coefficient, Nusselt number, friction factor, and Reynolds number are presented in Equations (5.4-5.7).

(a) The Nusselt number is defined by Equation (5.4).

$$Nu = \frac{hD}{k} \tag{5.4}$$

(b) The friction factor is defined by Equation (5.5).

$$f = \frac{\Delta P}{\left(\frac{L}{D}\right)\left(\frac{\rho v^2}{2}\right)} \tag{5.5}$$

(c) The Reynolds number is defined by Equation (5.6).

$$Re = \frac{4\dot{m}}{\pi D \mu} \tag{5.6}$$

(d) The Prandtl number is defined by Equation (5.7).

$$Pr = \frac{\mu C_p}{k} \tag{5.7}$$

The temperature dependent thermal conductivity of stainless steel is found from a linear curve fit of data found in the ASM Handbook. The resulting linear fit for the temperature dependent is the following function:

$$k_w(T) = 0.0127\ .\ T + 13.23188 \tag{5.8}$$

5.3 Experimental procedure

An investigation of the heat transfer behavior of the nanofluids was performed by evaluating the Nusselt number and the heat transfer coefficient. The measurements were performed in the bulk velocity range of 0.3 to 1.3 m/s for the distilled water and the nanofluids, which caused the Re number to vary from 5,000 to 22,000. The heat transfer coefficients were calculated based on the measured values for the inlet, outlet, and inner wall temperatures and the flow rates. The pressure drops over the tube was measured, and from these results, the friction factors were calculated. From the insulation surface temperatures, convective and radioactive heat loss to the surroundings were evaluated and found negligible. The heat loss can be calculated by the Equation (5.9) and Figure 5.2 shows the 7.8% heat loss from the test section.

$$Heat\ loss = \dot{q}_{Num} - \dot{q}_{exp} \tag{5.9}$$

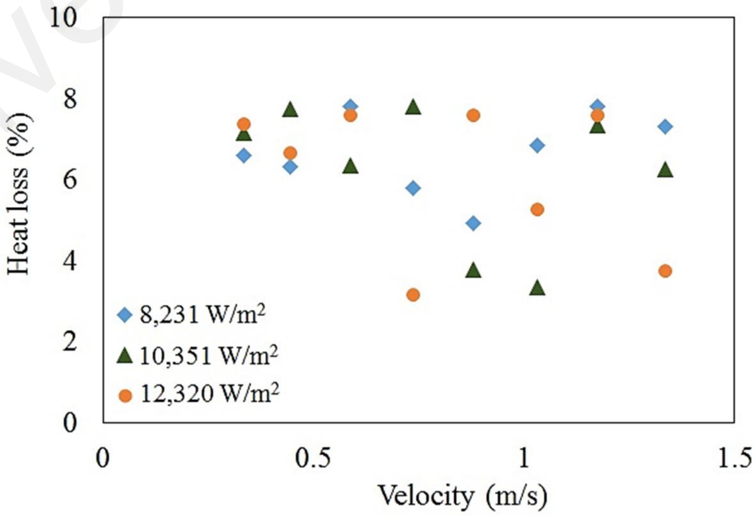

Figure 5.2 Heat loss calculation

While, the influence of external surface heat radiation is considered, the surface temperature of the bare duct shown in Figure 5.3, and the complete heat transfer rate of is calculated by the Equation (5.10-5.11).

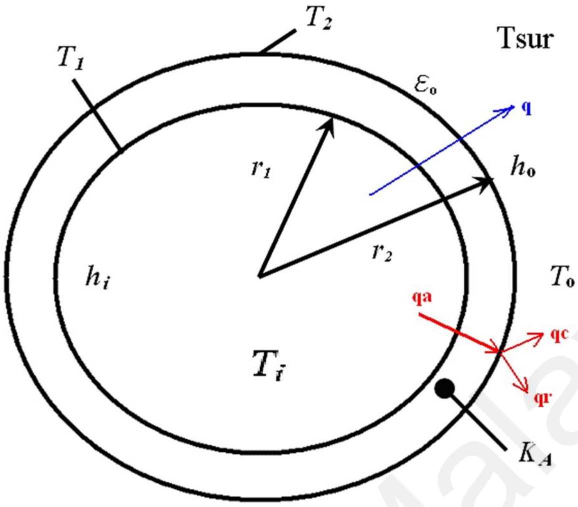

Figure 5.3 A non-insulated tube and its thermal resistance diagram

Since the test section surface area is very small compared with that of surroundings, thus the effect of emissivity of surroundings can be neglected.

$$q_a = q_c + q_r \tag{5.9}$$

$$q_c = \frac{T_2 - T_1}{\frac{1}{h_0 2\pi r_2 L}} \tag{5.10}$$

$$q_r = \sigma\varepsilon(T_2^4 - T_{sur}^4) \tag{5.11}$$

According to Wong et al. (2011), the convective heat coefficient ratio percentage between radiation and convection is defined as Equation (5.12). If the value of $HR <$ 10%, the influence of heat radiation can be neglected. Figure 5.4 shows the insulation temperature (T_2) and ambient temperature versus of fluid velocity at different heat flux for the water run.

$$HR = \frac{q_r}{q_c} \times 100 \tag{5.12}$$

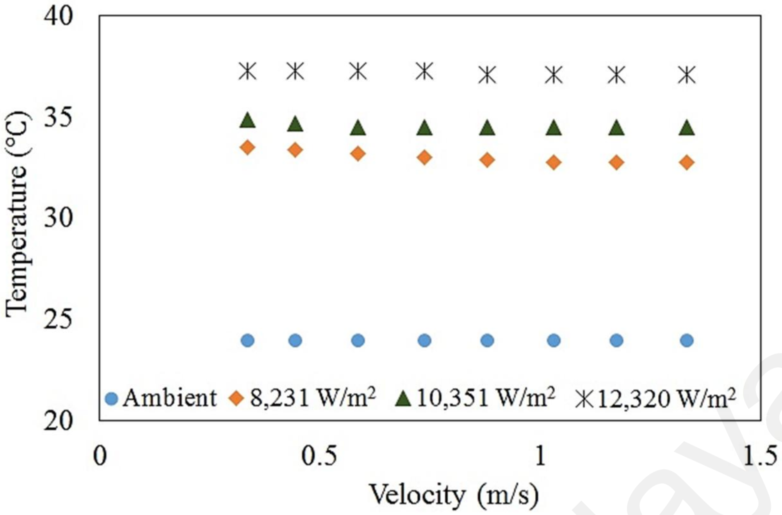

Figure 5.4 Outer insulation and surrounding temperature at different velocity for the water run

In order to demonstrate the main differences between the heat transfer characteristics of situations with considering heat radiation, the detail data of an insulated is listed in Table 5.1.

Table 5.1 insulation details

Insolation thickness (t)	Insulation thermal conductivity (k_s)	Heat transfer coefficient for the outside of insulation (h_{sur})	Emissivity of the insulation (ε)
15mm	0.038W/m.K	10W/m^2.K	0.8

From the practical numerical results of this study, it found that the heat radiation could be neglected due to the HR=5.8%.

Comparisons of the Nusselt numbers or the heat transfer coefficients at an equal Reynolds number is unreliable and is uninteresting from a practical perspective (W Yu et al., 2010). The comparison of nanofluids at the same Reynolds number is common in the literature for nanofluid fields (Bitaraf Haghighi, et al., 2012; Davarnejad et al., 2013; Rea et al., 2009; Sadeghinezhad, et al., 2014). Based on many literatures, comparing the heat transfer at the same flow rates (pumping power) is considered a more appropriate method in a nanofluids study (Bitaraf Haghighi, et al., 2012; Haghighi et al., 2014; Kazi, et al., 2014). Additionally, comparing the heat transfer coefficients for two different fluids at the same Reynolds number requires a higher flow rate (pumping power) for the fluid and a higher viscosity. Hence, the higher heat transfer at same Re number is not only because of the nanofluids performance, but might be due to the higher flow rate of nanofluids like viscosity effect (for measuring at same Re number) (Bitaraf Haghighi, et al., 2012). Due to these reasons, it might be better to choose constant velocity instead of constant Re number (Sadeghinezhad, et al., 2014).

5.4 Validation test for distilled water

To validate the reliability of the experimental setup for calculating the Nusselt number and the convective heat transfer coefficient and for providing a baseline to compare the GNP nanofluid data, tests were initially conducted for distilled water (DW). The experimental results for DW at constant heat flux conditions were compared with the results from the standard equations, such as the Gnielinski, Petukhov, and Dittus–Boelter equations for turbulent flow (Kayhani et al., 2012).

The Gnielinski equation for turbulent flow is given in Equation (5.13)

$$Nu = \frac{\left(\frac{f}{8}\right)(Re - 1000)Pr}{1 + 12.7\left(\frac{f}{8}\right)^{0.5}(Pr^{2/3} - 1)} \tag{5.13}$$

which is applied in the range of $0.5<Pr<2000$ and $3000<Re<5\times10^6$.

The friction factor for a fully developed turbulent flow depends on the Re number and is calculated by the Colebrook equation, given in Equation (5.14).

$$\frac{1}{\sqrt{f}} = -2.0\log\left(\frac{\varepsilon/D}{3.7} + \frac{2.51}{Re\sqrt{f}}\right) \tag{5.14}$$

The Dittus–Boelter equation for turbulent flow is given in Equation (5.15)

$$Nu = 0.023Re^{0.8}Pr^{0.4} \tag{5.15}$$

which is applied in the range of $Re>10^4$, $0.6<Pr<200$.

The Petukhov equation for turbulent flow is given in Equation (5.16)

$$Nu = \frac{\left(\frac{f}{8}\right) RePr}{1.07 + 12.7\left(\frac{f}{8}\right)^{0.5} \left(Pr^{2/3} - 1\right)} \tag{5.16}$$

which is applied in the range of 0.5<Pr<2000 and 3000<Re<5×10^6.

Figure 5.5 shows a comparison between the experimentally average Nusselt number and the data from the above-mentioned equations (Equations (5.13-5.16)). The experimental data and classical correlations agree well. Data from the Petukhov equation and the experimental Nusselt number for distilled water are better than the data from the other equations and validate the accuracy of the experimental setup with an error rate of less than 6%. Based on the literature (Yunus, 2003), at lower Re number the Gnielinski equation is more accurate and at higher Re number Petukhov equation is more accurate and this is find in the reliability test of the experimental setup.

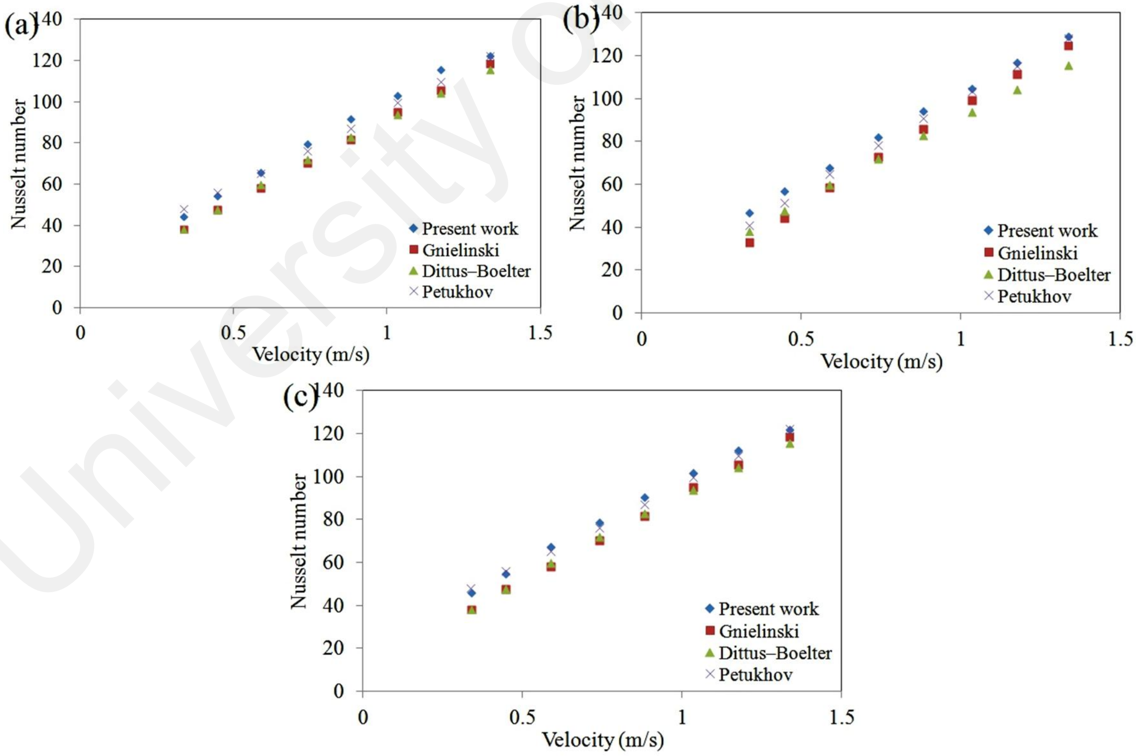

Figure 5.5 Measured average Nusselt number and the prediction correlations for distilled water versus the velocity at a different heat flux; (a) 8,231 W/m^2, (b) 10,351 W/m^2, (c) 12,320 W/m^2

The data from the experimental friction factor are derived from the measurements of the pressure drop along the length of the test section. To verify the friction factor data, the experimental results for DW are validated by the Blasius equation (Chandra Sekhara Reddy et al., 2014) and the Power law (Kazi, et al., 2014).

The Blasius Equation (5.17) is the most simple equation for solving the Darcy friction factor. Because the Blasius equation has no term for pipe roughness, it is valid only to smooth pipes. However, the Blasius equation is sometimes used in rough pipes because of its simplicity. The Blasius equation is valid up to the Reynolds number 10^5.

$$f = \frac{0.316}{Re^{0.25}} \tag{5.17}$$

Figure 5.6 shows the validation of the friction loss data from the experimental investigation, and the above-mentioned equations have an error rate of less than 10%.

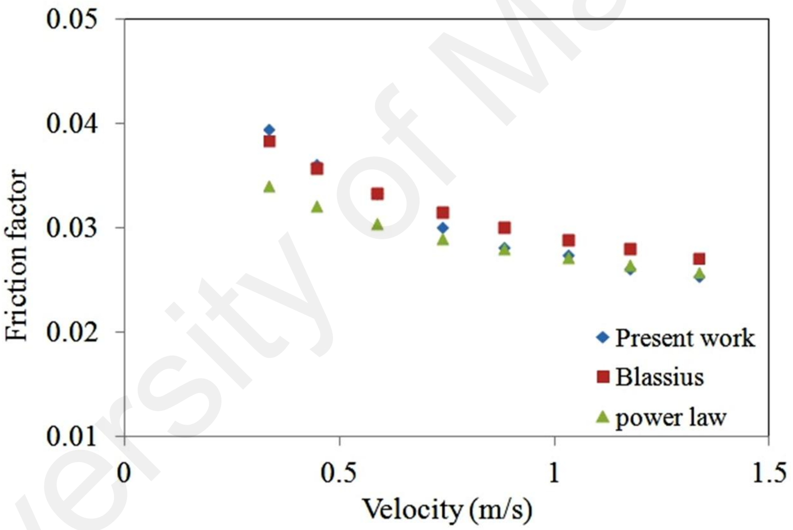

Figure 5.6 Frictional head loss as a function of the velocity for distilled water

5.5 Uncertainty analysis of the test results

The uncertainty analysis of the measured data along with that of the relevant parameters obtained from the data reduction process is presented in Table 5.2 and is estimated based on the error propagation method (Kumaresan et al., 2013; Taylor, 1997).

Table 5.2 Uncertainty ranges.

Variable name	Uncertainty range
Nu, avg	±6%
Nu, Local	±8%
h, avg	±6%
h, local	±9%
f	±10%

The full uncertainty analysis could be found in APPENDIX B.

5.6 Data reproducibility

In the pipe flow studies for DW as the base fluids for data reproducibility. Figure 5.7 represents heat transfer coefficient as a function of velocity for two runs of DW at the bulk temperature of 30°C. It is observed that the data reproduced well, test rig was highly accurate and remains within < 1% error.

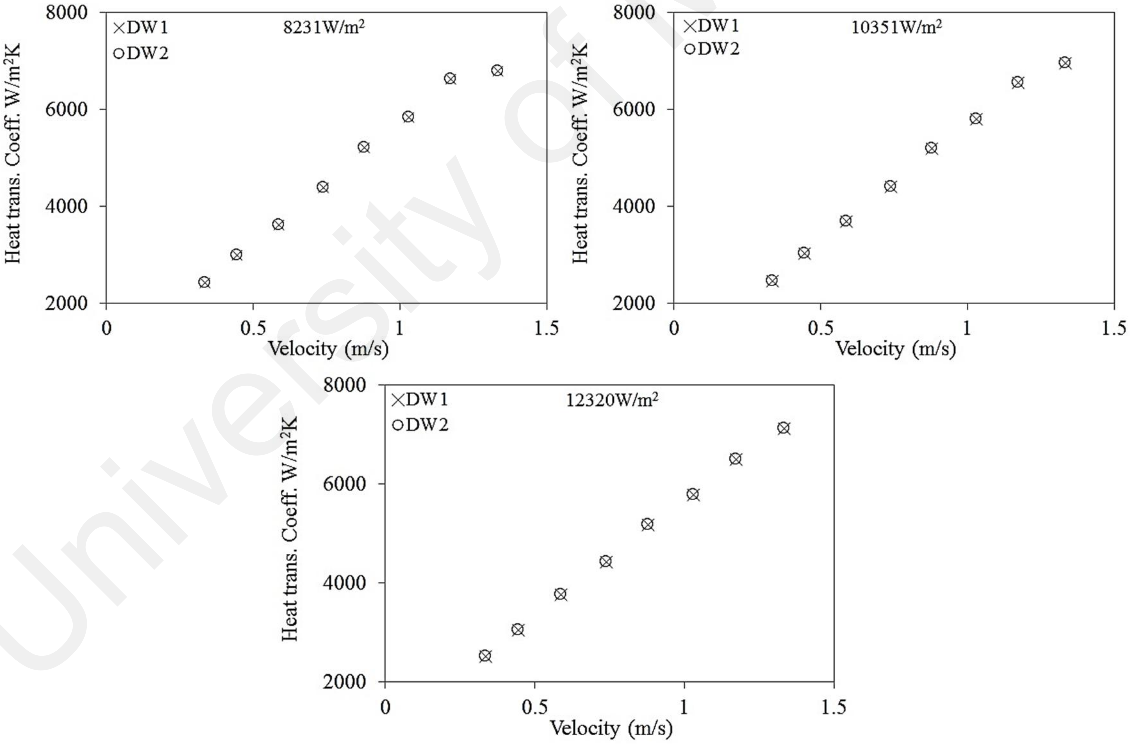

Figure 5.7 Heat transfer coefficient as a function of velocity for two different water runs for three different heat fluxes.

Similarly, the frictional pressure drop ($\Delta P/L$) data for two runs of DW at bulk temperature 30°C are presented in Figure 5.8. The reproducibility is good and remains within < 1% error.

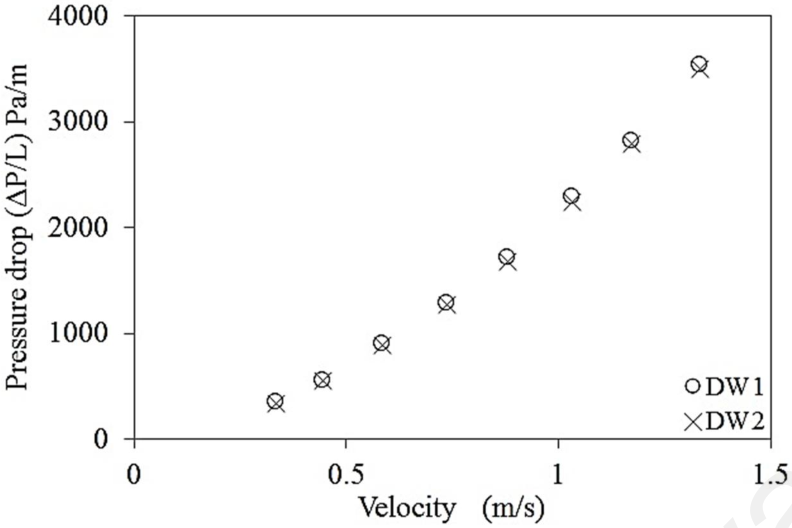

Figure 5.8 Frictional head loss as a function of velocity for two different DW runs.

CHAPTER 6

HEAT TRANSFER AND FRICTION FACTOR

6.1 Convective heat transfer to GNPs nanofluids

Forced convective heat transfer is preferred and used in heat transfer applications because of its controllability and applicability. To perform the tests on the heat transfer to nanofluids, a series of experiment were conducted with GNPs nanofluids at different concentrations and heat fluxes.

6.1.1 Effect of heat flux

Figure 6.1 shows the variations of the Nusselt number (Nu) and convective heat transfer coefficient as well as the variation in the flow rate at different heat fluxes. Figure 6.2 shows the Nusselt number and the convective heat transfer coefficient at different heat fluxes for the 0.1 wt% GNP500 nanofluids. The convective heat transfer coefficient was increased up to 131%, 146%, and 160% for the heat fluxes of 8,231, 10,351, and 12,320 W/m^2, respectively, at a weight percentage of 0.1 for the GNP 500 nanofluids. Additionally, the Nusselt number (Nu) was increased up to 75%, 79%, and 83% for the heat fluxes of 8,231, 10,351, and 12,320 W/m^2, respectively. The convective heat transfer coefficient increased along with the fluid velocity and the particle concentration, which may indicate an improvement in the heat transfer potential of the GNP 500 nanofluids compared with distilled water. In addition, the Nusselt number and the convective heat transfer coefficient were largely influenced by the particle's Brownian motion, the thermo-physical properties (viscosity and thermal conductivity), and the specific surface area of the nanoparticles (Madhesh et al., 2014). Therefore, the higher concentration, heat flux, and nanofluid velocity increased the value of the convective heat transfer coefficient. The improved heat convection performance of the GNP nanofluid resulted from the higher thermal conductivity of the nanofluid and the disordered movement of the GNP nanoparticles (Madhesh, et al., 2014).

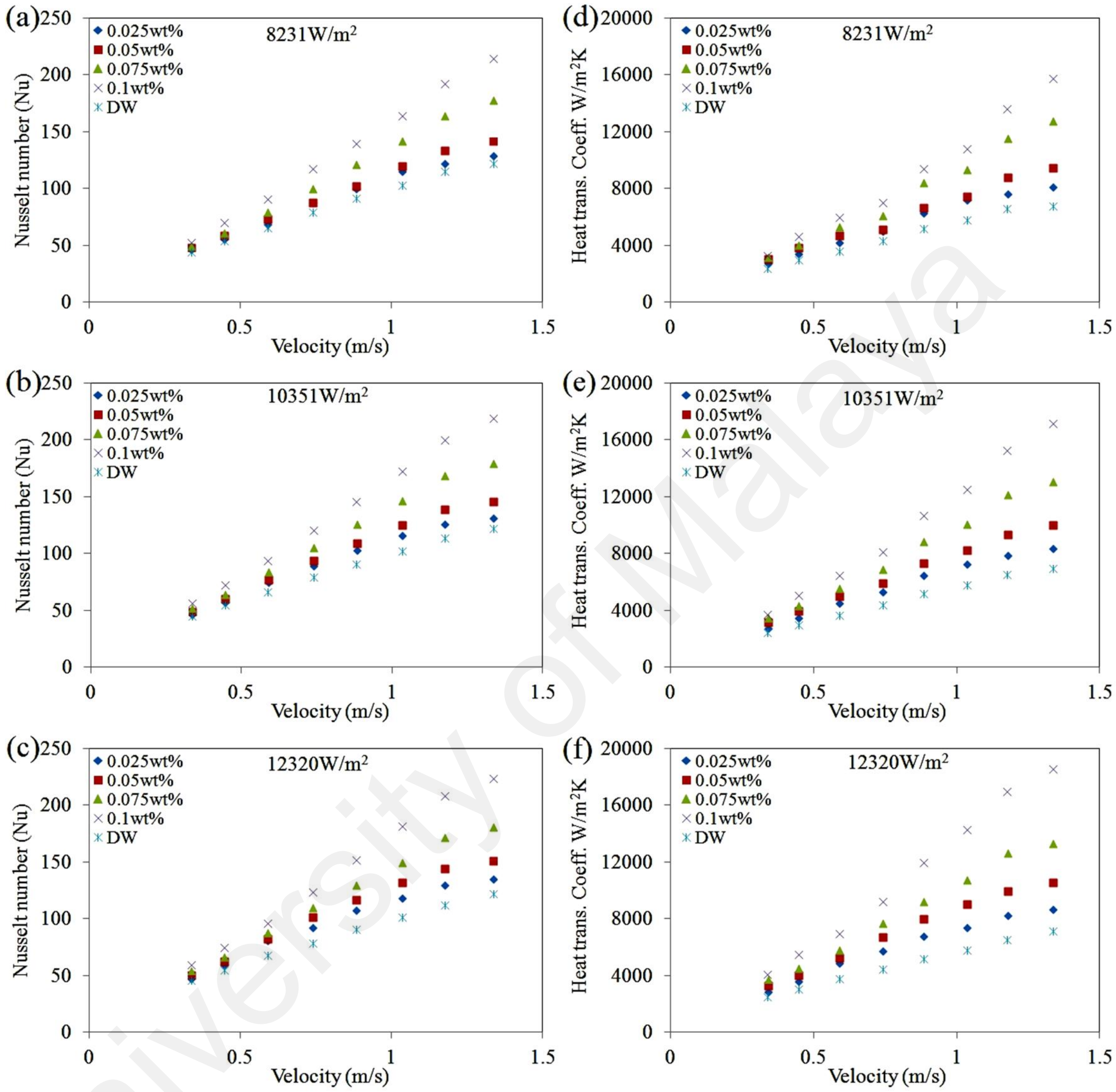

Figure 6.1 Variation of the (a, b, c) Nusselt numbers and (d, e, f) convective heat transfer coefficients of the GNP 500 nanofluids as a function of the velocity at different heat fluxes.

A significant enhancement in the Nusselt number and the convective heat transfer coefficient up to 0.1 wt% of the GNP 500 nanofluid was due to the improved thermal conductivity and the reduced thermal resistance between the flowing nanofluid and the inner wall surface of the tube. Figure 6.1f shows the largest enhancement of the convective heat transfer coefficient, which was 18%, 48%, 88%, and 160% for the 0.025, 0.05, 0.075, and 0.1 wt%, respectively, at a heat flux of 12,320 W/m^2. This substantial enhancement is obtained by adding a very small amount of GNP 500 nanoparticles to the distilled water. In the present investigation, the highest enhancement of the thermal conductivity was observed at approximately 25% of 0.1 wt% of the GNP nanofluid.

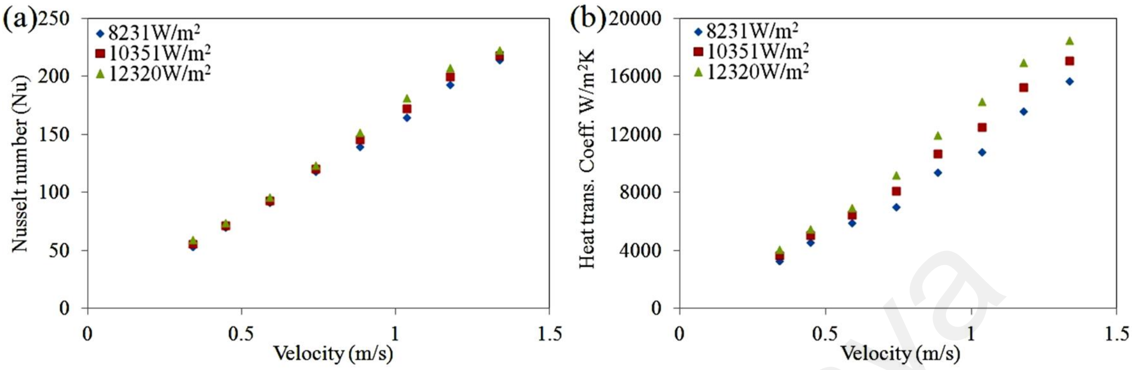

Figure 6.2 (a) Nusselt number, (b) heat transfer coefficient as a function of the velocity for 0.1 wt% of the GNP 500 nanofluid at different heat fluxes

6.1.2 Effect of specific surface area

A series of experiments on convective heat transfer was carried out for the GNPs nanofluids at three different specific surface areas (300, 500, and 750 m^2/g) and heat flux of 12,320 W/m^2. Figure 6.3 shows the variations of the Nusselt number (Nu) and convective heat transfer coefficient as well as the variation in the flow rate at different specific surface areas. Figure 6.4 shows the Nusselt number and the convective heat transfer coefficient at specific surface area for the 0.1 wt% GNPs nanofluids. The convective heat transfer coefficient was increased up to 83%, 160%, and 200% for the specific surface areas of 300, 500, and 750 m^2/g, respectively, at 0.1 wt%. Additionally, the Nusselt number (Nu) was increased up to 58%, 83%, and 100% for the specific surface areas of 300, 500, and 750 m^2/g, respectively. The convective heat transfer coefficient increased along with the fluid velocity, the particle concentration and specific surface area, which may indicate an improvement in the heat transfer potential of the GNPs nanofluids compared with distilled water.

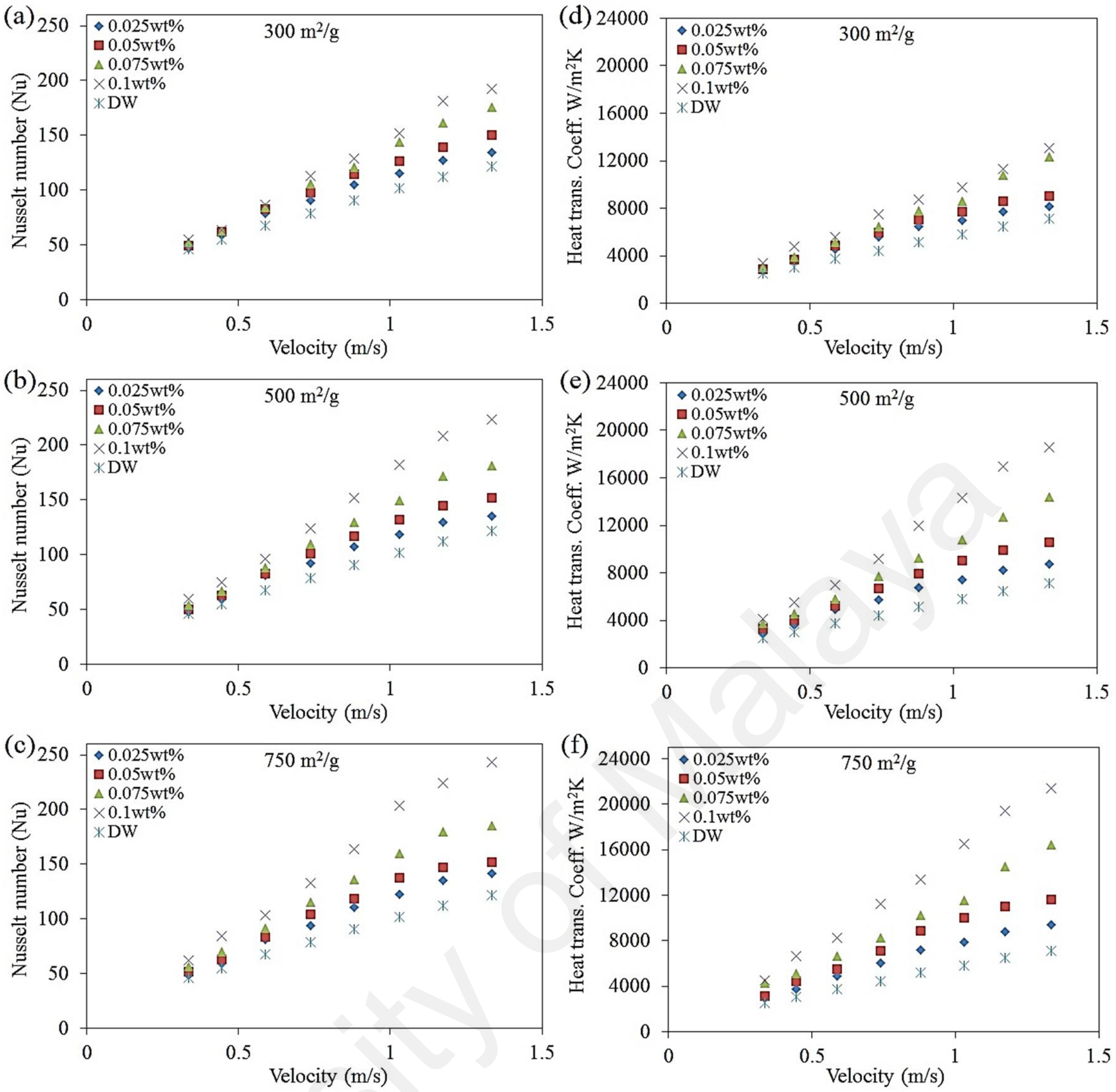

Figure 6.3 Variation of the (a, b, c) Nusselt numbers and (d, e, f) convective heat transfer coefficients of the GNP nanofluids as a function of the velocity at different specific surface area and heat flux of 12,320 W/m^2

Figure 6.3f shows the largest enhancement of the convective heat transfer coefficient, which was 31%, 63%, 130%, and 200% for the 0.025, 0.05, 0.075, and 0.1 wt%, respectively, at specific surface area of 750 m^2/g and higher velocity. This substantial enhancement is obtained by adding a very small amount of GNP nanoparticles to the distilled water.

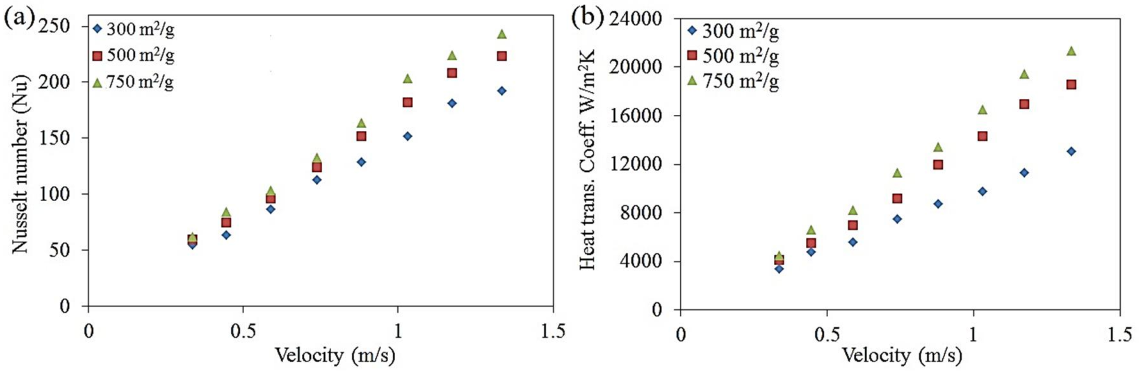

Figure 6.4 (a) Nusselt number, (b) heat transfer coefficient as a function of the velocity for 0.1 wt% of the GNPs nanofluid at different specific surface area and heat flux of 12,320 W/m^2

6.1.3 Fully developed flow

Previous studies claimed that the reasons for the heat transfer enhancement of the nanofluids included the mixing effects of the particles near the wall, particle migration, particle shape and re-arrangement, the Brownian motion of the particles, the thermal conductivity enhancement, a reduction of the boundary layer thickness, and a delay in the boundary layer development (Albadr et al., 2013; D. Kim et al., 2009). In addition, the thermal entry length for a fully developed flow in the turbulent region should be expressed as $x > 10D_i$ (Haghighi, et al., 2014). According to the experimental findings, there are two reasons for the convective heat transfer enhancement of the nanofluids: delay and disturbance of the thermal boundary layers and the excellent thermal conductivity enhancement of the GNP nanofluid. The chaotic movements created from the Brownian motion and the migration of GNP nanoparticles could affect the development of the thermal boundary layer in the entrance region (D. Kim, et al., 2009).

Figure 6.5 shows the local Nusselt number versus the axial position for 0.1 wt% of the GNP 500 nanofluids at different velocities with three different heat fluxes. The local Nusselt number could be calculated from the measured data, including the bulk and wall temperatures and the heat flux of the test section. The results clearly show negligible variations in the Nusselt number data of the GNP nanofluids under the fully developed condition of the turbulent flow region and the local Nusselt number in the thermally developing region because there is a slight enhancement of the local Nusselt number. In the thermally developed region, the surface temperature will also increase linearly in the flow direction because the heat transfer coefficient is constant (Sadeghinezhad, et al., 2014). Thus, the difference between the local and the bulk mean fluid temperatures are constant and are independent of the axial position. At a short distance from the end of the heated section in the thermal entry region, both the wall and bulk temperatures tend to be the same value, which is dependent on the overall heat balance (Sadeghinezhad, et al., 2014). The results in Figure 6.5 also show that the temperature difference of the wall and bulk liquid increases as the heat flux increases.

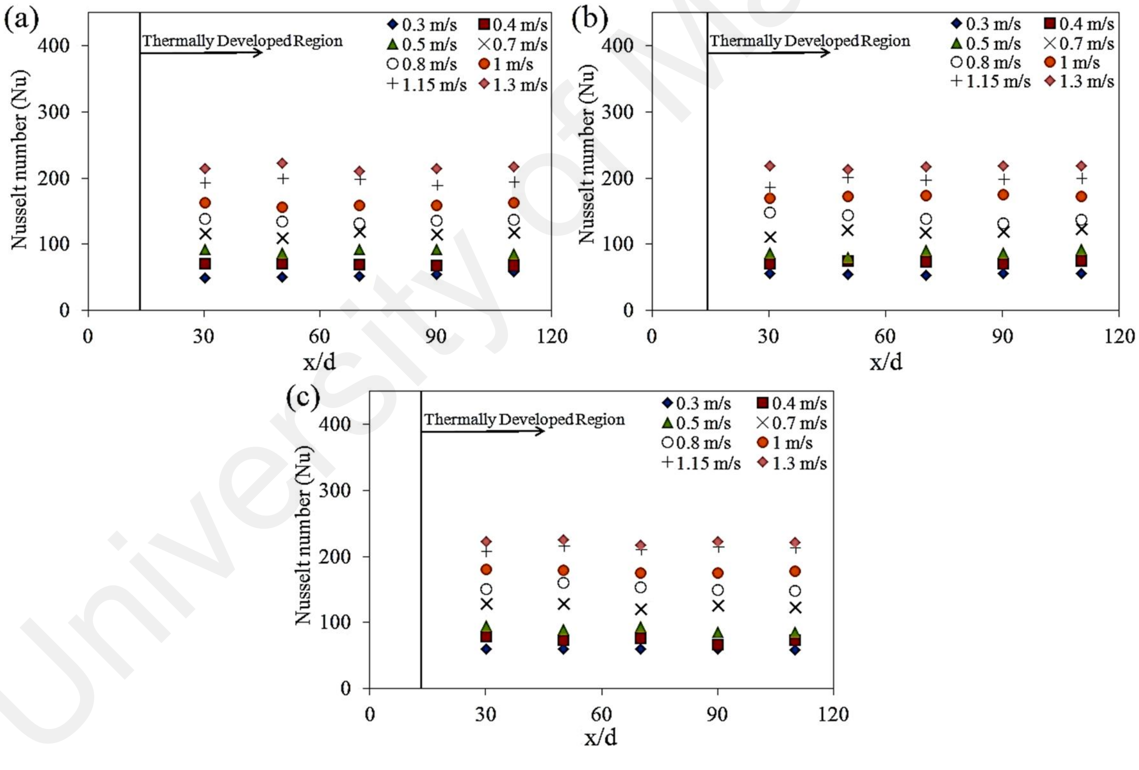

Figure 6.5 Comparison of the local Nusselt number versus the non-dimensional axial distance (X/D) at 0.1 wt% of the GNP 500 nanofluid under various heat fluxes: (a) 8,231 W/m^2, (b) 10,351 W/m^2, and (c) 12,320 W/m^2.

Figure 6.6 shows the local Nusselt number versus the axial position for 0.1 wt% of the GNPs nanofluids at different velocities with three different specific surface areas.

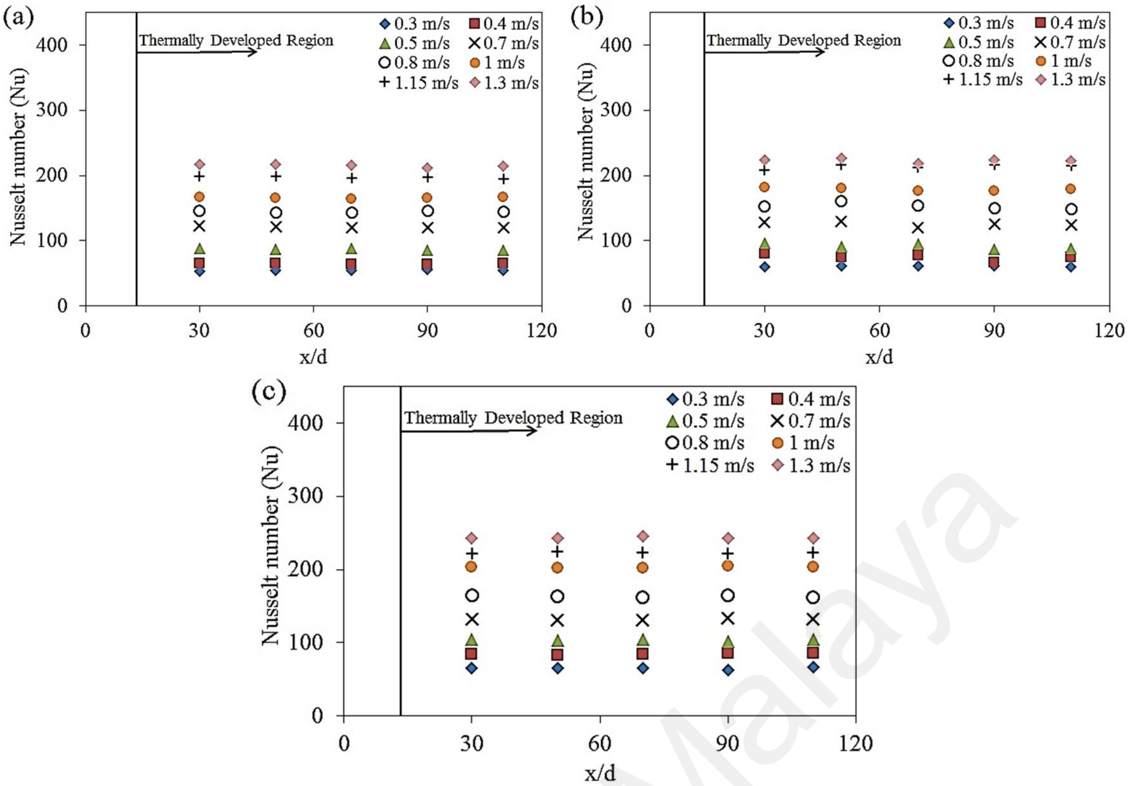

Figure 6.6 Comparison of the local Nusselt number versus the non-dimensional axial distance (x/d) at 0.1 wt% of the GNP nanofluid under heat flux of 12,320 W/m^2 and various specific surface areas of: (a) 300 m^2/g, (b) 500 m^2/g, and (c) 750 m^2/g.

The inner wall surface temperature at different GNPs concentrations for highest velocity of 1.3m/s is shown in Figure 6.7. The GNPs nanofluid is seen to reduce the surface temperature significantly, and the reduction increases with increasing of the concentration and specific surface area. Furthermore, at specific surface area of 750 m^2/g, the difference between inner wall temperatures become higher than the 300 m^2/g. It can be proved that the in all the cases at fully developed region and the surface temperature increases linearly in flow direction.

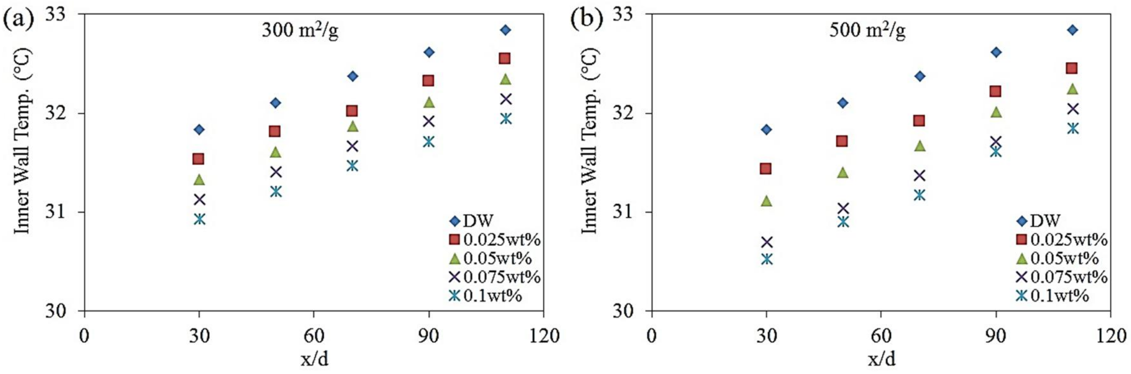

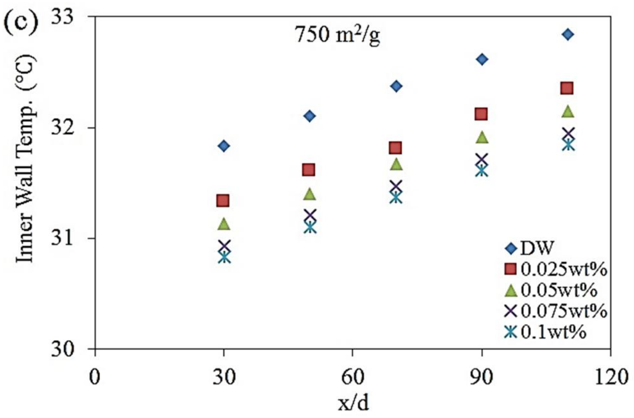

Figure 6.7 Inner wall temperature as a function of the non-dimensional axial distance (x/d) at higher velocity (1.3 m/s) for heat flux of 12,320 W/m^2 and different specific surface areas: (a) 300 m^2/g, (b) 500 m^2/g, and (c) 750 m^2/g.

6.2 Pressure drop of the nanofluid

6.2.1 Effect of concentration

To use the nanofluids in practical applications, the flow features of the GNP nanofluids should be determined in addition to the heat transfer measurements. The experimental results show that the pressure drop and the friction factor depend on the GNP concentration and the flow velocity (Figure 6.8). Table 6.1 shows the pressure drop increments of the GNP nanofluids for different flow velocities range of 0.3-1.3 m/s.

Table 6.1 Pressure drop increment of the GNP nanofluids at different concentrations

Concentration (wt%)	Increment (%)
0.025	0.4 to 9.1
0.05	1 to 10.2
0.075	2.8 to 13.1
0.1	3.4 to 14.6

The increased pressure drop and friction factor appear based on the viscous drag effects of the GNP nanofluids. This expression could be validated from Equation (5.5), wherein the friction factor as a function of the pressure drop was primarily influenced by the density gradient of the GNP nanofluids that resulted from an increase in the GNP nanoparticle concentrations. The GNP nanoparticle density is an important parameter for the increased friction factor and pressure drop of the nanofluids (Madhesh, et al., 2014).

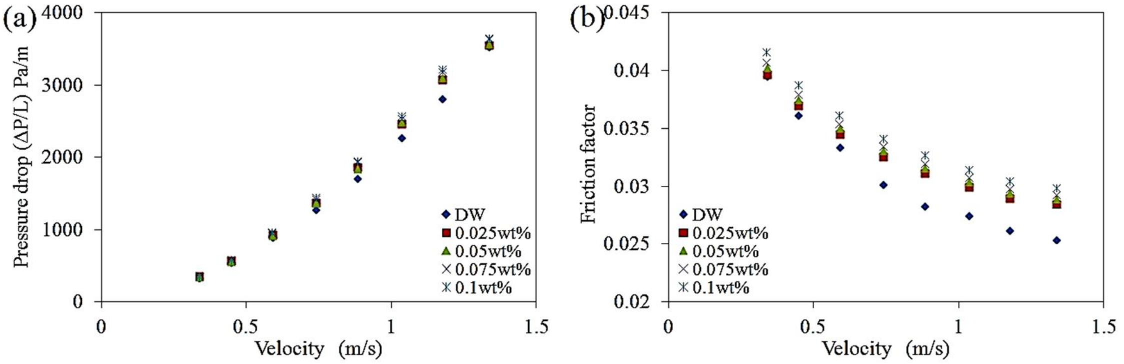

Figure 6.8 Variation of (a) pressure drop and (b) friction factor of the GNP 500 nanofluid as a function of velocity.

6.2.2 Effect of specific surface area

The experimental results show that the pressure drop and the friction factor depend on the GNPs concentration and the flow velocity (Figure 6.9).

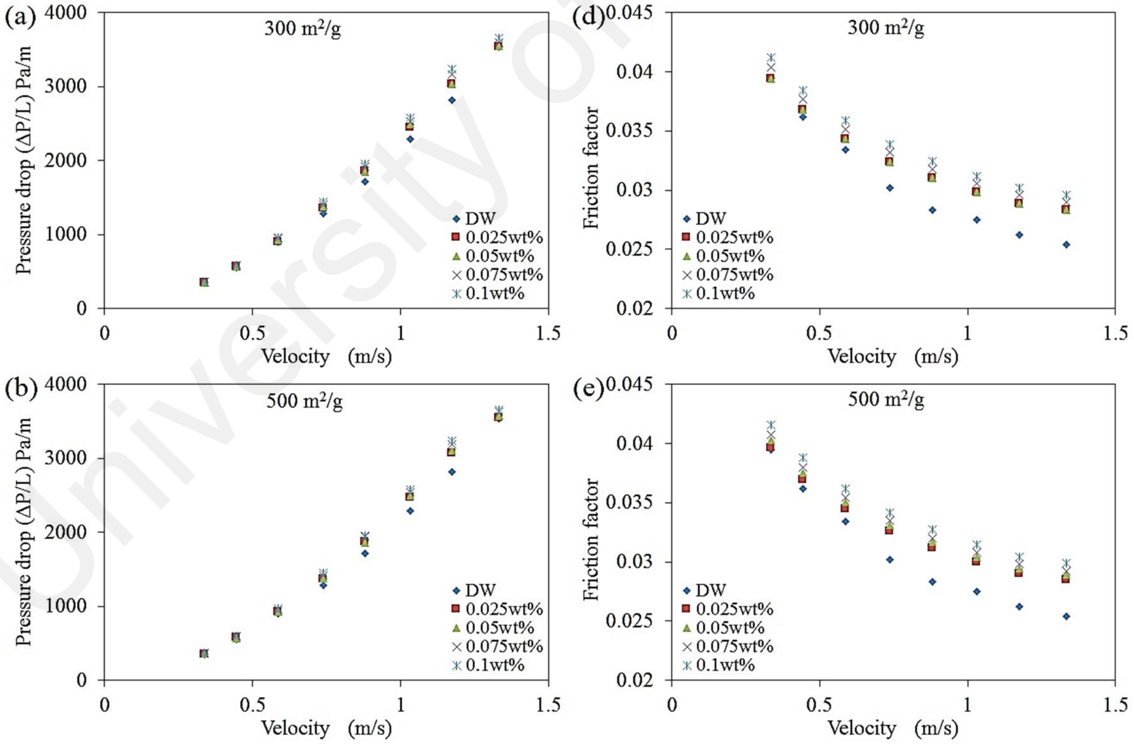

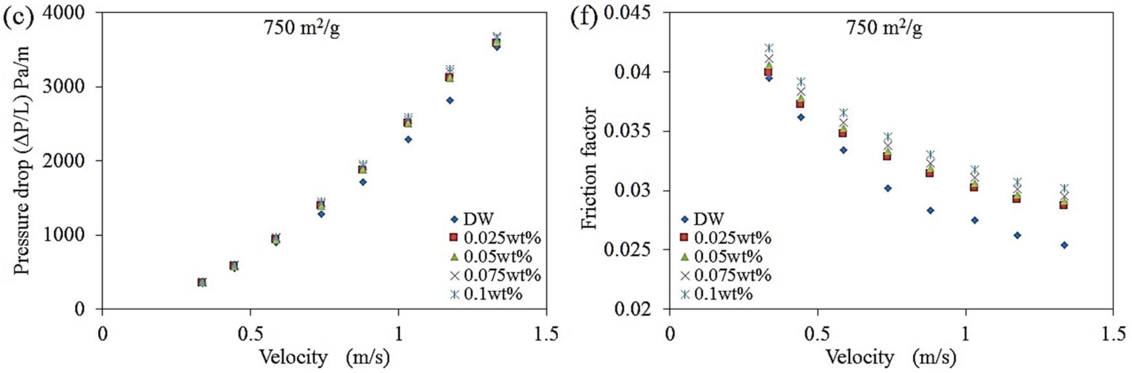

Figure 6.9 Variation of (a, b, c) pressure drops and (d, e, f) friction factors of the GNP nanofluids as a function of velocity with heat flux of 12,320 W/m^2 and different specific surface areas.

Table 6.2 shows the pressure drop increments of the GNP nanofluids for different flow velocities range of 0.3-1.3 m/s.

Table 6.2 Pressure drop increment of the GNP nanofluids at different specific surfaces area.

Concentration (wt%)	Specific surface area (m^2/g)		
	300	500	750
	Increment (%)		
0.025	0.06 to 8.3	0.4 to 9.1	2.9 to 10
0.05	0.2 to 8.9	1 to 10.2	2 to 10.6
0.075	1.6 to 12.1	2.8 to 13.1	5.6 to 13.2
0.1	3.3 to 14.5	3.4 to 14.6	3.5 to 14.7

6.2.3 Pumping power

The design of a heat exchanger for efficient heat transfer and minimum pumping power is important in terms of energy savings and could cause considerable errors when assessing the performance of nanofluids (pumping power and heat transfer) in various thermal applications. The pumping power or work required to circulate a coolant can be calculated by Equation (6.1).

$$\mathbf{P}_{Pump} = \Delta P \frac{\dot{m}}{\rho} \tag{6.1}$$

where ΔP is the pressure drop, $m^{\cdot}$ is the mass flow rate and ρ is the fluid density. In the actual case of a fully developed condition and a turbulent region in a circular tube with uniform heat flux at the wall, the expression for the pumping power could be introduced by Equation (11) (Mansour et al., 2007).

$$\left(\frac{\dot{W}}{\dot{W}_{bf}}\right)=\left(\frac{\mu}{\mu_{bf}}\right)^{0.25}\left(\frac{\rho_{bf}}{\rho}\right)^{2} \tag{6.2}$$

Figure 6.10 shows that the pumping power increases linearly with the GNP nanoparticle concentration. Compared with distilled water, no significant augmentation in the pressure drop and in the pumping power was required for the GNP nanofluids in any of the experimental runs; there was only a minor pumping power penalty (≈ 10%) due to the enhanced viscosity of the nanofluids. The effect of the GNP nanoparticles is small, and the GNP nanofluids behave similarly to pure fluid. In conclusion, for the heat transfer performance of the GNP nanofluid compared with the base fluid at a constant Reynolds number or at a constant flow rate, the data from a constant flow rate comparison show good results under certain conditions, such as the use of the same pumping power for the nanofluid and the base fluid.

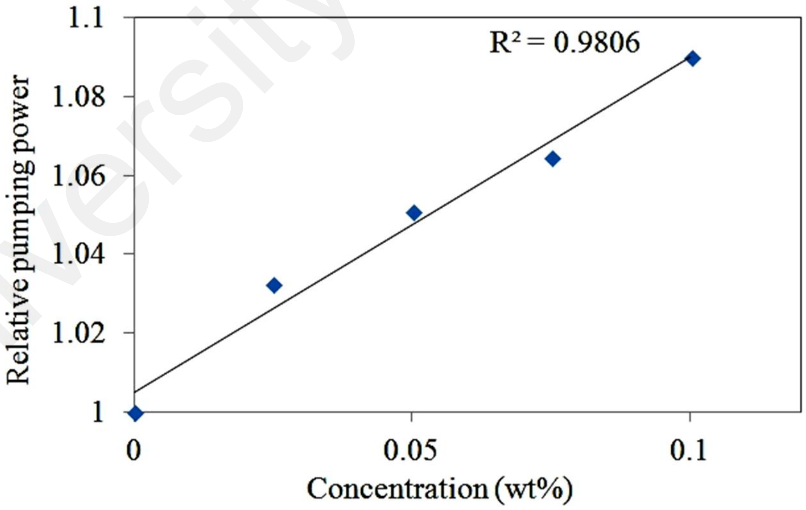

Figure 6.10 Effect of the GNP 500 nanofluid concentrations on the pumping power.

Figure 6.11 shows that the pumping power increases linearly with the GNP nanoparticle concentration and changing of the specific surface areas.

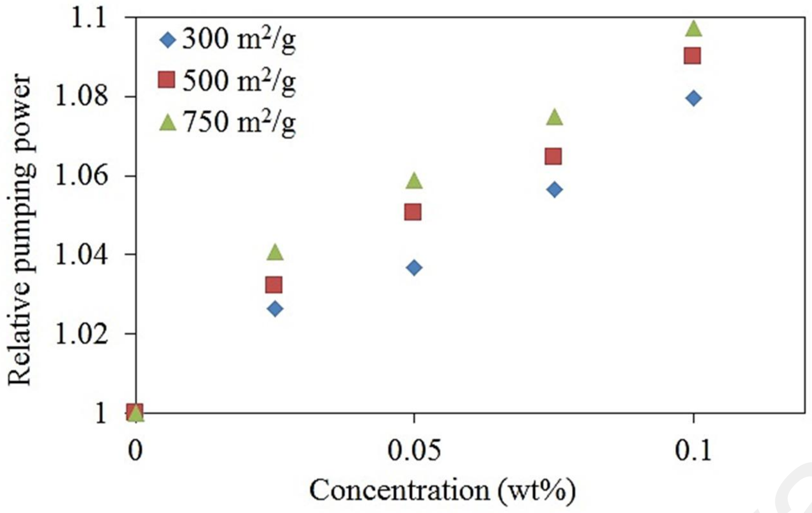

Figure 6.11 Effect of the GNP nanofluid concentrations on the pumping power at different specific surface areas.

6.2.4 Thermal performance factor

The thermal performance factor of the GNP nanofluid can be used to evaluate the usefulness of GNP nanofluids for application in thermal systems. The thermal performance factor is defined by Equation (6.3), and a higher thermal performance factor indicates greater usefulness (Hemmat Esfe et al., 2014).

$$\eta = \left(\frac{Nu}{Nu_{bf}}\right) / \left(\frac{f}{f_{bf}}\right)^{1/3} \tag{6.3}$$

Figure 6.12 shows that the thermal performance factor of the GNP 500 nanofluid at a higher heat flux is higher than that of at a lower heat flux and increases with the increase of velocity. This is a result of the superior efficiency of the fluid disturbance and thus the heat transfer caused by the higher thermal conductivity values at the similar pumping power. It also shows that the lowest concentration and the higher velocity of the GNP nanofluid are not as advantageous because the heat transfer enhancement effects are mitigated by the unfavorable effects of the pressure drop augmentation. The highest thermal performance of the GNP 500 nanofluid increased to 1.66, 1.70, and 1.77 for the GNP nanofluid at 8,231, 10,351, and 12,320 W/m^2, respectively, for a 0.1 wt% concentration. Finally, an analysis of the heat transfer and the pressure drop data via the thermal performance factor reveals that in spite of the pressure drop and the pumping power penalty, the GNP nanofluid at concentrations of 0.075 and 0.1 wt% is a good alternative for conventional working fluids in heat transfer applications.

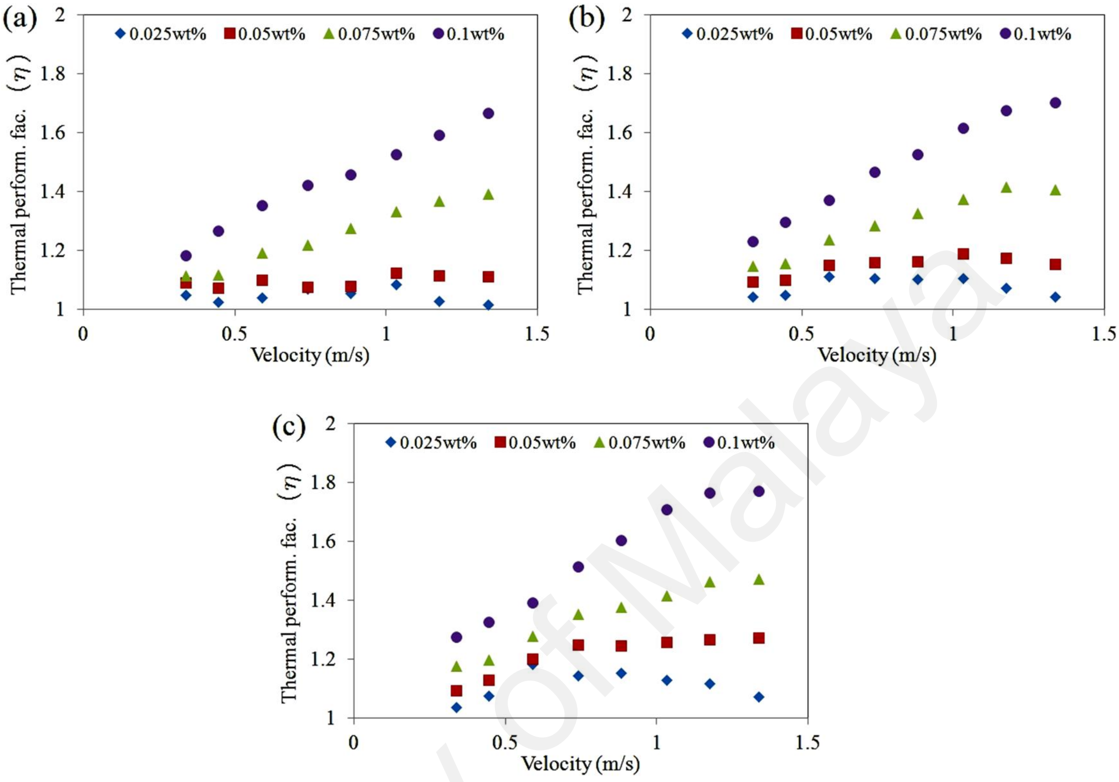

Figure 6.12 Variations of the thermal performance factor of GNP 500 nanofluids with the velocity at different heat fluxes: (a) 8,231 W/m^2, (b) 10,351 W/m^2, and (c) 12,320 W/m^2.

Figure 6.13 shows that the thermal performance factor of the GNP nanofluid at a higher specific surface area is higher than that of at a lower specific surface area and increases as the velocity increases. It also shows that the lowest concentration and the higher velocity of the GNP nanofluid are not as advantageous because the heat transfer enhancement effects are mitigated by the unfavorable effects of the pressure drop augmentation. The highest thermal performance of the GNP nanofluid increased to 1.51, 1.74, and 1.89 for the GNP nanofluid at specific surface area of 300, 500, and 750 m^2/g, respectively. However, the use of nanofluids are specific requirement guided, where heat transfer is given much emphasis irrespective friction loss.

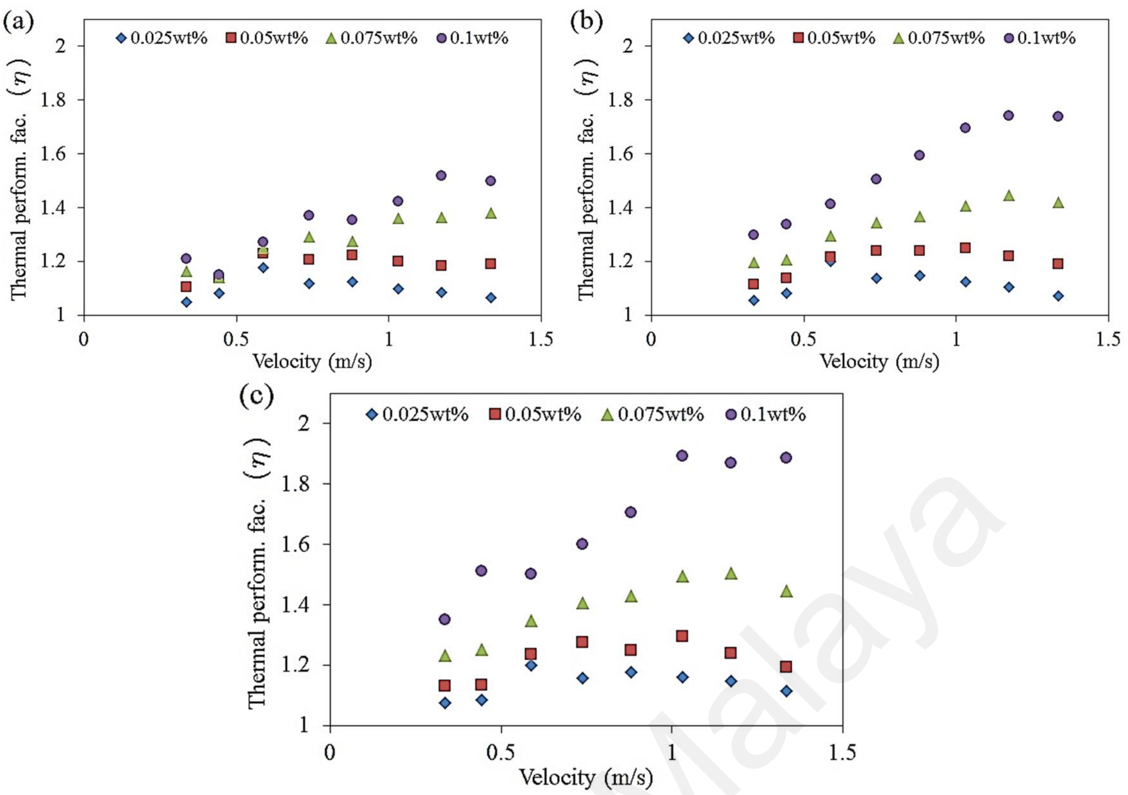

Figure 6.13 Variations of the thermal performance factor with the velocity at different heat fluxes: (a) 300 m^2/g, (b) 500 m^2/g, and (c) 750 m^2/g.

6.2.5 Entropy generation

In order to verify the performance of GNP 500 nanofluid at 0.1wt%, the entropy generation of nanofluid was calculated. The entropy generation analysis of nanofluids is known as a useful application to analyze thermal design optimization through minimizing it, and then better working conditions can be performed for a heat exchangers (Vincenzo Bianco et al., 2014; Hassan, et al., 2013; Roy et al., 2012; Sadeghinezhad, et al., 2014).

As previously mentioned, entropy generation of nanofluid flow through a circular tube is evaluated, therefore, in the following, the necessary equations are introduced and discussed.

$$S_{gen,T} = S_{gen,t} + S_{gen,f} \tag{6.4}$$

$$S_{gen,t} = \frac{q^2.\pi.D^2.L}{Nu.k_{nf}.T_{ave}} \tag{6.5}$$

$$S_{gen,f} = \frac{32.m^3.f.L}{\rho^2.T_{ave}.\pi^2.D^5} \tag{6.6}$$

$$T_{ave} = \frac{T_{in} - T_{out}}{\ln(T_{in}/T_{out})} \tag{6.7}$$

Figure 6.14 shows that the entropy generation of GNP nanofluid at 0.1wt% and 1.3 m/s was decreased by increasing of heat flux. Entropy generation shows the irreversibility of the system, therefore by reducing it, a more efficient system is obtained.

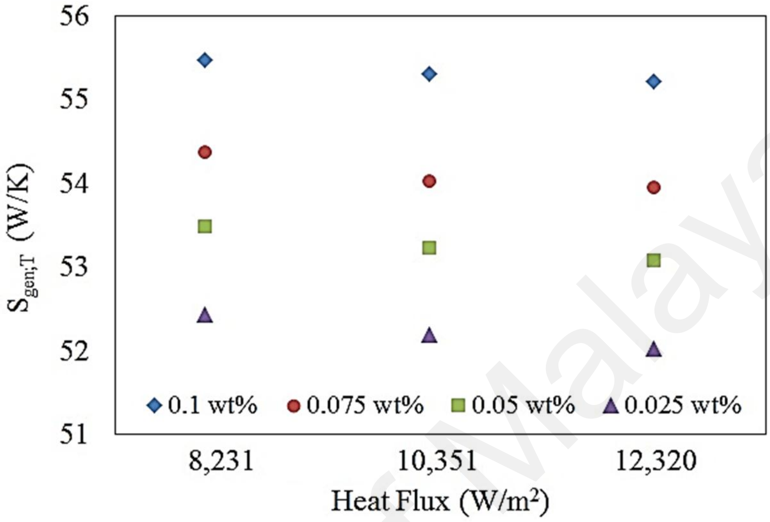

Figure 6.14 Entropy generation of GNP500 nanofluid versus heat flux and 1.3 m/s

6.3 Numerical investigation of heat transfer to GNP 500 nanofluids

The prediction of convective heat transfer has a vital importance because it directly affects design and operational conditions. It means that the better the prediction, the higher the accuracy of heat transfer performance evaluation. Although conventional heat transfer applications are accurately predicted by heat transfer correlations or solutions to differential equations, there are still debates on estimation of relatively new subjects such as convective heat transfer of nanofluids.

According to literature, and as mentioned in the previous section, there are two ways of modeling convective heat transfer of nanofluids; these are single phase modeling and two phase modeling. Single phase modeling assumes base fluid and nanoparticles mix homogeneously, there is no additional mechanism to contribute to heat transfer other than existing mechanisms for pure fluids. Two phase modeling states that there are other mechanisms caused by the relative motion between the base fluid and the nanoparticles; such as thermophoresis and thermal dispersion.

In the current study, single phase modeling of the convective heat transfer of nanofluid is performed. However, there are still several differences from conventional theories or correlations used to estimate convective heat transfer, which may affect heat transfer performance of nanofluids. In addition, the single phase modeling is relatively simpler approach and there is not too much difference between the two approaches especially for higher nanoparticle volumetric fractions as used in the current study (Sadeghinezhad et al., 2015).

6.3.1 Description of the configuration

An investigation of the heat transfer behavior of the nanofluids was performed by evaluating the velocity and the surface temperature. The measurements were performed in velocity range varied from 0.3-1.3m/s and heat flux varied from 8,231 W/m^2 to 12,320 W/m^2, the weight percentage of nanoparticles varied between 0.025wt% to 0.1wt%. A single-phase model adopted here to describe the turbulent heat transfer of the GNP 500 nanofluids in a horizontal stainless steel tube that was subjected to a uniform heat flux at its outer surface, as shown in Figure 6.15.

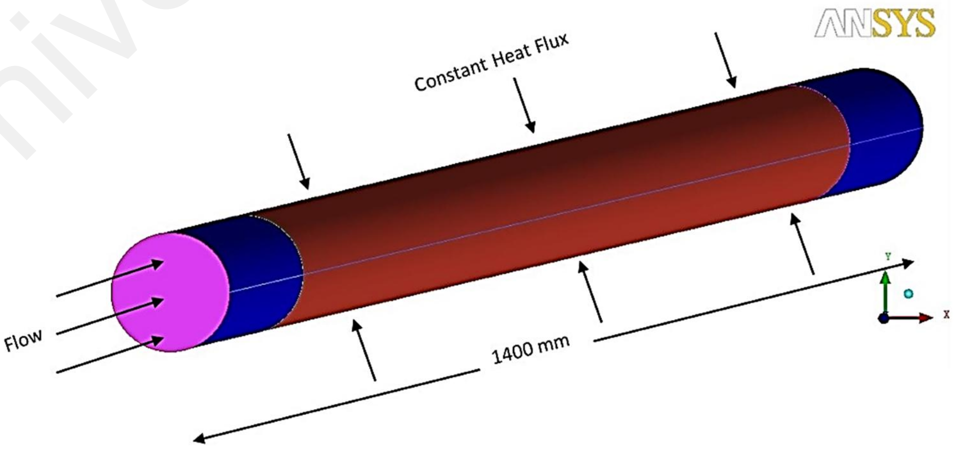

Figure 6.15 3D schematic view of the test sections.

6.3.2 Governing equations

Continuity, momentum and energy equations in three dimensions are used for incompressible fluid. According to control volume method based on converting the governing equations to algebraic equations of Herrmann (Schlichting et al., 2000) that is defined below:

$$\frac{\partial U_i}{\partial x_i} = 0 \tag{6.8}$$

$$\frac{\partial (U_i\, U_j)}{\partial x_j} = -\frac{\partial p}{\partial x_i} + \frac{\partial}{\partial x_j}\left(\mu \frac{\partial U_i}{\partial x_j} - \overline{\rho u_i u_j}\right) \tag{6.9}$$

$$\frac{\partial (U_i\, T_j)}{\partial x_j} = -\frac{\partial}{\partial x_i}\left(\frac{\mu}{\Pr}\frac{\partial T_i}{\partial x_j} - \overline{\rho u_i t_j}\right) \tag{610}$$

The Reynolds stresses and heat fluxes are, respectively, given as:

$$\overline{\rho u_i u_j} = -\mu_t\left(\frac{\partial U_i}{\partial x_j} + \frac{\partial U_j}{\partial x_i}\right) + \frac{2}{3}\delta_{ij} k] \tag{6.11}$$

$$\overline{\rho u_i t_j} = -\frac{\mu_t}{\sigma_\theta}\frac{\partial T_i}{\partial x_j} \tag{6.12}$$

The standard k-ε model has two transport equations for the turbulence kinetic energy and energy dissipation that are solved together with the equations of balance by the finite volume method Launder (B. Launder et al., 1974). The corresponding transport equations given below:

$$\frac{\partial \rho k U_i}{\partial x_j} = -\frac{\partial}{\partial x_j}\left[\left(\mu + \frac{\mu_t}{\sigma_k}\right)\right]\frac{\partial k}{\partial x_j} + \rho(G_b - \varepsilon) \tag{6.13}$$

$$\frac{\partial \rho \varepsilon U_i}{\partial x_j} = -\frac{\partial}{\partial x_j}\left[\left(\mu + \frac{\mu_t}{\sigma_k}\right)\right]\frac{\partial \varepsilon}{\partial x_j} + \rho\frac{\varepsilon}{k}(c_{1\varepsilon}G_b - c_{2\varepsilon}\varepsilon) \tag{6.14}$$

$$G_b = \mu_t\left(\frac{\partial u_i}{\partial x_j} + \frac{\partial u_j}{\partial x_i}\right)\frac{\partial u_i}{\partial x_j} \tag{6.15}$$

$$\mu_t = \rho c_\mu \frac{k^2}{\varepsilon} \tag{6.16}$$

The standard constants used in the k-ε model for turbulent flow are $\mathrm{C}_{1\varepsilon} = 1.44, \mathrm{C}_{2\varepsilon} = 1.92, \mathrm{C}_{3\varepsilon} = 0.09, \sigma_{\mathrm{k}} = 1.0,$ and $\sigma_{\varepsilon} = 1.3$ (B. E. Launder et al., 1974).

6.3.3 k-epsilon vs. k-omega turbulence modelling

K-Epsilon is used for fully turbulent flow (high Reynolds number). It cannot handle low Re, and also the flow separations. The reason why it is used so widely because of the low computation time and resource requirement in the industries. Based on the literatures, the several reasons for the k-epsilon model to become "popular" in comparison to other eddy viscosity models, these reasons are:

1. It is mainly devised for high-Re fully developed turbulent flow, such flow is manifested in the majority of engineering problems.
2. Literature records are crowded with thousands of successful CFD calculations, in nearly all industrial/engineering problems, using the k-epsilon model. Therefore, fluid dynamicists always "give it a try" with the k-epsilon when they tackle a problem for the first time.
3. It converges easily in most commercial FV codes, even with higher order numerical schemes.
4. There are several variants of the k-epsilon model, which are fine-tuned and corrected for specific engineering problems. Shih's realizable k-epsilon, Richardson number corrected k-epsilon are popular examples.

K-Omega is majorly used for near wall problems. Moving away from the wall K-Omega turns out to be same as k-epsilon. So, for the complex boundary layer problems or transition flow, K-Omega works better with fine resolution in mesh at the walls.

6.3.3.1 Standard k-ε

The baseline two-transport-equation model solving for kinetic energy k and turbulent dissipation ε. Turbulent dissipation is the rate at which velocity fluctuations dissipate. This is the default k– ε model. Coefficients are empirically derived; valid for fully turbulent flows only. In the standard k- ε model, the eddy viscosity is determined from a single turbulence length scale, so the calculated turbulent diffusion is that which occurs only at the specified scale, whereas in reality all scales of motion will contribute to the turbulent diffusion. The k- ε model uses the gradient diffusion hypothesis to relate the Reynolds stresses to the mean velocity gradients and the turbulent viscosity. It performs poorly for complex flows involving severe pressure gradient, separation, and strong streamline curvature. The most disturbing weakness is lack of sensitivity to adverse pressure gradients; another shortcoming is numerical stiffness when equations are integrated through the viscous sublayer which are treated with damping functions that have stability issues (Menter, 1993). (Notes: The author's self-investigation for flow through a pipe is consistent with the statements that this model is valid for flows without separation and for fully turbulent flow). Compared to a finned problem which had separation and which predicted erroneous results with the k- ε model, this pipe flow did not have separation and results of k- ε and k- ω models showed good agreement for high Reynolds numbers. In this pipe flow, as Reynolds number was decreased, the difference between the inlet pressures predicted by the k- ε and k- ω models increased. It is reported that the results for temperature are less sensitive to model choice and for velocity seem indifferent. Pressure results are highly sensitive to both the model choice and the mesh.

6.3.3.2 Standard k- ω

A two-transport-equation model solving for kinetic energy k and turbulent frequency ω. This is the default k–ω model. This model allows for a more accurate near wall treatment with an automatic switch from a wall function to a low-Reynolds number formulation based on grid spacing. It demonstrates superior performance for wall-bounded and low Reynolds number flows and shows potential for predicting transition. In this case, options account for transitional, free shear, and compressible flows. The k-ω model uses the gradient diffusion hypothesis to relate the Reynolds stresses to the mean velocity gradients and the turbulent viscosity. It solves one equation for turbulent kinetic energy k and a second equation for the specific turbulent dissipation rate (or turbulent frequency) ω. This model performs significantly better under adverse pressure gradient conditions. The model does not employ damping functions and has straightforward Dirichlet boundary conditions, which leads to significant advantages in numerical stability. This model underpredicts the amount of separation for severe adverse pressure gradient flows.

Pros: Superior performance for wall-bounded boundary layer, free shear, and low Reynolds number flows. Suitable for complex boundary layer flows under adverse pressure gradient and separation.

6.3.4 Numerical procedure

ANYSYS ICEM software was used to create the geometry and meshing as illustrated in Figure 6.16. The governing equations were solved by computational fluid dynamic software ANSYS FLUENT 14 based on associated boundary and initial conditions. According to (Patankar, 1980) the finite volume method was applied to discretize the governing equations in the computational domain. The SIMPLE algorithm was used for couple velocity and pressure drop (Mahmoudi et al., 2012; Rahgoshay et al., 2012), a second order upwind scheme for momentum and energy equations were considered. Non-uniform quadrilateral grids were used for meshing the solution domain. In order to obtain high accuracy data, the residual sum was computed and set for each iteration and the convergence criterion was less than 10^{-5} for the continuity, and smaller than 10^{-6} for all equations and it was confirm the accuracy of the simulation.

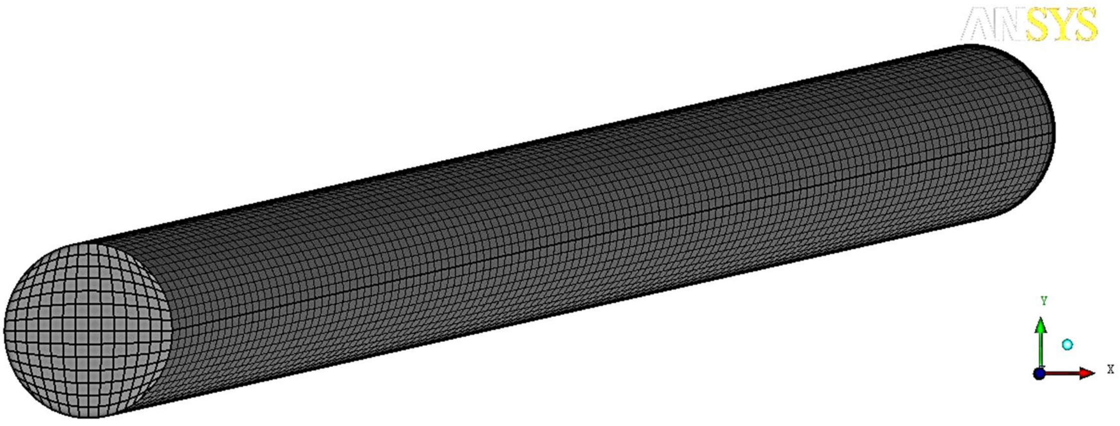

Figure 6.16 3D view of mesh.

6.3.5 Grid independence

In order to evaluate the grid independent results four sizes of grid were adopted for DW at flow rate of 1.3m/s and uniform heat flux of 12,320 W/m^2 with different dimensional units of x, y, z, as shown in Table 6.3. The second grid is represents the grid independence due to the difference in average Nusselt number between the second and fourth grid was less than 0.7%, whereas the difference between the first one and the second one in 0.33% and between second and third one is 0.18% and between third and forth one is only 0.60.

Table 6.3. Grid independent for pure water at q=12,320 W/m^2 and 1.3m/s.

Size of grid	X=15, Y=15, Z=600	X=20, Y=20, Z=1200	X=25, Y=25, Z=1500	X=30, Y=30, Z=1800
Grid no.	1	2	3	4
Nu_{ave}	123.5541751	123.9607365	124.1866204	124.9396083

6.3.6 Validation of the numerical method for the case of distilled water

The numerical results for DW at constant heat flux conditions were compared with the experimental results of DW. Figure 6.17 shows that the comparison between the experimental tube surface temperature and the data from the numerical simulation for velocity of 0.3m/s and 1.3m/s at different heat fluxes. It can be seen that linear increases in surface temperature along the pipe and those increment occurred with increase of velocity and heat fluxes for both experimental and numerical results. There is a good agreements between numerical and experimental data with an error of less than 2% for DW.

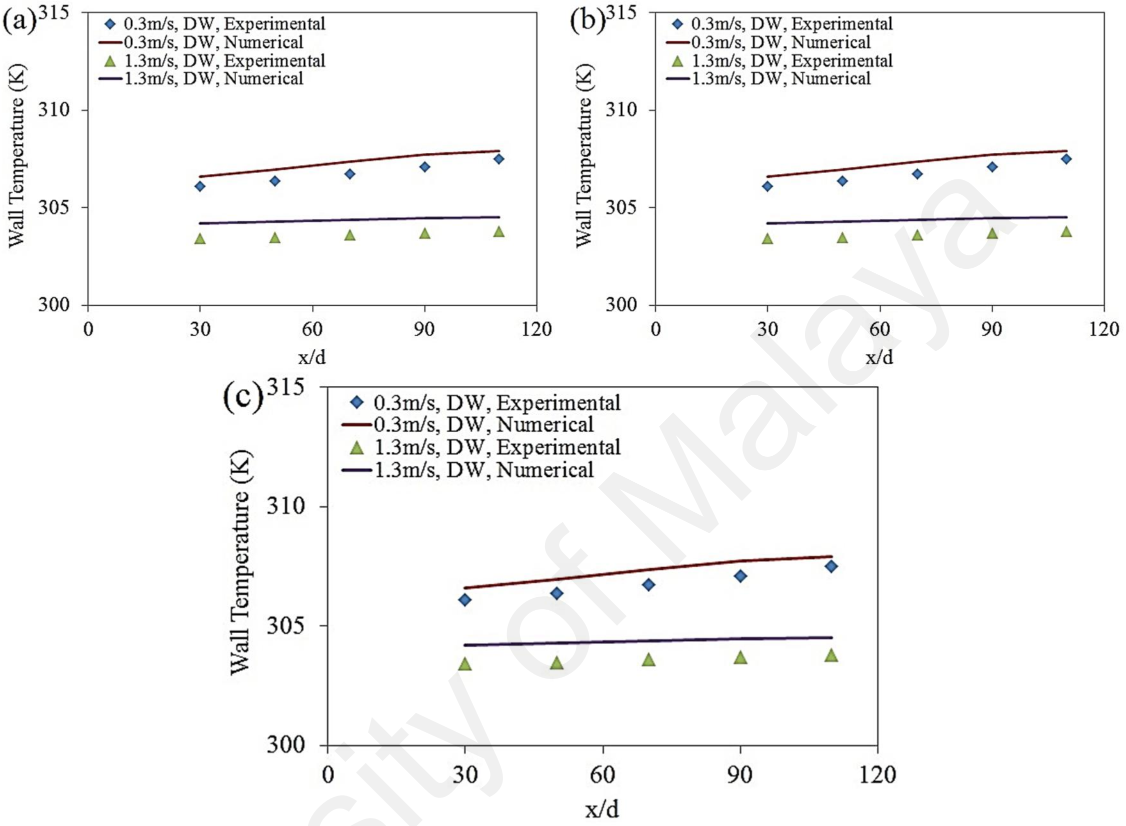

Figure 6.17 Measured surface temperature and the numerical data for DW versus the non-dimensional axial distance (x/d) at different heat fluxes; (a) 8,231 W/m^2, (b) 10,351 W/m^2, (c) 12,320 W/m^2.

6.3.7 Comparison between numerical and experimental results of GNP nanofluid

Figure 6.18 shows the numerical and experimental wall surface temperature at different axial distance for GNP nanofluid at velocity of 0.3m/s and 1.3m/s. It was observed that the surface temperature increases when the heat flux increases and that depends on GNP concentration in the suspentions. Wall temperature distribution results are compared with the experimental results and were found with the error of 4% for GNP nanofluid. As seen in Figure 6.18, the temperatures significantly decreased on increases of the particle concentration. Experimental and numerical results are shown that the use of the GNP nanofluid has better heat transfer characteristics than the using of DW. As velocity increases, the deviation between the numerical and experimental wall temperature become less and at higher velocity has revers effect. This effect is due to the fact that the corresponding velocity profiles become more uniform as Reynolds number increases (Vincenzo Bianco et al., 2011).

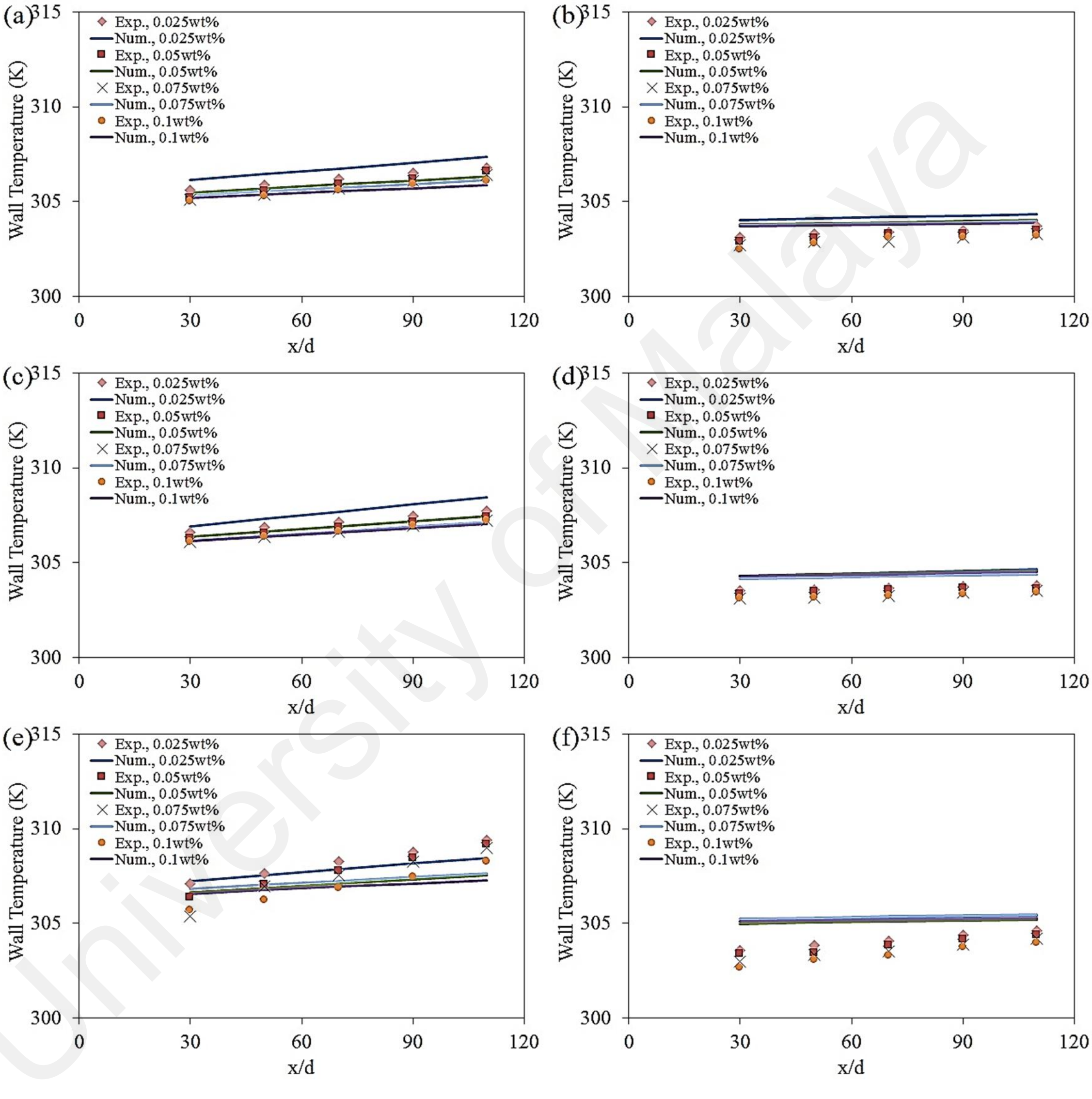

Figure 6.18 Distribution of wall temperatures of tube surface for different heat fluxes and velocities; (a) 8,231 W/m^2, 0.3m/s, (b) 8,231 W/m^2, 1.3m/s, (c) 10,351 W/m^2, 0.3m/s, (d) 10,351 W/m^2, 1.3m/s, (d) 12,320 W/m^2, 0.3m/s, (f) 12,320 W/m^2, 1.3m/s

6.3.8 Comparison of the Nusselt number

Average Nusselt numbers of the GNP nanofluids as a function of the velocity at different heat fluxes are presented in Figure 6.19. Generally, for all cases the average Nusselt numbers of the GNP nanofluids experienced good increment with increase of velocity in both numerical and experimental results. Effect of weight concentrations of the GNP nanofluids on average Nusselt numbers has been noted where the highest average Nusselt number showed at 0.1Wt%, 1.3m/s and heat flux of 12,320 W/m^2 due to the improved thermal conductivity and the reduced thermal resistance between the flowing nanofluid and the inner wall surface of the tube. The Nusselt number (Nu) was increased up to 75%, 79%, and 83% for the heat fluxes of 8,231, 10,351, and 12,320 W/m^2, respectively.

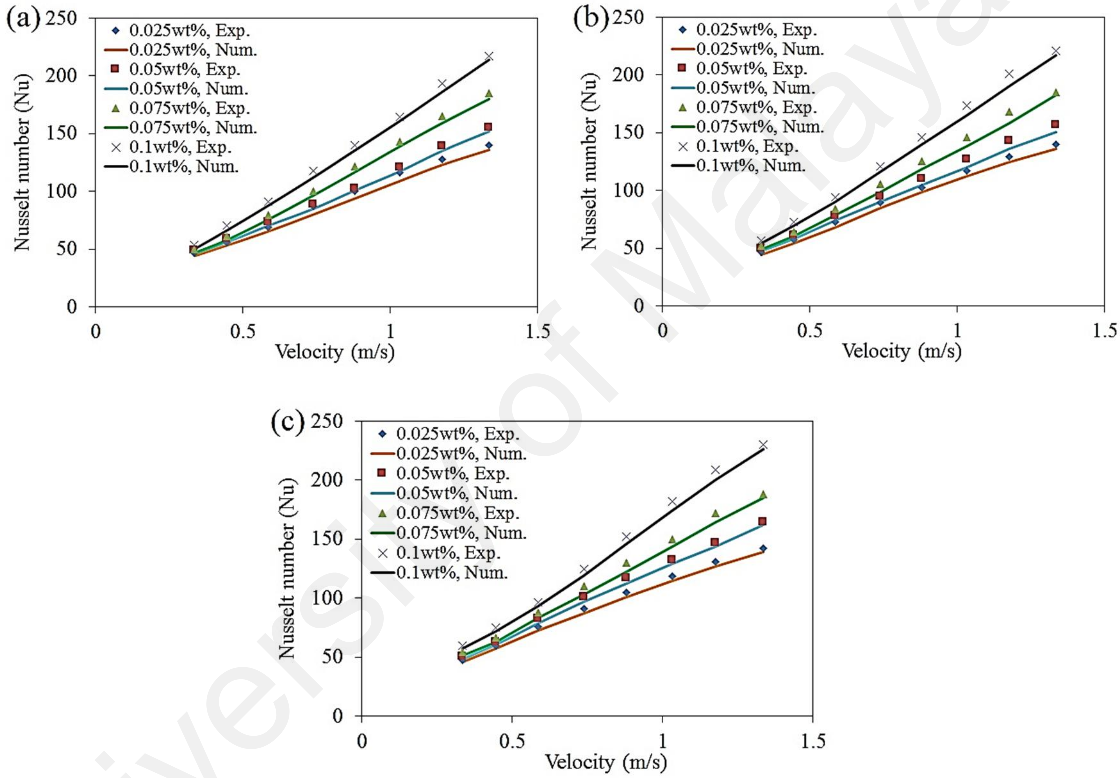

Figure 6.19 Variation of the average Nusselt numbers of the GNP nanofluids as a function of velocity at different heat fluxes: (a) 8,231 W/m^2, (b) 10,351 W/m^2, (c) 12,320 W/m^2.

6.4 Effect of nanofluid production on heat transfer

In this additional section, effect of different nanofluids on fully developed heat transfer coefficient values for different types of nanofluids at highest concentration as function of velocity was investigated. Figure 6.20 shows that all five nanofluids have enhancement in the overall convective heat transfer coefficient, and the highest enhancement is 317% for NDG, when the heat transfer coefficients to each other at the same fluid velocity were compared.

This effect was much more realized at higher concentrations of nanofluids by which, the heat transfer rate was suppressed, and that could be signified by the constricted movement of the thermally conductive particulates within the nanofluid, leading to an eventual reduction in the molecular momentary diffusion. This, in turn, indicates a tradeoff between the effective heat transport and rheological behavior of the nanofluids. The heat transfer by convection was largely influenced by the particle size, lower molecular momentum diffusivity, flow restriction, and an increase in both the dynamic viscosity and thermal boundary layer thickness.

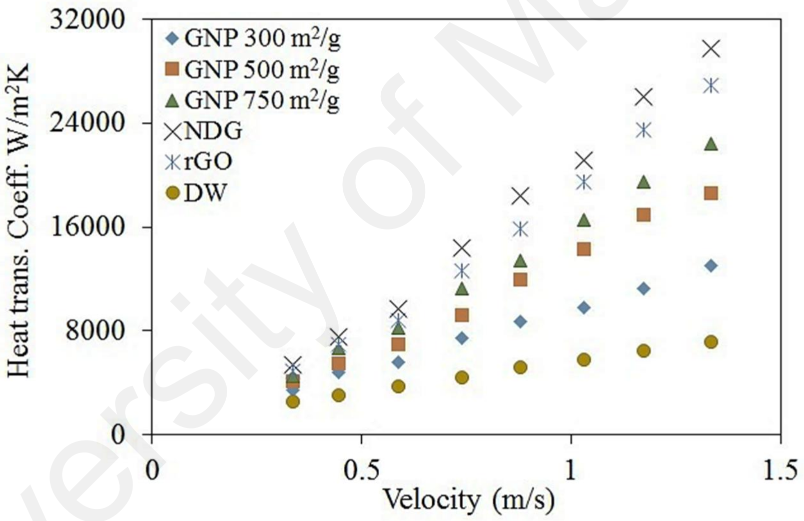

Figure 6.20 Comparison of the convective heat transfer coefficient at highest concentration (0.1wt%) and heat flux of 12,320 W/m^2

As shown in Figure 6.21, the increased pressure drop could be related to the viscous drag effects and density gradient of nanoparticles dispersed in the base fluid. It is noteworthy that, during the flow of nanofluids, the formation of the temporal flocculation (or nanoclusters) of nanoparticles in the fluid medium, which had not been fragmented and re-structured to primary particles, would have resembled the higher viscosity of nanofluids. This aspect could be verified further from Equation (5.5), wherein the friction factor as a function of the pressure drop was largely dependent on the density gradient of the nanofluids experienced with increased concentrations of nanoparticles (Sadeghinezhad, et al., 2014). Moreover, the nanofluid layer in close vicinity to the inner tube wall surface was prone to higher shear stress with relatively low velocity, which manifested in low viscosity with the addition of nanoparticles. However, the rotation of nanoclusters, which has to be in line with the direction of fluid flow, was expected to be constricted by the momentary shear disturbances encountered around the nanoparticles (Madhesh, et al., 2014). It is thus found that, the density of the nano-particles also plays a vital role, thus, the resistance offered to the flow with increased in concentration, has led to the increased friction and pressure drop of nanofluids, compared to the base fluid.

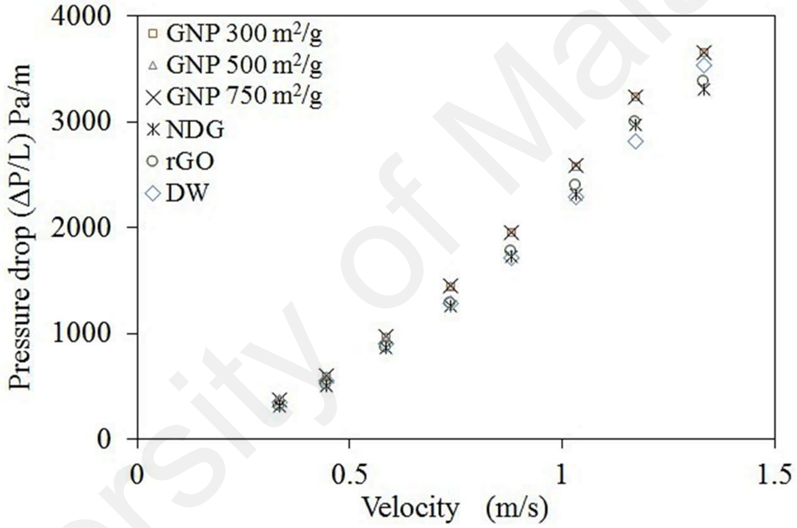

Figure 6.21 Variation of pressure drop of the different nanofluid (0.1wt%) as a function of the velocity with heat flux of 12,320 W/m^2.

Table 6.4 shows the pressure drop increments of the nanofluids for different flow velocity ranges of 0.3-1.3 m/s.

Table 6.4 Pressure drop increment of the nanofluids at higher concentration and heat flux of 12,320 W/m^2.

Nanofluids	Increments (%)
GNP 300 m^2/g	3.3 to 14.5
GNP 500 m^2/g	3.4 to 14.6
GNP 750 m^2/g	3.5 to 14.7
NDG	6 to 10.1
G-rGO	4.2 to 8

6.5 CONCLUSIONS

In this Chapter, forced convective heat transfer to nanofluids is investigated considering the heat transfer coefficient and the Nusselt number enhancement at constant flow rate. It is concluded that the heat transfer coefficient of a nanofluid is enhanced with respect to the base fluid at a constant velocity. This enhancement comes from the thermal conductivity enhancements. On the other hand, the usage of nanofluids depends also on the pumping power performance of nanofluids. In this Chapter, the estimation of the nanofluid heat transfer is achieved. The constant velocity analyses help to understand the nanofluid heat transfer value deviation from the conventional theories. Hence, the higher heat transfer at same Re number is not only because of the nanofluids performance, but might be due to the higher flow rate of nanofluids (for measuring at same Re number, where the higher viscosity reduces Re number). Due to these reasons, it might be better to choose constant velocity instead of constant Re number. Therefore, it is required to investigate pumping power behavior of the nanofluids and a comparison between the base fluids and nanofluids is also needed to understand the performance enhancement performed.

The performance comparison between the nanofluids and the base fluids is actually more important than the heat transfer estimation because this issue determines whether the nanofluid should be used instead of the base fluid. The heat transfer estimation is crucial parameter that affects the heat transfer/pumping power considerations.

The convective heat transfer performance and the flow characteristics of a GNP nanofluid flowing in a horizontal tube with various heat fluxes in a fully developed turbulent region were experimentally investigated. Aqueous GNP nanofluids at different specific surface area (300, 500, and 750 m^2/g) with various concentrations ranging from 0.025 to 0.1 wt% were prepared using a two-step method without any surfactant. The convective heat transfer characteristics and the pressure drop were measured for the flow through a circular tube. The following conclusions were obtained.

1. The use of the GNP nanofluid provides significantly higher heat transfer coefficients up to 200%.
2. The convective heat transfer coefficient increases as the flow rate and heat flux increase.
3. A significant enhancement of the convective heat transfer coefficient and the Nusselt number up to 0.1 wt% of the GNPs was provided using the improved thermal conductivity and the reduced thermal resistance that were offered by the GNP nanofluid on the inner wall surface of the tube.
4. The pressure drop and the friction factor of the nanofluid increased by 0.06% to 14.7% compared to the base fluid. Therefore, the nanofluid results in only a minor penalty in terms of the pumping power, which indicates that it is suitable for some specific practical applications.
5. An increase of the thermal performance could be obtained as 1.66, 1.70, and 1.77 for the GNP nanofluid at 8,231, 10,351, and 12,320 W/m^2, respectively, for a 0.1 wt% concentration. The GNP nanofluid at concentrations of 0.075 and 0.1 wt% provides a good option for the replacement of the conventional working fluids in heat transfer applications.
6. An increase of the thermal performance could be obtained as 1.51, 1.74, and 1.89 for the GNP nanofluid at specific surface areas of 300, 500, and 750 m^2/g, respectively. The GNPs nanofluids at concentrations of 0.075 and 0.1 wt% provides a good option for the replacement of the conventional working fluids in heat transfer applications.
7. The convective heat transfer coefficient enhancement was 317% for NDG, when compared with the heat transfer coefficients of others at the same fluid velocity.

Additional work is required to investigate the effects of the different nanoparticle concentrations and the different parameters of the convective heat transfer coefficients and flow features of the nanofluids.

CHAPTER 7

CONCLUSIONS AND RECOMMENDATIONS

Currently there is an exponential growth in use of nanofluid in heat transfer area including electronic technologies etc. With their decrease in size and increase in the rate of operation, problems arise with the their thermal management. Research is being done on enhancing the heat removal of these systems by using nanofluids. Numerous papers in literature report on the enhanced heat transfer rate using nanofluids compared with conventional fluids such as water. Most of the papers reported in literature tested nanofluids in either the fully turbulent flow regime or laminar flow regime and only a few reported on the transitional flow regime. An experimental system was developed in order to test different volume concentrations of various types of nanofluids.

This chapter discusses on the conclusions derived from the results of the experiments and recommends further procedure and experiments which could have been done if limitations in experimental instruments and time were not a factor to conduct further research.

7.1 Conclusions

In conclusion, there are many variables must be accounted for when dealing with nanofluid (colloid) experiments. The conceptual and theoretical developments of colloid and surface science lead to a far better understanding of nanofluid properties and behavior. Some properties such as size and stability are easily altered by concentration, pH, and temperature modifications.

1. The increase of thermal conductivity as a function of concentration of particles in nanofluids, which could be predicted by effective medium theory.
2. Effect of particle size on thermal conductivity enhancement is very limited.
3. The viscosity of nanofluid increases non-linearly with particle concentration.
4. Temperature effects on viscosity to the same degree in both nanoparticle colloids as well as base fluids.

The thermal conductivity research shows that some specific parameters of nanofluids whose effects on thermal conductivity are not closely observed in most of the studies. These parameters are extent of clustering of nanoparticles, particle size distribution of nanoparticles, duration and severity of ultrasonic vibration applied to the nanofluid and temperature of the nanofluid.

There are several mechanisms proposed to explain the thermal conductivity enhancement of nanofluids, such as Brownian motion of nanoparticles, clustering of nanoparticles and liquid layering around nanoparticles. Due to the lack of systematic experimental data in the literature, it is difficult to analyze the relative significance of these mechanisms. Most of the theoretical models based on these mechanisms include some empirical constants. It is possible to correctly predict experimental results to some extent by adjusting the values of these constants. On the other hand, at present, a complete theoretical model of thermal conductivity that takes all of the parameters into account is not available.

When it comes to the theoretical studies about the thermal conductivity of nanofluids, it is seen that the relative significance of the proposed enhancement mechanisms of thermal conductivity are not known. Development of new theoretical models that combine the effects of numerous enhancement mechanisms and comparison of these models' predictions with systematically obtained experimental data will provide insight to the theoretical explanation of anomalous thermal conductivity enhancement with nanofluids.

When it comes to the convective heat transfer to nanofluids, in the theoretical analysis part, and classical correlations for DW shows that the experimental data provides accurate results.

Examination of convective heat transfer coefficient, h_c for the flow of nanofluids shows that h_c is higher for the case of nanofluids which is mainly due to the flattening in the radial temperature profile as a consequence of thermal dispersion. Fully developed Nusselt numbers and heat transfer coefficients are also determined for nanofluids with different particle volume fractions and it is seen that the effect of thermal conductivity enhancement on heat transfer coefficient enhancement is more pronounced than the effect of Nusselt number enhancement, due to quotient form of expression for Nu number. Investigation of the effect of nanofluid particle size on heat transfer results in complicated trends due to the opposing effects of thermal conductivity and thermal dispersion on heat transfer in terms of particle size dependence. Evaluation of heat transfer performance is also analyzed by considering constant pumping power case and observing the heat transfer performance criterion, which depends on the boundary condition, for the nanofluids and the base fluids. However, the recommendation of nanofluid as advantageous alternative to conventional heat transfer liquid limited to specific applications.

It is concluded that heat transfer performance depends on different important parameters for the fully developed region. Actually, the theoretical analysis gives similar results for the boundary conditions but may have slightly different performance ratios. The important parameters depend on nanofluid thermo-physical properties and nanofluid convective heat transfer behavior.

7.2 Recommendations for Future Work

A very broad spectrum of work was covered surrounding nanofluids, hence not every aspect could be covered in detail and thus some questions are still unanswered. Therefore, future recommended work should include the followings:

1. The preparation of nanofluids is a critical part, if not the most important part, when wanting the optimal heat transfer performance. In a poorly prepared nanofluid the nanoparticles settle out of suspension, which leads to a large increase in viscosity due to the agglomeration of the nanoparticles. Most preparation methods found in the literature are for metallic nanoparticles and very few exist for non-metallic. Hence, intensive studies should be conducted for the discovery of proper preparation technique for carbon based nanofluids.
2. After a properly prepared nanofluid an investigation on the thermal conductivity and viscosity should be done. There exists numerous correlations for the thermal conductivity and viscosity but they are all study specific, and they can only be used for that specific nanofluid. Hence a study on the thermal conductivity and viscosity for nanofluids of different nanoparticle should be performed in order to get unified correlations.

BIBLIOGRAPHY

Abdulagatov, I. M., & Azizov, N. D. (2006). Experimental study of the effect of temperature, pressure and concentration on the viscosity of aqueous NaBr solutions. *Journal of solution chemistry, 35*(5), 705-738.

Akhavan, O., Kalaee, M., Alavi, Z., Ghiasi, S., & Esfandiar, A. (2012). Increasing the antioxidant activity of green tea polyphenols in the presence of iron for the reduction of graphene oxide. *Carbon, 50*(8), 3015-3025.

Alawi, O. A., Sidik, N. A. C., Mohammed, H. A., & Syahrullail, S. Fluid flow and heat transfer characteristics of nanofluids in heat pipes: A review. *International Communications in Heat and Mass Transfer, 56*, 50–62.

Albadr, J., Tayal, S., & Alasadi, M. (2013). Heat transfer through heat exchanger using Al_2O_3 nanofluid at different concentrations. *Case Studies in Thermal Engineering, 1*(1), 38-44.

Amrollahi, A., Hamidi, A., & Rashidi, A. (2008). The effects of temperature, volume fraction and vibration time on the thermo-physical properties of a carbon nanotube suspension (carbon nanofluid). *Nanotechnology, 19*(31), 315701.

Aravind, S. J., Baskar, P., Baby, T. T., Sabareesh, R. K., Das, S., & Ramaprabhu, S. (2011a). Investigation of structural stability, dispersion, viscosity, and conductive heat transfer properties of functionalized carbon nanotube based nanofluids. *The Journal of Physical Chemistry C, 115*(34), 16737-16744.

Aravind, S. J., & Ramaprabhu, S. (2011b). Surfactant free graphene nanosheets based nanofluids by in-situ reduction of alkaline graphite oxide suspensions. *Journal of Applied Physics, 110*(12), 124326.

Assael, M., Chen, C.-F., Metaxa, I., & Wakeham, W. (2004). Thermal conductivity of suspensions of carbon nanotubes in water. *International Journal of Thermophysics, 25*(4), 971-985.

Assael, M., Metaxa, I., Arvanitidis, J., Christofilos, D., & Lioutas, C. (2005). Thermal conductivity enhancement in aqueous suspensions of carbon multi-walled and double-walled nanotubes in the presence of two different dispersants. *International Journal of Thermophysics, 26*(3), 647-664.

Azizi-Toupkanloo, H., Goharshadi, E. K., & Nancarrow, P. (2013). Structural, electrical, and rheological properties of palladium/silver bimetallic nanoparticles prepared by conventional and ultrasonic-assisted reduction methods. *Advanced Powder Technology, 25*(2), 801-810.

Azizian, R., Doroodchi, E., McKrell, T., Buongiorno, J., Hu, L., & Moghtaderi, B. (2014). Effect of magnetic field on laminar convective heat transfer of magnetite nanofluids. *International Journal of Heat and Mass Transfer, 68*, 94-109.

Azmi, W., Sharma, K., Sarma, P., Mamat, R., & Anuar, S. (2014). Comparison of convective heat transfer coefficient and friction factor of TiO_2 nanofluid flow in a tube with twisted tape inserts. *International Journal of Thermal Sciences, 81*, 84-93.

Baby, T. T., & Ramaprabhu, S. (2011). Synthesis and nanofluid application of silver nanoparticles decorated graphene. *Journal of Materials Chemistry, 21*(26), 9702-9709.

Batchelor, G. (1977). The effect of Brownian motion on the bulk stress in a suspension of spherical particles. *Journal of Fluid Mechanics, 83*(01), 97-117.

Behabtu, N., Young, C. C., Tsentalovich, D. E., Kleinerman, O., Wang, X., Ma, A. W., et al. (2013). Strong, light, multifunctional fibers of carbon nanotubes with ultrahigh conductivity. *Science, 339*(6116), 182-186.

Behi, M., & Mirmohammadi, S. A. (2012). *Investigation on Thermal Conductivity, Viscosity and Stability of Nanofluids.* Royal Institute of Technology (KTH).

Berger, C., Song, Z., Li, X., Wu, X., Brown, N., Naud, C., et al. (2006). Electronic confinement and coherence in patterned epitaxial graphene. *Science, 312*(5777), 1191-1196.

Bianco, V., Chiacchio, F., Manca, O., & Nardini, S. (2009). Numerical investigation of nanofluids forced convection in circular tubes. *Applied Thermal Engineering, 29*(17), 3632-3642.

Bianco, V., Manca, O., & Nardini, S. (2011). Numerical investigation on nanofluids turbulent convection heat transfer inside a circular tube. *International Journal of Thermal Sciences, 50*(3), 341-349.

Bianco, V., Manca, O., & Nardini, S. (2014). Entropy generation analysis of turbulent convection flow of Al_2O_3–water nanofluid in a circular tube subjected to constant wall heat flux. *Energy Conversion and Management, 77*(0), 306-314.

Bigelow, W. C., Pickett, D. L., & Zisman, W. A. (1946). Oleophobic monolayers: I. Films adsorbed from solution in non-polar liquids. *Journal of Colloid Science, 1*(6), 513-538.

Bitaraf Haghighi, E., Anwar, Z., Lumbreras, I., Mirmohammadi, S. A., Behi, M., Khodabandeh, R., et al. (2012). *Screening Single Phase Laminar Convective Heat Transfer of Nanofluids in a Micro-tube.* Paper presented at the Journal of Physics: Conference Series.

Branch, C. A. (1991). *Heat transfer and heat transfer fouling in evaporators with Kraft pulp black liquor.* University of Auckland.

Buongiorno, J., Venerus, D. C., Prabhat, N., McKrell, T., Townsend, J., Christianson, R., et al. (2009). A benchmark study on the thermal conductivity of nanofluids. *Journal of Applied Physics, 106*(9), 094312-094312-094314.

Cappella, B., & Dietler, G. (1999). Force-distance curves by atomic force microscopy. *Surface Science Reports, 34*(1–3), 1-104.

Chakraborty, S., & Padhy, S. (2008). Anomalous electrical conductivity of nanoscale colloidal suspensions. *ACS nano, 2*(10), 2029-2036.

Chandra Sekhara Reddy, M., & Vasudeva Rao, V. (2014). Experimental investigation of heat transfer coefficient and friction factor of ethylene glycol water based TiO_2 nanofluid in double pipe heat exchanger with and without helical coil inserts. *International Communications in Heat and Mass Transfer, 50*, 68-76.

Chang, C., & Powell, R. L. (1994). Effect of particle size distributions on the rheology of concentrated bimodal suspensions. *Journal of Rheology (1978-present), 38*(1), 85-98.

Chen, L., Xie, H., & Yu, W. (2012). Multi-walled carbon nanotube/silver nanoparticles used for thermal transportation. *Journal of Materials Science, 47*(14), 5590-5595.

Chen, Y.-j., Wang, P.-y., & Liu, Z.-h. (2013). Application of water-based SiO_2 functionalized nanofluid in a loop thermosyphon. *International Journal of Heat and Mass Transfer, 56*(1), 59-68.

Chen, Y., Lee, Y. D., Vedala, H., Allen, B. L., & Star, A. (2010). Exploring the chemical sensitivity of a carbon nanotube/green tea composite. *ACS nano, 4*(11), 6854-6862.

Chien, H.-T., Tsai, C.-I., Chen, P.-H., & Chen, P.-Y. (2003). *Improvement on thermal performance of a disk-shaped miniature heat pipe with nanofluid.* Paper presented at the Electronic Packaging Technology Proceedings, 2003. ICEPT 2003. Fifth International Conference on.

Choi, C., & Kim, M. (2011). Wettability Effects on Heat Transfer. In D. A. Ahsan (Ed.), *Two Phase Flow, Phase Change and Numerical Modeling*: intechopen.

Choi, S. U. S., & Eastman, J. (1995). *Enhancing thermal conductivity of fluids with nanoparticles*: Argonne National Lab., IL (United States).

Chu, K., Li, W.-s., & Tang, F.-l. (2013). Flatness-dependent thermal conductivity of graphene-based composites. *Physics Letters A, 377*(12), 910-914.

Colburn, A. P. (1933). A method of correlating forced convection heat transfer data and a comparison with fluid friction. *Trans Am Inst Chem Eng, 29*, 174-210.

Colebrook, C. F. (1939). Turbulent Flow in Pipes, with particular reference to the Transition Region between the Smooth and Rough Pipe Laws. *Journal of the ICE, 11*(4), 133-156.

Davarnejad, R., Barati, S., & Kooshki, M. (2013). CFD simulation of the effect of particle size on the nanofluids convective heat transfer in the developed region in a circular tube. *SpringerPlus, 2*(1), 1-6.

Deng, D., Pan, X., Yu, L., Cui, Y., Jiang, Y., Qi, J., et al. (2011). Toward N-doped graphene via solvothermal synthesis. *Chemistry of Materials, 23*(5), 1188-1193.

Ding, Y., Alias, H., Wen, D., & Williams, R. A. (2006). Heat transfer of aqueous suspensions of carbon nanotubes (CNT nanofluids). *International Journal of Heat and Mass Transfer, 49*(1), 240-250.

Dittus, F., & Boelter, L. (1930). Heat Transfer in Automobile Radiators of the Tubular Type. *University of California Publications in Engineering, 2*, 43.

Dongxiao, H., Zhaoguo, M., Daxiong, W., Canying, Z., & Haitao, Z. (2011). Thermal properties of carbon black aqueous nanofluids for solar absorption. *Nanoscale Research Letters, 6*, 457.

Ebrahimnia-Bajestan, E., Niazmand, H., Duangthongsuk, W., & Wongwises, S. (2011). Numerical investigation of effective parameters in convective heat transfer of nanofluids flowing under a laminar flow regime. *International Journal of Heat and Mass Transfer, 54*(19), 4376-4388.

Einstein, A. (1906). A new determination of molecular dimensions. *Ann. Phys, 19*(2), 289-306.

Epstein, N. (1988). Monitoring Fouling. *Proceedings of Fouling in Heat Exchangers Course, University of Auckland, New Zealand*, 5.1-5.35.

Fang, X., Fan, L., Ding, Q., Wang, X., Yao, X., Hou, J., et al. (2013). Increased thermal conductivity of eicosane-based composite phase change materials in the presence of graphene nanoplatelets. *Energy Fuels, 27*(7), 4041-4047.

Fernández-Seara, J., Uhía, F. J., Sieres, J., & Campo, A. (2007). A general review of the Wilson plot method and its modifications to determine convection coefficients in heat exchange devices. *Applied Thermal Engineering, 27*(17), 2745-2757.

Ganguly, S., Sikdar, S., & Basu, S. (2009). Experimental investigation of the effective electrical conductivity of aluminum oxide nanofluids. *Powder Technology, 196*(3), 326-330.

Gnielinski, V. (1976). New equations for heat and mass-transfer in turbulent pipe and channel flow. *International Chemical Engineering, 16*(2), 359-368.

Goharshadi, E., Azizi-Toupkanloo, H., & Karimi, M. (2014). Electrical conductivity of water-based palladium nanofluids. *Microfluidics and Nanofluidics*, 1-6.

Goharshadi, E. K., & Azizi-Toupkanloo, H. (2013). Silver colloid nanoparticles: Ultrasound-assisted synthesis, electrical and rheological properties. *Powder Technology, 237*, 97-101.

Goharshadi, E. K., & Berenji, A. R. (2006). A new equation of state for predicting the thermodynamic properties of liquid alkali metals. *Journal of nuclear materials, 348*(1), 40-44.

Goharshadi, E. K., Ding, Y., Jorabchi, M. N., & Nancarrow, P. (2009). Ultrasound-assisted green synthesis of nanocrystalline ZnO in the ionic liquid [hmim][NTf< sub> 2</sub>]. *Ultrasonics sonochemistry, 16*(1), 120-123.

Goodwin, J. W., & Hughes, R. W. (2008). *Rheology for chemists: an introduction*: Royal Society of Chemistry.

Graphene: Synthesis, Properties, and Phenomena. (2013). Wiley-VCH Verlag GmbH & Co. KGaA.

Grote, K. (2013). *The influence of multi-walled carbon nanotubes on single-phase heat transfer and pressure drop characteristics in the transitional flow regime of smooth tubes.* University of Pretoria.

Guo, H.-L., Su, P., Kang, X., & Ning, S.-K. (2013). Synthesis and characterization of nitrogen-doped graphene hydrogels by hydrothermal route with urea as reducing-doping agents. [10.1039/C2TA00887D]. *Journal of Materials Chemistry A, 1*(6), 2248-2255.

Hagen, K. D. (1999). *Heat transfer with applications*: Prentice Hall Englewood Cliffs, New Jersey, USA.

Haghighi, E. B., Saleemi, M., Nikkam, N., Khodabandeh, R., Toprak, M. S., Muhammed, M., et al. (2014). Accurate basis of comparison for convective heat transfer in nanofluids. *International Communications in Heat and Mass Transfer, 52*, 1–7.

Haghshenas Fard, M., Esfahany, M. N., & Talaie, M. R. (2010). Numerical study of convective heat transfer of nanofluids in a circular tube two-phase model versus single-phase model. *International Communications in Heat and Mass Transfer, 37*(1), 91-97.

Han, Z., & Fina, A. (2011). Thermal conductivity of carbon nanotubes and their polymer nanocomposites: a review. *Progress in polymer science, 36*(7), 914-944.

Hassan, M., Sadri, R., Ahmadi, G., Dahari, M. B., Kazi, S. N., Safaei, M. R., et al. (2013). Numerical Study of Entropy Generation in a Flowing Nanofluid Used in Micro-and Minichannels. *Entropy, 15*(1), 144-155.

Hemmat Esfe, M., Saedodin, S., Mahian, O., & Wongwises, S. (2014). Heat transfer characteristics and pressure drop of of COOH-functionalized DWCNTs/water nanofluid in turbulent flow at low concentrations. *International Journal of Heat and Mass Transfer, 73*, 186-194.

Hone, J. (2004). Carbon nanotubes: thermal properties. *J. Nanosci. Nanotechnol, 6*, 603-610.

Hwang, Y., Lee, J.-K., Lee, J.-K., Jeong, Y.-M., Cheong, S.-i., Ahn, Y.-C., et al. (2008). Production and dispersion stability of nanoparticles in nanofluids. *Powder Technology, 186*(2), 145-153.

Hwang, Y., Lee, J., Lee, C., Jung, Y., Cheong, S., Lee, C., et al. (2007). Stability and thermal conductivity characteristics of nanofluids. *Thermochimica Acta, 455*(1), 70-74.

Iijima, S. (1991). Helical microtubules of graphitic carbon. *nature, 354*(6348), 56-58.

Jang, S. P., & Choi, S. U. (2004). Role of Brownian motion in the enhanced thermal conductivity of nanofluids. *Applied physics letters, 84*(21), 4316-4318.

Kakaç, S., & Pramuanjaroenkij, A. (2009). Review of convective heat transfer enhancement with nanofluids. *International Journal of Heat and Mass Transfer, 52*(13–14), 3187-3196.

Kalteh, M., Abbassi, A., Saffar-Avval, M., & Harting, J. (2011). Eulerian–Eulerian two-phase numerical simulation of nanofluid laminar forced convection in a microchannel. *International journal of heat and fluid flow, 32*(1), 107-116.

Kayhani, M., Soltanzadeh, H., Heyhat, M., Nazari, M., & Kowsary, F. (2012). Experimental study of convective heat transfer and pressure drop of TiO_2 water nanofluid. *International Communications in Heat and Mass Transfer, 39*(3), 456-462.

Kazi, S. N. (2001). *Heat transfer to fibre suspensions : studies in fibre characterisation and fouling mitigation.* University of Auckland.

Kazi, S. N., Duffy, G. G., & Chen, X. D. (2014). Validation of heat transfer and friction loss data for fibre suspensions in a circular and a coaxial pipe heat exchanger. *International Journal of Thermal Sciences, 79*, 146-160.

Keblinski, P., Eastman, J. A., & Cahill, D. G. (2005). Nanofluids for thermal transport. *Materials Today, 8*(6), 36-44.

Kim, D., Kwon, Y., Cho, Y., Li, C., Cheong, S., Hwang, Y., et al. (2009). Convective heat transfer characteristics of nanofluids under laminar and turbulent flow conditions. *Current Applied Physics, 9*(2), e119-e123.

Kim, P., Shi, L., Majumdar, A., & McEuen, P. (2001). Thermal transport measurements of individual multiwalled nanotubes. *Physical review letters, 87*(21), 215502.

Kole, M., & Dey, T. K. (2013). Enhanced thermophysical properties of copper nanoparticles dispersed in gear oil. *Applied Thermal Engineering, 56*(1–2), 45-53.

Krieger, I. M., & Dougherty, T. J. (1959). A mechanism for non-Newtonian flow in suspensions of rigid spheres. *Transactions of The Society of Rheology (1957-1977), 3*(1), 137-152.

Kroto, H., & Heath, J. (1985). 0’Brien S, et a1. C60: Buckminsterfullerene. *Nature, 3*(18), 162-163.

Kumar, V., & Nigam, K. D. P. (2012). Process intensification in green synthesis. *Green Processing and Synthesis, 1*(1), 79-107.

Kumaresan, V., Mohaideen Abdul Khader, S., Karthikeyan, S., & Velraj, R. (2013). Convective heat transfer characteristics of CNT nanofluids in a tubular heat exchanger of various lengths for energy efficient cooling/heating system. *International Journal of Heat and Mass Transfer, 60*, 413-421.

Larson, R. G. (2005). The rheology of dilute solutions of flexible polymers: Progress and problems. *Journal of Rheology (1978-present), 49*(1), 1-70.

Launder, B., & Sharma, B. (1974). Application of the energy-dissipation model of turbulence to the calculation of flow near a spinning disc. *Letters Heat Mass Transfer, 1*, 131-137.

Launder, B. E., & Spalding, D. (1974). The numerical computation of turbulent flows. *Computer methods in applied mechanics and engineering, 3*(2), 269-289.

Lee, D. (2007). Thermophysical properties of interfacial layer in nanofluids. *Langmuir, 23*(11), 6011-6018.

Lee, G.-J., & Rhee, C. K. (2014). Enhanced thermal conductivity of nanofluids containing graphene nanoplatelets prepared by ultrasound irradiation. *Journal of Materials Science, 49*(4), 1506-1511.

Lee, J.-H., Lee, S.-H., Choi, C. J., Jang, S. P., & Choi, S. U. (2010). A review of thermal conductivity data, mechanisms and models for nanofluids. *International Journal of Micro-Nano Scale Transport, 1*(4), 269-322.

Lee, K. J., Yoon, S. H., & Jang, J. (2007). Carbon nanofibers: a novel nanofiller for nanofluid applications. *Small, 3*(7), 1209-1213.

Lee, S. W., Kim, K. M., & Bang, I. C. (2013). Study on flow boiling critical heat flux enhancement of graphene oxide/water nanofluid. *International Journal of Heat and Mass Transfer, 65*, 348-356.

Lee, S. W., Park, S. D., Kang, S., Bang, I. C., & Kim, J. H. (2011). Investigation of viscosity and thermal conductivity of SiC nanofluids for heat transfer applications. *International Journal of Heat and Mass Transfer, 54*(1–3), 433-438.

Li, N., Wang, Z., Zhao, K., Shi, Z., Gu, Z., & Xu, S. (2010). Large scale synthesis of N-doped multi-layered graphene sheets by simple arc-discharge method. *Carbon, 48*(1), 255-259.

Li, X., Wang, H., Robinson, J. T., Sanchez, H., Diankov, G., & Dai, H. (2009). Simultaneous nitrogen doping and reduction of graphene oxide. *Journal of the American Chemical Society, 131*(43), 15939-15944.

LotfizadehDehkordi, B., Kazi, S., Hamdi, M., Ghadimi, A., Sadeghinezhad, E., & Metselaar, H. (2013). Investigation of viscosity and thermal conductivity of alumina nanofluids with addition of SDBS. *Heat and Mass Transfer, 49*(8), 1109-1115.

Lu, Y., Zhang, F., Zhang, T., Leng, K., Zhang, L., Yang, X., et al. (2013). Synthesis and supercapacitor performance studies of N-doped graphene materials using o-phenylenediamine as the double-N precursor. *Carbon, 63*(0), 508-516.

Luckham, P. F., & Ukeje, M. A. (1999). Effect of particle size distribution on the rheology of dispersed systems. *Journal of colloid and interface science, 220*(2), 347-356.

Lv, R., Li, Q., Botello-Méndez, A. R., Hayashi, T., Wang, B., Berkdemir, A., et al. (2012). Nitrogen-doped graphene: beyond single substitution and enhanced molecular sensing. *Scientific reports, 2*.

Madhesh, D., Parameshwaran, R., & Kalaiselvam, S. (2014). Experimental investigation on convective heat transfer and rheological characteristics of Cu–TiO_2 hybrid nanofluids. *Experimental Thermal and Fluid Science, 52*, 104-115.

Mahmoudi, A. H., Shahi, M., & Talebi, F. (2012). Entropy generation due to natural convection in a partially open cavity with a thin heat source subjected to a nanofluid. *Numerical Heat Transfer, Part A: Applications, 61*(4), 283-305.

Mansour, R. B., Galanis, N., & Nguyen, C. T. (2007). Effect of uncertainties in physical properties on forced convection heat transfer with nanofluids. *Applied Thermal Engineering, 27*(1), 240-249.

Marcano, D. C., Kosynkin, D. V., Berlin, J. M., Sinitskii, A., Sun, Z., Slesarev, A., et al. (2010). Improved Synthesis of Graphene Oxide. *ACS Nano, 4*(8), 4806-4814.

Marquis, F., & Chibante, L. (2005). Improving the heat transfer of nanofluids and nanolubricants with carbon nanotubes. *Jom, 57*(12), 32-43.

Martinelli, R. C. (1947). Heat transfer to molten metals. *Trans. ASME, 69*(8), 947.

Maruyama, H., Tomita, K., Kariya, R., & Arai, F. (2011). *Evaluation method of thermal conductivity of single carbon nanotube in liquid using quantum dot hydrogel sensor.* Paper presented at the Nanotechnology (IEEE-NANO), 2011 11th IEEE Conference on.

Mehrali, M., Latibari, S. T., Mehrali, M., Indra Mahlia, T. M., & Cornelis Metselaar, H. S. (2013a). Preparation and properties of highly conductive palmitic acid/graphene oxide composites as thermal energy storage materials. *Energy, 58*, 628-634.

Mehrali, M., Latibari, S. T., Mehrali, M., Mahlia, T. M. I., Metselaar, H. S. C., Naghavi, M. S., et al. (2013b). Preparation and characterization of palmtic acid/ graphene nanoplatelets composite with remarkable thermal conductivity as a novel shape-stabilized phase change material. *Applied Thermal Engineering, 61*(3), 633–640.

Mehrali, M., Latibari, S. T., Mehrali, M., Metselaar, H. S. C., & Silakhori, M. (2013c). Shape-stabilized phase change materials with high thermal conductivity based on paraffin/graphene oxide composite. *Energy Conversion and Management, 67*, 275-282.

Mehrali, M., Moghaddam, E., Seyed Shirazi, S. F., Baradaran, S., Mehrali, M., Tahan Latibari, S., et al. (2014a). Synthesis, mechanical properties and in vitro biocompatibility with osteoblasts of calcium silicate–reduced graphene oxide composites. *ACS applied materials & interfaces, 6*(6), 3947–3962.

Mehrali, M., Sadeghinezhad, E., Tahan Latibari, S., Kazi, S. N., Mehrali, M., Zubir, M. N. B. M., et al. (2014a). Investigation of thermal conductivity and rheological properties of nanofluids containing graphene nanoplatelets. *Nanoscale Research Letters, 9*(1), 1-12.

Mehrali, M., Sadeghinezhad, E., Tahan Latibari, S., Mehrali, M., Togun, H., Zubir, M. N. M., et al. (2014b). Preparation, characterization, viscosity, and thermal conductivity of nitrogen-doped graphene aqueous nanofluids. *Journal of Materials Science, 49*(20), 7156-7171.

Mehrali, M., Seyed Shirazi, S. F., Baradaran, S., Mehrali, M., Metselaar, H. S. C., Kadri, N. A. B., et al. (2014b). Facile synthesis of calcium silicate hydrate using sodium dodecyl sulfate as a surfactant assisted by ultrasonic irradiation. *Ultrasonics sonochemistry, 21*(2), 735-742.

Memari, M., Golmakani, A., & Dehkordi, A. M. (2011). Mixed-convection flow of nanofluids and regular fluids in vertical porous media with viscous heating. *Industrial & Engineering Chemistry Research, 50*(15), 9403-9414.

Menter, F. R. (1993). Zonal Two Equation k- Turbulence Models for Aerodynamic Flows. *AIAA Paper #93-2906, 24th Fluid Dynamics Conference, July 1993*

Minea, A. A., & Luciu, R. S. (2012). Investigations on electrical conductivity of stabilized water based Al_2O_3 nanofluids. *Microfluidics and nanofluidics, 13*(6), 977-985.

Moffat, R. J. (1988). Describing the uncertainties in experimental results. *Experimental Thermal and Fluid Science, 1*(1), 3-17.

Moghaddam, M. B., Goharshadi, E. K., Entezari, M. H., & Nancarrow, P. (2013). Preparation, characterization, and rheological properties of graphene–glycerol nanofluids. *Chemical Engineering Journal, 231*, 365-372.

Nabeel Rashin, M., & Hemalatha, J. (2013). Synthesis and viscosity studies of novel ecofriendly ZnO–coconut oil nanofluid. *Experimental Thermal and Fluid Science, 51*(0), 312-318.

Nadagouda, M. N., & Varma, R. S. (2008). Green synthesis of silver and palladium nanoparticles at room temperature using coffee and tea extract. *Green Chemistry, 10*(8), 859-862.

Nanda, J., Maranville, C., Bollin, S. C., Sawall, D., Ohtani, H., Remillard, J. T., et al. (2008). Thermal conductivity of single-wall carbon nanotube dispersions: role of interfacial effects. *The Journal of Physical Chemistry C, 112*(3), 654-658.

Nasiri, A., Shariaty-Niasar, M., Rashidi, A. M., & Khodafarin, R. (2012). Effect of CNT structures on thermal conductivity and stability of nanofluid. *International Journal of Heat and Mass Transfer, 55*(5–6), 1529-1535.

Navrátilová, Z., & Maršálek, R. (2012). Application of Electrochemistry for Studying Sorption Properties of Montmorillonite. In D. M. Valaskova (Ed.), *Clay Minerals in Nature - Their Characterization, Modification and Application* (pp. 273-294): InTech.

Nieto de Castro, C. A., Murshed, S. M. S., Lourenço, M. J. V., Santos, F. J. V., Lopes, M. L. M., & França, J. M. P. (2012). Enhanced thermal conductivity and specific heat capacity of carbon nanotubes ionanofluids. *International Journal of Thermal Sciences, 62*(0), 34-39.

Nikuradse, J. (1933). Strömungsgesetze in Rauhen Rohren ForschHft. *Ver. Dt. Ing, 361*.

Nikuradse, V. (1932). gesetzmabigkeiten der turbulent stromung in glatten rohren. *Forschungsheft, 356*.

Novoselov, K., Geim, A. K., Morozov, S., Jiang, D., Zhang, Y., Dubonos, S., et al. (2004). Electric field effect in atomically thin carbon films. *Science, 306*(5696), 666-669.

Nune, S. K., Chanda, N., Shukla, R., Katti, K., Kulkarni, R. R., Thilakavathy, S., et al. (2009). Green nanotechnology from tea: phytochemicals in tea as building blocks for production of biocompatible gold nanoparticles. *Journal of materials chemistry, 19*(19), 2912-2920.

Özerinç, S., Kakaç, S., & Yazıcıoğlu, A. G. (2010). Enhanced thermal conductivity of nanofluids: a state-of-the-art review. *Microfluidics and Nanofluidics, 8*(2), 145-170.

Panchakarla, L. S., Subrahmanyam, K. S., Saha, S. K., Govindaraj, A., Krishnamurthy, H. R., Waghmare, U. V., et al. (2009). Synthesis, Structure, and Properties of Boron- and Nitrogen-Doped Graphene. *Advanced Materials, 21*(46), 4726-4730.

Patankar, S. (1980). *Numerical heat transfer and fluid flow*: CRC Press.

Paul, G., Chopkar, M., Manna, I., & Das, P. (2010). Techniques for measuring the thermal conductivity of nanofluids: a review. *Renewable and Sustainable Energy Reviews, 14*(7), 1913-1924.

Petukhov, B., & Kirilov, V. (1958). The problem of heat exchange in the turbulent flow of liquids in tubes. *Teploenergetika, 4*(4), 63-68.

Popiel, C. O., & Wojtkowiak, J. (1998). Simple Formulas for Thermophysical Properties of Liquid Water for Heat Transfer Calculations (from 0°C to 150°C). *Heat Transfer Engineering, 19*(3), 87-101.

Powell, R. (1957). Experiments using a simple thermal comparator for measurement of thermal conductivity, surface roughness and thickness of foils or of surface deposits. *Journal of Scientific Instruments, 34*(12), 485.

Pradhan, N. R. (2010). Thermal Conductivity of Nanowires. *Nanotubes and Polymer-Nanotube Composites*.

Prandtl, L. (1960). *Führer durch die Strömungslehre*: F. Vieweg.

Rahgoshay, M., Ranjbar, A., & Ramiar, A. (2012). Laminar pulsating flow of nanofluids in a circular tube with isothermal wall. *International Communications in Heat and Mass Transfer, 39*(3), 463-469.

Ramanathan, T., Abdala, A., Stankovich, S., Dikin, D., Herrera-Alonso, M., Piner, R., et al. (2008). Functionalized graphene sheets for polymer nanocomposites. *Nature Nanotechnology, 3*(6), 327-331.

Ramires, M. L., de Castro, C. A. N., Nagasaka, Y., Nagashima, A., Assael, M. J., & Wakeham, W. A. (1995). Standard reference data for the thermal conductivity of water. *Journal of Physical and Chemical Reference Data, 24*, 1377.

Rea, U., McKrell, T., Hu, L.-w., & Buongiorno, J. (2009). Laminar convective heat transfer and viscous pressure loss of alumina–water and zirconia–water nanofluids. *International Journal of Heat and Mass Transfer, 52*(7–8), 2042-2048.

Roetzel, W., Prinzen, S., & Xuan, Y. (1990). *Measurement of thermal diffusivity using temperature oscillations.* Paper presented at the Proceeding of the Twenty-First International Thermal conductivity, Lexington, Kentucky.

Rohsenow, W. M., Hartnett, J. P., & Ganic, E. N. (1985). Handbook of heat transfer applications. *New York, McGraw-Hill Book Co., 1985, 973 p. No individual items are abstracted in this volume., 1.*

Roy, G., Gherasim, I., Nadeau, F., Poitras, G., & Nguyen, C. T. (2012). Heat transfer performance and hydrodynamic behavior of turbulent nanofluid radial flows. *International Journal of Thermal Sciences, 58*(0), 120-129.

Sadeghinezhad, E., Mehrali, M., Tahan Latibari, S., Mehrali, M., Kazi, S. N., Oon, S., et al. (2014). Experimental investigation of convective heat transfer using graphene nanoplatelet based nanofluids under turbulent flow conditions. *Industrial & Engineering Chemistry Research, 53*(31), 12455–12465.

Sadeghinezhad, E., Togun, H., Mehrali, M., Sadeghi Nejad, P., Tahan Latibari, S., Abdulrazzaq, T., et al. (2015). An experimental and numerical investigation of heat transfer enhancement for graphene nanoplatelets nanofluids in turbulent flow conditions. *International Journal of Heat and Mass Transfer, 81*, 41-51.

Sadri, R., Ahmadi, G., Togun, H., Dahari, M., Kazi, S. N., Sadeghinezhad, E., et al. (2014). An experimental study on thermal conductivity and viscosity of nanofluids containing carbon nanotubes. *Nanoscale Research Letters, 9*(1), 151.

Schlichting, H., & Gersten, K. (2000). *Boundary-layer theory*: Springer.

Sen Gupta, S., Manoj Siva, V., Krishnan, S., Sreeprasad, T., Singh, P. K., Pradeep, T., et al. (2011). Thermal conductivity enhancement of nanofluids containing graphene nanosheets. *Journal of Applied Physics, 110*(8), 084302-084302-084306.

Sengupta, R., Bhattacharya, M., Bandyopadhyay, S., & Bhowmick, A. K. (2011). A review on the mechanical and electrical properties of graphite and modified graphite reinforced polymer composites. *Progress in Polymer Science, 36*(5), 638-670.

Shames, I. H., & Shames, I. H. (1982). *Mechanics of fluids*: McGraw-Hill New York, NY.

Shanbedi, M., Heris, S. Z., Baniadam, M., Amiri, A., & Maghrebi, M. (2012). Investigation of heat-transfer characterization of EDA-MWCNT/DI-water nanofluid in a two-phase closed thermosyphon. *Industrial & Engineering Chemistry Research, 51*(3), 1423-1428.

Shao, Y., Zhang, S., Wang, C., Nie, Z., Liu, J., Wang, Y., et al. (2010). Highly durable graphene nanoplatelets supported Pt nanocatalysts for oxygen reduction. *Journal of Power Sources, 195*(15), 4600-4605.

Sun, Z., Pöller, S., Huang, X., Guschin, D., Taetz, C., Ebbinghaus, P., et al. (2013). High-yield exfoliation of graphite in acrylate polymers: a stable few-layer graphene nanofluid with enhanced thermal conductivity. *Carbon*.

Sundar, L. S., & Sharma, K. (2007). Thermal Conductivity Enhancement of Metallic Oxide Nanoparticles in Distilled Water. *International Journal of Materials Science, 2*(3).

Symon, K. (1971). *Mechanics* (Vol. 3rd Edition): Addison Wesley.

Taylor, J. R. (1997). *An introduction to error analysis: the study of uncertainties in physical measurements*: University science books.

Thakur, S., & Karak, N. (2012). Green reduction of graphene oxide by aqueous phytoextracts. *Carbon, 50*(14), 5331-5339.

Togun, H., Safaei, M. R., Sadri, R., Kazi, S. N., Badarudin, A., Hooman, K., et al. (2014). Numerical simulation of laminar to turbulent nanofluid flow and heat transfer over a backward-facing step. *Applied Mathematics and Computation, 239*, 153-170.

Tong, X., Wang, H., Wang, G., Wan, L., Ren, Z., Bai, J., et al. (2011). Controllable synthesis of graphene sheets with different numbers of layers and effect of the number of graphene layers on the specific capacity of anode material in lithium-ion batteries. *Journal of Solid State Chemistry, 184*(5), 982-989.

Tsai, C., Chien, H., Ding, P., Chan, B., Luh, T., & Chen, P. (2004). Effect of structural character of gold nanoparticles in nanofluid on heat pipe thermal performance. *Materials Letters, 58*(9), 1461-1465.

Vandsburger, L. (2010). *Synthesis and Covalent Surface Modification of Carbon Nanotubes for Preparation of Stabilized Nanofluid Suspensions*.

Von Karman, T. (2012). Turbulence and skin friction. *Journal of the Aeronautical Sciences (Institute of the Aeronautical Sciences), 1*(1).

Wakeland, S., Martinez, R., Grey, J. K., & Luhrs, C. C. (2010). Production of graphene from graphite oxide using urea as expansion–reduction agent. *Carbon, 48*(12), 3463-3470.

Wang, B., Hao, J., & Li, H. (2013). Remarkable improvements in the stability and thermal conductivity of graphite/ethylene glycol nanofluids caused by a graphene oxide percolation structure. *Dalton Transactions*.

Wang, Y., Shi, Z., & Yin, J. (2011). Facile synthesis of soluble graphene via a green reduction of graphene oxide in tea solution and its biocomposites. *ACS applied materials & interfaces, 3*(4), 1127-1133.

Wehling, T., Novoselov, K., Morozov, S., Vdovin, E., Katsnelson, M., Geim, A., et al. (2008). Molecular doping of graphene. *Nano letters, 8*(1), 173-177.

Wei, D., Liu, Y., Wang, Y., Zhang, H., Huang, L., & Yu, G. (2009). Synthesis of N-doped graphene by chemical vapor deposition and its electrical properties. *Nano letters, 9*(5), 1752-1758.

Wen, D., & Ding, Y. (2004a). Effective thermal conductivity of aqueous suspensions of carbon nanotubes (carbon nanotube nanofluids). *Journal of Thermophysics and Heat Transfer, 18*(4), 481-485.

Wen, D., & Ding, Y. (2004b). Experimental investigation into convective heat transfer of nanofluids at the entrance region under laminar flow conditions. *International journal of heat and mass transfer, 47*(24), 5181-5188.

Wilson, E. E. (1915). A basis for rational design of heat transfer apparatus. *Trans. ASME, 37*(47), 47-82.

Wong, K.-L., Salazar, J. L. L., Prasad, L., & Chen, W.-L. (2011). The inaccuracy of heat transfer characteristics for non-insulated and insulated spherical containers neglecting the influence of heat radiation. [doi: 10.1016/j.enconman.2010.10.016]. *Energy conversion and management, 52*(3), 1612-1621.

Wu, K.-J., Zhao, C.-X., Xu, G.-H., & He, C.-H. (2012). Investigation of convective heat transfer with liquids in microtubes. *Industrial & Engineering Chemistry Research, 51*(27), 9386-9395.

Xuan, Y., & Li, Q. (2003). Investigation on convective heat transfer and flow features of nanofluids. *Journal of Heat transfer, 125*(1), 151-155.

Yang, P., Li, X., Yang, H., Wang, X., Tang, Y., & Yuan, X. (2013). Numerical investigation on thermal conductivity and thermal rectification in graphene through nitrogen-doping engineering. *Applied Physics A, 112*(3), 759-765.

Yang, Y., Zhang, Z. G., Grulke, E. A., Anderson, W. B., & Wu, G. (2005). Heat transfer properties of nanoparticle-in-fluid dispersions (nanofluids) in laminar flow. *International Journal of Heat and Mass Transfer, 48*(6), 1107-1116.

Yasmin, A., Luo, J.-J., & Daniel, I. M. (2006). Processing of expanded graphite reinforced polymer nanocomposites. *Composites Science and Technology, 66*(9), 1182-1189.

Yeganeh, M., Shahtahmasebi, N., Kompany, A., Goharshadi, E. K., Youssefi, A., & Šiller, L. (2010). Volume fraction and temperature variations of the effective thermal conductivity of nanodiamond fluids in deionized water. *International Journal of Heat and Mass Transfer, 53*(15–16), 3186-3192.

Yousefi, T., Shojaeizadeh, E., Veysi, F., & Zinadini, S. (2012). An experimental investigation on the effect of pH variation of MWCNT–H_2O nanofluid on the efficiency of a flat-plate solar collector. *Solar Energy, 86*(2), 771-779.

Yu, W., & Choi, S. (2003). The role of interfacial layers in the enhanced thermal conductivity of nanofluids: a renovated Maxwell model. *Journal of Nanoparticle Research, 5*(1-2), 167-171.

Yu, W., France, D., Timofeeva, E., Singh, D., & Routbort, J. (2010). Thermophysical property-related comparison criteria for nanofluid heat transfer enhancement in turbulent flow. *Applied Physics Letters, 96*(21), 213109.

Yu, W., Xie, H., & Bao, D. (2010). Enhanced thermal conductivities of nanofluids containing graphene oxide nanosheets. *Nanotechnology, 21*(5), 055705.

Yu, W., Xie, H., Wang, X., & Wang, X. (2011). Significant thermal conductivity enhancement for nanofluids containing graphene nanosheets. *Physics Letters A, 375*(10), 1323-1328.

Yunus, A. C. (2003). Heat transfer: a practical approach. *MacGraw-Hill*.

Zeinali Heris, S., Etemad, S. G., & Nasr Esfahany, M. (2006). Experimental investigation of oxide nanofluids laminar flow convective heat transfer. *International Communications in Heat and Mass Transfer, 33*(4), 529-535.

Zhang, Y., Ma, H.-L., Zhang, Q., Peng, J., Li, J., Zhai, M., et al. (2012). Facile synthesis of well-dispersed graphene by γ-ray induced reduction of graphene oxide. *Journal of Materials Chemistry, 22*(26), 13064-13069.

Zheng, R., Gao, J., Wang, J., Feng, S.-P., Ohtani, H., Wang, J., et al. (2011). Thermal percolation in stable graphite suspensions. *Nano letters, 12*(1), 188-192.

Zhi, C., Xu, Y., Bando, Y., & Golberg, D. (2011). Highly Thermo-conductive Fluid with Boron Nitride Nanofillers. *ACS nano, 5*(8), 6571-6577.

Zhou, S.-Q., & Ni, R. (2008). Measurement of the specific heat capacity of water-based Al_2O_3 nanofluid. *Applied Physics Letters, 92*(9), 093123-093123-093123.

Zhu, H., Li, C., Wu, D., Zhang, C., & Yin, Y. (2010). Preparation, characterization, viscosity and thermal conductivity of CaCO3 aqueous nanofluids. *Science China Technological Sciences, 53*(2), 360-368.

APPENDIX A

CALIBRATION METHODS

A.1 Calibration of the test section

A.1.1 Heated section

The thermocouples for measuring surface temperatures are cautiously installed a little away from the inside contact face of heat transfer surface so that there is no interruption of boundary layer. The present investigation has used the same technique.

Figure A.1 presents a close-up view of the heater wall of pipe flow test rig. As the wall thermocouple cannot measure the exact temperature at the surface of the pipe without disturbing the flow, the thermocouples were installed a small distance away from the heater wall. A calibration experiment was carried out to determine the temperature drop between the thermocouple and the surface. The wall resistance was determined using a Wilson plot (Fernández-Seara, et al., 2007; Kazi, 2001).

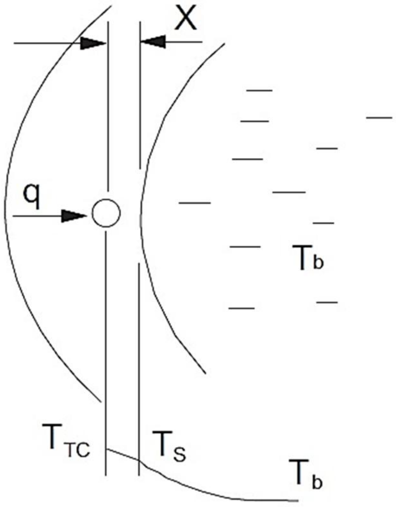

Figure A.1 Temperature drop through the heated wall.

The temperature profile between the thermocouple and the fluid inside the circular pipe is also shown in Figure A.1. With an energy balance around the thermocouple, the resistance could be estimated so a steady-state energy balance around the thermocouple results in Equation (A.1).

$$\dot{q} = U(T_{TC} - T_b) = \frac{\lambda}{x}(T_{TC} - T_w) = h_c(T_w - T_b) \tag{A.1}$$

The Equation (A.1) can be rearranged to give the overall heat transfer coefficient U, in terms of h_c, x and λ as shown in equation (A.2).

$$\frac{1}{U} = \frac{1}{h_c} + \frac{x}{\lambda} \tag{A.2}$$

The aim of the Wilson plot technique is to calculate the term λ/x shown in Equation (A.2). A rearrangement of equation (A1.9) results in the following Equation (A.3) for the overall heat transfer coefficient U.

$$U = \frac{\dot{q}}{(T_{TC} - T_b)} \tag{A.3}$$

It can be observed that U is a function of the thermocouple and bulk temperatures, which are measurable quantities. The remaining quantities to be measured in equation (A.2) are h_c and λ/x. The film heat transfer coefficient h_c is a function of liquid velocity. A simple rearrangement of the Dittus- Boelter correlation for convective heat transfer under fully developed turbulent flow conditions results in the relationship stated in equation (A.4).

$$h_c = Ku^{0.8} \tag{A.4}$$

where, K is a constant and u is the flow velocity.

Equation (A.4) is only valid if one assumes constant physical properties. Substituting equation (A.4) into equation (A.2) in order to give the heat transfer coefficient as a function of the wall resistance and the bulk velocity, results in the following equation (A.5).

$$\frac{1}{U}=\frac{1}{K}u^{-0.8}+\frac{x}{\lambda} \tag{A.5}$$

Therefore a plot of 1/U versus $1/u^{0.8}$ for each thermocouple should give a straight line of slope 1/K and y-intercept λ/x. This is the basis of the Wilson plot technique. However there remains some confusion as to what exponent of u to use. Wilson (1915) in his paper suggested to use $u^{-0.82}$. Branch (1991) used $u^{-0.75}$ with success. Epstein (1988) suggested that more reliable values of the intercept could be found if the exponent on the velocity term was found by least squares analysis of the data. It should be noted that the velocity exponent is a function of the Prandtl number. It ranges from 0.78 at Pr = 0.7 to 0.90 at Pr = 100 for Re = 5×10^4 (Rohsenow et al., 1985).

In the present investigation the method of non-linear regression suggested by Epstein (1988) was used. Calibration data for the test section with water as the test fluid are plotted in Wilson plot form in Figure A.2 to Figure A.4. The values of wall resistances (λ/x) were obtained from intercepts on y axes of Figure A.2 to Figure A.4. The values of the exponents n along with λ/x values are presented in Table A.1.

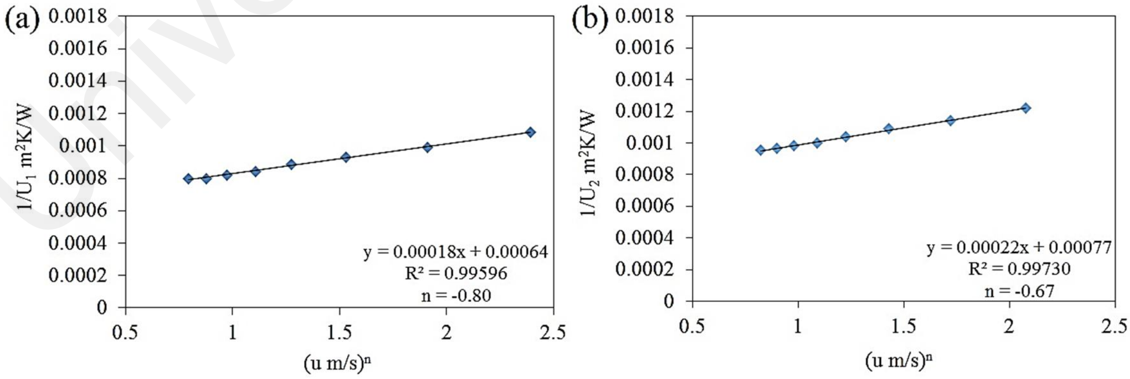

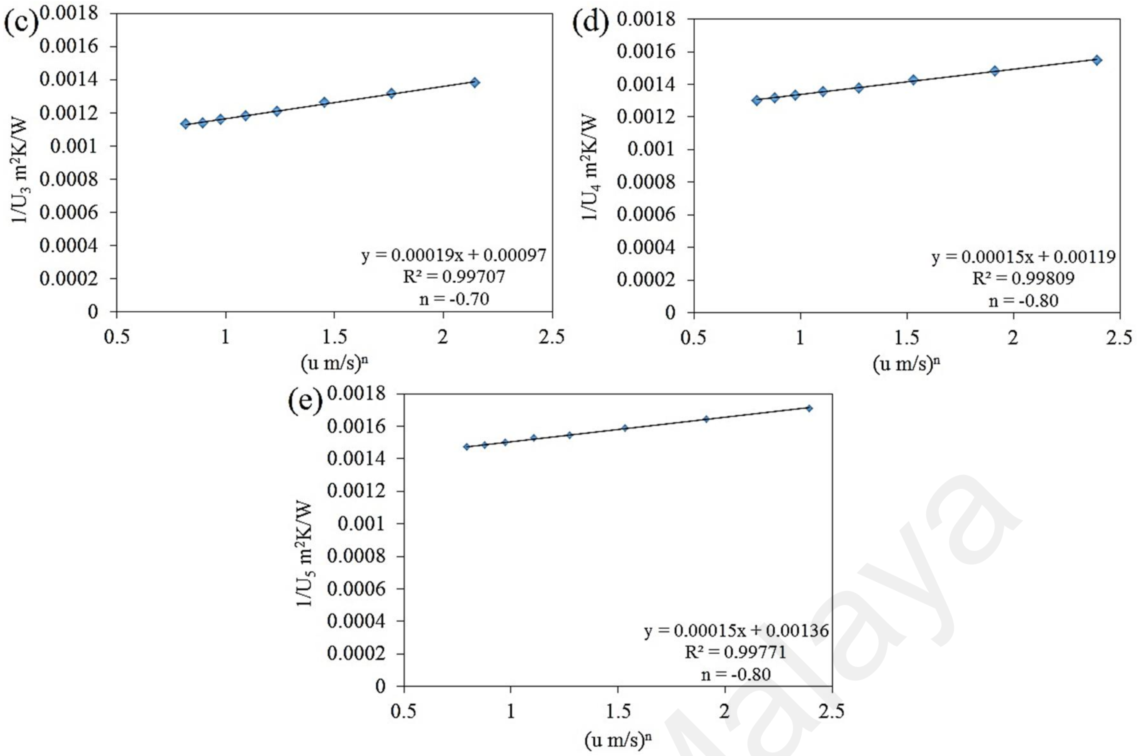

Figure A.2 1/U as a function of u^n for the thermocouples (a) number 1, (b) number 2, (c) number 3, (d) number 4, and (d) number 5. The calibration experiment was conducted with DW at bulk temperature 30℃, and heat flux 8,231 W/m^2

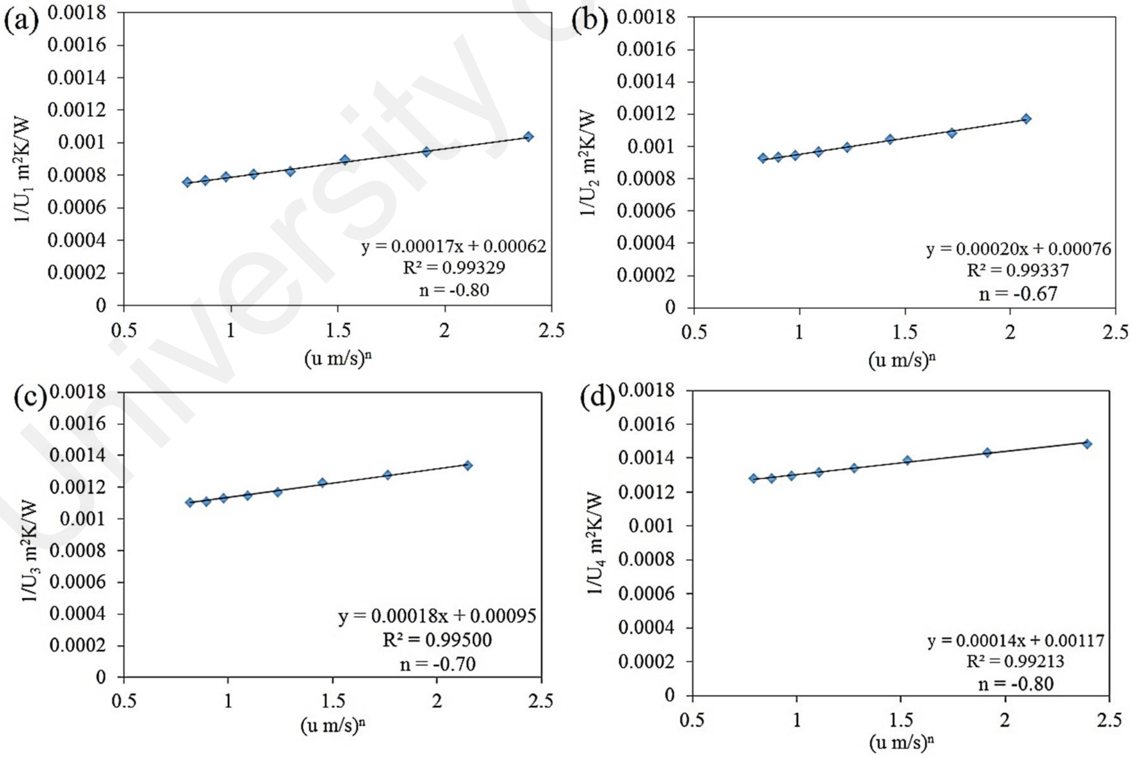

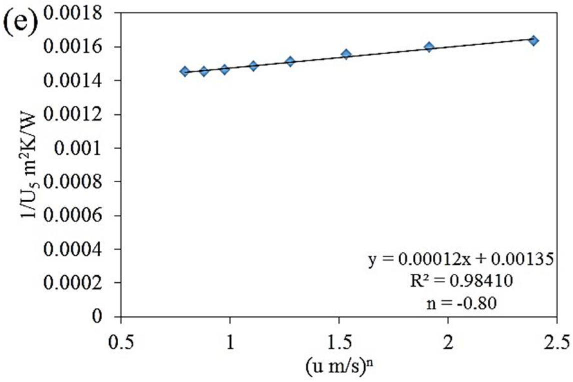

Figure A.3 1/U as a function of u^n for the thermocouples (a) number 1, (b) number 2, (c) number 3, (d) number 4, and (d) number 5. The calibration experiment was conducted with DW at bulk temperature 30℃, and heat flux 10,351 W/m^2

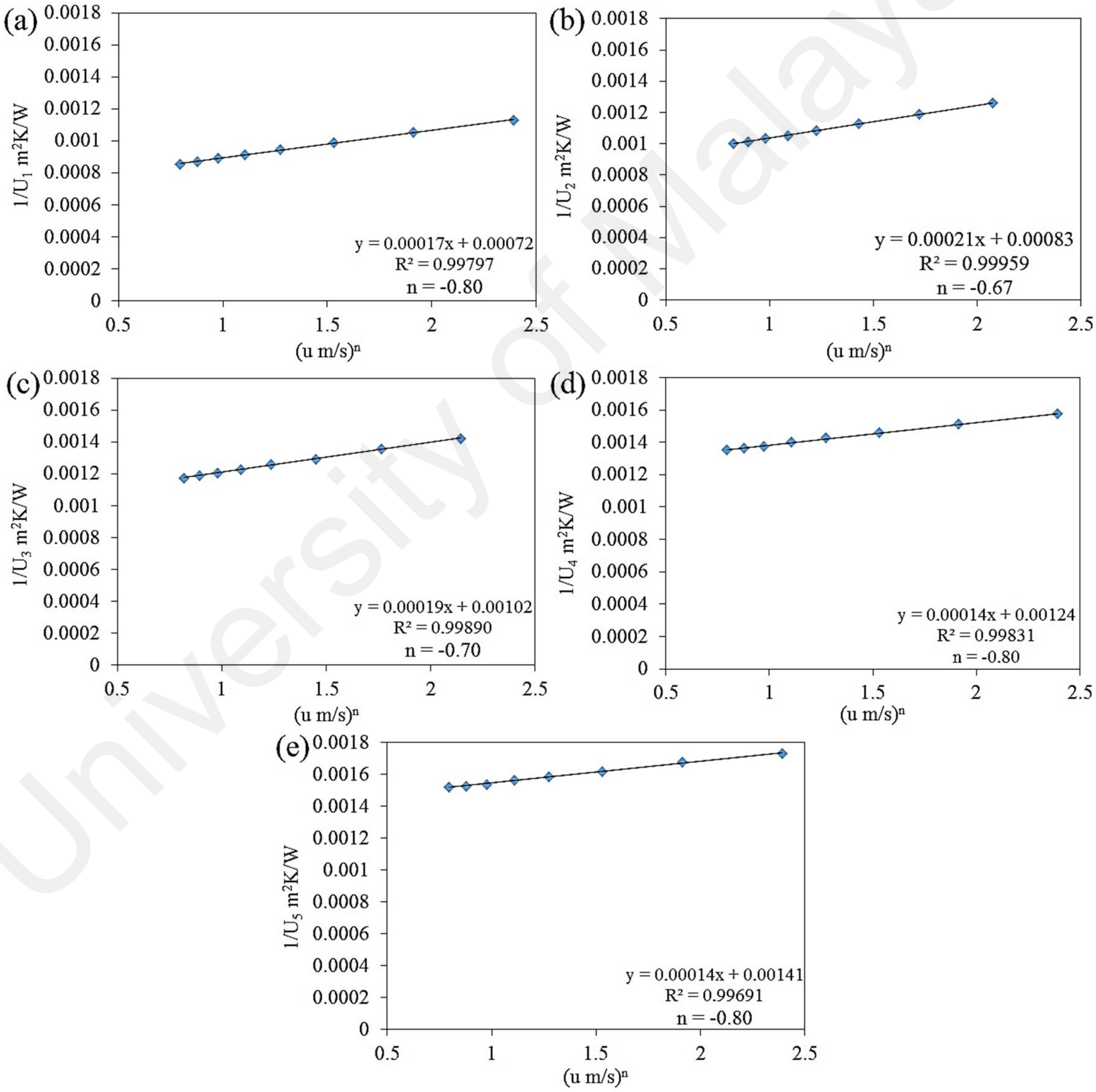

Figure A.4 1/U as a function of u^n for the thermocouples (a) number 1, (b) number 2, (c) number 3, (d) number 4, and (d) number 5. The calibration experiment was conducted with DW at bulk temperature 30℃, and heat flux 12,320 W/m^2

Table A.1 λ/x value of each thermocouple installed at the test section

Thermocouple number	Wall resistance (λ/x) W/m^2K		
	8,231 W/m^2	10,351 W/m^2	12,320 W/m^2
1	1538.46	1463.675	1388.89
2	1234.57	1198.68	1162.79
3	1010.1	990.487	970.874
4	862.069	847.701	833.333
5	751.88	743.587	735.294

APPENDIX B

UNCERTAINTY ANALYSIS

B.1 Introduction

In order to obtain the desired objectives of the current study, it is necessary to obtain heat transfer and friction factors for a constant heat flux boundary condition. In order to determine the accuracy of these two parameters an uncertainty analysis is performed as well as for the non-dimensional parameters such as the Reynolds and Nusselt numbers. In the case of the heat transfer parameter, the uncertainty of the heat transferred, the energy balance obtained, mass flow rates, inlet, outlet and wall temperatures are analyzed. For the friction factors the uncertainty of the differential pressure transducer, mass flow rates and dimensions of the test section are analyzed.

B.2 Theory

The result R of the experiment is calculated from a set of measurements using a group of equations. The result R is a function of several variables and is given by Moffat (1988) as:

$$R = f\,cn(x_1, x_2, \ldots, x_n) \tag{B.1}$$

Hence the effect of the uncertainty in a single measurement on the calculated result, if only that one measurement were in error, then it would be:

$$\delta R = \frac{\partial R}{\partial x_i} \cdot \delta x_i \tag{B.2}$$

The partial derivative of R with respect to x_i is the sensitivity coefficient for the result R with respect to the measurement x_i. For several independent variables, the uncertainty of R can be found by a root-sum-square method. Hence for several independent variables the uncertainty of R is described by Moffat (1988) as:

$$\delta R = \left[\sum_{i=1}^{n} \left(\frac{\partial R}{\partial x_i} \cdot \delta x_i\right)^2\right]^{0.5} \tag{B.3}$$

Terms in the uncertainty equations that 3 times smaller than the largest term are suppressed by the root-sum-square method. Hence small terms have very small effects Moffat (1988).

B.3 Uncertainties

B.3.1 Uncertainties of the instrumentation

Instrumentation that is used in the current study include thermocouples, magnetic flow meters, pressure transducers and the power supply. Shown in Table B.2 are the uncertainties of each instrument used in the study. The uncertainty falls within the 95% confidence level.

Table B.2 Ranges and accuracies of instruments used

Instrument and sensor type	Range	Uncertainty
Type K thermocouple	0-300°C	±0.1°C
RTD (PT-100) sensor	0-200°C	±0.1°C
Schmierer, Electromagnetic Flow Meter	0.03 m/s ~ 12 m/s	±0.5%
ALIADP, Differential Pressure Transmitter (DPT)	0-25 kPa	±0.075%
Power supply	0 - 260 V	0.33 V
	0 - 12 A	0.04 A

B.3.2 Heat transfer uncertainties

B.3.2.1 Inlet and outlet and section temperatures

Since only one thermocouple was used to measure inlet temperature and one thermocouple to measure the outlet thermocouple the uncertainty of the measurement remains 0.1°C. For the stations also only one thermocouple was used and here the uncertainty is 0.1°C.

B.3.2.2 Fluid properties

All fluid properties and their uncertainties were calculated from the formulations obtained by Popiel et al. (1998). The uncertainties of the properties are given in Table B.3.

Table B.3 Uncertainties of fluid properties

Property	Uncertainty
Specific heat	2%
Thermal conductivity	5%
Dynamic viscosity	1%

B.3.2.3 Heat transfer coefficient

The heat transfer coefficient is calculated from Equation (B.4).

$$h(x) = \frac{\dot{q}}{T_w(x) - T_b(x)} \tag{B.4}$$

with its uncertainty given by Equations (B.5-B.6).

$$\delta h(x) = \left[\left(\frac{\partial h(x)}{\partial \dot{q}} \cdot \delta \dot{q}\right)^2 + \left(\frac{\partial h(x)}{\partial T_w} \cdot \delta T_w\right)^2 + \left(\frac{\partial h(x)}{\partial T_b} \cdot \delta T_b\right)^2\right]^{0.5} \tag{B.5}$$

$$\begin{aligned}\delta h(x) = \Bigg[\left(\frac{\delta \dot{q}}{T_w(x) - T_b(x)}\right)^2 &+ \left(\frac{-\dot{q}}{(T_w(x) - T_b(x))^2} \cdot \delta T_w\right)^2 \\ &+ \left(\frac{-\dot{q}}{T_w(x) - T_b(x)} \cdot \delta T_m\right)^2\Bigg]^{0.5}\end{aligned} \tag{B.6}$$

The wall temperatures are measured at 13 sections, and between each section the local heat transfer coefficients are calculated. The average heat transfer coefficient is obtained by adding all the local heat transfer coefficients and then dividing the result by 12.

$$h_{avg} = \frac{1}{n} \cdot (h(x_1) + \cdots + h(x_n)) \tag{B.7}$$

$$\delta h_{avg} = \left[\left(\frac{\partial h_{avg}}{\partial h(x_1)} \cdot \delta h(x_1)\right)^2 + \cdots + \left(\frac{\partial h_{avg}}{\partial h(x_n)} \cdot \delta h(x_n)\right)^2\right]^{0.5} \tag{B.8}$$

hence the uncertainty of the average heat transfer coefficient is determined by equation B.9

$$\delta h_{avg} = \frac{1}{n} \cdot (\delta h(x_1)^2 + \cdots + \delta h(x_n)^2)^{0.5} \tag{B.9}$$

B.3.2.4 Heat flux

The heat flux is calculated from Equation (B-10).

$$\dot{q}_{in} = \dot{Q}_{in}/A_s \tag{B.10}$$

with its uncertainty given by Equations (B.11-B.12).

$$\delta\dot{q}_{in} = \left[\left(\frac{\partial \dot{q}_{in}}{\partial \dot{Q}_{in}} \cdot \delta \dot{Q}_{in}\right)^2 + \left(\frac{\partial \dot{q}_{in}}{\partial A_s} \cdot \delta A_s\right)^2\right]^{0.5} \tag{B.11}$$

$$\delta\dot{q}_{in} = \left[\left(\frac{\partial \dot{Q}_{in}}{A_s}\right)^2 + \left(-\frac{\dot{Q}_{in}}{A_s^2} \cdot \delta A_s\right)^2\right]^{0.5} \tag{B.12}$$

B.3.2.5 Heat transfer

The input heat transfer uncertainty is calculated from Equation (B.13).

$$\dot{Q} = V \cdot I \tag{B.13}$$

with the uncertainty given by Equations (B.14-B.15)

$$\delta\dot{Q} = \left[\left(\frac{\partial \dot{Q}}{\partial V} \cdot \delta V\right)^2 + \left(\frac{\partial \dot{Q}}{\partial I} \cdot \delta I\right)^2\right]^{0.5} \tag{B.14}$$

$$\delta\dot{Q} = [(I \cdot \delta V)^2 + (V \cdot \delta I)^2]^2 \tag{B.15}$$

B.3.2.6 Heat transfer area

The heat transfer area is calculated from Equation (B.16).

$$A_s = \pi \cdot D \cdot L \tag{B.16}$$

with its uncertainty given by Equations (B.17-B.18).

$$\delta A_s = \left[\left(\frac{\partial A_s}{\partial D} \cdot \delta D\right)^2 + \left(\frac{\partial A_s}{\partial L} \cdot \delta L\right)^2\right]^{0.5} \tag{B.17}$$

$$\delta A_s = [(\pi \cdot \delta D \cdot L)^2 + (\pi \cdot D \cdot \delta L)^2]^{0.5} \tag{B.18}$$

B.3.2.7 Perimeter of test section

The perimeter of the test section is calculated from Equation (B.20).

$$P = \pi \cdot D \tag{B.20}$$

with its uncertainty given by Equation (B.21-B.22).

$$\delta P = \left[\left(\frac{\partial P}{\partial D} \cdot \delta D\right)^2\right]^{0.5} \tag{B.21}$$

$$\delta P = \pi \cdot \delta D \tag{B.22}$$

B.3.3 Dimensionless parameters

Since all the fluid flow and heat transfer equations are in terms of dimensionless parameters, the uncertainties of these parameters are needed to be determined. The Nusselt, Reynolds and Prandtl numbers are mainly used in this study of heat transfer and their respective uncertainties are shown below.

$$Nu_{avg} = \frac{h_{avg} \cdot D}{k} \tag{B.23}$$

with its uncertainty given by Equations (B.24-B.26).

$$\delta Nu_{avg} = \left[\left(\frac{\partial Nu_{avg}}{\partial h_{avg}} \cdot \delta h_{avg}\right)^2 + \left(\frac{\partial Nu_{avg}}{\partial D} \cdot \delta D\right)^2 + \left(\frac{\partial Nu_{avg}}{\partial k} \cdot \delta k\right)^2\right]^{0.5} \tag{B.24}$$

$$\delta Nu_{avg} = \left[\left(\frac{D}{k} \cdot \delta h_{avg}\right)^2 + \left(\frac{h_{avg}}{k} \cdot \delta D\right)^2 + \left(-\frac{h_{avg}}{k^2} \cdot \delta k\right)^2\right]^{0.5} \tag{B.25}$$

$$Re = \frac{4 \cdot \dot{m}}{\mu \cdot D \cdot \pi} \tag{B.26}$$

with its uncertainty given by Equations (B.27-B.28).

$$\delta Re = \left[\left(\frac{\partial Re}{\partial \dot{m}} \cdot \delta \dot{m}\right)^2 + \left(\frac{\partial Re}{\partial \mu} \cdot \delta \mu\right)^2 + \left(\frac{\partial Re}{\partial D} \cdot \delta D\right)^2\right]^{0.5} \tag{B.27}$$

$$\begin{aligned}\delta Re = \Bigg[\left(\frac{4}{\mu \cdot D \cdot \pi} \cdot \delta \dot{m}\right)^2 + \left(-\frac{4 \cdot \dot{m}}{\mu^2 \cdot D \cdot \pi} \cdot \delta \mu\right)^2 \\ + \left(-\frac{4 \cdot \dot{m}}{\mu \cdot D^2 \cdot \pi} \cdot \delta D\right)^2\Bigg]^{0.5}\end{aligned} \tag{B.28}$$

B.3.4 Friction factor uncertainties

The friction factors are calculated from its simplified Equation (B.29).

$$f = \frac{\Delta P \cdot \rho \cdot \pi^2 \cdot D^5}{8 \cdot L \cdot \dot{m}^2} \tag{B.29}$$

with its uncertainty given by Equations (B.30-B.31).

$$\begin{aligned}\delta f = \Bigg[\left(\frac{\partial f}{\partial \Delta P} \cdot \delta \Delta P\right)^2 + \left(\frac{\partial f}{\partial \rho} \cdot \delta \rho\right)^2 + \left(\frac{\partial f}{\partial D} \cdot \delta D\right)^2 + \left(\frac{\partial f}{\partial L} \cdot \delta L\right)^2 \\ + \left(\frac{\partial f}{\partial \dot{m}} \cdot \delta \dot{m}\right)^2\Bigg]^{0.5}\end{aligned} \tag{B.30}$$

$$\begin{aligned}\delta f = \Bigg[\left(\frac{\rho \cdot \pi^2 \cdot D^5}{8 \cdot L \cdot \dot{m}^2} \cdot \delta \Delta P\right)^2 + \left(\frac{\Delta P \cdot \pi^2 \cdot D^5}{8 \cdot L \cdot \dot{m}^2} \cdot \delta \rho\right)^2 \\ + \left(\frac{\Delta P \cdot \rho \cdot \pi^2 \cdot 5 \cdot D^4}{8 \cdot L \cdot \dot{m}^2} \cdot \delta D\right)^2 + \left(\frac{\Delta P \cdot \rho \cdot \pi^2 \cdot D^5}{8 \cdot L^2 \cdot \dot{m}^2} \cdot \delta L\right)^2 \\ + \left(-\frac{\Delta P \cdot \rho \cdot \pi^2 \cdot D^5}{8 \cdot L \cdot \dot{m}^3} \cdot \delta \dot{m}\right)^2\Bigg]^{0.5}\end{aligned} \tag{B.31}$$

B.4 Summary

The uncertainties of all the values discussed are presented in Table B.4.

Table B.4 Uncertainty ranges.

Variable name	Uncertainty range
Nu, avg	±6%
Nu, Local	±8%
h, avg	±6%
h, local	±9%
f	±10%

APPENDIX C

CLEANING OF TEST SECTION

C.1 Cleaning procedure

After completion of the one nanofluid testing run, the loop is drained completely and flushed several times to remove the remaining nanoparticles. It is preferred in many cases to use an alternative solvent family which consist the aqueous solution of chelating agent. Thus this agents should not have threat to damage to equipment during or after cleaning. Two different chelating agent were used in this experiment, as shown in Figure C.5.

Figure C.5 Chelating agent, which is used in this cleaning procedure.

At steady solution temperature of 30°C, degreaser + antifoam and then decon 90 were pumped to the system separately for several times. After each run, the loop was cleaned and flushed by using DW for 3 times and each times for 1 hr. However in order to ensure of that, there are no surface modifications or fouling in the system, DW run is once again performed and compared to theory. Figure C.6 represents heat transfer coefficient as a function of velocity before and after cleaning runs for DW at the bulk temperature of 30°C. It is observed that the data reproduced well, test rig was highly accurate and remains within the confidence level of 95% and rms error < 1%. It is therefore concluded that no major modification of the tube surface occurred due to the usage of nanofluids.

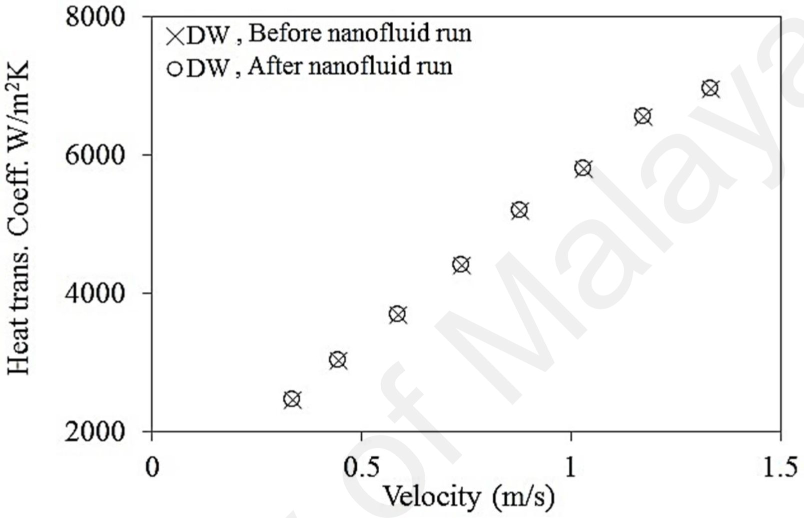

Figure C.6 Heat transfer coefficient for DW retest.

LIST OF PUBLICATIONS AND AWARDS

Related to thesis:

1- Experimental investigation of convective heat transfer using graphene nanoplatelet based nanofluids under turbulent flow conditions

Industrial and Engineering Chemistry Research, vol. 53, no. 31, pp. 12455–12465, 2014

2- Investigation of thermal conductivity and rheological properties of nanofluids containing graphene nanoplatelets

Nanoscale Research Letters, vol. 9, no. 1, 2014

3- Preparation, characterization, viscosity, and thermal conductivity of nitrogen-doped graphene aqueous nanofluids

Journal of Materials Science, vol. 49, no. 20, pp. 7156–7171, 2014

4- Experimental and numerical investigation of graphene nanoplatelets nanofluids flow in circular pipe,

Submitted to International Journal of Heat and Mass Transfer

5- Experimental convective heat transfer studies of graphene nanoplatelet aqueous nanofluids with different specific surface areas in a turbulent flow regime,

Submitted to Experimental Thermal and Fluid Science

6- Electrical conductivity of aqueous nitrogen-doped graphen nanofluids

Submitted to Microfluidics and Nanofluidics

7- Facile Synthesis of green reduced graphene Oxide nanofluid

Submitted to International Journal of Heat and Mass Transfer

Unrelated to the thesis:

1- Numerical simulation of laminar to turbulent nanofluid flow and heat transfer over a backward-facing step
Applied Mathematics and Computation, vol. 239, pp. 153–170, 2014

2- Comparison of the finite volume and lattice boltzmann methods for solving natural convection heat transfer problems inside cavities and enclosures
Abstract and Applied Analysis, vol. 2014, 2014

3- Sustainability and environmental impact of ethanol as a biofuel
Reviews in Chemical Engineering, vol. 30, no. 1, pp. 51–72, 2014

4- A review of studies on forced, natural and mixed heat transfer to fluid and nanofluid flow in an annular passage
Renewable and Sustainable Energy Reviews, vol. 39, pp. 835–856, 2014

5- Numerical study of entropy generation due to coupled laminar and turbulent mixed convection and thermal radiation in an enclosure filled with a semitransparent medium
The Scientific World Journal, vol. 2014, 2014

6- A comprehensive literature review of bio-fuel performance in internal combustion engine and relevant costs involvement
Renewable and Sustainable Energy Reviews, vol. 30, pp. 29–44, 2014

7- Simulation of heat transfer to separation Air flow in a concentric pipe
International Communications in Heat and Mass Transfer, vol. 57, pp. 48–52, 2014

8- Preparation and characterization of palmitic acid/graphene nanoplatelets composite with remarkable thermal conductivity as a novel shape-stabilized phase change material
Applied Thermal Engineering, vol. 61, no. 2, pp. 633–640, 2013

9- A comprehensive review of bio-diesel as alternative fuel for compression ignition engines
Renewable and Sustainable Energy Reviews, vol. 28, pp. 410–424, 2013

10- Computational simulation of heat transfer to separation fluid flow in an annular passage
International Communications in Heat and Mass Transfer, vol. 46, pp. 92–96, 2013

11- A review of milk fouling on heat exchanger surfaces
Reviews in Chemical Engineering, vol. 29, no. 3, pp. 169–188, 2013

12- Numerical study of turbulent heat transfer in separated flow: Review
International Review of Mechanical Engineering, vol. 7, no. 2, pp. 337–349, 2013

13- Investigation of viscosity and thermal conductivity of alumina nanofluids with addition of SDBS
Heat and Mass Transfer/Waerme- und Stoffuebertragung, vol. 49, no. 8, pp. 1109–1115, 2013

14- Numerical study of entropy generation in a flowing nanofluid used in micro- and minichannels
Entropy, vol. 15, no. 1, pp. 144–155, 2013

15- Numerical simulation of heat transfer to separation air flow in an annular pipe
International Communications in Heat and Mass Transfer, vol. 39, no. 8, pp. 1176–1180, 2012

16- A comprehensive review of milk fouling on heated surfaces
Critical reviews in food science and nutrition (just-accepted)

17- Numerical investigation of heat transfer enhancement in a rectangular heated pipe for turbulent nanofluid

The Scientific World Journal, Volume 2014 (2014)

18- Basic effects of pulp refining on fibre properties- A review

Carbohydrate Polymers (just-accepted)

19- Thermo-physical properties and convective heat transfer to nanofluids: A review

Submitted to Nanoscale Research Letters

20- A review of mineral fouling on heat exchanger surfaces

Submitted to Reviews in Chemical Engineering (RevChemEng)

21- A comprehensive review of fouling mitigation with chemical and natural fiber additives

Submitted to Reviews in Chemical Engineering (RevChemEng).

22- Preparation of nitrogen-doped graphene/palmitic acid shape stabilized composite phase change material with remarkable thermal properties for thermal energy storage,

Applied Energy (just-accepted)

Book Chapter:

1- Heat Transfer to Separation Flow in Heat Exchangers.

S. N. Kazi (Ed.), An Overview of Heat Transfer Phenomena (pp. 497-525): InTech.

Patent:

1- Graphene nanoplatelets (GNPs) nanofluid use as an advanced fluid for heat exchanging liquids

Just-accepted

Conference:

1- A review of fouling mitigation with chemical and natural fiber additives, 2nd International Conference on Mechanical, Automotive and Aerospace Engineering (ICMAAE 2013), 2-4 July 2013, Kuala Lumpur
2- Numerical Study of Turboprop Engine performance at Off-design Condition, First Management and Engineering Congress, Singapore, 2013, Singapore.
3- Numerical Study of the effect of coal diameter on pulverized coal combustion to reduce pollutants, 2nd International Conference on Mechanical, Automotive and Aerospace Engineering (ICMAAE 2013), Kuala Lumpur, 2013, Malaysia